Chest Wall Deformity from Tissue Expanders Identified on Chest MR Angiography of Perforator Flap Angiography studies

Nancy Ruiz-Uribe[1], Hanieh Attari, MD[1], Joshua Levine, MD[2], Martin R. Prince, MD, PhD[1,3]

[1]Weill Cornell Medical College & New York Presbyterian Hospital, [2]New York Eye and Ear Infirmary of Mount Sinai, Plastic Surgery, [3]Columbia University College of Physicians and Surgeons, New York, NY, USA

Purpose: MR angiography of the chest evaluates perforators and internal mammary vasculature in patients undergoing autologous free-flap breast reconstruction. It lowers the risk of complications and fat necrosis after surgery by assuring that the transplant vessels are patent and providing sufficient blood flow to reconstruction site. Commonly, a tissue expander is used following mastectomy, to help with stretching the skin and creating a pocket for breast reconstruction. Although tissues expanders are considered MR unsafe due to the artifact produced by their internal magnets as well as migration/rotation, we routinely image patients with fully expanded tissue expanders prior to breast reconstruction. We have noticed that the chest wall under the tissue expander is often caved inward and this has been corroborated at surgery.

In this study, we retrospectively reviewed chest MR angiography studies in patients with tissue expanders or implants undergoing autologous free flap breast reconstruction performed in our medical center to determine prevalence of chest wall compression.

Methods: From January 1, 2013 to August 31, 2018 eighty-five patients with tissue expanders or implants underwent chest MR angiography preoperatively for autologous free-flap breast reconstruction. In these patients, the chest wall was evaluated for volume of deformity/compression by the tissue expander and for sternal angle that tilts as the chest wall collapses on one side.

Results: Chest wall deformity was more significant with tissue expanders than implants (p<0.0001). In 36 patients with expanders the estimated volume of chest wall compression was 24±10.7 ml on left and 52±34 ml on right side (p<0.0001). With unilateral tissue expanders, sternal angle measured a mean of 10.5±6 degrees compared to 3.6±4 in patients with only implants and no history of tissue expander (p<0.0001). Pleural enhancement was identified in one case under the side of chest compression by tissue expander, suggesting an inflammatory/remodeling process.

Figure 1. Chest Wall Compression by Expanders (L) vs. Implants (R)

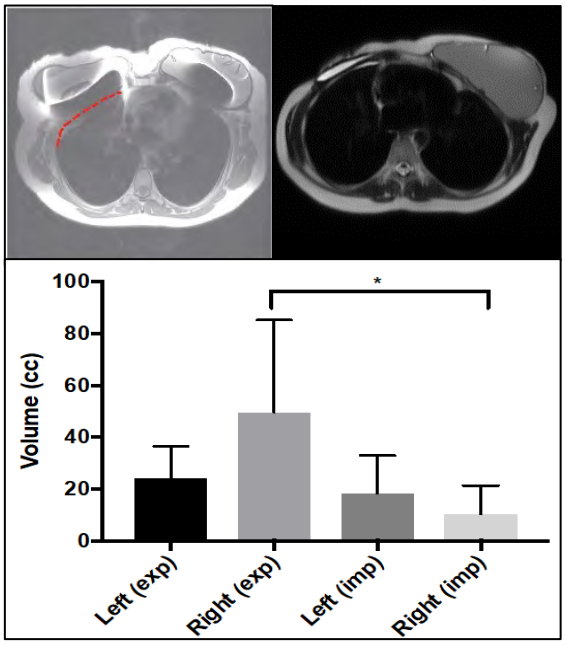

Figure 2. Sternum angle deflection

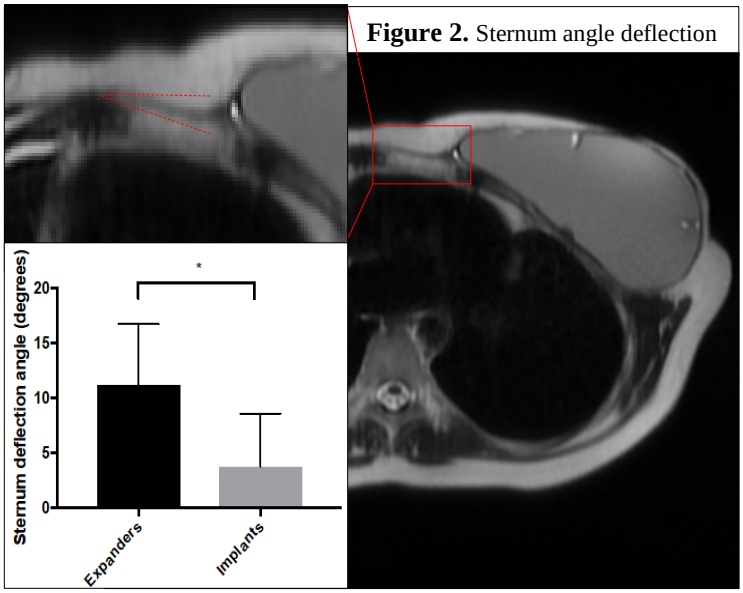

Table 1. charachteristics of patients with Tissue expanders

	Right	Left
No. of patients	36	
Age (years)	49±8, range: 30-67	
Volume of expansion (ml)	620±344	516±274
Volume of compression (ml)	52±34	24±10.7
Sternal angle deflection (degree)	10.5±6	

Discussion: These data in 85 patients show that not only is MRI in patients with tissue expanders safe, but that it also identifies an important tissue expander complication: chest wall compression deformity. This deformity leads to a higher autologous fat transplantation volume requirement to achieve symmetrical results which can be predicted based upon the volume of chest deformity.

Assessment of Pulmonary Artery Stiffness in Patients With Heart Failure Using Cardiac Magnetic Resonance

Xuewen Hou,Mahsa Zamani,Paulius Bucius,Neye Marthe, Tanacli Radu,Lukas Stoiber,Sebastian Kelle
Department of Internal Medicine/Cardiology, German Heart Center Berlin and Charité University Medicine Berlin, Berlin, Germany

Purpose: Increased arterial stiffness is an emerging biomarker in the assessment of cardiovascular event risk[1].This study sought to evaluate indexes of pulmonary artery (PA) stiffness in patients with heart failure(HF)using cardiac magnetic resonance (CMR).

Methods:17 healthy volunteers(9 male,mean age 63)and 55 patients with HF were enrolled in this study.According to the 2016 ESC guidelines for the diagnosis and treatment of heart failure[2],patients were divided them into 3 groups:individuals with HF and preserved left ventricular ejection fraction(LVEF)(HFpEF)(n=20,11 male,mean age 76),HF and mid-range LVEF (HFmEF)(n=18,12 male,mean age 67),HF and reduced LVEF(HFrEF)(n=17,13 male,mean age 65).All participants underwent CMR imaging.2D cine phase-contrast images perpendicular to the pulmonary trunk were obtained on a 1.5T Philips MRI scanner. The maximal and minimal PA area (end-systolic lumen area and end-diastolic lumen area,respectively)were measured using specialized software (Medis,Qflow).Indexes of PA stiffness(Pulsatility and Pulse wave velocity)were determined.

Results: As shown in Figure 1,all quantified indexes showed increased PA stiffness in patients with HF subgroups(HFpEF,HFmEFand HFrEF) in comparison with those healthy volunteers.The value of PA pulsatility of patients with HFpEF(26.87±9.33) and HFrEF(26.19±7.60) were significantly lower than healthy volunteers (44.80±4.60),and pulsatility of patients with HFmEF(23.04±5.83) was lowest of all groups ($p < 0.0001$ for all three)(Fig.1A).The value of PA Pulse wave velocity of healthy volunteers (2.05±0.50) was significantly lower than HF subgroups [HFrEF(2.79±0.90), HFmEF (2.87±0.82) and HFpEF(3.02±0.66),respectively] ($p < 0.005$ for all three) , and there was no statistical difference between HF subgroups(Fig. 1B).

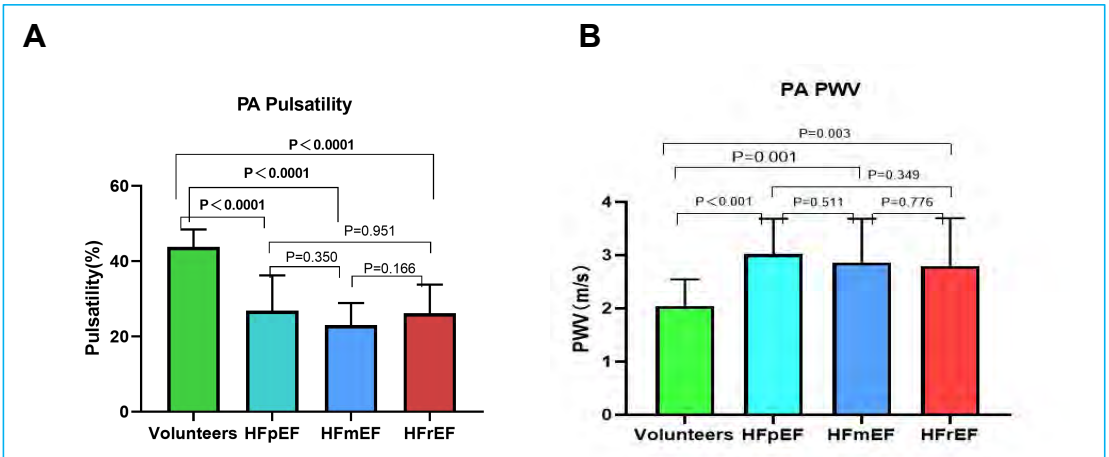

Figure 1. Comparison for PA pulsatility (A), and Pulse wave velocity (B) in healthy volunteers and HF Patient subgroups

Discussion: We used CMR to noninvasively assess pulmonary artery stiffness.Our results demonstrated that PA stiffness was increased in patients with HF compared to that of the healthy subjects.Additional studies in larger patient groups are necessary to evaluate the role of PA stiffness in HF patients.

References: 1. Laurent S, Alivon M, Beaussier H,Boutouyrie P.Aortic stiffness as a tissue biomarker for predicting future cardiovascular events in asymptomatic hypertensive subjecta. Ann.Med.44(Suppl.1),S93-S97. 2.European Journal of Heart Failure(2016)18,891-975.

Highly Accelerated NCE-MRA Using *k*-space Subtraction with Phase and Intensity Correction (KSPIC): Improved Reconstruction Accuracy and Background Suppression

Hao Li[1], Andrew Nicholas Priest[1], Martin John Graves[1] and David John Lomas[1]

[1] Department of Radiology, University of Cambridge and Addenbrooke's Hospital, Cambridge, United Kingdom

Purpose: To develop a compressed sensing (CS) reconstruction method for highly accelerated subtractive non-contrast-enhanced MRA (NCE-MRA), which applies an intensity correction to suppress background tissue, together with a phase correction procedure to restore the polarity of negative signal.

Methods: Fig. 1 shows the flow chart of the proposed *k*-space Subtraction with Phase and Intensity Correction (KSPIC). Firstly, a fast CS reconstruction with only one iteration is performed on 10% equally-spaced slices selected along the readout direction. Secondly, a robust regression model using iteratively reweighted least squares[1] is used to acquire the linear regression coefficient for the bright-blood vs dark-blood images (weighted towards background pixels). Next, complex subtraction is performed on the *k*-space data, using the linear regression coefficient as the weighting factor. A CS reconstruction with 10 iterations is then performed on the full subtracted dataset. Finally, a background phase reference is reconstructed from the symmetric central part of the bright-blood dataset and is used to restore the polarity of the negative signal caused by complex subtraction. CS reconstruction is performed using the Split-Bregman algorithm[2] with total variation minimisation. SPIRiT[3] was used for parallel imaging reconstruction.

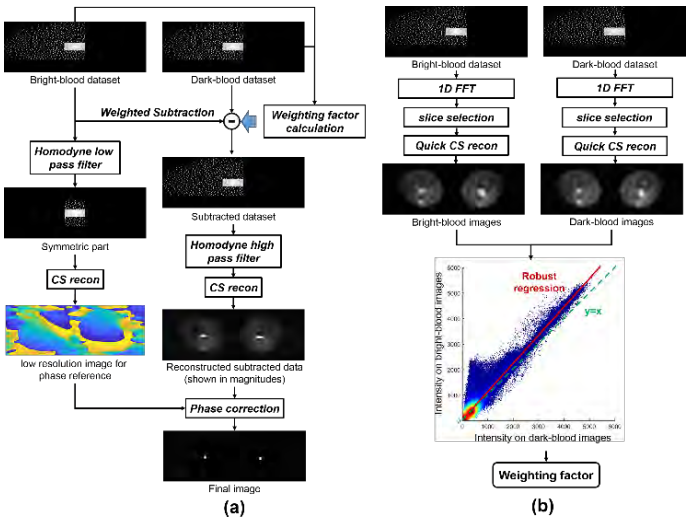

Fig. 1. Flow charts of (a) the reconstruction process and (b) the weighting factor calculation procedure.

Nine healthy subjects were imaged using a 1.5 T Discovery MR450 system (GE Healthcare, WI) and a 32 channel cardiac array coil. Parameters included ETL 60-90, FOV 40-44 cm, slice thickness 2 mm, TE 60ms, TR 2 or 3 heartbeats depending on heart-rate. Six fully sampled femoral Fresh Blood Imaging (FBI)[4] datasets (224×224×80, 360 TRs) were acquired for retrospective reconstruction. Correlation coefficients (CC) and the normalized mean square error (NMSE) were calculated between the reference images (fully sampled) and the retrospectively reconstructed images using the acceleration factors (AFs) from 4 to 20. For the prospective study, 5 groups of accelerated FBI datasets (320×320×80) were acquired, and each group includes 4 datasets accelerated by 10× (84 TRs), 15× (58 TRs), 20× (44 TRs) and 25× (36 TRs) respectively.

Results: Fig. 2 shows the performance of conventional magnitude subtraction (MS), *k*-space subtraction (KS) and KSPIC in prospectively accelerated datasets using AF from 10 to 25. Fig. 3 shows NMSE and CC for retrospectively accelerated datasets using AF from 4 to 20. Both KSPIC and MS achieved large CC and small NMSE for small AFs, but the performance of MS degraded rapidly with increasing AFs. KS has the worst performance, which is mainly due to the artefacts caused by negative signal with reversed polarity. KSPIC also has the best arterial depiction and image quality with large AFs as shown in Fig 2. When the AF is large, increased noise level and artefacts can be observed on MS results, and missing small branches can be noticed in KS (red arrows). Moreover, residual venous signal can be observed on both MS and KS (yellow arrows) but is absent from KSPIC images.

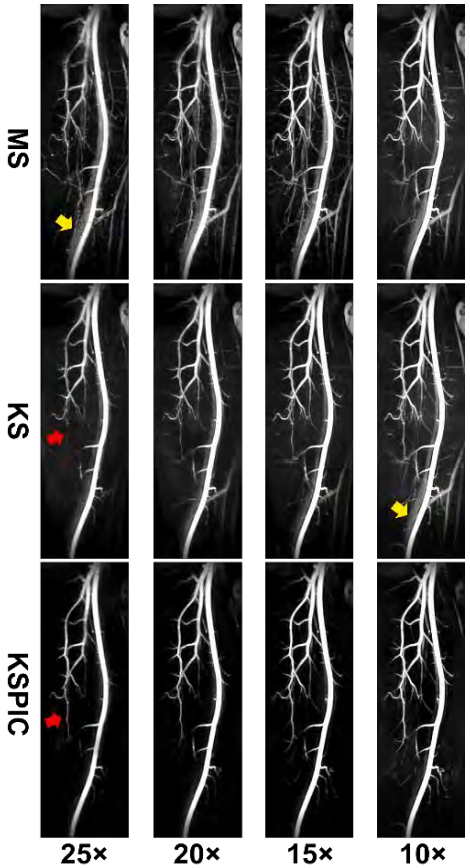

Fig. 2. Example MIP images for different methods with varying acceleration factors.

Conclusion: The proposed KSPIC improves reconstruction accuracy, image quality and background tissue suppression of highly accelerated subtractive NCE-MRA. Compared with conventional magnitude subtraction and k-space subtraction approaches, KSPIC permits good image quality to be maintained up to higher acceleration factors.

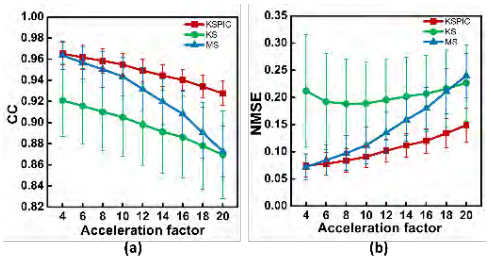

Fig. 3. Plots of NMSE and CC against acceleration factor for different methods.

Reference: 1. Li et al., ISMRM. 2018:922. 2. Goldstein et al., SIAM J Imaging Sci. 2009;2:323. 3. Lustig et al., MRM. 2010;64(2):457-471. 4. Miyazaki et al., JMRI. 2000; 12:776–783.

Performance of a dedicated carotid PET/MRI coil

S.M. Mueez Aizaz[1,2], Rik P.M. Moonen[1,2], Roel Wierts[1], Jochem A.J. van der Pol[1], Hans Zwart[3], Abe J. van der Werf[3], Joachim E. Wildberger[1,2], Jan A. Bucerius[1,2], M. Eline Kooi[1,2]

[1]Radiology and Nuclear Medicine, Maastricht University Medical Center, Maastricht, Netherlands; [2]CARIM School for Cardiovascular Diseases, Maastricht University, Maastricht, Netherlands, [3]Machent B.V, Roden, Netherlands.

Introduction: Dedicated carotid radiofrequency (RF) coils allow high resolution carotid vessel wall imaging.[i] An RF MRI coil introduces attenuation, which can result in a bias in PET quantification.[ii] One method to correct for the attenuation is to create an attenuation map for the coil based on CT images, however this is complex for surface coils.[iii] The method we present is to use a dedicated PET-lucent RF coil. In this study, we compare the performance of a newly developed dedicated PET/MRI carotid coil against an original model designed for MRI-only use, in a phantom and patient study.

Methods: A 3.0T Siemens Biograph mMR PET/MRI scanner was used to test the performance of the different coils in a phantom and in patients. The coils under investigation were the PACC-SB30 (PET/MRI coil) and PACC-ST30 (MRI-only coil), i.e. 4-channel bilateral carotid coils (Machnet BV, Roden, The Netherlands).

Phantom Study: A 14-cm-diameter cylindrical phantom filled with an aqueous solution of 18F-fluordeoxyglucose (18F-FDG) was scanned without dedicated coils (baseline), then with the PET/MRI coil (Figure 1A) and finally with the MRI-only coil. Acquisition time was adjusted for the amount of radioactive decay. A CT attenuation map of the phantom was manually co-registered to the images to generate attenuation-corrected PET reconstructions (without correcting for coils). Regions-of-interest (ROIs) were drawn (2 cm diameter) in each transversal 2 mm PET slice at the typical position of the carotid artery relative to the coil. The decay-corrected normalized activity (in %) was calculated and compared with baseline values. The signal to noise ratio (SNR) of MR images of the phantom were also calculated.

Patient Study: Three patients scheduled to receive 2MBq/kg activity of 18F-FDG for a clinical examination volunteered for this study. The study was approved by the local ethics committee and all patients provided written informed consent. Directly following the clinical exam, patients were subsequently scanned for 10 minutes with the PET/MRI coil, the MRI-only coil and without a dedicated coil. Attenuation maps were generated using only the body coil to ensure that the same correction is performed in all configurations and differences on the PET image are caused by attenuation from the coil under investigation. ROIs were drawn on both left and right carotid arteries on the fused PET/MR images adjacent to the center of the coil and the mean standardized uptake values (SUV_{mean}) were compared. One-way ANOVA was performed to check for significant difference between the mean values from the coils followed by post hoc test (Tukey HSD) to check for significant difference between each of the coils. The SUV_{max} of a lesion (Figure 1B) in a patient with oropharyngeal cancer was also compared.

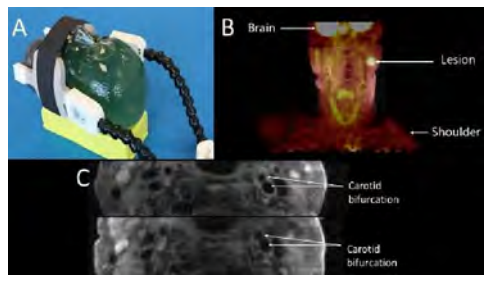

Figure 1. (A) PET/MRI coil placed around a phantom head. (B) Coronal fused PET/MR image acquired with the PET/MRI coil only of a patient with oropharyngeal cancer (note that the MRI field-of-view (FOV) is smaller than the PET FOV). (C) Two transversal MR images of the left carotid bifurcation acquired with a 3D T1w SPACE sequence. The upper image is acquired with a PET/MRI coil and the lower image with an MRI-only coil. The image quality of the two images is very similar.

Results: Phantom Study: Figure 2 shows a graphical representation of the normalized activity as a function of longitudinal position (i.e. adjoining transversal PET slices). The PET/MRI coil demonstrates only a slight decrease (3-4%, at the order of scan-rescan variation) at the position of the coil. The MRI-only coil shows a more substantial decrease (up-to 10%) in this region. In contrast with the MRI-only coil, the signal loss of the dedicated PET/MRI coil at the electronic housing is outside the region that would normally be imaged with the coil. The SNR using the PET/MR coil (104.45±17.9) as compared to the MR-only coil (82.84±13.69) was not significantly different (p=0.35).

Patient Study: The SUV_{mean} (mean ± standard error) were 1.34±0.15 for the PET/MRI coil (n=6), 1.03±0.13 (n=4) for MRI-only and 1.17±0.22 (n=6) for baseline (no dedicated coil). The SUVs acquired with the PET/MRI coil were significantly higher than with the MRI-only coil (p=0.039) (Figure 3). SUVs of the other configurations were not significantly different. The SUV_{max} of the lesion visible in a patient with oropharyngeal cancer acquired with the PET/MRI coil was 6.1, while 5.8 without a dedicated coil.

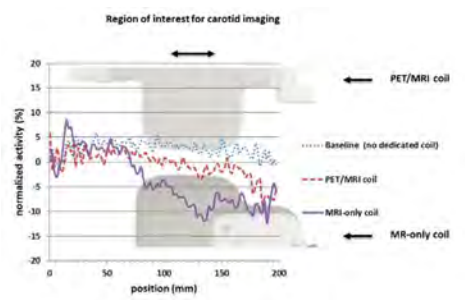

Figure 2. Normalized activity values in the ROI as a function of the longitudinal position for the different coils. In the background both coils are shown for reference: grey areas are coil elements (foam covered), white is the electronics housing (plastic; higher attenuation).

Discussion: The phantom experiments showed that the difference between the SUV with the PET/MRI coil and baseline is less than 4% in the region of interest, while a more pronounced decrease in the SUV is observed with the MRI-only coil. There is no significant difference in MR image quality (SNR) observed. In the patient study, a non-significantly different SUV for the PET/MRI coil compared to baseline is in-line with the phantom results. A significantly lower SUV observed with the MRI-only coil in comparison to the PET/MRI coil demonstrates that significant attenuation effects are resolved by the PET-lucent design. The non-significant difference between the MRI-only coil and the baseline SUV values in the patients may be due to the low sample size.

Conclusion: The phantom study clearly demonstrates significantly less attenuation by the dedicated PET/MRI coil as compared to the MRI-only coil. Initial data from three patients show similar findings.

Acknowledgements This project has received funding from the European Union (EU) Horizon 2020 research and innovation program under the Marie Skłodowska- Curie grant agreement No. 722609 and from Stichting de Weijerhorst.

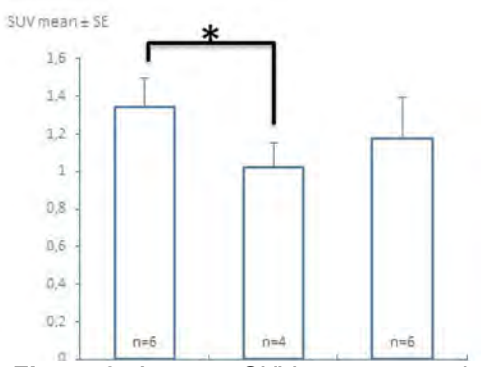

Figure 3. Average SUV mean ± standard error of the carotid arteries. * represents significant difference.

References:

i Saba, L., C. Yuan, T. S. Hatsukami, N. Balu, Y. Qiao, J. K. DeMarco, T. Saam, A. R. Moody, D. Li, C. C. Matouk, M. H. Johnson, H. R. Jager, M. Mossa-Basha, M. E. Kooi, Z. Fan, D. Saloner, M. Wintermark, D. J. Mikulis, B. A. Wasserman and N. Vessel Wall Imaging Study Group of the American Society of (2018). "Carotid Artery Wall Imaging: Perspective and Guidelines from the ASNR Vessel Wall Imaging Study Group and Expert Consensus Recommendations of the American Society of Neuroradiology." AJNR Am J Neuroradiol 39(2): E9-E31.

ii Delso, G., A. Martinez-Moller, R. A. Bundschuh, R. Ladebeck, Y. Candidus, D. Faul and S. I. Ziegler (2010). "Evaluation of the attenuation properties of MR equipment for its use in a whole-body PET/MR scanner." Phys Med Biol 55(15): 4361-4374.

iii Mootaz Eldib, Jason B., Philip M Robson, Claudia Calcagno, David D Faul, Charalampos Tsoumpas, Zahi A Fayad (2015). "Markerless attenuation correction for carotid MRI surface receiver coils in combined PET/MR imaging." Physics in Medicine & Biology: 4705–4717

Application of k_Z-Space-Based Processing for Providing Improved Through-Plane Resolution in 2D Multi-slice Imaging of the Prostate

S Kargar, EA Borisch, RC Grimm, *A Kawashima, EG Stinson, SJ Riederer
Mayo Clinic, Rochester MN USA; *Mayo Clinic, Scottsdale AZ USA

Purpose: To apply the method of k_Z-space-based processing [1] for improved through-plane resolution of T2-weighted spin-echo and diffusion-weighted 2D multi-slice prostate MRI.

Methods: Millimeter and potentially sub-mm through-plane resolution is provided by compensating for the ≈3 mm thick slice profile while also accounting for aliasing. Slices are acquired with modest slice-to-slice overlap using a conventional multi-slice sequence with multiple passes to suppress slice-to-slice interference. The method was first applied to T2-weighted spin-echo (T2SE) imaging of the prostate. In a study of 16 patients, reference images were first acquired using a standard T2SE sequence comprised of 25-28 3 mm thick axial sections, acquired on average in 4:40 m:s. These were compared with the k_Z-based multislice (KZM) approach which acquired 75-84 overlapped 3 mm thick slices in 6:40 m:s and reconstructed to 1 mm effective slice thickness. The KZM acquisition used fewer averages than the standard to limit scan time. Results were compared using prostate-MRI-specific criteria for sharpness as well as overall image quality. To assess further potential, the KZM was also applied to diffusion-weighted imaging (DWI) of the prostate, which also uses 2D multi-slice acquisition but typically coarser resolution. Diffusion results were also compared in patients using similar evaluation criteria.

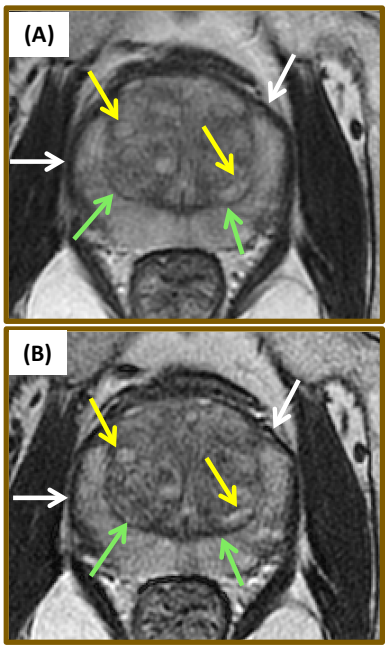

Figure 1. Comparison of conventional (A) and improved through-plane resolution (B) T2SE images of prostate in axial orientation. Note improved sharpness of prostate capsule in (B) (white arrows), zonal differentiation (green), and nodules in transition zone (yellow).

Results: For all sharpness criteria the KZM method was superior to the conventional acquisition but with some modest reduction in overall image quality, primarily due to motion. A sample comparison is shown in Figure 1. Initial results in prostate DWI show that the regularization of the estimation process requires adjustment to account for the differences in resolution and SNR of DWI vs. T2SE, but improved depiction of high contrast lesions is feasible.

Discussion: Super-resolution methods have been widely studied in MRI [2] but historically have been based on reconstruction in the spatial domain [3]. The KZM method transforms the 80-100 slices into k_Z-space for reconstruction. It has been shown here to work for two specific sequences, T2SE and DWI of prostate, and may be applicable to MRA [4].

References: [1] Kargar S, Magn Reson Med, epub Mar 2019; [2] Van Reeth E, Concepts in MRI 40A:306 (2012); [3] Irani M, CVGIP 53:231 (1991); [4] Koktzoglou, Magn Reson Med 79:683 (2018)

Free-Breathing Fast Low-Angle Shot Quiescent-Interval Slice-Selective MR Angiography for Improved Detection of Vascular Stenoses in the Pelvis and Abdomen

Akos Varga-Szemes, MD, PhD[1]; Alanna Emily Aherne, MD[2]; U. Joseph Schoepf, MD[1]; Thomas M. Todoran, MD[3]; Ioannis Koktzoglou, PhD[4,5], Robert R. Edelman, MD[2,4]

[1]Division of Cardiovascular Imaging, Department of Radiology, Medical University of South Carolina, [2]Department of Radiology, Feinberg School of Medicine, Northwestern University, [3]Division of Cardiology, Department of Medicine, Medical University of South Carolina, [4]Department of Radiology, Northshore University HealthSystem, [5]Department of Radiology, University of Chicago Pritzker School of Medicine

Purpose: Balanced steady-state free precession (bSSFP)-based quiescent-interval slice-selective (QISS) magnetic resonance angiography (MRA) is accurate for the non-contrast evaluation of peripheral artery disease (PAD); however, drawbacks include the need for breath-holding and sensitivity to off-resonance artifacts. The purpose of this study was to evaluate the image quality and diagnostic accuracy in the pelvis and abdomen of free-breathing fast low-angle shot (FLASH)-based QISS techniques in comparison to standard QISS in patients with PAD, using computed tomographic angiography (CTA) as the reference.

Methods: Twenty-seven patients (69±10 years, 17 men) with PAD were enrolled in this IRB approved, HIPAA compliant prospective study between April and December 2018. Patients underwent non-contrast MRA using standard bSSFP-based QISS and prototype free-breathing radial-FLASH and Cartesian-FLASH-based QISS at 3T. A subset of patients (n=22) also underwent CTA as the reference standard. Nine arterial segments per patient were evaluated spanning the abdomen, pelvis, and upper thigh regions. Objective (signal intensity ratio (SIR) and relative standard deviation (SD)) and subjective image quality (4-point scale) and stenosis (>50%) were evaluated by two readers and compared using one-way analysis of variance, Wilcoxon and McNemar tests, respectively.

Results: A total of 179 vascular segments were available for analysis by all QISS techniques. No significant difference was observed among bSSFP, radial-FLASH, and Cartesian-FLASH-based techniques in SIR ($p=0.428$) and relative SD ($p=0.220$). Radial-FLASH-based QISS demonstrated the best image quality ($p<0.0001$) and the highest inter-reader agreement ($\kappa=0.721$). The sensitivity values of bSSFP, radial-FLASH, and Cartesian-FLASH-based QISS for the detection of >50% stenosis were 76.0%, 84.0%, and 80.0%, respectively, while specificity values were 97.6%, 94.0%, and 92.8%, respectively. Moreover, FLASH-based QISS consistently reduced off-resonance artifacts compared to the bSSFP-based approach.

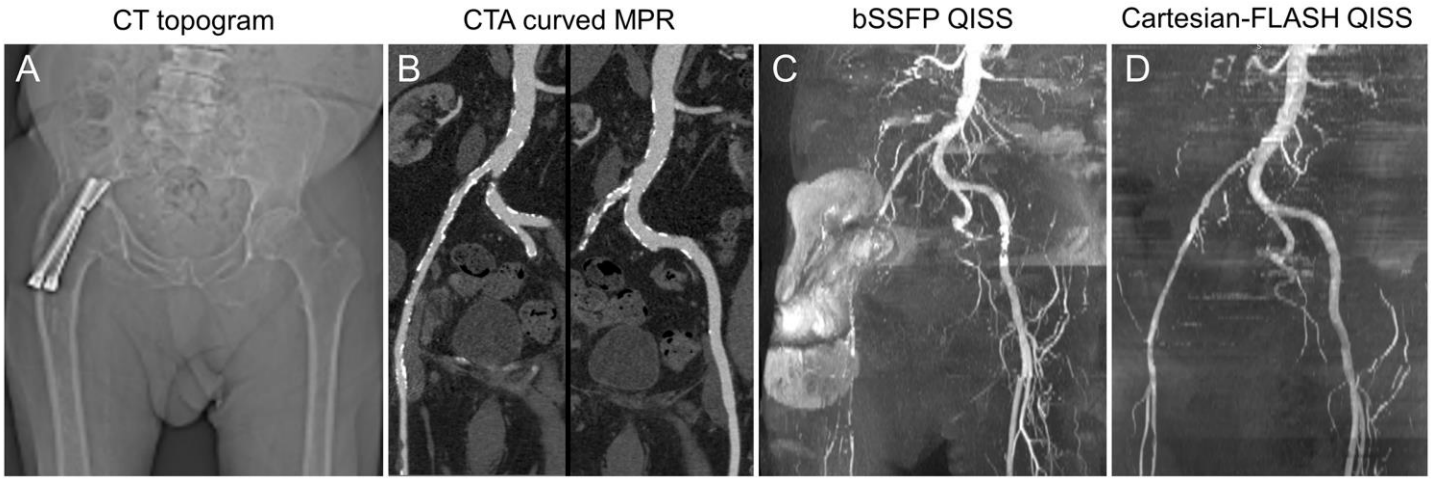

Discussion: Free-breathing FLASH-based QISS MRA techniques provide improved image quality and sensitivity, high specificity, and reduced off-resonance artifacts for vascular stenosis detection in the abdomen and pelvis.

Efficacy of Gadoterate Meglumine-enhanced MRA in evaluating thoracic aortic diseases compared with Gadobutrol-enhanced MRA.

Alyssa Singer, Louise Collins, Ali Serhal, Pascale Aouad, Julie Blaisdell, James Carr
Northwestern University, Chicago, IL, United States

Purpose:
Contrast enhanced (CE) magnetic resonance angiography (MRA) and computed tomographic (CT) angiography are equally valid techniques for imaging patients with thoracic aortic disease, although contrast-enhanced MRA lacks radiation exposure (1). Macrocyclic gadolinium-based contrast agents are being used with increased frequency in CE MRA, though it is unclear whether the available macrocyclic agents differ in clinical performance. The purpose of this study is to assess whether gadoterate meglumine- and gadobutrol-enhanced MRA provide similar image quality and comparable aortic measurements.

Figure 1. Sagittal contrast enhanced MRA of the thoracic aorta using Gadoterate Meglumine (a) and Gadobutrol (b) demonstrating similar image quality.

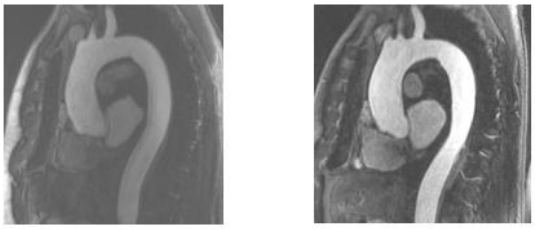

(a) (b)

Methods
Twenty-seven patients with known or suspected thoracic aortic disease receiving clinically-indicated, gadobutrol-enhanced MRA examinations of the thoracic aorta were prospectively recruited under an IRB approved protocol to undergo a similar gadoterate meglumine-enhanced MRA for research purposes. The gadoterate meglumine research MRA occurred on average 4.8 weeks following the standard of care exam. Injection rate and contrast volume were made consistent for both studies. Thoracic aortic diameter measurements were calculated at the levels of the sinus of Valsalva, Sino-tubular junction, ascending aorta, proximal arch, distal arch and distal descending aorta for both scans (according to AHA guidelines). Diameters obtained from the gadobutrol-enhanced MRAs and gadoterate meglumine-enhanced MRAs were assessed for absolute agreement using two-way mixed effects model ICCs. Qualitative analysis was performed by two blinded radiologists by scoring 4 arterial segments for image quality using a 5-point Likert scale and artifact and wall conspicuity using a 4-point Likert scale. Qualitative ratings were compared using Wilcoxon signed-rank tests ($\alpha = 0.05$).

Table 1. Level of agreement between the aortic diameters (mm) of Gadoterate Meglumine and Gadobutrol enhanced MRA

	Aortic Diameters (mm) Gadoterate Meglumine MRA	Aortic Diameters (mm) Gadobutrol MRA	ICC (95% CI)
Sinus of Valsalva	4.1±0.4	4.2±0.4	0.96 (0.9-0.98)
Sino-Tubular Junction	3.6±0.5	3.6±0.5	0.95 (0.87-0.98)
Ascending Aorta	3.8±0.6	3.8±0.6	0.98 (0.95-0.99)
Proximal Arch	3.4±0.5	3.4±0.5	0.95 (0.90-0.98)
Distal Arch	2.6±0.3	2.7±0.3	0.91 (0.64-0.97)
Distal Descending Aorta	2.5±0.3	2.5±0.3	0.92 (0.83-0.96)

Note: diameters are presented as mean ± SD

Results
There was excellent agreement of all thoracic aortic measurements between the gadoterate meglumine-enhanced and gadobutrol-enhanced scans (Table 1). Additionally, both reviewers showed no significant difference in qualitative ratings of image quality, artifact, or wall conspicuity at all assessed levels of the aorta when comparing scans performed with each contrast agent (Table 2).

Table 2. Qualitative image scores for Gadobutrol and Gadoterate Meglumine

		IQ_Root	Art_Root	Wall_Root	IQ_Arch	Art_Arch	Wall_Arch	IQ_AAo	Art_AAo	Wall_AAo	IQ_DAo	Art_DAo	Wall_DAo
Reader 1													
	Gadoterate Meglumine	3.85	3.26	3.26	4.26	3.74	3.87	4.26	3.81	3.78	4.37	3.85	3.81
	Gadobutrol	3.7	3.22	3.26	4.3	3.74	3.85	4.15	3.7	3.74	4.52	3.93	3.93
	P value	0.43	0.825	0.963	0.796	1	0.655	0.591	0.366	0.763	0.317	0.48	0.317
Reader 2													
	Gadoterate Meglumine	3.81	3.04	3.26	4.26	3.59	3.78	4.37	3.63	3.7	4.59	3.89	3.89
	Gadobutrol	3.93	2.93	3.52	4.22	3.59	3.68	4.19	3.44	3.66	4.52	3.74	3.79
	P value	0.653	0.519	0.198	0.819	1	0.48	0.244	0.132	1	0.527	0.157	0.414

IQ=Image Quality, Art=Artifact, Wall=Wall Conspicuity/Sharpness, Arch=Aortic arch, AAo=Ascending arch, Dao=Descending arch

Discussion
Comparison of gadoterate meglumine-enhanced and gadobutrol-enhanced MRA scans of the thoracic aorta showed excellent agreement of thoracic aorta measurements as well as comparable qualitative ratings of image quality, artifact, and wall conspicuity at each level of the aorta assessed in this study, suggesting the two agents perform similarly.

References

1. Laura A. Freeman, Phillip M. Young, Thomas A. Foley, Eric E. Williamson, Charles J. Bruce, Kevin L. Greason. CT and MRI Assessment of the Aortic Root and Ascending Aorta. American Journal of Roentgenology. 2013;200: W581-W592. 10.2214/AJR.12.9531

Correlations between cardiothoracic MRI and external seismocardiogram recordings

Ethan M. I. Johnson, J. Alex Heller, Florencia Garcia Vicente, Roberto Sarnari, Daniel Gordon, Brenda Herrera, Alex J. Barker, Mozziyar Etemadi, Michael Markl
Northwestern University, Evanston / Chicago, United States

Purpose Cardiovascular disease results in multifarious changes of cardiac function and flow that are detectable by cardiac and 4D flow MRI (CMR), but exams are complex and costly. Seismocardiography (SCG) can be done with ease and low cost by wearable devices placed on the torso. SCG signals derive from mechanical forces that transmit through the chest wall from the beating heart and pulsatile aortic blood flow. They characterize the cyclic reverberations from cardiac function and flow [1], and they can be indicative of changes in cardiac function [1,2]. Here, we explore correlations in SCG signal features and CMR metrics of thoracic aorta flow from a cohort of healthy subjects to establish normal ranges. We also make preliminary comparison of the healthy cohort to a small sample of valve disorder patients to explore potential aortic flow-related clinical interpretation of SCG measurements. With quantitative relationships established for SCG and CMR metrics, it may be possible to translate quick, simple SCG recordings into tests for potentially abnormal cardiac function and flow that would suggest need for comprehensive CMR examination.

Methods A normal cohort dataset of SCG and CMR measurements was collected from 28 healthy subjects (12 female; ages 53y±19y) and 6 patients: 3 bicuspid aortic valve (BAV), 3 mechanical valve implants. A wearable cardiac sensor recorded supine SCG immediately prior to MR with 4D flow covering thoracic aorta and short-axis CINE SSFP covering left ventricle (LV) base to apex. SCG recordings were time-referenced to ECG R-waves and time-normalized to systole duration, and a beat-averaged spectrogram was computed. SCG metrics used were net change from positive to negative peak in rapid ejection (scgdev) and average spectral energy in time-frequency regions of end-diastole (enddia) / early-systole (earlysys) / end-systole (endsys) and 10–60Hz (lo-f) / 120–240Hz (hi-f). MR images were analyzed to quantify blood velocities and to annotate end-systole (min. LV volume) and aortic valve open/close. CMR metrics were computed from velocity (V), acceleration (A) and flow (Q) in a 2D cut-plane of the proximal ascending aorta with a frame-by-frame ROI. Linear correlation coefficients (R) and paired t-test significance values (p) were calculated between all metrics.

Results Several significant correlations (p<0.05) between CMR and SCG metrics are seen (Fig.2a), including earlysys lo-f vs. max(V_{mean}) (R=0.43, p=0.02) and enddia hi-f vs. max(Q) (R=0.40, p=0.03). Aligning SCG signals to cardiac valve events causes some correlations to gain or lose significance (Fig.2b). When aligned to aortic close, the endsys hi-f SCG energy in patients conspicuously differs from the distribution observed in the normal cohort (Fig.2c).

Discussion Correlations observed between SCG and CMR metrics have intuitive time-correspondence within the cardiac cycle, e.g., the maximal flow acceleration occurs in early systole and correlates with early-systole SCG energy. Correlated metrics also co-vary with known demographic relationships [3], such as observed reduction of both aortic flow velocities and SCG energies with increased age. The lower-frequency SCG range primarily captures bulk motion [2], while the higher frequency is more sensitized to valve motion and flow [4]. Comparing the normal cohort to a limited number of valve-disorder patients, a marked difference in SCG energy distributions exists. This may, with further study, support development of an easy clinical test that could be used to refer for comprehensive cardiac MR examination. Taken together, these suggest great possible value of SCG use in studying cardiac disease, especially in conjunction with MR, e.g., by providing quick, quantitative measurements indicative of potential abnormal function that require follow-up with MR.

References [1] Wiens AD, et al. IEEE J BHI 19.4 (2015): 1435–1442. [2] Inan OT, et al. IEEE J BHI 19.4 (2015): 1414–1427. [3] Mohiaddin RH, et al. J Appl Radiol 74.1 (1993): 492–497. [4] Goda MA, Hajas P. Proc Comp Cardiol (2016): 1133–1136.

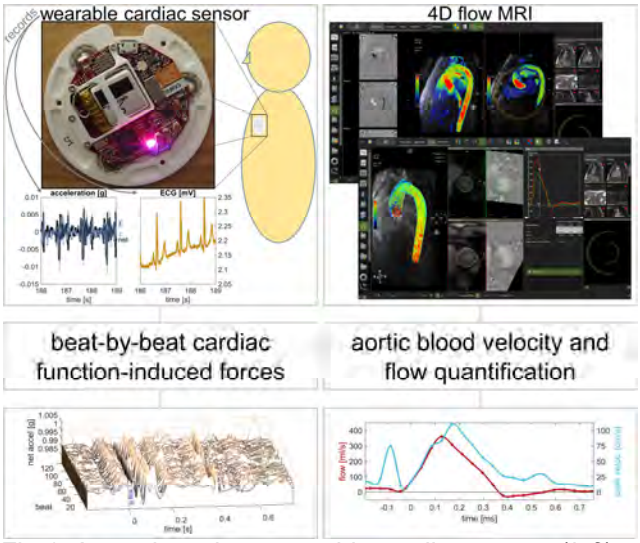

Fig.1: A non-invasive, wearable cardiac sensor (*left*) measures ECG and physical chest accelerations to form seismocardiogram (SCG) signals; 4D flow cardiac MR imaging (*right*) quantifies dynamics of blood flow in the thoracic aorta.

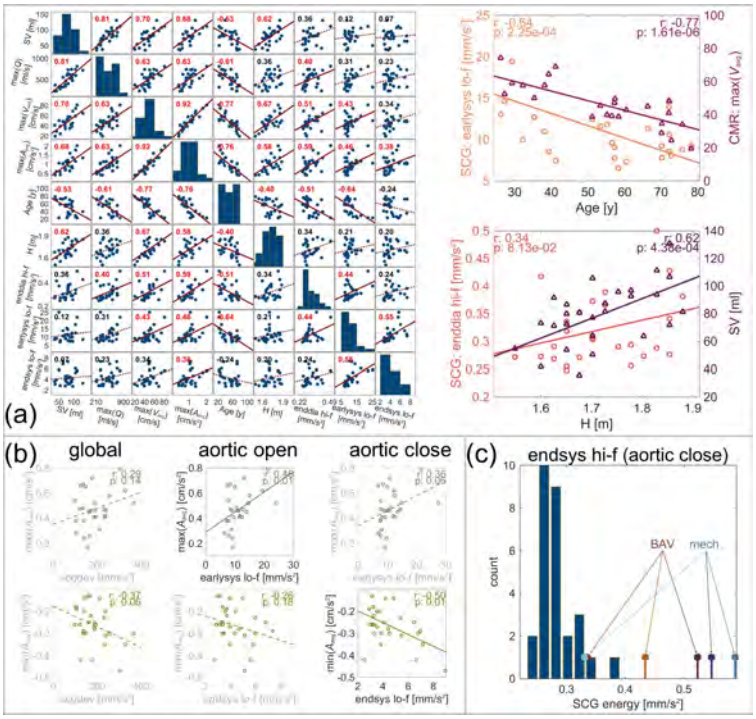

Fig.2: Several correlations in SCG features and CMR function / flow metrics (a) are found to be statistically significant (a, *red*) and co-vary with underlying physiology (a, *right*). Significance changes when SCG features are aligned to cardiac events (b), and the healthy cohort's SCG energies differ from patients' (c).

Intracranial Vessel Wall Imaging of Cerebral Amyloid Angiopathy and Cerebral Amyloid Angiopathy-Related Inflammation

Vance T. Lehman MD[a], Jonathan Graff-Radford MD[b], Ashima Makol MBBS[b], Alejandro Rabinstein MD[b], Waleed Brinjikji MD[a], Guiseppe Lanzino MD[d], John Huston III MD[a]

[a]Department of Radiology, Mayo Clinic, Rochester MN [b]Department of Neurology, Mayo Clinic, Rochester MN [c]Department of Rheumatology Mayo Clinic, Rochester MN [d]Department of Neurologic Surgery, Mayo Clinic, Rochester MN

Purpose. Cereberal amyloid angiopathy related conditions typically have unremarkable luminal MRA findings. The aim of this study was to characterize and compare the conventional MR and angiographic imaging, to vessel wall imaging MRI (VWMRI) findings in patients with cerebral amyloid angiography (CAA) or cerebral angiopathy related inflammation (CAA-ri).

Methods. All patients evaluated at our institution between 2015 and 2017 with a diagnosis of either cerebral amyloid angiopathy (CAA) or cerebral amyloid angiopathy-related inflammation (CAA-ri) who underwent (VWMRI) evaluation were included. Final consensus diagnoses were obtained with both rheumatology and neurology evaluation. Available MRI, angiographic, and VWMRI examinations were characterized.

Results. Ten patients were identified, including six with a consensus diagnosis of CAA-ri and four with CAA. Cortical vessel wall enhancement was identified in five of six (83%) of CAA-ri cases and zero of four (0%) of non-inflammatory CAA cases. In all five cases (100%), the cortical vessel wall enhancement co-localized to adjacent leptomeningeal enhancement. Leptomeningeal enhancement was present in all six (100%) of cases with CAA-ri and two of four (50%) of cases of CAA. Luminal narrowing suggestive of vasculitis was seen in zero (0%) of cases of CAA-ri and one (25%) case of CAA.

Conclusions. Cortical vessel wall enhancement, but not leptomeningeal enhancement, may be a useful to distinguish CAA-ri from CAA. The findings also suggest that cortical vessel wall enhancement that co-localizes to a regional area of leptomeningeal enhancement is a feature of CAA-ri. Findings on luminal angiography including MRA and conventional angiogram did not differentiate CAA from CAA-ri. Further

Fresh Blood Imaging (FBI) with centric ky-kz trajectory and exponential refocusing flop angle: Comparison with standard FBI

Mitsue Miyazaki[1,2], Masaaki Umeda[2], Yoshimori Kassai[2], Lijun Zhang[3], Katsumi Nakamura[4]

1 Department of Radiology, University of California, San Diego, La Jolla, CA; 2 Canon Medical Systems Corporation, Tochigi, Japan; 3 Canon Medical Systems, China; 4 Tobata General Hospital, Japan

Purpose: To advance fresh blood imaging (FBI) using centric ky-kz trajectory and exponential flop angle for tremendous reduction of scan time and N/2 artifacts.

Materials and Methods: FBI utilizes a physiological signal difference between systolic and diastolic triggered images [1,2]. The centric ky-kz trajectory [3] is implemented in FBI (cFBI), acquiring multiple slice-encodings (SEs) and phase-encodings (PEs) per TR; whereas, standard FBI acquires one SE per TR. By applying exponential flop angle (eFA), cFBI enables reduction of specific absorption rate (SAR) and shorten the scan time. The design of eFA is having high flop angles (Hflop) at the center of k space (about 36 lines or more) for bright blood imaging and exponentially decreasing flop angles at periphery of k space to reduce SAR. Having about 36-line Hflop of 180 deg was required to ensure depiction of bright blood. Imaging of cFBI was performed maintaining Hflop of 180 deg. and varying low flop angles (Lflop), as Hflop/Lflop of 180/90, 180/60, and 180/30 deg. Imaging parameters are: for cFBI (TR of 2RR intervals) and standard FBI (TR of 3RR intervals due to SAR), TEeff of 60 ms, 1NAQ, 256x256 matrix, 120 1.8-mm slices, FOV of 40x40 cm, and parallel imaging of 3. All experiments were performed using a 3T clinical system on healthy subjects (6 males, 24-68 yo).

Results: By varying Lflop to 90, 60, and 30 deg with maintaining Hflop of 180 deg., the visualization of major vessels were similar. The scan times of cFBI with Hflop/Lflop of 180/90, 180/60, and 180/30 deg. were reduced to about 1/2 to 1/3 (1:30-2:00 min) by acquiring multiple SEs and PEs data compared to standard FBI. Regarding artifacts, standard FBI often causes N/2 artifacts in the PE direction that degrade image quality; whereas, cFBI minimizes N/2 artifacts. As shown in Fig. 1, cFBI with 180/60 deg. shows an excellent image without N/2 artifacts.

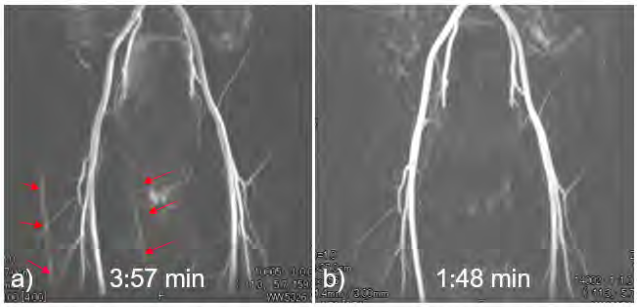

Fig. 1. The iliac-femoral MRA images obtained by a) standard FBI and b) cFBI on a healthy subject. The scan time is listed on the image. Note that b) cFBI shows a clean image without N/2 artifacts; whereas, a) standard FBI shows N/2 artifacts (red arrows).

Discussion and Conclusion: Advanced cFBI with eFA enables high resolution quality NC-MRA images with the fast acquisition time without major artifacts like N/2 artifacts. Compared to standard FBI, cFBI reduces the scan time to 1/3 to 1/2, opening a possibility of scanning entire peripheral vasculature in 5 to 6 mins.

References:

1. Miyazaki M, Sugiura S, Tateishi F, et al. J. Magn Reson Imaging 2000;12:776–783.
2. Miyazaki M, Takai H, Sugiura S, et al. Radiology 2003;227:890–896.
3. Busse RF, Brau ACS, Vu A, et al. Magn Reson in Med 2008;60:640–649.

Free-running 3D Joint Myocardial T_1 and T_2 Mapping with Whole-heart Coverage and Isotropic Spatial Resolution

Haikun Qi[1], Aurelien Bustin[1], Olivier Jaubert[1], Gastao Cruz[1], Huijun Chen[2], René Botnar[1], Claudia Prieto[1]
[1] *School of Biomedical Engineering and Imaging Sciences, King's College London, London, United Kingdom*
[2] *Center for Biomedical Imaging Research, School of Medicine, Tsinghua University, Beijing, China*

Introduction

Quantitative T_1 and T_2 myocardial tissue characterization has shown to be useful for the diagnosis of various cardiomyopathies[1]. Obtaining co-registered myocardial T_1 and T_2 maps in a single scan has potential to improve sensitivity, specificity and reader confidence for early diagnosis and treatment monitoring[1]. However, current myocardial T_1 and T_2 mapping techniques are usually performed sequentially at 3 short axis slices under breath-holds, thereby suffering from limited coverage, moderate spatial resolution and patient fatigue. Free-breathing approaches, however, usually require respiratory gating, leading to unpredictably long scan time. To address these limitations, we sought to develop a free-running (free-breathing, retrospective cardiac binning) high-resolution 3D whole-heart joint myocardial T_1 and T_2 mapping technique, which is achieved with 3D golden angle radial acquisition with T_2 and inversion recovery (IR) preparations, and combined dictionary-based low-rank inversion[2] and undersampled patch-based multi-contrast reconstruction (HD-PROST)[3].

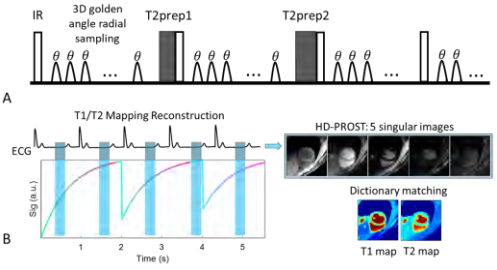

Fig.1. A: Schematic diagram of the proposed T_2 and IR prepared 3D golden angle radial sequence. B: Cardiac and contrast data binning. Five singular images are reconstructed with HD-PROST and joint T_1-T_2 maps are obtained via dictionary matching.

Methods

Sequence Design: The proposed sequence (Fig.1A) consists of: combination of T_2 preparation with variable echo times and IR pulses to generate images with different T1 and T2 contrasts; spoiled GRE readout with low flip angle; water selective excitation pulse for fat suppression; 3D golden angle radial sampling for flexible retrospective cardiac and contrast binning.

Motion Estimation/Correction: Retrospective cardiac binning can be performed using the simultaneously recorded ECG time stamps. Self-navigated respiratory signal is estimated from the multi-channel k-space center of all spokes using independent component analysis[4] and used to assign the measured k-space data into 5 respiratory bins. Subsequently, low-resolution images at diastole are reconstructed for each respiratory bin using the central k-space region, and 3D translational respiratory motion is estimated via registration of each respiratory bin to the end-expiration. The 3D translational respiratory motion is then used to correct the acquired data by applying the corresponding phase shift in k-space.

Image reconstruction: Schematic reconstruction process for obtaining myocardial T_1 and T_2 maps is shown in Fig.1B. Retrospective binning is performed with temporal windows of 187ms along cardiac dimension and 196ms along contrast direction. After binning, HD-PROST reconstruction with dictionary-based low-rank inversion[2,3] is used to reconstruct 5 singular images. Co-registered T_1 and T_2 maps are obtained via dictionary matching.

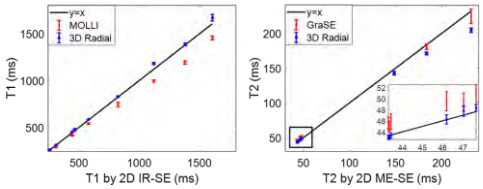

Fig. 2. Phantom T_1, T_2 measurements with 2D MOLLI, 2D GraSE and the proposed 3D joint T_1-T_2 mapping method in comparison with gold standard 2D IR-SE and ME-SE.

MR Imaging: Acquisitions were performed on a T_1/T_2 phantom and 5 healthy subjects on a 1.5T Philips scanner with the following parameters for the proposed sequence: FOV=200mm^3, resolution = 2mm^3, TR/TE= 10.3ms/4.6ms, flip angle = 6°, number of readouts after magnetization preparation = 195, scan duration = 11.2min. The proposed 3D joint T_1-T_2 framework and the clinical references 2D T_1 MOLLI[5] and 2D T_2 GraSE[6] mapping methods were validated in a standardized T_1/T_2 phantom using a 2D IR spin echo (IR-SE) and multi-echo spin echo (ME-SE) as T_1 and T_2 reference, respectively. For in vivo imaging, in addition to the proposed free-breathing joint T_1-T_2 3D mapping technique, 2D MOLLI and GraSE scans were performed under breath-holds at diastole in the mid short-axis view for comparison.

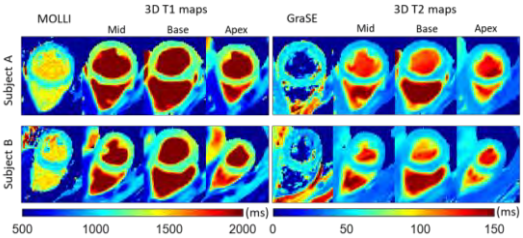

Fig. 3. Short-axis 2D MOLLI, 2D GraSE and the proposed 3D joint T_1-T_2 mapping results for two healthy subjects. Representative basal and apical slices from the proposed 3D approach are also shown for each subject.

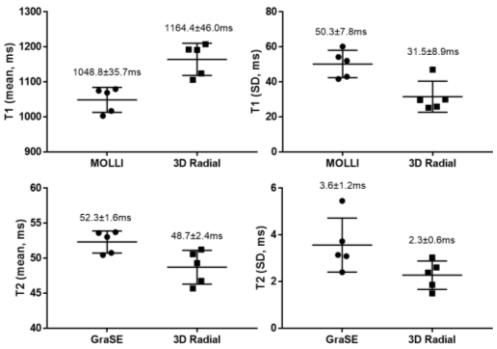

Fig.4 Mean and standard deviations of septum T_1 and T_2 values of all 5 healthy subjects measured with 2D MOLLI, 2D GraSE and the proposed 3D joint T_1-T_2 mapping technique.

Results

In the phantom (Fig.2), T_1 estimations with the proposed method were in good agreement with the reference 2D IR-SE sequence, whereas, MOLLI severely underestimated long T_1 values. For T_2, in comparison with 2D ME-SE, the proposed approach showed better accuracy than GraSE for short and intermediate T_2 values (<150ms). In vivo diastolic myocardial 3D maps obtained with the proposed joint T_1-T_2 mapping approach were visually comparable to 2D MOLLI and GraSE (Fig.3). In the septum, higher T_1 and slightly lower T_2 values were obtained with the proposed method, compared with MOLLI and GraSE (Fig.4), which was in agreement with the phantom findings. The standard deviations of the T_1 and T_2 values in the septum were lower with the proposed 3D method, indicating better precision than with the 2D methods.

Discussion & Conclusions

A novel free-running 3D joint myocardial T1-T2 mapping technique with whole-heart coverage and isotropic spatial resolution is proposed. High quality co-registered 3D T1 and T2 maps were generated from a single scan, which were shown to have good accuracy and precision in comparison to spin echo reference sequences in a T1/T2 phantom. The promising results warrant further validation in healthy subjects and patients with heart disease.

References: 1. Messroghli DR, et al. J Cardiovasc Magn Reson 2017;19(1):75. 2. Asslander J, et al. Magn Reson Med 2018;79(1):83-96. 3. Bustin A, et al. Magn Reson Med 2018. 4. Qi H, et al. ISMRM 2019 (p409). 5. Messroghli DR, et al. J Magn Reson Imaging 2007;26(4):1081-1086. 6. Sprinkart AM, et al. J Cardiovasc Magn Reson 2015 17:12.

title:

Contrast Enhanced Compressed Sensing Coronary MRA: preliminary results

Kuniaki Hirai, Tomoyuki Kido, Masashi Nakamura, Akira Kurata, Yuki Tanabe, Hitoshi Miki, Michaela Schmidt, Christoph Forman, Teruhito Kido, Teruhito Mochizuki,

<Purpose>

Coronary MR Angiography (MRA) has advantage such as no disturbance of coronary calcium and no need of radiation exposure. Biggest shortage of the conventional MRA is long acquisition time (about 15min). “Compressed sensing (CS)” is a new technique to address this shortage (long acquisition time). We applied CS to coronary MRA, and compared CS coronary MRA and conventional coronary MRA.

<Methods>

In 20 clinical cases, both CS coronary MRA and conventional coronary MRA were acquired after contrast injection, using 3T MR system (Skyra, Siemens). We compared CS coronary MRA and conventional coronary MRA in the following points; (1) acquisition time, (2) visual image quality in 4-grade scale (1 as poor to 4 to excellent), and (3) visualization length of the coronary artery.

<Results>

Average acquisition times were 3.6 vs 15.3 min for CS and for conventional coronary MRA ($p<0.01$). Acquisition time of the CS coronary MRA was about 1/4 of the conventional coronary MRA. (2) Mean image quality scores were 3.6 vs. 3.7 (ns). (3) Average visible vessel lengths were 14.3 ± 3.0 cm (CS) and 14.6 ± 2.8 cm (conventional) for RCA ($p=0.642$), 12.9 ± 3.1 cm (CS) and 12.2 ± 3.1 cm (conventional) for LAD ($p=0.927$), 9.1 ± 2.4 cm (CS) and 9.6 ± 2.2 cm (conventional) for LCx ($p=0.515$), respectively.

< Conclusion >

CS coronary MRA can save acquisition time, which will encourage more use of coronary MRA in the clinical setting.

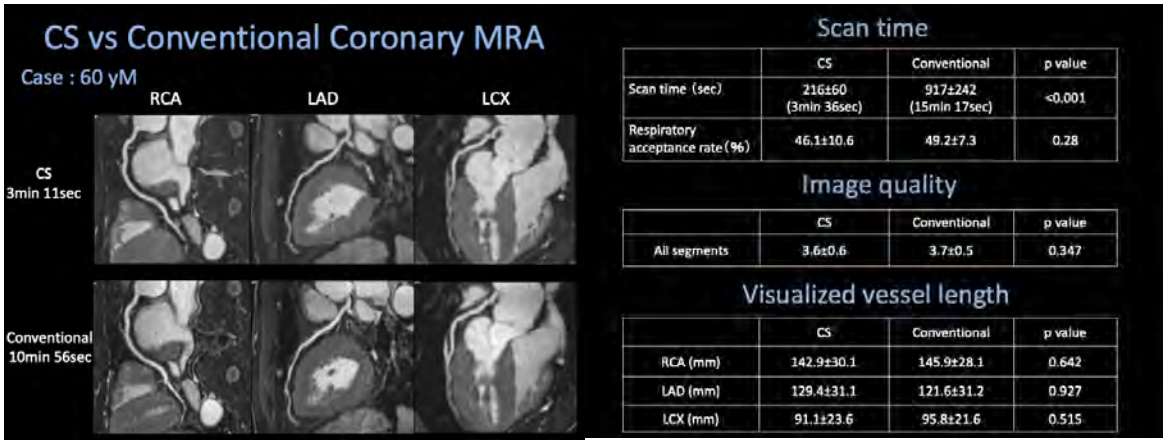

4D Flow MRI-derived Pulse Wave Velocity in the Normal Aorta

Kelly Jarvis, PhD[1], Michael B. Scott, MS[1,2], Alireza Vali, PhD[1], Mohammed Elbaz, PhD[1], James C. Carr, MD[1], Michael Markl, PhD[1,2]

[1]Radiology, [2]Biomedical Engineering, Northwestern University, Chicago, USA

Purpose: Aortic pulse wave velocity (PWV) is a surrogate measure of aortic stiffness (increases with age and atherosclerosis) and important for the assessment of cardiovascular disease. PWV has been estimated using 2D phase contrast MRI and 4D flow MRI by characterizing flow waveforms along the aorta. In previous studies, we found diameter increases and blood velocity decreases with age in the normal aorta[1,2]. However, the impact of these changes (and changes in global cardiac function) on PWV is unclear. The goal of this study was to systematically investigate the relationship between 4D flow MRI-derived PWV, cardiac function, aortic size and flow parameters in a volunteer cohort with wide age range.

Methods: 4D flow MRI (spatial res. ~2-3 mm^3, temporal res. ~40ms, venc=150-250 cm/s) was acquired in 100 controls (50% male, age=46+/-15[19-79] years) to derive aortic 3D segmentation, flow parameters (velocity, wall shear stress=WSS) and PWV. A phase contrast MR angiogram was calculated to segment the aorta. An automated analysis workflow (Fig.1) was developed to extract aortic centerline and place analysis planes. Time-delay between flow waveforms was calculated using cross-correlation methodology previously described[3-5]. Global cardiac function (end-diastolic & end-systolic volume, stroke volume, ejection fraction) was assessed by standard cine-MRI (2D CINE SSFP).

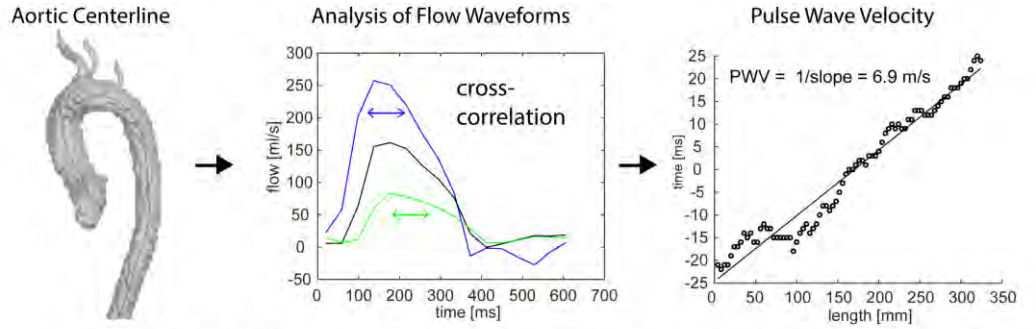

Figure 1: 4D flow MRI Analysis. The 3D aortic centerline was generated (left) and flow waveforms analzyed at plane locations every 4 mm using cross-correlation to determine time-delay (middle). Utilizing time-delay and distance along the centerline for all locations, global aortic PWV was calculated using linear regression (right).

Table 1: Correlation Results

	r	p-Value
age	0.76	0.000
gender	0.08	0.416
HR	0.10	0.346
EF	0.02	0.870
EDV/BSA	-0.30	0.002
ESV/BSA	-0.24	0.016
SV/BSA	-0.29	0.003
MyoMass_diast/BSA	0.18	0.071
AAo Mean Velocity	-0.38	0.000
Arch Mean Velocity	-0.57	0.000
DAo Mean Velocity	-0.69	0.000
AAo Mean WSS	-0.36	0.000
Arch Mean WSS	-0.57	0.000
DAo Mean WSS	-0.72	0.000
AAo Vmax	0.18	0.076
Arch Vmax	-0.49	0.000
DAo Vmax	-0.65	0.000
AAo WSSmax	0.01	0.910
Arch WSSmax	-0.44	0.000
DAo WSSmax	-0.66	0.000
AAo Diameter/BSA	0.30	0.002
Arch Diameter/BSA	0.29	0.003
DAo Diameter/BSA	0.31	0.002

p<.05: shaded values. HR: heart rate, EF: ejection fraction, EDV: end-diastolic volume, ESV: end-systolic volume, SV: stroke volume. Volumes of interest were AAo=asending aorta, Arch=aortic arch, DAo=descending aorta.

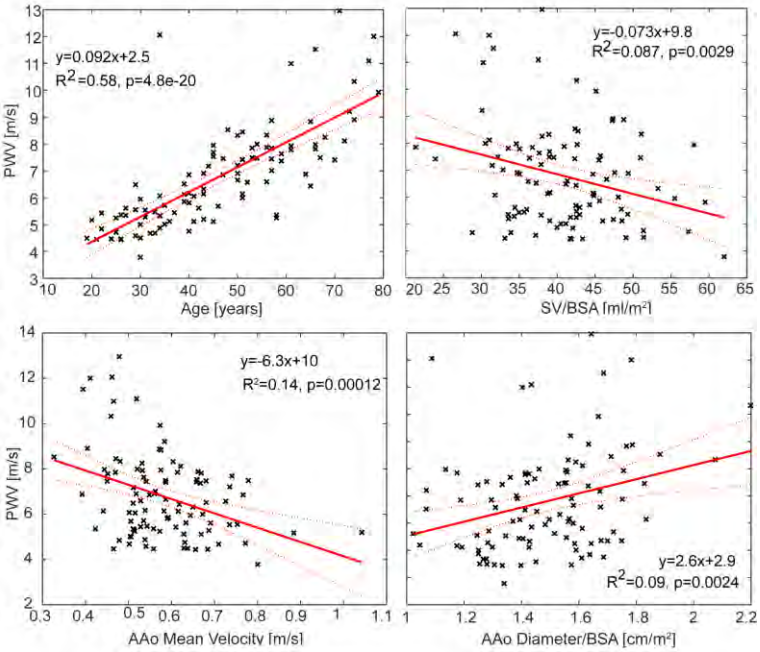

Figure 2: Regression results for PWV versus age (top left), stroke volume normalized by BSA (top right), AAo mean velocity (bottom left) and median diameter along AAo (bottom right). Solid red line = line of best fit. Dashed red line = confidence bounds. BSA: body surface area

Results: See Table 1 and Fig.2. PWV had a strong positive correlation with age (r=.76, p<.001), weak-moderate negative correlation with cardiac functional parameters (EDV/BSA: r=-.30, p=.002; ESV/BSA: r=-.24, p=.02; SV/BSA: r=-.29, p=.003), moderate-strong negative correlation with mean aortic velocity (AAo: r=-.38, p<.001; Arch: r=-.57, p<.001; DAo:, r=-.69, p<.001) as well as mean WSS (AAo: r=-.36, p<.001; Arch: r=-.57, p<.001; DAo: r=-.72, p<.001) and moderate positive correlation with aortic diameter (AAo: r=.30, p=.002; Arch: r=.29, p=.003; DAo: r=.31, p=.002).

Discussion: PWV derived by 4D flow MRI can detect the expected strong correlation with age in the normal aorta—as we age, the aorta stiffens (i.e. PWV increases). This is associated with a decline in cardiac function (EDV, ESV, SV), aortic dilation and reduced flow parameters (velocity and WSS). Results demonstrate using age-matched control cohorts is critically important to detect abnormal PWV.

Funding Sources: Grant support by NIH, NHLBI T32 HL134633

References: [1]Garcia, et al. Eur Heart J Cardiovasc Imaging. 2016;17(8):877-884. [2]van Ooij P, et. al. J Magn Reson Imaging 2016;43(5):1239-1249. [3]Fielden, et al. J Magn Reson Imaging 2008;27(6):1382-1387. [4]Markl, et al. Magn Reson Med 2010;63(6):1575-1582. [5]Wentland AL, et al. J Magn Reson Imaging 2013;37(4):853-859.

Deep learning for fully automated preprocessing and 3D segmentation of aortic 4D flow MRI

Michael B. Scott[1,2], Haben Berhane[3], Joshua D. Robinson[3], Cynthia K. Rigsby[3], Michael Markl[1,2]
[1]Department of Radiology, [2]Department of Biomedical Engineering, Northwestern University, Chicago IL, USA, [3]Lurie Children's Hospital of Chicago, Chicago, IL, USA

Purpose: 4D flow MRI provides spatially and time resolved information on 3D blood flow dynamics and is promising for the evaluation of altered cardiovascular hemodynamics in patients with aortic diseases. However, 4D flow data analysis can be time-consuming, cumbersome, and require user input, limiting clinical translation and inter-rater reproducibility. Current 4D flow data analysis includes phase offset correction, de-noising, and velocity anti-aliasing followed by a semi-manual 3D segmentation of the volume of interest. The purpose of this study was to apply deep learning concepts and train convolutional neural networks (CNNs) to fully automate data preprocessing and segmentation.

Methods: Cohort and imaging: Scans from 210 pediatric subjects (110 male, average 13 years) were used in this IRB-compliant retrospective study. 4D flow was acquired at 1.5T (Aera, Siemens) with spatial resolution 1.2-3.5mm^3, temporal resolution 37-45ms, venc 120-400cm/s. The subjects were split into 100 training, 10 validation, and 100 testing scans. All 210 datasets underwent manual pre-processing (phase-offset correction, de-noising in Matlab) and 3D segmentation (Mimics, Materialise) which served as labels for CNN training and ground truth for CNN testing.

Neural networks: Four CNNs based on a 3D U-Net architecture [1] with 3D DenseNet layers [2] were trained for 1) phase offset correction, 2) denoising, 3) velocity anti-aliasing, and 4) 3D segmentation. CNNs consisted of symmetric architecture with four encoding and decoding layers. Encoding layers were composed of DenseNet layers, featuring a series of 3D-convolution, batch normalization, and a linear rectified unit, with each preceding feature map concatenated after every convolution. As such, every feature extracted throughout the network was efficiently utilized throughout. Max-pooling was applied to half the total number of features in the encoding layer, except in the slice direction, allowing for a dynamic number of slices and ensuring consistency across slices. Decoder layers upsampled feature maps to double their dimensions. All CNN used a dice-loss and cross-entropy loss, with additional penalties added for phase offset or noise masks that overlapped the final segmentation and for incorrect velocity values after antialiasing.

The velocity antialiasing network was trained by simulating a lower venc (0.7, 0.5, and 0.3 of technologist-selected venc) in datasets with no aliasing and compared against a conventional antialiasing algorithm. A pipeline with four CNN allowed for fully automated preprocessing of 4D flow MRI (figure 1). Phase offset and noise correction CNNs generate correction masks from the standard deviation of the 4D flow data. Corrected data was used as an input to the velocity antialiasing CNN, phase contrast angiograms calculated from antialiased data were input into the segmentation CNN.

Performance: To assess the performance of the neural networks, a voxel-wise receiver-operator curve (ROC) and dice score were calculated for the phase offset and denoising masks as well as the 3D segmentation. Anti-aliasing performance was evaluated by counting the number of voxels within the aorta 3D segmentation volume that were marked as aliased and comparing to a conventional antialiasing algorithm using a Wilcoxan rank sum test. Training on a Nvidia GTX 1080-Ti took 6 hours or phase offset and noise correction, 26 hours for anti-aliasing, and 6 hours for segmentation.

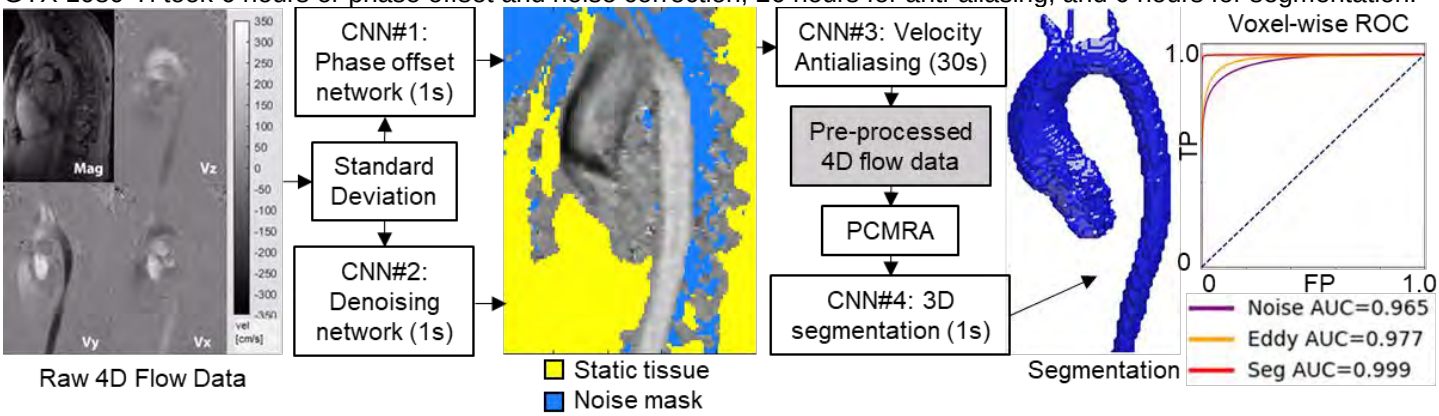

Figure 1: pipeline for fully automated preprocessing of aorta 4D flow. For ROC curve (right) shows the performance of each network, TP = true positive rate, FP = false positive rate.

Results: Fully automated CNN based 4D flow analysis was performed with significantly reduced processing time (~1s for phase offset, denoising, and 3D segmentation; 30s for velocity antialiasing) compared to manual processing time (~15min) per subject. CNN testing for phase offset, denoising, and 3D segmentation networks revealed excellent performance compare to ground truth (Dice scores: 0.93±0.05, 0.95±0.02, 0.95±0.03; AUC in ROC analysis: 0.977, 0.965, and 0.999). The antialiasing CNN demonstrated improved performance compared to standard techniques and identified an average of 1397 aliased voxels within the aorta volume, compared to 729 by the conventional algorithm (p=0.005).

Discussion: This study shows rapid (~30s), fully-automated aortic 4D flow MRI preprocessing and segmentation with excellent performance compared to ground truth obtained by manual analysis. This allows inexperienced users to quickly process 4D flow data with high reproducibility and should enable fully-automated one-click hemodynamic analysis.

References: (1) *Çiçek, Ö, et al., MICCAI 2016*, (2) *Huang, G, et al., 2017 IEEE CVPR*

Vessel Wall Imaging in Previously Unruptured, Untreated Brain Arteriovenous Malformations

Laura Eisenmenger MD,[1] David Saloner PhD,[2] Daniel Cooke MD,[2] Steve Hetts MD,[2] Nerissa Ko MD MAS,[2] Tarik Tihan MD PhD,[2] Adib Abla MD,[2] Christopher Hess MD PhD,[2] Helen Kim MPH PhD[2]
1. University of Wisconsin – Madison, 2. University of California, San Francisco.

Purpose: Brain arteriovenous malformations (bAVMs) are high-flow, shunting lesions that are a major cause of intracranial hemorrhage in younger persons.(1) Hemodynamics likely play an important role in flow-mediated inflammation in bAVMs, with our prior studies demonstrating silent microhemorrhages and inflammatory cell infiltration in and around bAVM lesions.(2, 3) Advanced imaging techniques such as vessel wall imaging (VWI) promise improved anatomic characterization of vessel wall changes in bAVMs; however, the underlying causes are unclear. In particular, VWI has been hypothesized to help in identifying the site-of-rupture in ruptured bAVMs,(4) and enhancement may be a marker of unstable lesions prone to rupture (5); however, we propose that vessel wall enhancement is a more complex process. The purpose of this study was to present a series of unruptured, untreated bAVM cases with VWI.

Methods: VWI was obtained using black-blood pre- and post-gadolinium 3D CUBE T1 (Figure 1). Two neuroradiologists identified the number of feeding arteries and draining veins, evidence of remote hemorrhage, and the distribution and degree of AVM enhancement. Presence or absence of vessel wall and/or perivascular enhancement inside and outside the nidus was assessed. Percent of AVM enhancement (1-25%, 25-50%, 50-75%, or 75-100%) was also evaluated.

Results: VWI was obtained in 8 cases with no prior definitive bAVM treatment (resection, stereotactic radiosurgery, or embolization) or history of symptomatic hemorrhage. 2/8 were Spetzler-Martin grade (SMG) 3, 4/8 were SMG grade 4, and 2/8 were SMG 5 bAVMs, ranging in size from 3.4 to 9.5cm. All lesions exhibited enhancement on VWI inside the nidus (yellow arrow), and 3/8 had perivascular enhancement in the nidus. No subjects had perivascular enhancement outside the nidus. Within the nidus, half of subjects had >50% enhancement (2/8 had 75%-100%, 2/8 had 50-75%, 1/8 had 25-50%, and 3/6 had 1-25%). There was no enhancement of the feeding arteries in any of the bAVMs.

Discussion: While contrast enhancement has been seen in ruptured and post-treatment AVMs, our cases all had vessel wall enhancement prior to any treatment or clinically apparent hemorrhage. Although the cause of enhancement is uncertain, altered vascular flow is likely a contributing factor. Future studies with clinical and radiographic follow-up using 4D flow MRI and histopathology could help to further understand the underlying etiology.

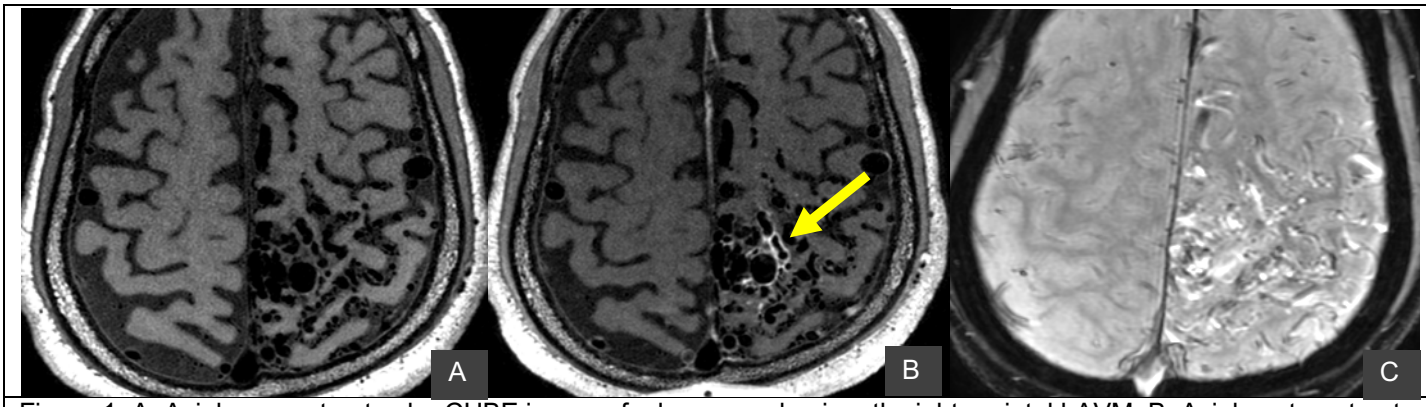

Figure 1. A. Axial pre-contrast cube CUBE image of a large, predominantly right parietal bAVM. B. Axial post-contrast CUBE images demonstrating areas of vessel wall enhancement within the nidus (yellow arrow) as well as areas of perivascular enhancement. C. Susceptibility-weighted image shows no evidence of prior hemorrhage.

References:

1. Kim H, Al-Shahi Salman R, McCulloch CE, Stapf C, Young WL, Coinvestigators M. Untreated brain arteriovenous malformation: patient-level meta-analysis of hemorrhage predictors. Neurology. 2014;83(7):590-7.
2. Kim H, Su H, Weinsheimer S, Pawlikowska L, Young WL. Brain arteriovenous malformation pathogenesis: a response-to-injury paradigm. Acta Neurochir Suppl. 2011;111:83-92.
3. Chen Y, Zhu W, Bollen AW, Lawton MT, Barbaro NM, Dowd CF, et al. Evidence of inflammatory cell involvement in brain arteriovenous malformations. Neurosurgery. 2008;62(6):1340-9; discussion 9-50.
4. Komatsu K, Takagi Y, Ishii A, Kikuchi T, Yamao Y, Fushimi Y, et al. Ruptured intranidal aneurysm of an arteriovenous malformation diagnosed by delay alternating with nutation for tailored excitation (DANTE)-prepared contrast-enhanced magnetic resonance imaging. Acta neurochirurgica. 2018;160(12):2435-8.
5. Petridis A, Cornelius J, Suresh M, Li L, Kamp M, et al. Contrast enhancement of vascular walls of intracranial high flow malformations in black blood MRI indicates high inflammatory activity. Chinese Neurosurgical Journal. 2018;4:13.

Effect of beta-blocker therapy on aortic 3D hemodynamics in patients with bicuspid aortic valve

Amirhossein Mozafarykhamseh[1], Ashitha Pathrose[1], Michael B Scott[1,2], Haben Berhane[3], Kelly Brooke Jarvis[1], James Carr[1], Michael Markl[1,2]

[1]Department of Radiology, [2] Department of Biomedical Engineering, Northwestern University, Chicago, [3]Department of Medical Imaging, Ann & Robert H. Lurie Children's Hospital of Chicago, Chicago

Purpose: In patients with bicuspid aortic valves (BAV), beta-blockers (BB) are assumed to slow dilatation of ascending aorta (AAo) by reducing wall shear stress (WSS) in aneurysmal regions[1,2]. However, data on effectiveness of BB use in BAV patients are lacking. The primary aim of this study was to assess BB induced changes in aortic peak velocity (PV) and WSS in a longitudinal 4D flow MRI study with BAV patients starting BB treatment. Findings were compared to matched control groups in BAV patients with no change in their BB therapy.

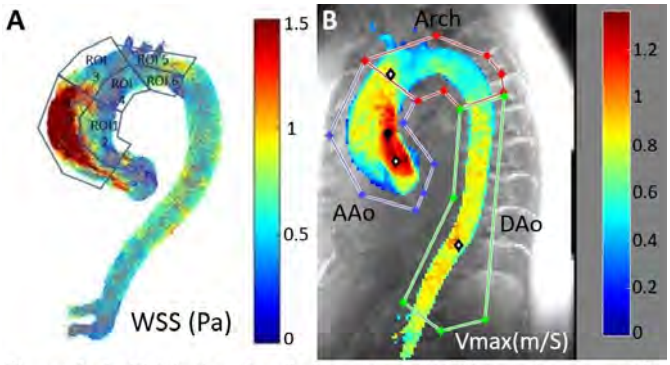

Figure 1; A: Distribution of wall shear stress (WSS) based on a systolic WSS maximum intensity projections (MIP) mapped onto a sagittal view of the thoracic aorta. **B:** Peak velocity MIP image with three regions representing AAo, arch and DAo.

Methods: This retrospective data included n=39 BAV patients with baseline and follow-up cardiothoracic MRI in 3 age-matched groups: BAV patients who started BB therapy after baseline scan (BB^c, n=13, age: 47.3±9.6 years, M:F: 10:3); patients who received continued BB therapy at baseline and follow-up (BB+, n=13, age: 51.1±9.4 years, M:F: 10:3), and patients without medication (BB-, n=13, age: 45.3±10.1 years, M:F: 12:1). All 4D flow data was corrected for Maxwell terms, velocity aliasing, and eddy currents using Matlab (Mathworks, MA). A 3D phase-contrast magnetic resonance angiogram (PC-MRA) was calculated from corrected data and a 3D segmentation of thoracic aorta was generated (Mimics, Materialise, Belgium). Peak systolic velocities were calculated by drawing three different regions of interest (ROIs): ascending aorta (AAo), aortic arch and descending aorta (DAo). Segmental AAo (4 regions) and aortic arch (2 regions) mean and maximum WSS were calculated (Figure 1).

Results: **Before/after comparison in BBc group:** There was no significant difference in PV in BB^c patients before and after the onset of BB therapy in AAo (2.34±1.03 m/s vs 2.67±1.38 m/s, p=0.19, range of change [-33%,134%]), arch (1.37±0.73 m/s vs 1.23±0.38 m/s, p=0.33, [-43% to 24%]) or DAo (1.20±0.31 m/s vs 1.13±0.28 m/s, p=0.12, [-23% to 36%]) regions . A similar trend was found in maximum and mean WSS in the AAo (maximum: 1.60±0.71 N/m^2 vs. 1.57±0.60 N/m^2, p=0.81, [-37% to 43%]; mean: 0.80±0.32 N/m^2 vs. 0.78±0.28 N/m^2, p=0.68, [-36% to 36%]) and arch regions (maximum: 1.23±0.58 N/m^2 vs. 1.15±0.46 N/m^2, p=0.47, [-58% to 32%]; mean: 0.71±0.24 N/m^2 vs. 0.72±0.26N/m^2, p=0.95, [-37% to 33%]).

Intergroup comparison: The intergroup analysis did not show any significant difference in the change in PV between baseline and follow up in AAo (BB+ group's range of change: [-34% to 60%], BB-: [-18% to 64%]), Arch (BB+: [-34% to 60%], BB-: [-18% to 64%]) or DAo regions (BB+: [-34% to 60%], BB-: [-18% to 64%]). A similar trend was found in maximum and mean WSS values between baseline and follow up in AAo (BB+ mean WSS: [-25% to 49%], BB- mean WSS: [-17% to 36%]; BB+ max WSS: [15% to 82%], BB- max WSS: [-22% to 21%]) and arch regions (BB+ mean WSS: [-34% to 65%], BB- mean WSS: [-16% to 35%]; BB+ max WSS: [-16% to 64%], BB- max WSS: [-7% to 30%]) (Table1).

Table 1: Comparison of absolute amount of change in PV and WSS values from baseline to follow-up

	BB^c	BB+	BB-	P-value
Peak AAo velocity(m/s)	0.32±0.86	0.08±0.61	0.22±0.47	0.64
Peak Arch velocity(m/s)	-0.13±0.47	0.05±0.30	0.07±0.36	0.32
Peak DAo velocity(m/s)	-0.06±0.15	-0.06±0.35	-0.02±0.2	0.88
Mean AAo WSS(Pa)	-0.01±0.17	0.02±0.15	0.04±0.11	0.58
Mean Arch WSS(Pa)	0.009±0.10	0.011±0.15	0.05±0.14	0.62
Max AAo WSS(Pa)	-0.02±0.43	0.10±0.28	0.06±0.22	0.58
Max Arch WSS(Pa)	-0.09±0.43	0.08±0.27	0.05±0.17	0.35

Discussion: BB treatment was not associated with any significant change in aortic 3D hemodynamics in BAV patients. Furthermore, no difference was found in aortic WSS and peak velocity between patients with onset of new BB treatment compared to patients with and without constant BB therapy. The proposed mechanism of action of BB therapy for potentially slowing AAo dilation is to reduce WSS on the aneurysmal segment of the aorta by reducing rate of pressure change in aorta (dP/dt). However, results of the current study do not show evidence of a change in peak systolic velocity or WSS between groups and suggest that BB therapy may not impact these parameters in BAV patients. Future work is needed to confirm these results in larger population-based studies and systematically investigate the impact of BB dosage. **References:** 1. Keane MG, et al. Circulation. 2000 2. Verma S, et al. NEJM. 2014

The Effect of the Injection Dose, Rate and Concentration on Carotid Dynamic Contrast-Enhanced MRI: a Simulation Study

Yajie Wang[1], Yishi Wang[1,2], Haikun Qi[3], Xian Liu[1], Hua Guo[1], Huijun Chen[1]

1. Center for Biomedical Imaging Research, School of Medicine, Tsinghua University, Beijing, China. 2. Philips Healthcare, Beijing, China. 3. School of Biomedical Engineering and Imaging Sciences, King's College London, London, United Kingdom.

Purpose: DCE-MRI is an effective tool to quantify inflammation in carotid atherosclerotic plaque[1-4]. However, the injection protocol of carotid DCE-MRI varies in different studies[1-4], and little is known on the effect of the injection protocol. The purpose of this study is to investigate the effect of the contrast injection protocol on the pharmacokinetic parameters estimation in carotid DCE-MRI using simulation.

Methods: Two carotid plaques (one with lipid-rich necrotic core (LRNC), one with intra-plaque hemorrhage (IPH)) were simulated using MATLAB. Effective injection rate was defined as injection rate×concentration. The injection dose (0.02: 0.02: 0.1 mmol/kg) and effective injection rate (0.1: 0.1: 2 mmol/s) were varied. The contrast concentration of the blood (arterial input function, AIF) was calculated using Verhoeven's model[5]. A two-compartment kinetic model was used[2]. Concentrations were converted to T_1 and T_2. K^{trans} (min^{-1}), v_P, T_{10} (ms) and T_{20} (ms) were set as in Table 1[2,6,7]. T_2^* effect was assumed to be proportional by a factor of 0.85 to T_2 effect[8]. The bright-blood DCE sequence[3] was simulated. Dynamic signals of the stationary tissues were calculated by spoiled gradient recalled echo sequence (SPGR) equation. Dynamic signals of the blood was calculated according to its velocity (laminar flow, max velocity = 120cm/s[5,9]). To simulate the changing contrast during imaging, dynamic images (temporal resolution = TR) and the k-space data were generated by adding dynamic signals to the relevant regions. The simulated k-space data (temporal resolution = dynamic phase) were synthesized by multiple k-space data (temporal resolution = TR). Ten average distributed time delays were tested to simulate the uncertainty of the time gap between contrast injection and image acquisition. Gaussian noise (SNR=20dB) was added to each k-space data independently. The reconstructed dynamic images were generated using IFFT. AIF was extracted based on the signal intensity of the lumen automatically. The contrast concentration was calculated. A two compartment kinetic model[2] was used to estimate K^{trans} and v_P pixel by pixel using least-squares algorithm. The plaque ROI$_{flow}$ was defined by v_P<0.5. The mean of the root mean square error (RMSE) of the K^{trans} map and v_P map within the plaque ROI were calculated. Under a certain injection protocol, the mean of the RMSE$_{flow}$ and standard deviation (sd) of the RMSE$_{flow}$ of different time delays were recorded.

Results and Discussion: High injection dose (~ 0.1 mmol/kg) with low effective injection rate (under 0.5 mmol/s) was beneficial to both mean and sd RMSE$_{flow}$ (Fig 1). Lower injection does resulted in ineffective enhancement of the carotid (Fig 2). Image artifacts caused by flowing blood (yellow arrow) and changing contrast during imaging (red arrow) were more severe at higher effective injection rate (Fig 2). Higher effective injection rate also resulted in inaccurate ROI selection (Fig 2), much higher AIF peak (Fig 2), and more severe underestimation of the AIF (Fig 2).This study gives optimized contrast injection protocol for the simulated bright-blood DCE protocol and provided a useful procedure to find the optimal injection protocol under a certain DCE-MRI acquisition protocol.

Table 1. Values of the K^{trans}, v_P, T_{10} and T_{20}.

	Blood	Vessel wall	LRNC	IPH
$K^{trans}(min^{-1})$	/	0.1	0.025	0.005
v_P	/	0.18	0.05	0.03
T_{10} (ms)	1932	685	850	350
T_{20} (ms)	275	69	37	107

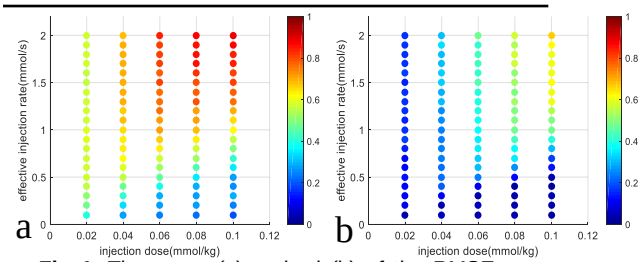

Fig 1. The mean (a) and sd (b) of the RMSE$_{flow}$ as a function of the injection dose and effective injection rate .

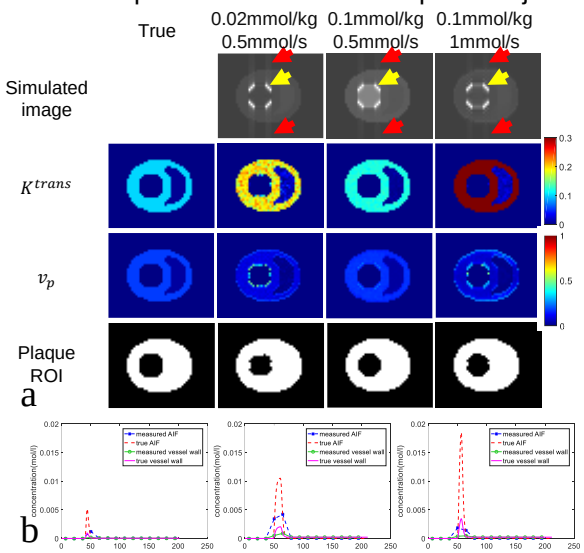

Fig 2. (a) Simulated images (cropped), estimated K^{trans} map, v_p map, and auto-generated plaque ROI, (b) measured and true AIF, measured and true vessel wall contrast concentration, under three typical injection protocols with their **worst time delays.**

Reference: [1] Sun J, et al. Stroke. 2013. [2] Chen H, et al. MRM. 2010. [3] Kerwin WS, et al. MRM. 2008. [4] Gaens ME, et al. Radiology. 2013. [5] L V. Technische Hogeschool. 1985. [6] G. Mihai SG, et al. ISMRM. 2011. [7] Stanisz GJ, et al. MRM. 2005. [8] Robert P, et al. JMRI. 2005. [9] Blackshear WM, et al. Stroke. 1980.

Radiomic characteristics of intracranial atherosclerotic plaques in vitro: an initial study using high resolution MRI

Zhang Shi[1], Chengcheng Zhu[2], Bing Tian[1], Qi Liu[1], Jianping Lu[1]
1. Department of Radiology, Changhai Hospital, Shanghai, China
2. Department of Radiology and Biomedical Imaging, UCSF, San Francisco, CA, USA

Purpose: Intracranial atherosclerotic disease (ICAD) is a major cause of ischemic cerebrovascular events worldwide. However, the pathology of intracranial plaque could be gotten in vivo. The study aims to evaluate the stability of intracranial atherosclerotic plaque in vitro and further analyze the radiomic features of the unstable plaque using the vessel wall imaging on 3.0 T magnetic resonance imaging (MRI) on the basis of pathological classification.

Methods:

Study Population: 40 atherosclerotic arteries from 14 cadavers (8 males and 6 females, average age 79.14±10.34 years old) were collected on the department of pathology in the university and the hospital from January 2013 to June 2015. 3.0T MRI was performed on the lesion. The resolution is 0.1mm x 0.1mm, slice thickness is 1mm. After the image scanning was completed, the vascular pathological specimen should be processed, and the plaque on MRI should be matched with the one on the pathology level.[1]

Pathological analysis: One experienced pathologist identified and segmented the main components of the plaque in every matched histologic section, including fibrous cap, lipid core, calcification, fibrous tissue and healthy vessel wall according to the American Heart Association classification.[2] The lesion types were judged 8 types: types I–II (initial lesion with foam cells or fatty streaks with multiple foam cell layers); type III (atheroma with extracellular lipid pools); types IV–V (plaque with a fibrous cap and lipid core); type VI (complex plaque with a surface defect, hemorrhage, or thrombus); type VII (calcified plaque) and type VIII (fibrotic plaque without a lipid core).22 According to the pathological classification criteria, the plaques were classified into stable plaque (types I,II, III, VII and VIII) and unstable one (types IV, V and VI).

Radiomic analysis: 3D-slice software was used to manually sketch the plaques on MRI to extract the radiomic characteristics. 109 quantitative radiomic features including intensity, shape based feature and textures were analyzed. Textures included gray level cooccurence matrix (GLCM), gray level run length matrix (GLRLM) and gray level size zone matrix (GLSZM). [3] Statistical analysis was carried out by random forest method.

Results: There are 49 stable plaques and 56 unstable ones by the pathological classification. The radiomic model of intracranial atherosclerotic plaques on the two sequences (T1, T2) had a better performance on discriminating the stability of the plaques (Table-2). In addition, the accuracy on T1 and T2 were 0.832, 0.813, and AUC value was 0.897 and 0.920, respectively. When combined with all the radiomic features, the accuracy was up to 0.861 and the AUC value was 0.945. (Figure-1)

Discussion: The results of this study indicated that the radiomic analysis could accurately identify the stable and unstable plaques in vitro, and the combination of the two sequences (T1WI, T2WI) has higher AUC (0.945) than the signal sequence. The accuracy of the model is 86.1%. In the previous radiomic study of atherosclerotic plaques in vivo[4], the model accuracy rate of all imaging features to comprehensively evaluate symptomatic and asymptomatic plaques was only 82.3% and the AUC was 0.943. This retrospective study showed that quantitative radiomic analysis was more accurate in differentiating unstable plaques with pathological classification criteria than symptomatic plaques in vivo with clinical symptoms classification. That is to say, the classification of atherosclerotic plaques based on the principle of pathological guiding classification was more accurate and reasonable. However, the resolution of this ex-vivo study is higher than the conventional vessel imaging scanning protocol. The low resolution in ex-vivo plaque will be carried out in order to verify if the radiomic analysis on the intracranial plaques in vitro is effective.

Key words: intracranial arteriosclerosis; 3.0T magnetic resonance imaging; radiomics; pathology

References:
1. Jiang YL, Peng WJ, et al. AJNR. (2017) PMID: 28684455
2. Stary HC, Chandler AB, et al. American Heart Association. (1995). PMID: 7648691
3. Aerts, Hugo JWL, et al. Nature communications (2014). PMID: 24892406
4. Shi Z, Zhu C, et al. European Radiology (2018). PMID: 29633002

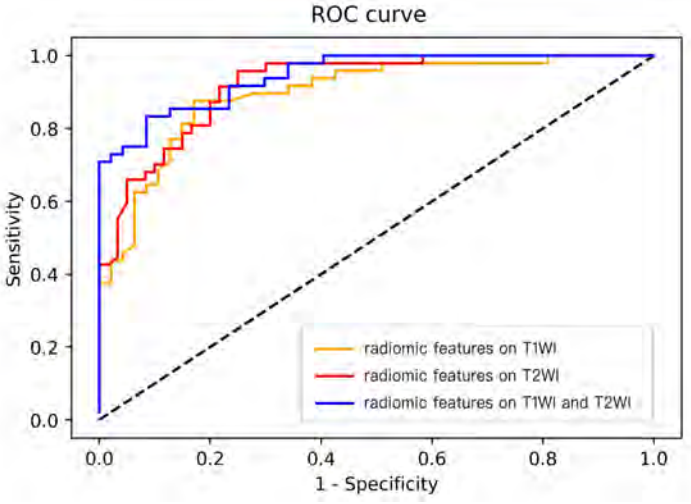

Figure 1: ROC curves to differentiate stable and unstable intracranial plaques.

Table 2. The diagnostic accuracy findings

	ACC	AUC	Se	Sp	LR+	1/LR-
Radiomics(T2WI)	0.832	0.897	0.841	0.804	4.289	5.053
Radiomics(T1WI)	0.813	0.920	0.823	0.800	4.113	4.509
All of radiomics	0.861	0.945	0.860	0.808	4.474	5.788

ACC=accuracy ; AUC= Area Under the Curve;

Se= sensitivity ; Sp= specificity ;

LR+= positive likelihood ratio ; 1/LR-= negative likelihood ratio

Progression of Plaque Burden on Intracranial Atherosclerosis Associated with Recurrent Stroke: A Follow-up Study by High-resolution Magnetic Resonance Imaging

Zhang Shi[1], Xuefeng Zhang[1], Bing Tian[1], Jianping Lu[1], Qi Liu[1]
[1]Department of Radiology, Changhai Hospital, Shanghai, China

Purpose: This study aimed to investigate the association between the progression of plaque on middle cerebral artery (MCA) and recurrent cerebrovascular events using high-resolution magnetic resonance imaging (HR-MRI).

Methods: Sixty-seven symptomatic patients with MCA stenosis underwent vessel wall HR-MRI for intracranial artery at baseline and ≥6 months after the first scan between September 2013 and September 2016, respectively. All the patients had clinical follow-up after the second magnetic resonance scan for ≤35 months until the onset of recurrent transient ischemic attack (TIA) or stroke. Atherosclerotic plaques from MCA were extracted as the region of interest (ROI) for quantitative evaluation. The stenosis value, plaque area/burden, lumen area and contrast enhancement ratio were extracted and calculated. The progression of plaque burden between the first and second magnetic resonance scans was measured. Univariate and multivariate Cox regression was used to calculate the hazard ratio (HR) and corresponding 95% confidence interval (95% CI) of intracranial plaque features in discriminating recurrent events. P-values <0.05 were considered as statistical significant. The intra-reader and inter-reader agreement in measuring morphology of intracranial artery and identifying plaque compositions was calculated by using intraclass correlation coefficient (ICC) and Cohen κ test, respectively.

Results: Sixty-seven patients (mean age: 57.3±11.3 years old; 50 males) were eligible for final statistics analysis. During a mean follow-up duration of 268.9±238.1 days, 24.6% of patients (n=16) experienced ipsilateral recurrent transient ischemic attack/stroke. Acute symptom (P=0.043), the mensal progression of intracranial wall volume (P=0.027) and the mensal progression of plaque burden (P=0.018) were significantly associated with recurrent events in the univariate analysis (Figure-1). The multivariate Cox regression indicated that only the progression of plaque burden (HR, 3.335; 95% CI, 1.154–9.639; P=0.026) was the independent risk factor to predict the recurrence of transient ischemia attack/stroke. ICC for plaque morphological measurements was ranging from 0.89 to 0.98 for intra-reader agreement and from 0.86 to 0.97 for inter-reader agreement, respectively

Discussion: In the present study, we found that the mensal change of plaque burden was superior to maximum wall area and maximum luminal area in predicting recurrent ischemic events. Enlarging plaques with a high progression rate may indicate an active inflammatory status in them. [1] This follow-up analysis of intracranial artery plaque on HR-MRI accurately predicted the symptomatic patients who would have a recurrent TIA or stroke. The mensal progression of plaque burden is independently associated with recurrent ischemic cerebrovascular events, and this measurement has added value in predicting future events.

Key Words: intracranial atherosclerosis; middle cerebral artery; ischemic stroke; magnetic resonance imaging

Reference: [1] Chen H, Ricks J, Rosenfeld M, Kerwin WS. Progression of experimental lesions of atherosclerosis: assessment by kinetic modeling of black-blood dynamic contrast-enhanced MRI. Magn Reson Med. 2013; 69:1712–1720.

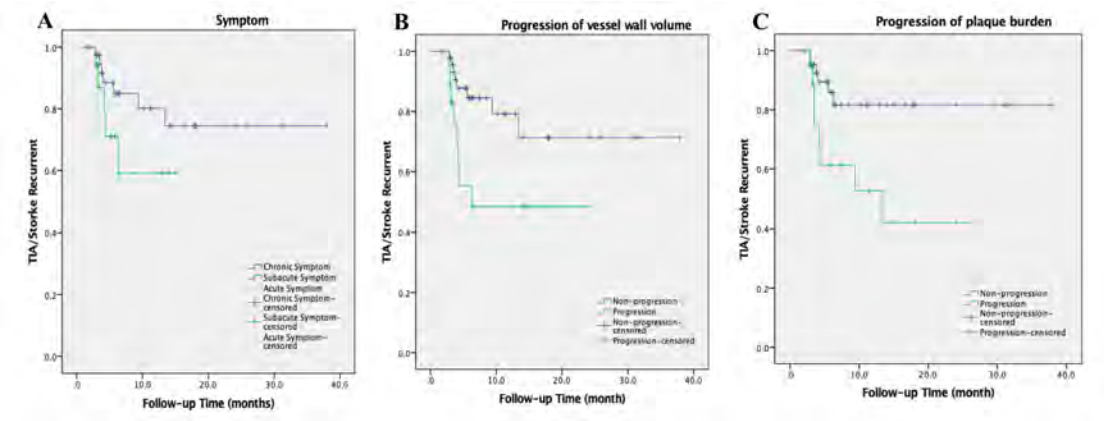

Figure-1 Kaplan–Meier analysis of survival free of recurrent transient ischemic attack (TIA)/stroke in the non-progression group and progression group over a total of 35-month follow-up.

Non-invasive Assessment of Splanchnic Flow in Patients Suspected of Mesenteric Ischaemia using MRI 4D Flow - Pilot Study

P Hall Barrientos[1], K Knight[2], D Black[2], A Vesey[2], G Roditi[3]
[1]Clinical Physics, NHS Greater Glasgow and Clyde, Glasgow, UK
[2]Academic Unit of Surgery, Glasgow Royal Infirmary, Glasgow, UK
[3]Radiology, Queen Elizabeth University Hospital, Glasgow, UK

Purpose: The most common cause of chronic mesenteric ischaemia is atherosclerosis which results in limitation of blood flow to the gastrointestinal tract. This usually manifests as abdominal pain provoked by eating with accompanying weight loss. Although atherosclerosis is a common problem, true mesenteric angina is relatively rare due to the presence of 3 main arteries supplying the gastro-intestinal tract: the celiac axis, superior mesenteric and inferior mesenteric arteries. If one vessel is stenosed or even occluded, the remaining vessels often provide collateral supply, overcoming any deficit. Patients with abdominal pain and a diagnosis of atherosclerotic disease are increasingly being referred for imaging to rule out mesenteric vascular insufficiency.This study aimed to evaluate a 4D flow work-in-progress package (Siemens) as a potential tool for the analysis of blood flow within the mesenteric vessels beyond the limitations of 2D single-slice based acquisitions.

Methods: The mesenteric vessels of seven people were scanned, 3 patients and 4 healthy volunteers. A baseline MRI was acquired after 6 hours of fasting followed by a post-meal MRI obtained 50 minutes after ingestion of 220ml EnsurePlus. Two 4D flow datasets were acquired, one focused over the superior mesenteric artery and the other over the portal vein. Standard 2D PC-MRI slices were acquired along the aorta (supra-coeliac, renal and infra-renal), portal vein (PV), splenic vessel (SV), superior mesenteric artery/vein (SMA/SMV).
Studies were performed on a 3 T Siemens Prisma with a body array coil and ECG gating. The sequences used were as follows: 4D flow: TR/TE 45.92/3.19 ms, spatial resolution 0.8 x 0.8 x 0.8 cm , flip angle = 7°, venc = 150-200 and 30-50 cm/s, ~ 20 cardiac phases and scan duration ~8 minutes. 2D: TR 51.9 ms, TE 5.1 ms, spatial resolution 0.8 x 0.8 x 5 mm, flip angle = 20°, venc 150 and 50 cm/s, ~30 cardiac phases and scan duration 9 s. 4D flow datasets were analysed using a work-in-progress package supplied by Siemens. 2D datasets were analysed using Argus by Siemens. Paired two-tailed Student p-values were calculated to detect the differences between 2D and 4D peak velocities and net flow, and pre- and post-meal net flow in the PV.

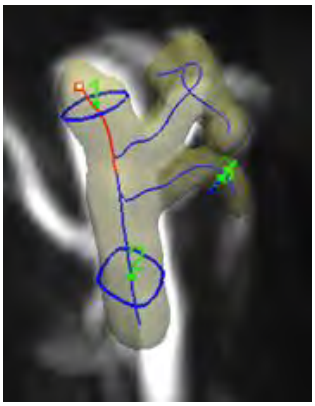

Figure 1. Segmentation of SMA

Results: In the volunteer cohort there was a marked increase in blood flow post-meal within the portal vein (p=0.009). This was not seen in the patient cohort (p=0.078). Similarly, there were significant changes within the SMA of volunteers (p=0.008) and none within the patient group (p=0.184),When 2D and 4D net flow measurements, in both aorta and PV, were compared it was found that 4D technique over estimated (p=0.02, mean bias 2.13 ± 11.7 mL/s).

Discussion:
The 4D Flow software has enabled measurement of flow parameters within the mesenteric vessels. The software has also enabled 3D visualisation of blood flow within the PV, SMV and SV, a shown in figure 1, which could enhance the current clinical diagnostic assessment methods. 2D flow acquisition of the smaller vessels such as the SV and IMV was challenging and time-consuming. It was crucial to determine the correct venc setting for the portal vein, as high venc settings created poorly visualised vessels. This study has given the ground work for a larger cohort study to be undertaken, as there is much interest in translating 4D flow imaging into clinical practice.

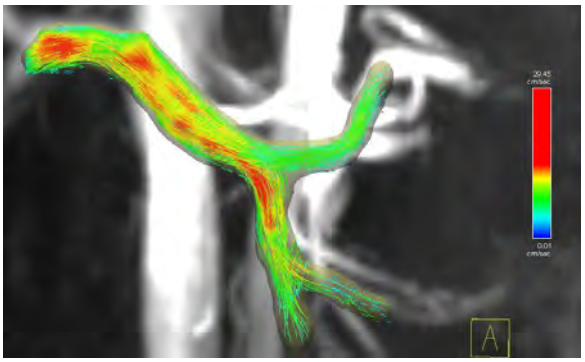

Figure 2. PV flow post-meal

References

1. Roldan-Alzate et al, *J Mag Reson Imaging*,42(4) 1009-1017, 2015
2. Stankovic et al, *Radiology*, 262(3):862-873, 2012
3. Lycklama A Nijeholt et al, *J Hepatol*, 26(2):298-304, 1997

High Resolution Multi-echo Time-of-flight MRA for Imaging of Intra-Renal Vasculature at 7T

Emma Doran[1], JM McAteer[1], C Mirfin[1], P Glover[1], S Francis[1], P Gowland[1], Catherine Ludman[2]
[1]SPMIC Dept of Physics, University of Nottingham, UK, [2] Nottingham University Hospitals NHS Trust, UK

Purpose

Ultra-high field strength MRA imaging offers the potential for using the benefits of increased SNR to effect significant increases in spatial resolution. Abdomino-pelvic imaging at 7T poses significant challenges, including the need for breath-hold imaging. We have used a multi-echo TOF angiography sequence in the kidney and achieved an increase in signal-to-noise ratio within a short acquisition time, by summing the echoes. We demonstrate images with 0.75 mm in-plane resolution enabling visualization of small distal vessels without the use of contrast agent.

Methods

TOF angiography was acquired in four subjects. Data was collected on a 7T Philips Achieva scanner with an MRCoils 8chTx/32chRx dipole array body coil. A 2D standard multiecho fast field echo sequence was used: TR= 30-39ms, 4 gradient echoes with flyback, TE/ΔTE= 5.3-7.9/7.0 – 8.9 ms, resolution 0.75 x 0.75 x 2.0 mm, 6 slices, SENSE 2.5. The target flip angle was 50^{o} (optimized in pilot measurements and not always achievable). B_1+ shimming was applied using a phase nulling method in regions of interest encompassing the right kidney. A DREAM B_1+ map was acquired to determine the achievable flip angle. B_0 shimming was performed using Philips volume shimtool. Maximum Intensity Projections (MIPs) were created from the first echo, and from the sum of all four echoes.

Results

Figure 1 shows example angiogram MIPs from the first echo and from summing across all four echoes. This can be seen to increase vessel-to-background contrast for improved visualization of smaller vessels at the cortico-medullary border. It can be seen that optimal 7T data gave excellent detail particularly in the cortex and highlights the improved visualization of small vessels by summing multiple echoes.

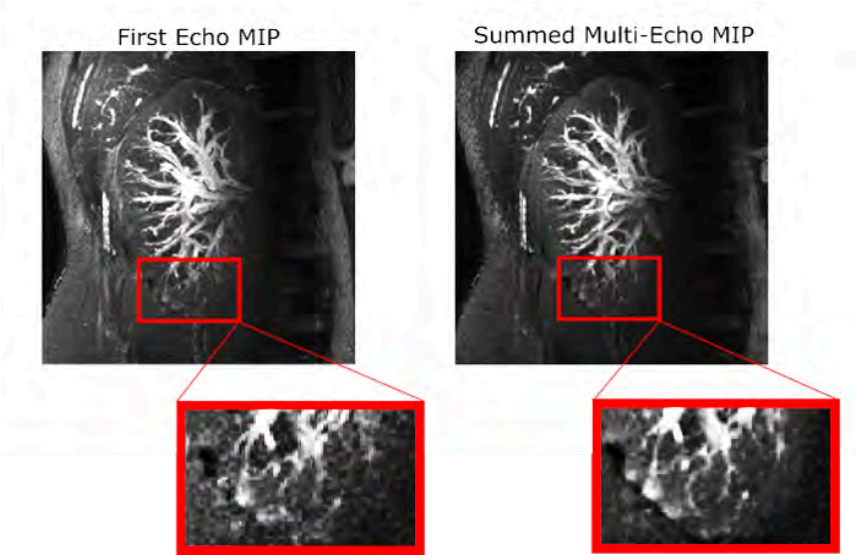

Figure 1: MIPs from first echo image data only (left) and summed multi-echo images (right) from one of the four healthy subjects imaged in this pilot study.

Discussion

Multi-echo TOF provides the increased CNR required to delineate small intrarenal arteries at high spatial resolution. Acquisition in a breath-hold is challenging; in this work, scan time was reduced by increasing the SENSE factor and compensating for reduced SNR by summing the multi-echo images. At 7T the longer T_1 relaxation time can increase CNR, particularly in small peripheral vessels. However, 7T results can be unpredictable, particularly due to a tendency for RF drop out centrally in the body. Tailored RF excitation may be useful in this regard. Intra-renal vessel imaging is pertinent to the investigation of chronic kidney disease (CKD) and as a potential marker of early end-organ damage in hypertension. We expect that further optimisation of small renal vessel imaging will also provide a useful basis for other applications of small vessel abdomino-pelvic MRA imaging.

Conclusion

Multi-echo TOF with summing of the echoes allows improved visualisation of the smaller arteries and arterioles within the kidney. 7T can produce high quality images of the small peripheral vessels but the results can be unstable with current shimming methods and available RF power.

Acknowledgements

Medical Research Council (MRC), Engineering and Physical Sciences Research Council (EPSRC) Oxford-Nottingham Biomedical Imaging Doctoral Training Centre (ONBI DTC)

References

1. Dumoulin CL, Souza SP, Feng H. Magn Reson Med. 5(1):47-57 (1987)
2. Grochowski C, Staśkiewicz G.. Neurol Neurochir Pol. 51(5):411-418 (2017)
3. de Boer A, Hoogduin J, Blankestijn P et al Magn Reson Mater Phy. 29:417-433 (2016)
4. Umutulu L, Maderwald S, Kraff O et al. JMRI 36:714-721 (2012)
5. Metzger GJ, Auerbach EJ, Akgun C et al. Magn Reson Med. 69:114-126 (2013)

Pressure and Flow Interplay in Aortic Dilation using 4D Flow Magnetic Resonance Imaging

Kevin Bouaou, Thomas Dietenbeck, Gilles Soulat, Sophia Houriez--Gombaud-Saintonge, Ioannis Bargiotas, Alain De Cesare, Umit Gencer, Alain Giron, Alban Redheuil, Emilie Bollache, Didier Lucor, Elie Mousseaux, Nadjia Kachenoura.

Sorbonne Université, INSERM, CNRS, Laboratoire d'Imagerie Biomédicale, Paris, France

Aims: The understanding and prediction of thoracic ascending aortic aneurysms (TAA) progression are not well established yet and aortic dissection still frequently occurs in normally sized or mildly dilated aortas. Despite known theoretical associations between pressures and blood flow patterns there are no studies focusing on their simultaneous evaluation. Our aim was to propose a comprehensive and quantitative evaluation of pressure-flow-wall interplay from 4D flow MRI in the setting of aortic dilation.

Methods: We studied 12 patients with TAA (67±14 years, 7 males) and 12 age-matched healthy subjects (63±12 years, 8 males) who underwent 4D flow MRI. The segmented velocity fields were used to estimate: 1) local ascending aortic (AA) pressure changes from Navier-Stokes equations-derived relative pressure maps (AADP, mmHg), 2) AA wall shear stress (AAWSS, Pa) by estimating spatial velocity derivatives at the aortic wall borders, 3) aortic flow vorticity using the λ2 method (AAV, s^{-1}).

Results: AA local pressure change (AADP) was significantly associated with both AAV (r=0.55, p=0.006) and AAWSS (r=0.69 p<0.001). Both associations remained significant after adjustment for maximal diameter (Dmax), age and BSA (p = 0.007 and p=0.003, respectively). Such positive associations indicate that local pressure variations affect local blood flow, generating flow current from high to low pressures and subsequently vortices inducing stress exerted on the AA wall. The strong negative association between AADP and BSA indexed Dmax (r=-0.70, p=0.01) found in the healthy subjects was not replicated in the TAA group, highlighting the heterogeneity of our TAA population. Indeed, patients with the most dilated aorta, as indicated by indexed Dmax, are not necessarily the most severe patients.

Conclusion: Local variations in pressures within the aorta, readily available by 4D flow MRI, are associated with flow disorganization as quantified by vorticity and with the increase in the stress exerted on the aortic wall, as quantified by wall shear stress.

Ungated QISS MR Angiography of the Peripheral Arteries using a Golden Angle Readout and Temporal Maximum Intensity Projection

Robert R. Edelman[1,2], Emily A. Aherne[2], Jianing Pang[3], Nondas Leloudas[1], Ioannis Koktzoglou[1,4]
[1]Radiology, NorthShore University HealthSystem, Evanston, Illinois, United States, [2]Radiology, Feinberg School of Medicine, Northwestern University, Chicago, Illinois, United States, [3]Siemens Medical Solutions USA Inc., Chicago, Illinois, [4]Radiology, Pritzker School of Medicine, University of Chicago, Chicago, Illinois

Purpose: ECG gating is generally required for non-contrast MRA techniques such as quiescent interval slice-selective (QISS) [1] and fresh blood imaging (FBI) [2] that are used to evaluate the lower extremity peripheral arteries. However, there are several drawbacks to the use of ECG gating including increased patient preparation time for lead placement and inaccurate triggering (due to arrhythmias or interference from the magnetohydrodynamic effect). It has been previously demonstrated that ungated QISS using a fast interrupted steady-state (FISS) readout can often match the image quality of ECG-gated QISS [3,4]. However, vascular stripe artifacts may still be present in some subjects, especially individuals with brisk triphasic flow. To address this issue, we implemented a golden angle radial readout allowing arbitrary temporal phases to be reconstructed, along with a temporal maximum intensity projection (temporal MIP) to eliminate the artifacts.
Methods: The study was IRB approved and all subjects gave written informed consent. Imaging was performed in volunteers and patients with peripheral arterial disease (PAD) at 1.5 Tesla (MAGNETOM Avanto, Siemens Healthcare, Erlangen, Germany). First, an ECG-gated single-shot 2D QISS sequence with a balanced steady-state free precession (bSSFP) readout and Cartesian k-space trajectory was acquired using 40 3mm-thick slices per station. This was followed by a prototype ungated QISS FISS acquisition using the same spatial resolution as ECG-gated QISS, radial trajectory with golden view angle increment, TI = 1100ms, 240 views, one shot. In addition to the full 240-view reconstruction, 3 to 6 sequential subsets of data (temporal phases) were generated (retrospective inline or offline Matlab reconstruction). Finally, a maximum intensity projection across all the temporal phases (temporal MIP) was created.

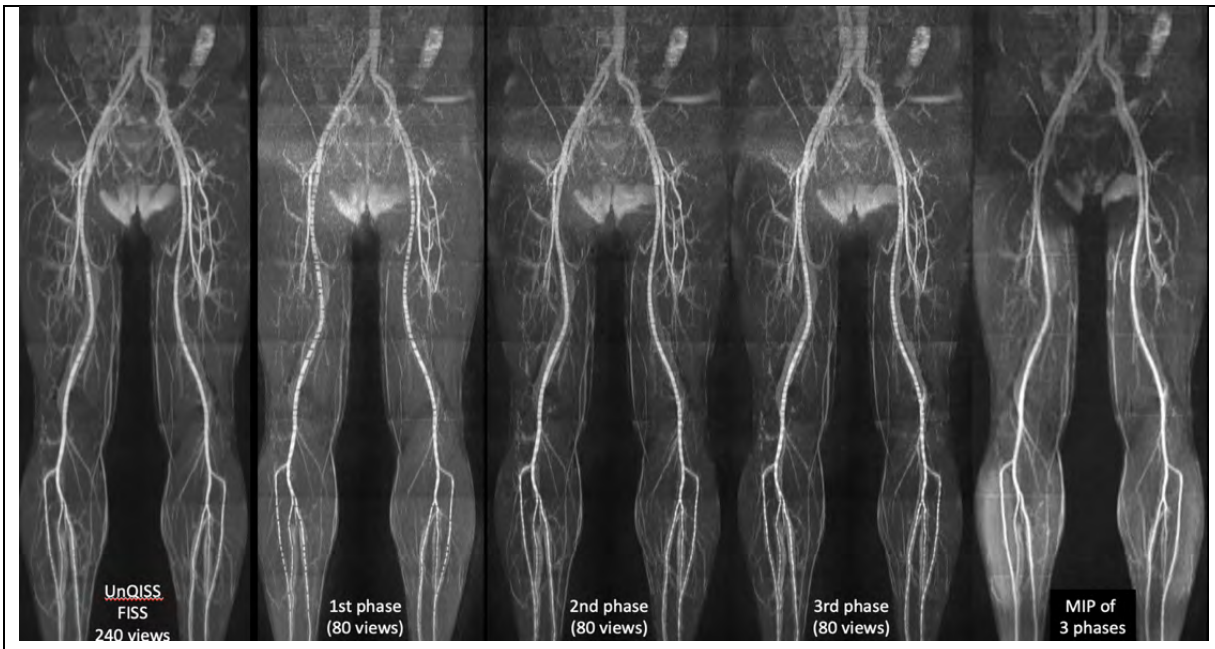

Results: In slices which showed uniform vascular signal with UnQISS FISS, all temporal phases consistently showed high signal within the arteries. However, in slices with vascular stripe artifacts, arterial signal varied among temporal phases. These variations were suppressed in the temporal MIP **(Fig. 1)**.

Discussion: Without the benefit of ECG gating, the traveling venous and in-plane saturation RF pulses used in the QISS pulse sequence are applied during arbitrary phases of the cardiac cycle that vary randomly from slice to slice. Should a venous saturation pulse be applied inferior to a slice during a period of reversed flow, inadvertently saturated arterial spins may flow retrograde into the slice resulting in stripe artifact. A similar problem occurs when an in-plane saturation pulse is randomly applied during a period of diastolic stasis when there is little or no inflow refreshment. To address this issue, several temporal phases are reconstructed for each slice. Images with reasonable image quality can be reconstructed from as few as 40 phases, although 80 radial views are preferred to minimize streaking and obtain diagnostic image quality. Since three 80-view phases span the duration of a typical cardiac cycle, at least one phase will likely coincide with brisk forward flow, giving high arterial signal. *As long as one phase has high arterial signal, the temporal MIP will suppress stripe artifacts that are present in images reconstructed from the full data set.* Minor drawbacks of the technique include increased venous signal and reduced signal-to-noise compared with images reconstructed from all views.

In conclusion, use of a temporal MIP in conjunction with ungated QISS shows promise to eliminate vascular stripe artifacts associated with brisk triphasic arterial flow. Further validation in patients with PAD appears warranted.

References: [1] Edelman RR et al. Magn Reson Med 2010;63:951. [2] Miyazaki M et al. Radiology 2003;227:890. [3] Koktzoglou I et al. Magn Reson Med 2018;79:2077. [4] Edelman RR et al. Magnetic Resonance Angiography 29th Annual International Conference, Stellenbosch, South Africa.

Funding: NIH grants R01 HL137920 and R01 HL130093.

High-Resolution MR Angiography of the Peripheral and Carotid Arteries using Stack-of-Stars QISS

Robert R. Edelman[1,2], Emily A. Aherne[2], Jianing Pang[3], Nondas Leloudas[1], Ioannis Koktzoglou[1,4]
[1]Radiology, NorthShore University HealthSystem, Evanston, Illinois, United States, [2]Radiology, Feinberg School of Medicine, Northwestern University, Chicago, Illinois, United States, [3]Siemens Medical Solutions USA Inc., Chicago, Illinois, [4]Radiology, Pritzker School of Medicine, University of Chicago, Chicago, Illinois

Purpose: For nonenhanced peripheral MRA, the 2D quiescent interval slice-selective (QISS) technique has been extensively validated as an accurate, non-contrast alternative to CTA and contrast-enhanced MRA [1]. For carotid MRA, an ungated version using a fast low angle shot (FLASH) readout has shown promise as an alternative to legacy time-of-flight (TOF) methods [2]. However, the use of very thin slices with a 2D acquisition is restricted by the signal-to-noise ratio (SNR) as well as gradient and RF pulse limitations. Empirically, we have found that the minimum, practically-attainable 2D slice thickness is about 1.5mm. Moreover, 2D slices have a non-rectangular slice profile that degrades the quality of multiplanar reconstructions even when thin slices are acquired, especially when using a balanced steady-state free precession (bSSFP) readout. By comparison, 3D acquisitions provide rectangular slice profiles and permit very thin slices to be obtained. We therefore implemented a thin-slab 3D stack-of-stars (SOS) QISS technique to determine if this would facilitate the acquisition of thinner slices with better image quality than is possible using existing 2D QISS approaches.

Methods: Imaging was performed in volunteers and patients at 1.5 and 3 Tesla (MAGNETOM Avanto or Skyra^{Fit}, Siemens Healthcare, Erlangen, Germany). For peripheral MRA, an ECG-gated single-shot 2D QISS sequence with a bSSFP readout and Cartesian k-space trajectory was acquired using slice thicknesses = 1.3 to 3.0mm with in-plane resolution = 1.0mm. For extracranial carotid MRA, a prototype ungated 2D QISS sequence with a FLASH readout and radial k-space trajectory as well as thin multi-slab 3D TOF MRA were obtained. The prototype stack-of-stars QISS sequence was acquired with 10 to 14 slices, 66.7 to 100% slice oversampling, 6/8 partial Fourier along the slice direction, slice thickness = 1.0 to 1.3mm (interpolated to 0.5 to 0.65mm), and in-plane resolution = 1.0mm. As with 2D QISS, an ECG-gated acquisition with bSSFP readout was used for peripheral MRA and ungated acquisition with FLASH readout for carotid MRA. Image quality was evaluated by an experienced reader and SNR was calculated.

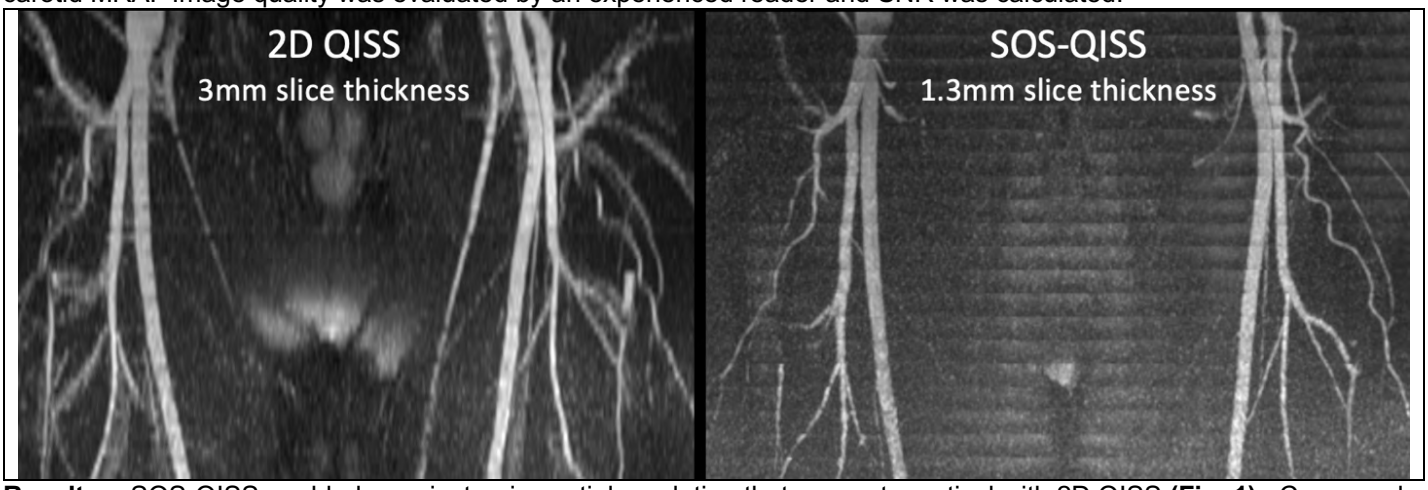

Results: SOS-QISS enabled near isotropic spatial resolution that was not practical with 2D QISS **(Fig. 1)**. Compared with thin-slice 2D QISS using equal voxels and sampling bandwidth, SOS-QISS provided a several-fold increase in SNR depending on imaging parameters. For carotid MRA, ungated SOS-QISS FLASH showed improved image quality compared with ungated 2D QISS FLASH, while reducing flow-related saturation artifact and providing better background signal suppression compared with 3D TOF.

Discussion: We have demonstrated that SOS-QISS MRA can substantially improve image quality for near-isotropic thin-slice imaging of the lower extremity vessels and carotid arteries compared with 2D QISS, while reducing flow-related saturation and improving background suppression in the carotid arteries compared with standard-of-care 3D TOF. The SNR improvement arises from the signal averaging inherent to a 3D acquisition, while the use of a thin (e.g. <20mm) slab in conjunction with a quiescent interval ensures adequate inflow of unsaturated spins. The reduction in saturation-related artifact in the carotid arteries arises from basic sequence design differences from TOF, specifically the use of a lower excitation flip angle, quiescent inflow time and infrequent application of the traveling venous saturation pulse. While further work is needed to optimize the 3D slab profiles, the technique offers promise as a useful adjunct to 2D QISS in situations where very thin slices are needed, e.g. for evaluation of small calf arteries or carotid bifurcations in the neck.

References: [1] Edelman RR et al. Magn Reson Med. 2010;63:951. [2] Koktzoglou I et al. Magn Reson Med. 2016;75:2072.
Funding: NIH grants R01 HL137920 and R01 HL130093.

3D Whole-Heart Imaging with Orientation-Independent 2D Image Navigators

Karl P. Kunze[1], Davide Piccini[2], Christoph Forman[3], Jianing Pang[4], Michaela Schmidt[3], Claudia Prieto[5], Rene Botnar[5], Radhouene Neji[1]**

*1: Siemens Healthcare Ltd., Frimley, UK. 2: Siemens Healthcare AG, Lausanne, Switzerland. 3: Siemens Healthcare GmbH, Erlangen, Germany. 4: Siemens Medical Solutions USA Inc., Chicago (IL), USA. 5: King's College London, London, UK. *: equal contribution*

Purpose: 2D image navigators (iNAVs) [1] have been shown to provide reliable translational respiratory motion estimation/correction for 3D whole-heart MRI, enabling 100% respiratory scan efficiency and short, predictable scan times. Conventionally, iNAVs are acquired with identical FOV and geometry as the imaging volume [1]. This limits the 3D whole-heart scan to coronal or sagittal planes, which are the ones enabling respiratory motion estimation in the most relevant direction (i.e. foot-head (FH)). However, as many cardiac MRI applications are conventionally acquired in transversal or double oblique orientations, we propose an orientation-independent iNAV (ind-iNAV) approach. This enables 2D translational respiratory motion estimation/correction for 3D images acquired in a different orientation, and adds flexibility, e.g. for transversal 3D acquisitions, to have an anterior-posterior (AP) readout direction, which is insensitive to AP motion, and to remove potentially unwanted volume in FH direction from the excitation.
Methods: The proposed 2D ind-iNAV approach enables separate planning by the user of slab thicknesses and positions for iNAV and 3D imaging volumes. It was implemented as a prototype sequence with two-point Dixon [2] spoiled GRE acquisition with T2-preparation and a variable-density spiral-like Cartesian trajectory [3, 4]. Five healthy subjects (age 54±7 years) were scanned on either 1.5T (n=3) or 3T (n=2) MR systems (MAGNETOM Aera/Skyra, Siemens Healthcare, Erlangen, Germany). For each subject, 3D imaging was performed in a coronal plane with iNAV in the same orientation (coronal iNAV/coronal 3D) as in [1], and also using ind-iNAV for coronal iNAV/transversal 3D and sagittal iNAV/transversal 3D setups. All iNAVs were performed with 14 readouts, FA=3 degrees. While the slab thickness was set to 40-80 mm for ind-iNAV, the iNAV was defined by the imaging volume. 3D whole-heart MRI acquisition parameters were for all cases: GRE-Dixon bipolar readout acquisition at 1.5T/3T, TE1=2.38/1.31 ms, TE2=4.76/2.77 ms, TR=6.6/4.8 ms, receiver BW=990/815 Hz/Px, $(1.05\ mm)^3$ isotropic resolution, FA=15 degrees, 3.5-5-fold undersampling, left-right phase-encoding and subject-specific mid-diastolic acquisition window of ~100 ms. 2D translational motion correction, Compressed Sensing reconstruction [4] and Dixon-water fat separation were implemented inline on the scanner.
Results: Average acquisition time across all scans was 9:26±0:53/8:53±0:31 (min:sec) for 1.5T/3T (not significantly different between orientations). Motion estimation and correction was successful for all orientations and resulted in comparable 3D image quality (Fig.1), demonstrating the ability of the ind-iNAV approach to correct for translational respiratory motion measured in FH also in transversal acquisitions. 3D image quality with respect to SNR appeared visually equivalent or slightly higher for transversal compared to coronal acquisitions.

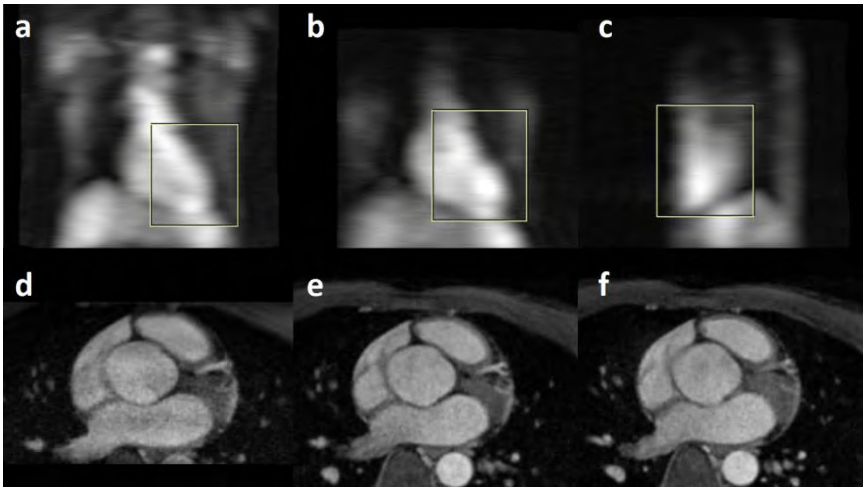

***Fig. 1**: Case at 1.5T, orientation-independent iNAVs (b/c) showing less unwanted signal compared to (a). Similar motion tracking and image quality for coronal acquisition reformatted in transversal orientation (d) when compared to transversal acquisitions (e/f) (water images only).*

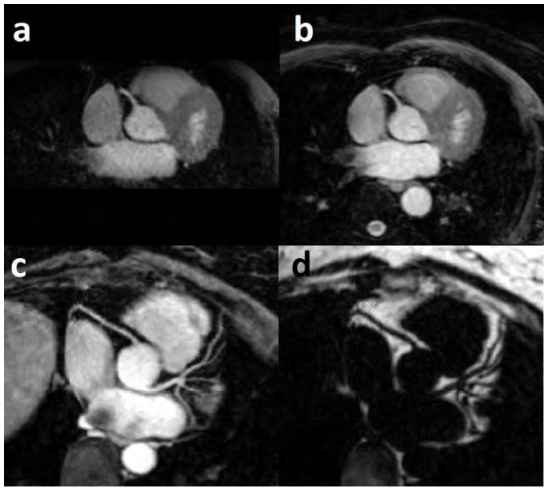

***Fig. 2**: Two 3T cases: 1st, reformatted coronal (a) vs. transversal acquisition (b). 2nd, water (c) and fat (d) images for the transverse acquisition reformatted showing the proximal system.*

Discussion: In this study we propose an orientation-independent 2D image navigator (iNAV) approach for 3D whole-heart GRE imaging. It improves flexibility in 3D imaging with respect to orientations and phase encoding directions, and can be extended to enable free-breathing whole-heart MRI for several cardiac applications conventionally performed in transversal or short axis planes such as 3D free-breathing late gadolinium enhancement.
References: [1] Henningsson M, Koken P, Stehning C, et al. MRM 2012;67:437-445. [2] Eggers H, Boernert, P. JMRI 2014:40:251-268. [3] Prieto C, Doneva M, Usman M, et al. JMRI 2015;41:738-746. [4] Bustin A, Ginami G, Cruz G, et al. MRM 2018;81:102-115. [5] Liu J, Rapin J, Chang T, et al. In: Proc. 20th ISMRM, Melbourne, Australia. 2012. p. 4249.

Proximal region of carotid atherosclerotic plaque shows more intraplaque hemorrhage: the Plaque At RISK (PARISk) study

Geneviève AJC Crombag[1,2], Floris HBM Schreuder[3], Faysal Benali[1],Dianne HK van Dam-Nolen[4], Madieke I Liem[5], Carlo Lucci[6], Anton F van der Steen[7], Mat JAP Daemen[8], Werner H Mess[9], Aad van der Lugt[4], Paul J Nederkoorn[5], Jeroen Hendrikse[6], Paul AM Hofman[1],Robert J van Oostenbrugge[2,10], Joachim E Wildberger[1,2], M Eline Kooi[1,2]

1 Department of Radiology and Nuclear Medicine, Maastricht University Medical Center, Maastricht, The Netherlands; 2 CARIM School for Cardiovascular Diseases, Maastricht University, Maastricht, The Netherlands; 3 Department of Neurology & Donders Institute for Brain Cognition & Behaviour, Radboud University Medical Center, Nijmegen, The Netherlands; 4 Department of Radiology and Nuclear Medicine, Erasmus MC, University Medical Center Rotterdam, Rotterdam, The Netherlands; 5 Department of Neurology, Amsterdam University Medical Centres, University of Amsterdam, Amsterdam, The Netherlands 6 Department of Radiology, Department of Radiology, University Medical Center Utrecht, Utrecht, The Netherlands; 7 Department of Biomedical Engineering, Erasmus MC, University Medical Center Rotterdam, Rotterdam, The Netherlands; 8 Department of Pathology, Amsterdam University Medical Centers, University of Amsterdam, Amsterdam, The Netherlands; 9 Department of Clinical Neurophysiology, Maastricht University Medical Center, Maastricht, The Netherlands; 10 Department of Neurology, Maastricht University Medical Center, Maastricht, The Netherlands

Background and aims: Intraplaque haemorrhage (IPH) contributes to enlargement of the lipid-core and plaque progression, leading to plaque destabilization. The mechanisms that contribute to IPH development are not completely understood. We hypothesise that development of IPH is affected by biomechanical and hemodynamic variables. The biomechanical load and wall shear stress are highest in the proximal region of the plaque. We aim to study non-invasively a possible difference in volume of IPH in the proximal versus the distal region of the plaque.

Methods: 88 symptomatic stroke patients with carotid stenosis included in the multicenter Plaque At RISK (PARISK) study demonstrated ipsilateral carotid IPH on multi-sequence MR images. IPH area was calculated with respect to the total vessel wall area. Differences in mean IPH percentages between proximal and distal regions were calculated using a paired samples t-test, while a McNemar test was used to reveal differences in proportions of a thin and/or ruptured fibrous cap.

Results: We found significantly larger area percentages of IPH in the proximal part of the plaque at 2, 4, and 6 mm from the position of maximal luminal narrowing, respectively: 14.4% vs. 9.6% (p=0.04), 14.7% vs. 5.4% (p < 0.001), and 11.1% vs. 2.2% (p=0.001) (Figure 1). Additionally, we found an increased proximal prevalence of a thin and/or ruptured fibrous cap on MRI (Figure 2).

Conclusion: We demonstrated that IPH is more prevalent on the proximal side of the plaque compared to the distal side. This may indicate that biomechanical and/or hemodynamical variables play an important role in the development of IPH.

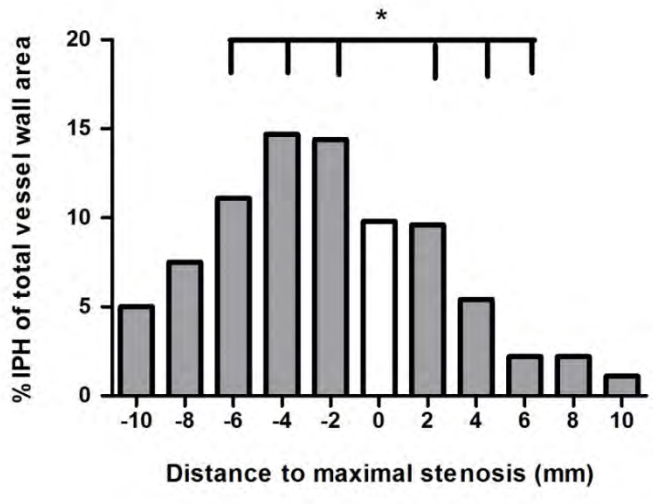

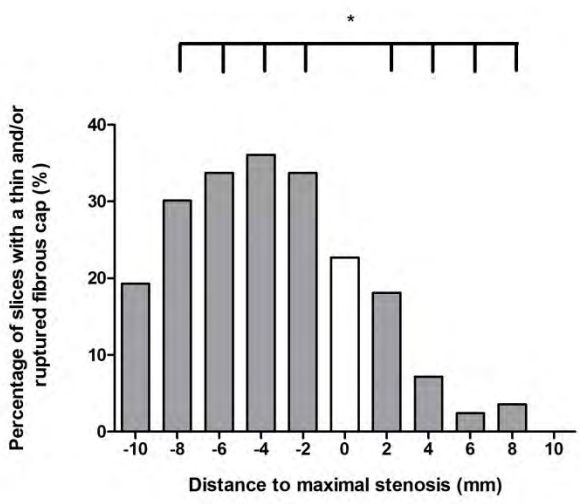

Figure 1 (left) Histogram showing significantly larger mean IPH areas in the proximal region of the plaque compared to the distal region. Mean IPH area percentages are shown for each slice in relation to the smallest lumen. The white bar indicates the slice with the narrowest lumen (distance = 0 mm), the bars on the left with the negative numbers are slices proximal and the bars on the right with the positive numbers indicate the slices distal to the smallest lumen. Each slice has a thickness of 2 mm.

Figure 2 Prevalence of a thin and/or ruptured fibrous cap plotted for each slice position with respect to the slice with the smallest lumen (0). The bars on the left with the negative numbers are slices proximal and the bars on the right with the positive numbers indicate the slices distal to the smallest lumen.

Start of antiplatelet therapy increases the prevalence of intraplaque hemorrhage in patients with advanced carotid artery lesions: a longitudinal MR imaging study

Geneviève AJC Crombag MD[1,2], Madieke I Liem MD[3], Eline Koornstra BSc[1], Floris HBM Schreuder MD[4], Dianne HK van Dam-Nolen MD[5], Carlo Lucci[6], Rob J van der Geest PhD[7], Mat JAP Daemen MD PhD[8], Anton F van der Steen MD PhD[9], Jeroen Hendrikse MD PhD[6], Werner E Mess MD PhD[10], Aad van der Lugt MD PhD[5], Joachim E Wildberger MD PhD[1,2], Robert J van Oostenbrugge MD PhD[2,11], Paul J Nederkoorn MD PhD[3], Marianne E Kooi PhD[1,2]

[1] Department of Radiology and Nuclear Medicine, Maastricht University Medical Center, Maastricht, The Netherlands; [2] CARIM School for Cardiovascular Diseases, Maastricht University Medical Center, Maastricht, The Netherlands; [3] Department of Neurology, Amsterdam University Medical Centers, Amsterdam, The Netherlands; [4] Department of Neurology, Donders Institute for Brain Cognition & Behaviour, Radboud University Medical Center, Nijmegen, the Netherlands; [5] Department of Radiology & Nuclear Medicine, Erasmus MC, University Medical Center Rotterdam, Rotterdam The Netherlands; [6] Department of Radiology, University Medical Center Utrecht, Utrecht, The Netherlands; [7] Department of Radiology, Leiden University Medical Center, Leiden, The Netherlands; [8] Department of Pathology, Amsterdam University Medical Centers, Amsterdam, The Netherlands; [9] Department of Biomedical Engineering, Erasmus MC, University Medical Center Rotterdam, Rotterdam, The Netherlands; [10] Department of Clinical Neurophysiology, Maastricht University Medical Center, Maastricht, The Netherlands; [11] Department of Neurology, Maastricht University Medical Center, Maastricht, The Netherlands

Purpose: Intraplaque hemorrhage (IPH) is an important feature of plaque vulnerability. Patients with a history of transient ischemic attack or stroke are treated with platelet aggregation inhibitors to prevent secondary myocardial infarction or ischemic stroke. Although antiplatelet medication is effective in reduction of clot formation, it also has adverse effects. This longitudinal study investigates the effect of antiplatelet agents on the prevalence of IPH.

Methods: 63 symptomatic patients underwent carotid MRI at baseline and after two years of follow-up. Presence of IPH in both carotid arteries was scored. Medication prescription before and after the index event and after follow-up was collected.

Results: A significant higher prevalence of any IPH was found two years after the index event (42.9% vs. 55.6%; p = 0.008) (Figure 1). Patients already using antiplatelet agents before the index event (n=19) did not show significantly more IPH (52.6% vs. 63.2%, p = 0.50) at follow-up. Patients who did not use platelet aggregation inhibitors before the index event (n=44) and were prescribed medication after the event, showed a significantly higher prevalence of IPH (38.6% vs. 52.3%, p=0.031) at follow-up (Table 1).

Conclusions: Patients who started antiplatelet therapy after the index event show a significant increase in bilateral IPH two years after inclusion, while no significant changes in IPH status were found in the patients that already use antiplatelet therapy before the index event. Future studies are warranted to investigate causal relationships.

Figure 1 Prevalence of intraplaque hemorrhage (IPH) at baseline and after two years follow-up. A significant increased prevalence of IPH was found during follow-up (42.9% vs. 55.6%; p = 0.008).

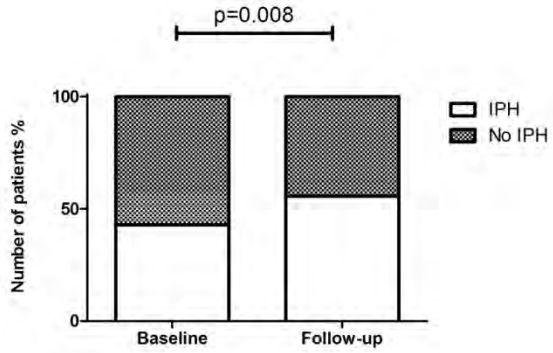

Table 1 Prevalence of intraplaque hemorrhage in patients who were using antiplatelet medication before the index event compared to those who were not, at baseline and follow-up.

		Baseline n (%)	Follow-up n (%)	p-value
Patients who used antiplatelet therapy before the index event (n=19)	Any IPH	10 (52.6)	12 (63.2)	0.500
Patients who did not use antiplatelet therapy before the index event (n=44)	Any IPH	17 (38.6)	23 (52.3)	**0.031**

Anatomic and Hemodynamic Predictors of False Lumen Growth Rate Among Patients with Medically Managed Type B Aortic Dissection

Nicholas S Burris MD[1], Ignas B Houben MD[2], C. Alberto Figueroa PhD[3,4]
David A Nordsletten PhD[2,4], Himanshu J Patel MD[2]
University of Michigan Departments of Radiology[1], Cardiac Surgery[2], Vascular Surgery[3], and Biomedical Engineering[4].

Purpose: Patients with chronic aortic dissection of the descending thoracoabdominal aorta are prone to long-term complications, most importantly false lumen (FL) aneurysm formation.[1] Aneurysm can be prevented by endovascular repair (TEVAR) in the acute/subacute phase allowing for aortic remodeling; however, TEVAR comes with potential complications not all patients are successfully treated by endovascular repair.[2] Recent studies have suggested that 4D Flow MRI derived hemodynamic features of the FL may be useful in better defining which patients are at highest risk for aneurysm formation. Specifically, elevated entry tear regurgitant fraction has been proposed as surrogate maker of FL pressurization due to insufficient outflow pathways, although there are many additional anatomic and hemodynamic parameters that could contribute.[3,4] The purpose of this study was to investigate the ability of various anatomic and hemodynamic parameters to independently predict FL growth rate using a multivariate analysis.

Patient Characteristics	Population Mean (SD)/ Frequency (%)	Aortic Growth Rate (mm/year) Pearson's *r*	p-value
Age (y)	50.7 ± 9.9	0.33	0.23
Hypertension, n (%)	13 (87%)	0.35	0.21
Baseline Aortic Diameter (mm)	38.9 ± 7.4	0.25	0.38
Age of Dissection (y)	3.6 ± 3.1	-0.57	**0.03**
Aortic Growth Rate (mm/year)	5.3 ± 5.9	1.0	--
False lumen:	--	--	--
Net Flow (L/min)	1.4 ± 1.4	-0.25	0.37
Peak Velocity (cm/sec)	65.8 ± 32.6	-0.24	0.38
FL-Vol_{CT} (L/min)	0.6 ± 0.3	0.47	0.10
Dominant Entry Tear:	--	--	--
Average Size (mm)	14.4 ± 6.5	0.02	0.93
Regurgitant Fraction (%)	29.0 ± 27.6	0.75	**<0.01**
Peak Velocity (cm/sec)	113.4 ± 35.9	0.24	0.38
Distance from Left Subclavian	40.3 ± 48.4	0.37	0.17

Multivariate Model				Adjusted R^2 = 0.78
Variable	β	SE	95% CI	p-value
Entry Tear Regurgitant Fraction	0.14	0.04	0.06 – 0.22	**<0.01**
Baseline Aortic Diameter	0.30	0.14	-0.03 – 0.63	0.07
Follow-up Interval²	-0.15	0.10	-0.37 – 0.08	0.17
Entry Tear Average Size	-0.01	0.18	-0.43 – 0.43	0.99
False Lumen Net Flow	-0.61	0.78	-2.46 – 1.24	0.46
False Lumen Peak Velocity	0.03	0.04	-0.07 – 0.14	0.51
Entry Tear Distance from LSC	0.07	0.02	0.01 – 0.13	**0.02**

Methods: Patients with dissection of the descending thoracic aortic (n=12 type B, n=3 repaired type A) were prospectively enrolled and underwent contrast-enhanced 4D Flow MRI covering the thoracic aorta. 4D Flow data was reconstructed and analyzed using commercially available software (Arterys, Inc). Various hemodynamic parameters were measured from 4D Flow data including flow volume and peak velocity in the true (TL) and false (FL) lumens. Entry tear regurgitant fraction was defined as the percent of retrograde diastolic flow relative to the systolic forward flow passing through the dominant entry tear. Baseline anatomic data was assessed by baseline clinical CT, and anatomy as research MRI was assessed using a combination of CE-MRA and 4D Flow magnitude data. Clinical information was abstracted by chart review. FL growth rate was calculated as the change in maximal aortic diameter between baseline CT and the research 4D Flow exam. FL outflow volume (FL-Vol_{CT}) was estimated by CT assessment of FL branch artery supply as per Sailer et al.[4] Multiple linear regression was performed to identify independent predictors of aortic growth rate.

Results: The average patient age was 50.7 ± 9.9 y and the majority were male (n=13, 87%). On baseline CT, the mean aortic diameter was 38.9 ± 7.4 mm, mean dominant entry tear size was 14.4 ± 6.5 mm. The mean follow-up interval between baseline CT and 4D Flow MRI was 1.8 ± 1.9 y and the mean growth rate was 5.3 ± 5.9 mm/year. Entry tear size was moderately correlated with FL net flow volume (r=0.57, p=0.02) and FL peak velocity (r=0.53, p=0.04). No significant association was identified between aortic growth rate and FL net flow (r=-0.25 p=0.37) or FL peak velocity (r=-0.24, p=0.38); however, there was a moderate, but non-significant correlation with FL-Vol_{CT} (r=0.47, p=0.1). Aortic growth rate was not significantly elevated in patients with partial FL thrombosis at MRI (7.5 ± 7.0 vs. 3.4 ± 4.5 mm/y, p=0.20). On multivariate analysis, aortic growth rate was independently predicted by entry tear regurgitant fraction (β 0.14, 95% CI: 0.06-0.22, p<0.01), and entry tear distance from the left subclavian artery (β 0.07, 95% CI: 0.01-0.13, p=0.004).

Discussion: Entry tear regurgitant fraction, as measured by 4D Flow MRI, and the entry tear distance from the left subclavian artery are independent predictors of FL growth rate after adjusting for a variety of other anatomic and hemodynamic factors. Entry tear regurgitant fraction showed stronger correlation with aortic growth rate than CT derived estimates of FL outflow. The underlying mechanism is believed to be an increased ratio of between FL inflow relative to FL outflow leading to FL pressurization and increased amounts of regurgitant (retrograde) flow at the entry tear during diastole, and has been confirmed by computational modeling studies[5]. Entry tear regurgitant fraction, as measured by 4D Flow MRI, may be a simple parameter that reflects the hemodynamic stress on the FL and may help guide surgical decision making in patients with type B dissection.

References: [1] Durham et al. J Vasc Surg. 2015 May;61(5):1192-8. [2] Nienaber et al. Circulation. 2009 Dec 22;120(25):2519-28.; [3] Burris et al. J Thorac Cardiovasc Surg. 2019 Feb;157(2):488-491; [4] Sailer et al. Circ Cardiovasc Imaging. 2017 Apr;10(4). [5] Rudenik et al. PLoS One. 2017 Jan 26;12(1):e0170888.

Phase Contrast MR renal blood flow characterizes disease progression in Autosomal Dominant Polycystic Kidney Disease

Hreedi Dev[1], Xiaorui Yin, Sadjad Riyahi, Stephanie Donohue, Warren O. Bobb, Jon D. Blumenfeld, Martin R. Prince

Weill Cornell Medicine Departments of Radiology[1] and Medicine[2] New York, NY 10021 USA

Purpose: In autosomal dominant polycystic kidney disease (ADPKD), the normal renal parenchyma is gradually destroyed and replaced by innumerable cysts that grow and enlarge the kidneys. Disease progression is difficult to assess because hundreds of cysts with heterogeneous imaging features are not easily segmented from the normal parenchyma. Since kidneys filter blood, renal blood flow is normally high, even at rest and can be expected to diminish as renal parenchyma is destroyed. Here we investigate the utility of a simple 2D PC MRA renal artery blood flow (BF) measurement to characterize renal parenchymal destruction in ADPKD.

Methods: 67 subjects with ADPKD with 3 or more MRI scans including T1, T2, SSFP and DWI pulse sequences as well as 2D cine phase contrast MRA at 1.5T (GE signa EXCITE at 23.0) using the 8-channel body array coil were retrospectively reviewed. 2D cine PC images were proscribed on SSFP images perpendicular to right and left renal arteries (RRA and LRA) about 1 cm from their origin on the aorta using the following parameters: TR/TE/flip= 9.5/5/30, matrix (freq/phase) = 256/128, slice thickness = 5 mm, peripheral pulse ox gating with 20 phases reconstructed across the R to R interval. Renal artery BF was measured from the 2D cine PC data using Medis CV flow software (Medis Netherlands) by placing a cursor on each renal artery and allowing automatic edge detection to find the lumen/wall border and automatically propagate to all 20 phases. A total renal BF was obtained by summing LRA BF with RRA flow. Also, a mean of LRA and vein BF, as well as sum of this mean with RRA (RRA + (LRA+LRV)/2) were calculated. Linear mixed effect model was utilized to assess association of baseline flow measurements with change in eGFR over time.

Results: The patients with the mean age of 47.4 (11.6) years were half females (49%) and followed up over the mean of 5 years (Min: 3 years, max: 8 years). Flow measurements exhibited excellent interobserver reliability for 3 raters with ICCs > 0.90. Baseline BF measurements were significantly associated with eGFR on the last follow up visit (*p*'s<0.01), except for RRA. Significant association with change in eGFR over time was seen for the baseline LRA (standardized β =5.32 [0.45 – 10.18], *p*=0.032) and RRA + (LRA+LRV)/2 (standardized β =7.91 [3.31 – 12.52], *p*=0.001) after adjustment for age, sex, time of follow up and height adjusted total kidney volume in a mixed effect model (Figure 2).

Discussion: These serial data from 67 ADPKD patients demonstrate that renal blood flow measurements on 2D cine phase contrast MRA correlate with eGFR, a biomarker of disease severity. A single measurement of left renal blood flow representing the mean of left renal artery flow (towards the left) and right renal vein flow (toward the right) gives the best results. As these vessels are adjacent and in theory have equal flow volumes, averaging their absolute values appears to compensate for phase shifts affecting the stationary tissues without requiring any extra scans or background subtraction. It is a rapid measurement that takes less time to process compared to total kidney volume or kidney cyst fraction measurements. Renal blood flow measurements may hold potential to assist in prediction of disease progression in ADPKD.

Fig 1. Correlation matrix of baseline renal measurements with future eGFR

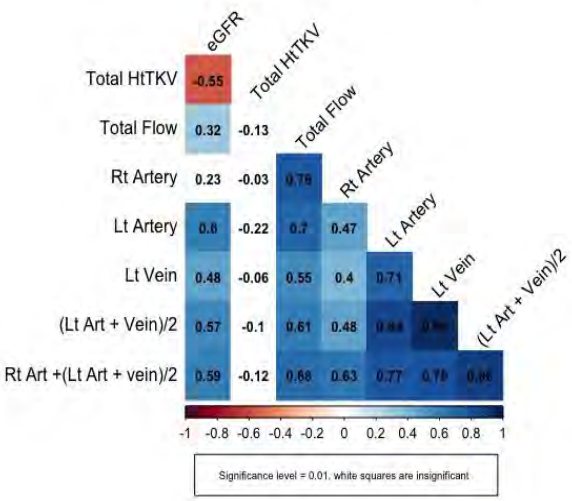

Fig 2. change in eGFE by change in Renal BF (mixed effect model)

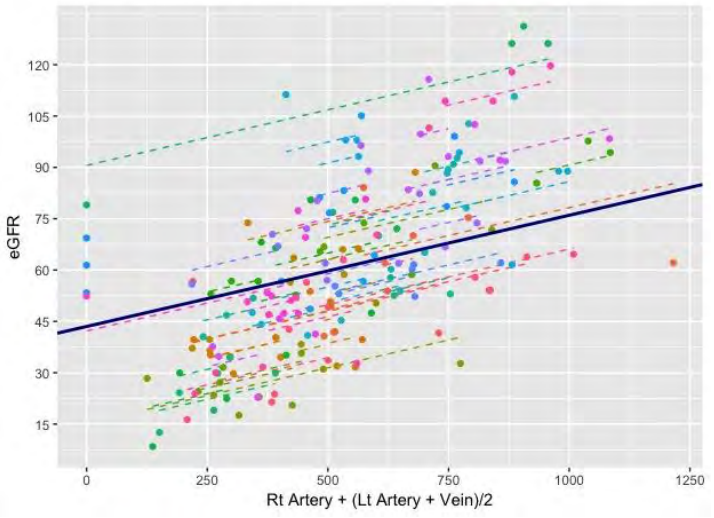

A Multi-Scale Variational Neural Network for Accelerating Free-breathing Whole-Heart 3D Coronary MR Angiography

Niccolo Fuin[1], Aurelien Bustin[1], Thomas Kuestner[1], René M Botnar[1], Claudia Prieto[1].
[1]School of Biomedical Engineering and Imaging Sciences, King's College London, UK.

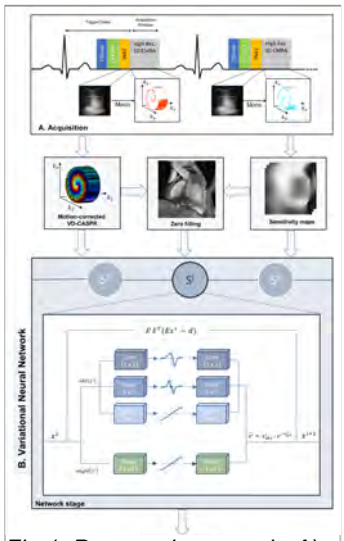

Fig.1: Proposed approach. A) motion compensated CMRA, B) VNN multiscale network.

Introduction: 3D whole-heart coronary MR angiography (CMRA) has shown significant potential to noninvasively visualize cardiac anatomy and coronary artery integrity. However, CMRA acquisition remains lengthy. Undersampled compressed sensing (CS) reconstruction approaches have been applied to accelerate CMRA[1]. For high acceleration factors, however, CS-based techniques suffer from residual aliasing artifacts, dependency on regularization parameters and long reconstruction times. In this work, we propose a novel Multi-Scale Variational Neural Network[2] (MS-VNN) to allow fast reconstruction of 3D high-resolution images from prospectively undersampled (5x and 9x) translational motion-corrected CMRA data. We combine this approach with 100% respiratory efficiency to enable the acquisition of high-quality 1.2mm^3 isotropic CMRA images in ~2-4 minutes, with a total reconstruction time of ~14 seconds. The proposed technique is compared with CS[3] for 5x and 9x acceleration.

Methods - *Acquisition:* Fifteen healthy subjects underwent free-breathing 3D CMRA acquisition with variable density spiral-like Cartesian sampling[4] on a 1.5T scanner. A 2D image-navigator[5] enables beat-to-beat translational respiratory motion estimation/correction and thus 100% respiratory scan efficiency (Fig.1A). Data were acquired using 3D bSSFP with TR/TE = 3.35/1.47 ms, FA = 90°, T2-preparation = 40 ms and 1.2 mm^3 isotropic resolution. Acquisitions were performed fully-sampled and with 5x and 9x acceleration.
VNN Architecture: Translational motion corrected undersampled k-space data and coil sensitivity maps are provided as input to the MS-VNN. In each of the 10 stages of the network, the initial reconstruction is updated according to the variational scheme in Fig.1B. A first path enforces data consistency to the motion corrected undersampled k-space data. The second path is a regularization operator that applies two parallel sets of real-valued filter kernels and corresponding activation functions to the magnitude and phase image of the complexed-valued image. For the magnitude image a multi-scale approach is applied with 3 parallel sets of 11x11, 5x5 and 1x1 filter kernels to better capture the small calibre of the coronaries. For the phase images, 1 set of 11x11 filter kernels are applied. The root mean-squared error was used as loss function.

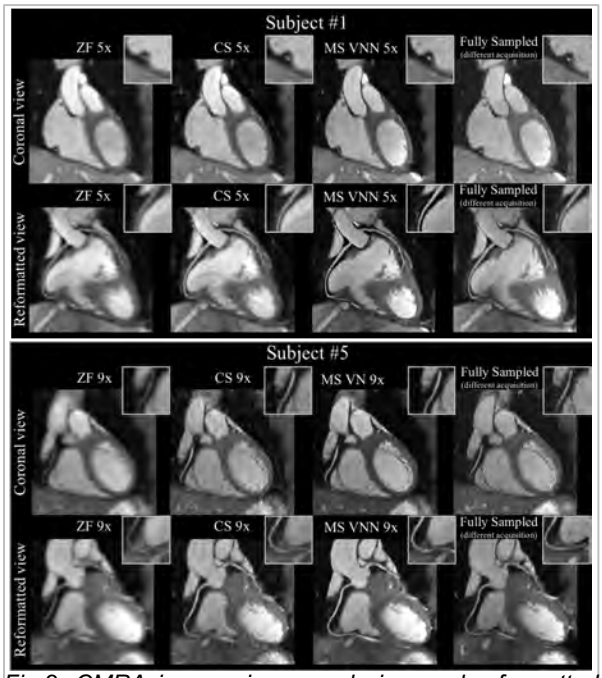

Fig.2: CMRA images in coronal view and reformatted along the left and right coronary arteries for 5x and 9x accelerations. Proposed MS-VNN achieves better quality than CS and comparable results to a fully sampled scan.

VNN Training: The network was trained on 2D complex-valued images obtained from retrospectively undersampled 5-fold or 9-fold 3D CMRA data of 10 subjects (2400 images). During the training procedure, the output of the VNN is compared to the corresponding fully sampled reference images. Training is performed with retrospective undersampling data to ensure that the effect of respiratory and cardiac motion in both input and output images is identical.
Experiments: Fully sampled and prospectively undersampled data of 5 healthy subjects (not included in the training) were used to evaluate the framework. The proposed approach was compared to zero-filled (ZF), and Wavelet-based CS[3] reconstructions. Vessel sharpness of the right and left coronary arteries was measured using SoapBubble[6].

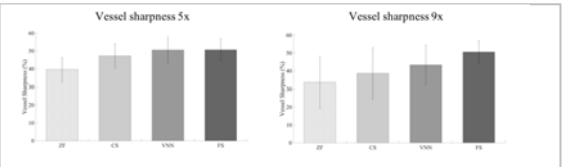

Fig. 3: Coronary vessel sharpness for 5 healthy subjects who underwent CMRA (1.2 mm^3 resolution) with 5x and 9x acceleration. ZF, CS, proposed MS-VNN and fully sampled scans are compared.

Results: The average acquisition time (m:s) was 18:55 for the fully sampled scan, 4:11 for 5-fold acceleration and 2:34 for 9-fold. The proposed MS-VNN achieves higher image quality than ZF and CS (Fig. 2), with image quality and coronary artery sharpness comparable to the fully-sampled image (Fig. 3). Reconstruction time was ~5min for CS and ~14s for the proposed MS-VNN.

Discussion: Free-breathing motion-compensated whole-heart 3D coronary images with 1.2mm^3 isotropic resolution were successfully obtained using a Multi-Scale VNN reconstruction approach. This method has shown improved image quality with respect to CS reconstructions, offering several advantages: i) high quality CMRA images, ii) short scan times, iii) no need for tuning of regularization parameters, iv) extremely fast reconstruction time, offering easy integration into clinical workflow.

References: [1]Akçakaya M, et al. Magn Res Med. 2014;71:815-822. [2]Hammernik K, et al. Magn Res Med. 2018;79:3055-3071. [3]Lustig M, et al. Magn Res Med. 2007;58(6):1182-1195. [4]Prieto C, et al. Journal of Magn Res Med. 2015;41:738-746. [5]Henningsson M, et al. Magn Res Med. 2012;67:437- 445. [6]Etienne A, et al. Magn Res Med. 2002;48:658-666.

Acceleration Mapping in the Human Aorta at 7T

Simon Schmidt[1], Sebastian Flassbeck[1], Mark E. Ladd[1], Sebastian Schmitter[1,2]

[1]*Medical Physics in Radiology, German Cancer Research Center (DKFZ), Heidelberg, Germany,* [2]*Physikalisch-Technische Bundesanstalt (PTB), Braunschweig and Berlin, Germany*

Purpose: Phase-contrast (PC) MRI enables the non-invasive characterization of hemodynamics in vivo. Typically, only the velocity is encoded, but higher order motion terms, such as acceleration, can be of clinical interest[1,2]. It is possible to derive acceleration maps from measured velocity data, but this approach has limitations. For correct acceleration quantification, 3-dimensional velocity maps are required, making acquisitions during a single breath hold unfeasible, and the resulting maps suffer from low signal-to-noise ratio (SNR), which limits the accuracy[3]. In contrast, by controlling the second gradient moment during acquisition, acceleration can also be directly measured as demonstrated at lower magnetic fields[4,5,6]. Here, we investigate the feasibility of acceleration mapping in the human aorta at 7T, while addressing the challenges of short T_2* at 7T by minimizing echo times (TE) and of heterogeneous flip angles (FA) by using B_1^+ phase shimming.

Methods: Tripolar gradients were inserted into a PC gradient echo (GRE) sequence between excitation and readout (Fig. 1) to control the zeroth (m_0), first (m_1) and second (m_2) gradient moments that are linked to spatial, velocity and acceleration encoding, respectively. While m_1 was always nulled to eliminate any velocity dependent phase, m_2 was varied in a 2-point balanced fashion using an acceleration sensitivity (AENC) of 70m/s². Additionally, the velocity vector field was acquired using a velocity sensitive 2D PC sequence (VENC=1.5m/s) with the following matched parameters: resolution=(2x2x5)mm³, FOV=380x166mm², GRAPPA=2, ECG, 2 lines per cardiac phase. Parameters that differed were: temporal resolution=42/35ms, TE=7.8/6.0ms for acceleration/velocity mapping, respectively. Each component of the acceleration and velocity vector was acquired in separate scans during breath-hold with a custom-built 8-channel transceiver coil. Prior to the PC measurements, the complex B_1^+ maps of each transmit channel were obtained using a fast estimation technique[7]. Homogeneity of the FA was improved by B_1^+ phase shimming targeted toward minimizing the coefficient of variation of the FA[8]. Measurements were performed on a 7T system (Siemens) with approval of the local ethics committee in a healthy female volunteer. From the obtained velocity vector field $\vec{v}$, the calculated acceleration was derived as: $\vec{a} = \frac{\partial \vec{v}}{\partial t} + \vec{v} \cdot \nabla \vec{v}$.

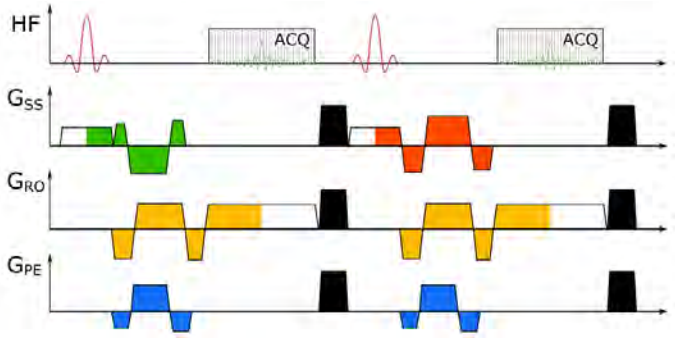

Figure 1: *Schematic sequence diagram of acceleration encoding along the slice-select axis. While m_2 is compensated on the readout (yellow) and phase-encode (blue) axes, a 2-point balanced encoding is applied on the slice-select axis (green/red). Spoiling gradients are marked in black.*

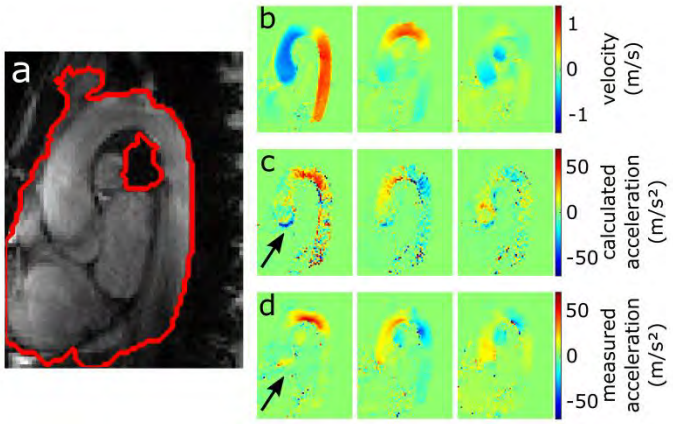

Figure 2: *a) Magnitude image and mask (red) used for the subfigures (b-d). All images correspond to the same time-frame in mid-systole and show the individual components of the vector fields: up-down, left-right and through-plane. b) Velocity maps obtained with PC imaging and corresponding calculated acceleration c). Note the increased noise in the calculated acceleration maps. d) Measured acceleration maps.*

Results: Fig. 2 a) shows a GRE magnitude image during mid-systole obtained with an optimized B_1^+ phase shim setting. The red area was used in Figure 2b)-d) to mask noise regions and to evaluate the standard deviation (std.) in the obtained maps at end-diastole. Although the measured velocity b) shows low velocity noise (std.=0.09m/s), the calculated acceleration c) yields poor acceleration quality (std.=27m/s²) compared to the measured acceleration d) (std.=4m/s²). Furthermore, since only a 2D acquisition could be performed, only the temporal term $\frac{\partial \vec{v}}{\partial t}$ and parts of the convective term ($\vec{v} \cdot \nabla \vec{v}$) could be computed, yielding deviations between the calculated and measured acceleration, especially in the aortic root (black arrow) of up to 65m/s².

Discussion: In this work we successfully showed the feasibility of acceleration mapping in the human aorta at 7T in combination with B_1^+ phase shimming to achieve a homogenous FA distribution. The tripolar gradients needed for acceleration mapping prolong the echo time and therefore lead to a signal reduction, which is enhanced at 7T due to the shorter T_2* compared to lower field strengths. Nevertheless, the measured acceleration maps show significantly improved image quality compared to the calculated maps. Furthermore, the convective acceleration cannot be completely calculated from 2D velocity data, which becomes significant in the aortic root for the given example. Therefore, the direct measurement of the acceleration vector field provides access to an additional hemodynamic parameter that might be of clinical interest, since acceleration is directly linked to force.

References: [1] Qinyun et al.: J.Appl.Physiol. 2006; [2] Vogel et al.: Circulation 2003; [3] Balleux-Buyens et al.: Phys.Med.Biol. 2006; [4] Forster et al.: Med.Phys. 2001; [5] Tasu et al.: MRM 1997; [6] Staehle et al.: MRM 2011; [7] Van de Moortele et al.: ISMRM 2009; [8] Schmitter et al.: JMRI 2016

Artificial intelligence-based fully automated 3D segmentation of the aorta from 4D flow MRI

Haben Berhane[1], Michael B. Scott[2], Mohammed S. M. Elbaz[2], Patrick McCarthy[3], Chris Malaisrie[3], James Carr[2], Ryan Avery[2], Joshua D. Robinson[1], Cynthia K. Rigsby[1], Michael Markl[2]

[1]Lurie Children's Hospital, Chicago, IL [2]Radiology, [3]Cardiac Surgery, Northwestern University, Chicago, IL

Purpose: 4D flow MRI provides spatiotemporally-resolved information on 3D blood flow dynamics enabling comprehensive hemodynamic evaluation. However, 4D flow MRI analysis can be cumbersome and time intensive. For the aorta, processing requires extensive manual input, particularly for 3D segmentation of the thoracic aorta. Currently, there is lack of robust methods for automated processing and analysis of 4D flow MRI, which would accelerate data analysis, facilitate clinical translation, and minimize inter-rater variability. Previous attempts at automated aortic segmentation have focused on atlas registration [1] or utilization of additional data such as cine SSFP [2]. However, these methods face challenges when dealing with patients of a wide array of ages or different aortic diseases. Deep learning and convolutional neural networks (CNN) have demonstrated excellent results in the segmentation of MR images [3]. Expanding on these developments, our goal was to develop a 3D hybrid DenseNet /U-Net CNN for 3D segmentation of the aorta from 4D flow MRI from a large diverse cohort of >1000 aortic 4D flow data sets spanning a wide range of ages and various aortic diseases with established ground truth (manual 3D segmentation of the aorta).

Methods: Our dataset is composed of 1013 aortic 4D Flow MRI scans (499 training, 101 validation, 413 testing) from Northwestern Memorial and Lurie Children's Hospital (1.5T or 3T Siemens; spatial res: 1.8-2.5mm^3). The cohort consists of controls (n=113), patients with bicuspid (n=397) and tricuspid (n=242) aortic valves, and pediatrics (n=278). Scans were processed to correct for phase offsets, noise and velocity aliasing, and a phase contrast MR angiogram was calculated to input to the CNN. A CNN with a U-net architecture [4] with 3D DenseNet [5] layers was used. A DenseNet layer consisted of a series of 3D convolutions (kernel size = [3x3x3]), batch normalization, and a linear rectified unit, with each preceding feature map concatenated together after every convolution—retaining all feature maps throughout. A convolution channel size of 12 was used throughout the network to manage the overall number of parameters and possible overfitting. Max-pooling was applied at the encoding sections in order to downsample the feature maps except at the slice length direction (kernel size: [2x2x1]) in order to have a variable input range. The decoding section followed the same structure except for up-convolution layers replacing max-pooling and the addition of skip connections. The final convolution uses a [1x1x1] kernel size with a softmax function. We used a composite loss function including cross entropy plus a dice loss, a constant learning rate of 0.001, ADAM optimizer, and a dropout rate of 0.1. We used two sets of metrics to evaluate against ground truth: 1) geometric metrics (dice scores (DS), the Hausdorff distance (HD), the average symmetrical surface distance (ASSD)) and 2) flow metrics (net flow at the ascending (AAo), arch, and descending aorta (DAo))—determined by semi-manually placing orthogonal planes. Inter-observer comparisons were performed on randomly selected a subgroup of (n=40) subjects.

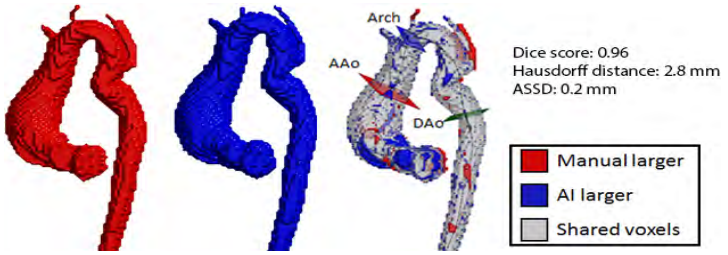

Figure 1: Example of manual (red) and automated (blue) segmentations. A difference map with plane placements and the evaluation metrics are on the right.

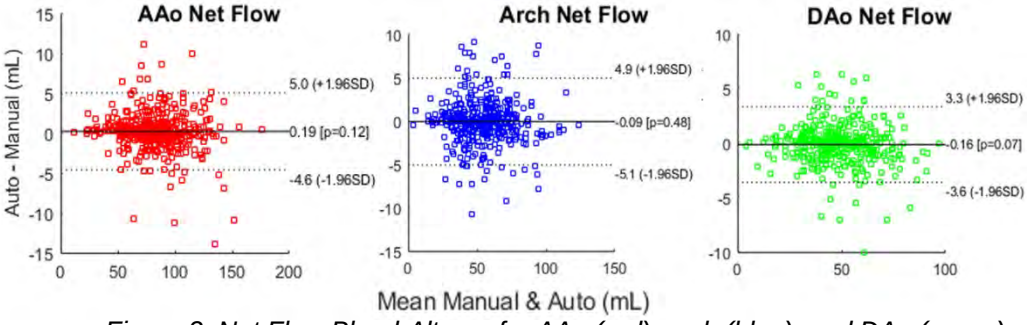

Figure 2: Net Flow Bland-Altman for AAo (red), arch (blue), and DAo (green)

Results: Total training time was 22 hours. Processing time for a single dataset was on average 1 second compared to 10.5 minutes manually. Figure 1 provides example result of the proposed automated vs. manual 3D aortic segementation. Validation data had a median DS: 0.920 [0.892-0.941], HD: 2.19 [2.00-2.58], ASSD: 0.378 [0.244-0.539], and testing data results were DS: 0.951 [0.930 – 0.966], HD: 2.80 [2.13 – 4.35], ASSD: 0.176 [0.119 – 0.290], indicating excellent agreement between fully automated and ground truth. Notably, we found a strong agreement in net flow between the manual and automated methods: AAo-manual: 82.5±25.4, auto: 82.7 ± 25.2; arch-manual: 52.6 [40.9-65.2], auto: 52.3 [40.8-65.1]; DAo-manual: 47.8±15.4, auto: 47.7±15.3. Bland-Altman plots of net flow (Figure 2) showed a low bias and excellent limits of agreement across all aortic regions. Inter-observer comparisons showed median values of: DS:0.950 [0.933-0.964], HD:2.45 [2.125-3.00], ASSD:0.173 [0.118-0.242].

Discussion: We present a 3D CNN which accurately and rapidly segments the thoracic aorta directly from 4D flow MRI. Our CNN demonstrates excellent agreement across all flow metrics, with results as good or better than our observers. We aim to extend this work to segment other major vessels and to generate time-resolved segementations.

References: [1] Bustamante, M. et al. *Med Image Anal*. 2018. [2] Odille, F. et al. *JMRI*. 2019. [3] Mazurowski, M.A. et al. *JMRI*. 2019. [4] Özgün Çiçek, et al. *arXiv*. 2016. [5] Huang, G. et al. *IEEE CVPR.* 2016.

MRI Quantitative T2* Mapping to Predict Dominant Composition of In Vitro Thrombus.

Detraz L[1], Pautre R[1], Mirza M[2], Castets C[3], Darcourt J[4], Labreuche J[5], Desal H[1], Serfaty JM[6], Toquet C[7,] Bourcier R[1].

1From the Departments of Neuroradiology (R.B., R.P., L.D., H.D.).
2Neuravi Thromboembolic Initiative (M.M.), Galway, Ireland.
3Siemens Healthineers France (C.C.), Saint-Denis, France.
4Department of Neuroradiology (J.D.), Hôpital Purpan, Centre Hospitalier Universitaire de Toulouse, Toulouse, France.
5Department of Biostatistics (J.L.), Université de Lille, Centre Hospitalier Universitaire Lille, Lille, France.
6Cardiac and Vascular Imaging (J.-M.S.), Hôpital René et Guillaume Laennec, Centre Hospitalier Universitaire de Nantes, Nantes, France.
7Department of Pathology (C.T.), Hôtel Dieu, Centre Hospitalier Universitaire de Nantes, Nantes, France.

PURPOSE:

MR imaging quantitative T2* mapping, which provides information about thrombus composition and specifically the red blood cell content, may be obtained in the setting of acute ischemic stroke before treatment. This could be useful to adapt the endovascular strategy. We aimed to analyze the red blood cell content of in vitro thrombi in relation to the thrombus-T2* relaxation time.

METHODS:

Thirty-five thrombus analogs of different compositions were scanned with an MR imaging quantitative T2* mapping sequence. Two radiologists, blinded to thrombus composition, measured the thrombus-T2* relaxation time twice at an interval of 2 weeks. Quantitative histologic evaluations of red blood cell content were performed. Inter- and intraobserver reproducibility of the thrombus-T2* relaxation time was assessed by calculating intraclass correlation coefficients. Finally, a Spearman product moment correlation between the thrombus-T2* relaxation time and red blood cell content was performed.

RESULTS:

The median thrombus-T2* relaxation time was 78.5 ms (range, 16-268 ms; interquartile range, 60.5 ms). The median red blood cell content was 55% (range, 0%-100%; interquartile range, 75%). Inter- and intraobserver reproducibility of the thrombus-T2* relaxation time was excellent (>0.9). The Spearman rank correlation test found a significant inverse correlation between thrombus-T2* relaxation time and red blood cell content ($\rho = -0.834$, $P < .001$).

DISCUSSIONS:

MR imaging quantitative T2* mapping can reliably identify the thrombus red blood cell content in vitro. This fast, easy-to-use sequence could be implemented in routine practice to predict stroke etiology and adapt devices or techniques for endovascular treatment of acute ischemic stroke.

Wall enhancement on black blood MRI is an independent predictor of symptomatic status of unruptured intracranial saccular aneurysm

Chengcheng Zhu[1], Xinrui Wang[2], Christopher Hess[1], David Saloner[1], Jianping Lu[2]

1. Department of Radiology and Biomedical Imaging, UCSF, San Francisco, CA, USA

2. Department of Radiology, Changhai Hospital, Shanghai, China

Purpose: Aneurysmal wall enhancement (AWE) on high-resolution magnetic resonance imaging (HR-MRI) has been described in ruptured aneurysms[1] and symptomatic unruptured intracranial saccular aneurysms[2] (UIAs). However, the sample size of previous symptomatic UIA studies are very limited (n<30) and whether AWE is an independent predictor of symptoms is still not clear. This study aims to investigate whether AWE is independently associated with symptomatic status of UIA in a larger cohort of patients using multivariate analysis.

Methods: 147 consecutive patients (71 male, mean age 58±11 years) with 87 symptomatic and 87 asymptomatic UIAs were recruited. Symptoms associated with UIA were carefully identified[2] including oculomotor nerve deficit, visual acuity loss, acute/chronic headache with a marked improvement after surgical intervention of the aneurysm and other symptoms such as hemiparesis due to brain parenchyma compression. All patients underwent 3T MRI and 3D rotational DSA. Pre- and post-contrast T_1-weighted 2D/3D black-blood fast-spin-echo MRI[3] was performed. Scanning parameter: TR/TE 700-1000ms/10ms; resolution: 0.4mm*0.4mm in-plane and 2mm slice thickness (2D) and 0.5mm isotropic (3D).

Image analysis: The degree of AWE was categorized into 3 grades: grade 0 indicates no AWE, grade 1 represents enhancement less than that of the pituitary infundibulum, and grade 2 is greater than that of the pituitary infundibulum. The extent of AWE was assessed as four grades (0-3): none, focal, heterogeneous and complete enhancement[4]. Aneurysm morphological parameters were measured on DSA, including size, aspect ratio and size ratio. Univariate and multivariate logistic regression analysis were performed to determine the factors associated with symptoms.

Results: In 87 UIAs with related symptoms, there were 6 areoculomotor nerve deficit,11 visual acuity loss,31 acute headache, 33 chronic headache and 8 other symptoms. As shown in the **Table,** in symptomatic UIAs, aneurysm size, size ratio, enhancement ratio and extend are significantly larger than asymptomatic UIAs. In multivariate analysis, only aneurysm size (OR 1.1) and AWE (OR 20.7) are independently associated with symptoms. AWE has 92% specificity and 74% sensitivity for symptoms. Figure shows a patient with persistent headache and an ICA aneurysm with AWE.

Discussion and Conclusions: To our knowledge, this is the largest study of AWE of symptomatic UIAs. Our results agree with previous smaller studies[1,2] (n=16 and 23) that AWE is more common in symptomatic UIAs, which may indicate vasa vasorum and inflammation as shown in histology. The unique advantage of our study is we demonstrate AWE is an independent and strong predictor that provides additional value to the current clinical risk model. AWE is a promising marker that should be included in future clinical trials to study its potential value to improve patient outcome.

Table. Characters of symptomatic and asymptomatic UIAs.

Variables	All (n=174)	Symptomatic (n=87)	Asymptomatic (n=87)	*P*	OR, 95% CI (Multivariate)	*P*
Age	58±11	58±11	58±11	0.75		
Sex (%)	71 (41)	29 (33)	42 (48)	0.06		
Hypertension (%)	90 (52)	44 (51)	46 (53)	0.88		
Smoking (%)	25 (14)	14 (16)	11 (13)	0.67		
Size (mm)	8.7±5.6	11.1±6.4	6.4±3.3	<0.001	1.1 (1.0,1.2)	0.04
Location (ICA/other)	75 (43)	41 (49)	34 (39)	0.36		
Aspect Ratio	1.29±0.48	1.34±0.42	1.23±0.53	0.16		
Size Ratio	2.78±1.59	3.36±1.62	2.17±1.32	<0.001		
Enhancement (%)	111 (64)	82 (94)	29 (33)	<0.001	20.7 (7.1,60.7)	<0.001
Enhancement Grade	0.8±0.7	1.3±0.6	0.4±0.6	<0.001		
Enhancement Extent	1.2±1.1	2.0±0.8	0.4±0.7	<0.001		

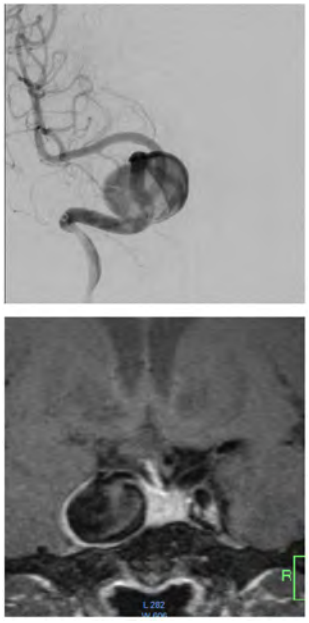

References: 1. Edjlali, Radiology 2018; 2. Fu, Clin Neuroradiol 2017; 3. Zhu, MAGMA 2016; 4. Zhu, Euro Rad 2018

Co-existing Extracranial and Intracranial Artery Atherosclerotic Plaques Predict Future Cardiovascular Events: A MR Vessel Wall Imaging Study

Jin Li[1,2], Dongye Li[1,3], Dandan Yang[1,3], Dan Zhou[2], Xihai Zhao[1]

1. Department of Biomedical Engineering, Tsinghua University, Beijing, China; 2. Department of Radiology, The Affiliated BenQ Hospital of Nanjing Medical University, Nanjing, China. 3. Beijing Institute of Brain Disorders, Capital Medical University, Beijing, China

Purpose: Previous studies have shown that the co-existing intra- and extracranial atherosclerotic diseases can predict future cardiovascular events [1,2]. However, it is still unknown that whether co-existing intra- and extracranial vulnerable plaques have stronger predictive value for future cardiovascular events. This study aimed to determine the relationship between co-existing intracranial and extracranial vulnerable plaques and future cardiovascular events utilizing MR vessel wall imaging.

Methods: Study sample: In total, 103 symptomatic subjects (mean age, 62.8±12.2 years; 77 males) were recruited. **MR imaging**: Intracranial and extracranial carotid artery MR imaging was conducted for all the patients on a 3.0T MR scanner (Achieva TX, Philips Healthcare, Best, The Netherlands) with custom-designed 36-channel neurovascular coil. A carotid multi-contrast protocol was performed with the following parameters: TOF, FFE, TR/TE 20/4.9 ms, and flip angle 20°; T1W, TSE, quadruple inversion recovery (QIR), TR/TE 800/10 ms; T2W, TSE, multislice double IR (MDIR), TR/TE 4800/50 ms; magnetization-prepared rapid acquisition gradient echo (MPRAGE): FFE, TR/TE 8.8/5.3 ms, and flip angle 15°. All sequences used the same FOV of 14×14 cm^2 and spatial resolution of 0.5×0.5×0.5 mm^3. The intracranial artery was imaged by acquiring 3D-TOF MRA: FFE, TR/TE 22/3.9 ms, flip angle 20°, FOV 20×20 cm^2, and spatial resolution 0.6×0.6×0.6 mm^3. **Follow-up:** All patients were followed-up one year and the occurrence of cardiovascular events was recorded. **Image review**: The intracranial artery stenosis was measured on 3D-TOF MRA images. The presence/absence of extracranial carotid plaque, lipid-rich necrotic core (LRNC), calcification, and intraplaque hemorrhage (IPH) was determined. The co-existing plaques were defined as presence of both intracranial artery stenosis and extracranial artery plaque, calcification, LRNC, or IPH. **Statistics**: Cox regression was performed to estimate the impact in terms of hazard ratio (HR) of possible determinants of cardiovascular events. The study protocol was approved by institutional review board and the consent form was obtained from each participant.

Results: Of the 103 included patients, 68 (66.0 %) had intracranial stenosis, of which 53, 35, 42, and 14 had co-existing plaque, calcification, LRNC, and IPH in carotid arteries, respectively. During the median follow-up time of 53 weeks (IQR, 52-60 weeks), 40 (38.8%) patients suffered from cardiovascular events. Univariate Cox regression analysis showed that co-existing intracranial stenosis and carotid plaque (HR, 3.34; 95% CI 1.62-6.87; P=0.001) and LRNC (HR, 2.55; 95% CI 1.33-4.90; P=0.005) were associated with cardiovascular events. After adjustment for age, gender, BMI, and history of stroke, these associations remained statistically significant (co-existing intracranial stenosis and carotid plaque: HR, 2.71; 95% CI 1.26-5.79; P=0.010; co-existing intracranial stenosis and carotid LRNC: HR, 2.41; 95% CI 1.24-4.69; P=0.010) (Fig 1 represents two survival functions from two types of co-existing diseases). Cardiovascular events were not associated with co-existing intracranial stenosis and carotid IPH and calcification (all P>0.05). (Fig 2 is a patient who had co-existing intracranial stenosis and extracranial carotid plaque at baseline and suffered from a recurrent stroke at one year during follow-up).

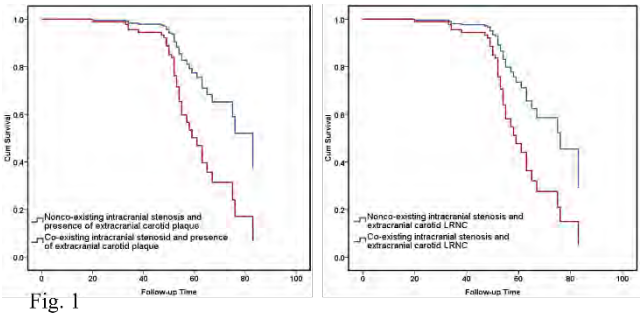

Fig. 1

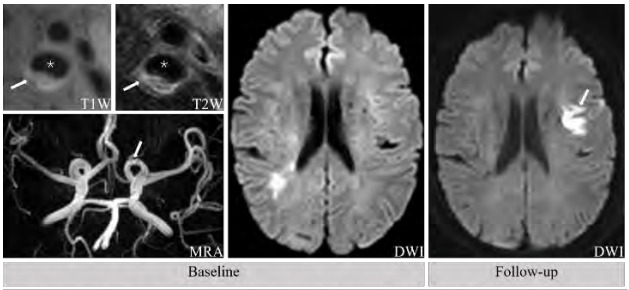

Fig 2. An example for a 63 years old male patient who had atherosclerotic plaque in the extracranial internal carotid artery (white arrows on T1W and T2W, respectively) and intracranial artery stenosis (white arrow on MRA). after a year of follow-up, a new acute infarction was detected in the left hemisphere on followed-up DWI images (white arrow).

Conclusions: Co-existing intracranial stenosis and carotid plaque and LRNC are independent predictors for cardiovascular events.

References: [1] Man BL, et al. Stroke. 2009;40:3211-5. [2] Wong KS, et al. Stroke. 2003;34:2361-6.

5D flow MRI for Cardiac and Respiratory Motion-resolved 3D hemodynamics using Gadoterate Meglumine and Ferumoxytol

Liliana Ma[1,2], Jérôme Yerly[3], Ryan Avery[1], Lorenzo Di Sopra[3], Christopher Roy[3], Davide Piccini[3,4], Alireza Vali[1], Daniel Kim[1,2], James Carr[1,2], Matthias Stuber[3], Michael Markl[1,2]

[1]Department of Radiology, Northwestern University, Chicago, IL, USA, [2]Department of Biomedical Engineering, Northwestern University, Evanston, IL, USA, [3]Department of Diagnostic and Interventional Radiology, Lausanne University Hospital and University of Lausanne, Switzerland, [4]Siemens Healthcare, Lausanne, Switzerland

Purpose: Recent advances in a Free-running framework have enabled highly accelerated radial 3D flow imaging that is resolved in both the cardiac and respiratory dimensions (5D flow).[1,3-5] However, while Cartesian 4D flow studies have compared the effects of different contrast agents on image quality, this has not yet been done for 5D flow.[1] The purpose of this study was thus to 1) evaluate and compare image quality of blood pool contrast agent ferumoxytol, and gadoterate meglumine, a gadolinium (Gd) chelate, in 5D flow MRI using signal- and contrast-to-noise ratios (SNR, CNR), and 2) to evaluate the potential of 5D flow MRI to resolve respiration-induced hemodynamic differences.

Methods: 5D flow imaging of the heart was acquired at 1.5 T in nine patients with aortic/valvular disease and one with a history of ischemic stroke using Gd contrast (8M, age 51.1±15.1 years, Dotarem, 0.1-0.2 mmol/kg, FA=15°), and three healthy volunteers (3F, 32-35 y) using ferumoxytol (Feraheme, 4 mg/kg, FA=25°-35°). 5D flow was also acquired in one volunteer and one patient with aortic disease for non-contrast evaluation of respiration-induced caval vein changes. Prototype 5D flow MRI consisted of continuous 3D radial sampling following a spiral phyllotaxis pattern (spatial res.=2.3 mm^3, recon. temp res.=50 ms, Venc=150 cm/s, TE/TR=2.9-3.1/4.9 ms). Interspersed superior-inferior projections were used to extract cardiac and respiratory signals to bin the continuously acquired data into a 6D dataset (kx-ky-kz-cardiac-respiratory-flow) for reconstruction using XD-GRASP.[5] Blood-myocardium CNR ([blood signal-myocardial signal]/background noise) and blood SNR were evaluated and averaged in three slices in the left ventricle in diastole. Line profiles were drawn through the myocardium for evaluation of edge sharpness (**Fig. 1B**). Magnitude (mag) image quality was evaluated on cardiac and respiratory-motion-resolved videos stepping through all slices and all time points (**Fig. 2**) by an experienced radiologist on a four-point Likert scale based on diagnostic utility (1=non diagnostic, 2=acceptable, 3=good, 4=excellent). Three-point scales (1=non diagnostic, 2=acceptable, 3=good) were used to further evaluate mag images for respiratory and cardiac motion-resolution and velocity images on ease of large vessel identification.

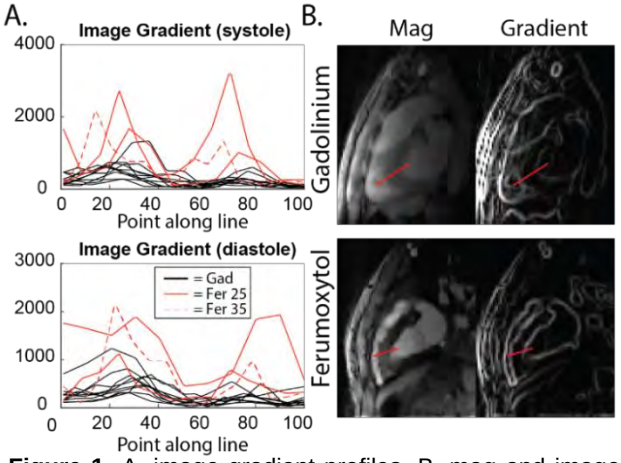

Figure 1: A, image gradient profiles, B, mag and image gradient examples for Gd (top) and ferumoxytol (fer, bottom). 25 and 35 indicate flip angles used for fer.

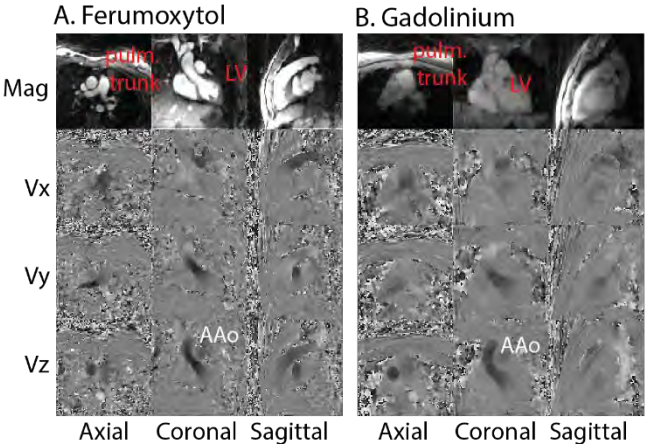

Figure 2: Single time frame of Ferumoxytol (A) and Gd (B) subjects from videos used for expert grading.

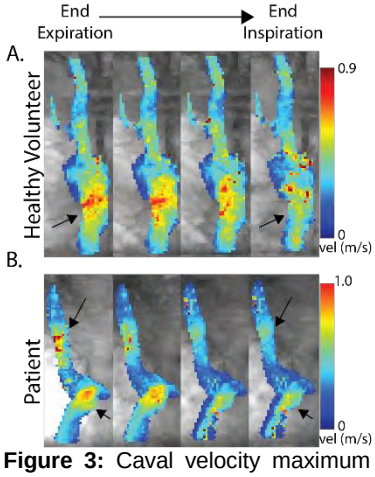

Figure 3: Caval velocity maximum intensity projections at one time point over four respiratory phases. Arrows depict areas with changing flow.

Results: 5D flow was successfully acquired in all subjects in 8:15-8:20 minutes. Ferumoxytol resulted in improved image sharpness in systole and diastole (**Fig. 1A**), as well as improved SNR and CNR (*SNR:* Gd= 35.5± 22.9 [range, 16.0-92.1], Fer=68.0±49.4 [35.6-125.0], *CNR*: Gd=5.6±6.0 [0.5-21.5], Fer=36.9 ± 24.2 [18.1-64.2]). Ferumoxytol scored consistently higher in all expert-ranked categories (image quality: 3.7±0.6 [3-4], motion resolution: 3, flow vessel identification: 3) compared to gadolinium (2±0.7 [1-3], 1.8±0.6 [1-3], 1.9±0.7[1-3], respectively). Initial 5D flow evaluation of non-contrast respiratory-hemodynamics suggest decreased flow and peak velocity in inspiration, compared to expiration (**Fig. 3**).

Discussion: The findings of this study suggest that 5D flow MRI can capture respiratory and cardiac-resolved hemodynamics within 9 minutes scan time, and ferumoxytol contrast agent can greatly improve image quality, motion evaluation, and velocity images . This study was limited by a small sample size and variable ferumoxytol protocol, due to the desire to evaluate the higher r1 and long intravascular half-life of ferumoxytol compared to Gd agents.[6] Noncontrast blood-myocardium borders were difficult to identify and thus not included in image quality analyses. Future studies will include a standardized protocol and more systematic evaluation of respiratory-resolved 3D hemodynamics in vivo.

References: [1] Ma L et al SCMR 2019, [2] Mukai et al. Int J Cardiovasc Imaging (2018) 10.1007/s10554; [3] Di Sopra L et al ISMRM 2017; [4] Coppo S et al, MRM (2015) 10.1002/mrm.25523. [5] Feng et al. MRM (2018) 10.1002/mrm.26745 [6] Hamilton et al. AJR (2012) 10.2214/AJR.10.5992

The Effect of Cellular Rejection in HTx Patients Monitored for Cardiac Allograft Vasculopathy.

Roberto Sarnari[1], Muhannad Aboud Abbasi[1], Arif Jivan[2], Alyssa M Singer[1], Julie Blaisdell[1], Alexander Ruh[1], Brandon Benefield[2], Daniel Lee[2], Kambiz Ghafourian[2], Jane E Wilcox[2], Sadiya S Khan[2], Esther E Vorovich[2], Jonathan D Rich[2], Allen S Anderson[2], Clyde W Yancy[2], Michael Markl[1,3], James C Carr[1]

[1]Dept. of Radiology, [2]Dept. of Cardiology,[3] Dept. of Biomedical Engineering - Northwestern University, Chicago IL

Introduction: Cardiac allograft vasculopathy (CAV) is a leading cause of graft failure beyond the first year after heart transplantation (HTx). Acute cellular rejection (ACR) episodes, due to autoimmune myocardial cellular infiltration, are also reported several years post-HTx. However, the impact of ACR on myocardial structure and function has not been clarified in HTx patients followed for CAV. Increased myocardial collagen deposition can be consequent to myocardial inflammatory processes in the mid and long term. Collagen tissue increment can lead to increased myocardial stiffness and diastolic dysfunction in patients with or without coronary artery disease. Cardiac magnetic resonance imaging (CMR) allows for extracellular volume (ECV) measurement as an indicator of myocardial collagen deposition. We hypothesized that ACR episodes have a role in elevating ECV in patients monitored for CAV.

Methods: Eighty-one HTx patients (age=50.1±15 years, 47M, time after HTx: 7.7±7 years) were prospectively recruited beyond the first year post-HTx for a CMR between August 2014 through November 2018. Fifty five patients, having complete history of ACR episodes during follow up and CAV 0 or 1 grade, were considered for analysis. CAV2 and 3 grade patients were excluded in order to minimize the confounding effect of significant coronary stenosis possibly having pro-fibrotic effect on the myocardium and thus leading to increased ECV. Patients were also excluded if they had no documented rejection episodes or if ECV could not be calculated. Patients underwent CMR at 1.5T (Magnetom Aera/Avanto, Siemens, Erlangen, Germany). Patients were divided into two groups based on median number of ACR occurring from the date of HTx to the most recent follow up: Group 1 (n=31 patients) and Group 2 (n=24 patients) >7 ACR. CMR scan included: SSFP cine images for global biventricular function, pre-and post-Gadolinium contrast T1. T1 maps were acquired as 3 short axis slices. ECV was calculated from pre and post-contrast T1 maps by semiautomatic contouring using a dedicated software (cvi42, Circle, Calgary, Canada) after reconstruction (Figure) Hematocrit drawn at the time of scan was used for ECV calculation. The most recent CMR scan was used for analysis. The ISHLT criteria was used to adjudicated CAV grade, based on degree of angiographic stenosis. ACR grade was assigned based on endomyocardial biopsy according to ISHLT grading system.

	≤7 ACR episodes	> 7 ACR episodes	P
# of patients (n)	31	24	N/A
Age (years)	47.5±17.6	56.0±14.0	0.08
Gender (male)	16/31	11/24	N/A
HTx to CMR (years)	8.3±5.0	6.4±3.6	0.23
Mean # of ACR	3.3±2.3	11.6±4.1	<0.01
CAV grade	CAV 0=10 CAV 1= 21	CAV 0=9 CAV 1=15	N/A
Heart rate	91.7±14.6	95.3±16.1	0.37
BP systolic	124.6±19.7	125.5±18.9	0.50
BP diastolic	77.0±10.2	79.0±9.0	0.73
LVEF (%)	59.4±9.0	58.4±8.5	0.53
RVEF (%)	51.6±8.6	48.9±10.7	0.39
LVEDV (ml)	107.6±27.6	107.6±25.2	0.89
LVESV (ml)	43.7±14.4	45.5±16.2	0.81
RVEDV (ml)	121.0±28.0	125.4±32.4	0.64
RVESV (ml)	58.3±15.4	65.1±24.0	0.53
T1 (msecs)	1022.3±52.2	1036.4±66.7	0.86
T2 (msecs)	49.8±2.8	50.8±3.9	0.33
ECV (%)	25.8±3.1	28.4±3.2	<0.01

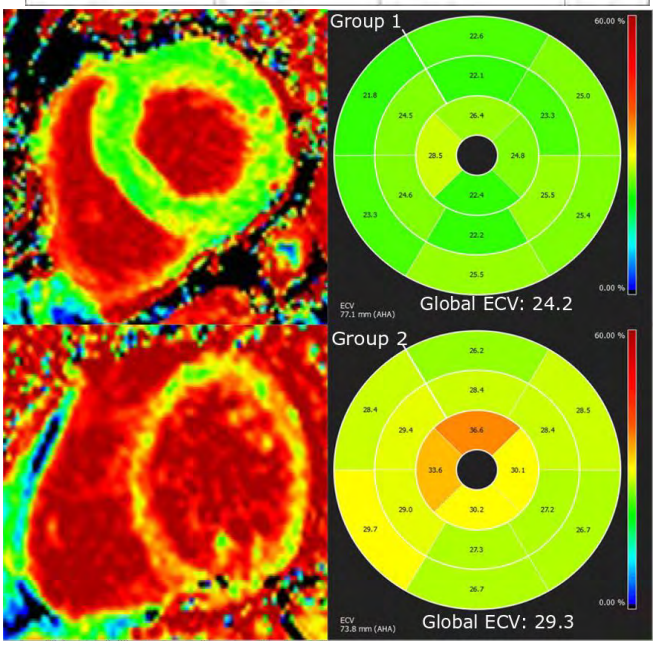

Results: Of 55 patients, 31 were in Group 1 and had a mean of 3.3±2.3 documented ACR episodes, the mean age was 47.5±17.6 and time from HTx to CMR=8.3±5 years The remaining 24 patients in Group 2had a mean number of 11.6±4.1 documented ACR episodes, the mean age was 56±14 and time from HTx to CMR=6.4±3.6 years. Demographics, structural and functional parameters are reported in the table. The total number of ACR episodes was 372 (332 grade 1R, 17 grade 2R; 14 grade 2 ACR episodes occurred in >7 ACR group). Patients with >7 ACR episodes had significantly elevated ECV compared to those with ≤7 ACR episodes (28.4±3.2 % vs. 25.8±3.1 %, p<0.01).

Conclusion: Increasing number of ACR episodes may play an important role on increasing myocardial ECV during long term follow up in HTx patients at CAV stage 0 and 1, thus being a contributing factor to myocardial fibrosis in low grade CAV.

Biventricular Velocities and T2-Relaxation Times are Altered in in Heart Transplant Patients with Cardiac Allograft Vasculopathy

Roberto Sarnari[1], Muhannad Aboud Abbasi[1], Arif Jivan[2], Rahim Gulamali[1], Alexander Ruh[1], Julie Blaisdell[1], Daniel Lee[2], Kambiz Ghafourian[2], Jane E Wilcox[2], Sadiya S Khan[2], Esther E Vorovich[2], Jonathan D Rich[2], Allen S Anderson[2], Clyde W Yancy[2], Michael Markl[1,3], James C Carr[1]

[1]Dept. of Radiology, [2]Dept. of Cardiology,[3] Dept. of Biomedical Engineering - Northwestern University, Chicago IL

Purpose: Heart transplantation (HTx) is associated with risk a of cardiac allograft vasculopathy (CAV) beyond the first year post-HTx. Invasive coronary angiography (ICA) is the reference modality, but it has limited sensitivity in early disease. The impact of CAV on regional LV function is difficult to quantify in early stage CAV and the role of RV is potentially underappreciated. Cardiac magnetic resonance (CMR) provides a non-invasive structural/functional assessment. Pre-and post-contrast T1 mapping allows for calculation of myocardial T1 and extracellular volume (ECV). Tissue phase mapping (TPM) allows for the measurement of myocardial velocities in both the left (LV) and right ventricle (RV). We hypothesize that multiparametric CMR (TPM velocities, T2, T1, ECV) is sensitive to detect structural and function changes associated with CAV in HTx patients beyond the first year post-HTx.

Methods: Eighty-one HTx patients (age=50.1±15 years, 47M, time after HTx: 7.7±7 years) were prospectively recruited beyond the first year post-HTx between August 2014 through November 2018 along with 18 matched controls (49±15 years, 12M). Patients who did not have TPM sequence performed (n=12) and one patient with Turner's syndrome were excluded from the analysis leaving 68 patients. These 68 HTx patients underwent CMR which included SSFP cine, pre and post Gd contrast T1 mapping and TPM for biventricular myocardial velocities assessment. T1 and T2 maps and TPM were acquired as 3 short axis slices at base, mid and apex. The ISHLT criteria was used to adjudicated CAV grade (0-3), based on ICA. Global and regional T1, T2, and ECV were calculated using a dedicated software (cvi42, Circle, Calgary, Canada) after reconstruction. Hematocrit drawn at the time of scan was used for ECV calculation. Segmental values were reported in the 16-segment AHA model. Myocardial velocities after manual TPM image contouring was reported in a 16+10 segment LV+RV AHA model. Segmental values were used to obtain peak and global values.

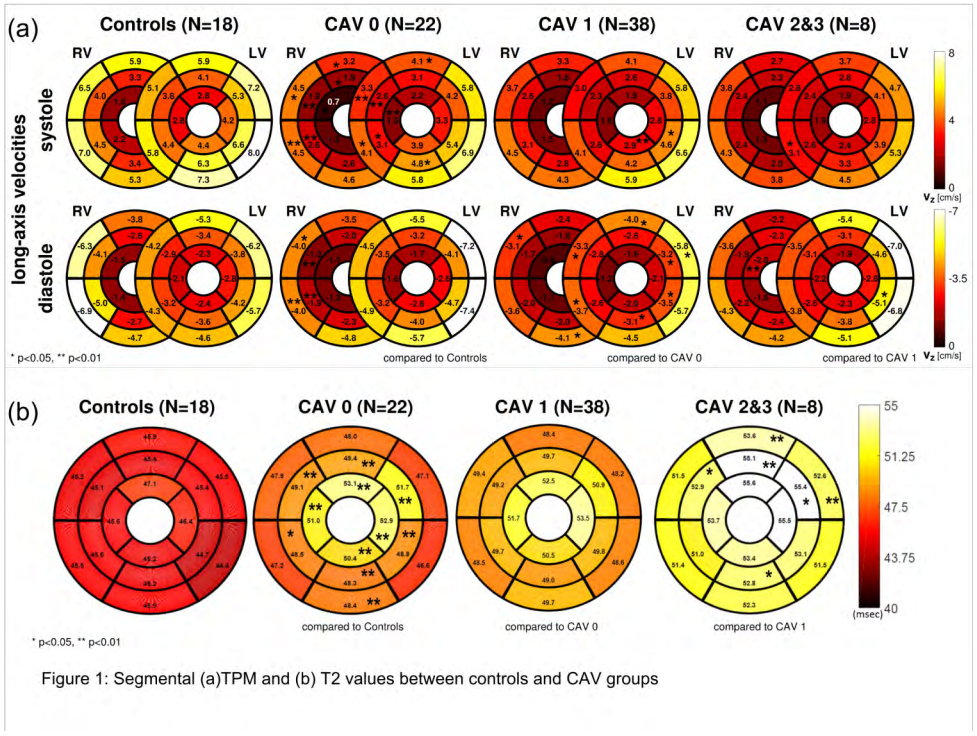

Figure 1: Segmental (a)TPM and (b) T2 values between controls and CAV groups

Results: The demographics of the 68 HTx patients (CAV 0=22, CAV1=38, CAV 2-3=8; age: 46±14, 55±16, 46±14, respectively; 18M, 22M, 8M respectively; time after HTx: 6±5, 8±6, 9±5 years, respectively).Whole HTx cohort vs. controls: demonstrated significantly reduced biventricular longitudinal (Vz) systolic velocities (LV-Vz: 5.2±2.1 vs 3.7±1, p<0.01, RV-Vz: 4.3±1.3 vs 2.9±1.1, p<0.01), reduced RV systolic radial velocity (RV-Vr: 4.1±0.9 vs 3.6±0.7), reduced RV systolic and diastolic twist (2.8±1.5 vs 1.7±1, p<0.01 and -3.1±1.6 vs -1.9±1, p<0.01, respectively). Global T2 was also significantly elevated in HTx patients when compared to controls (45.5±0.6 vs 50.1±1.6 ms). No significant difference was found for ECV between HTx patients and controls. Segmental analysis was performed for controls to CAV 0 group comparison and for inter-CAV groups' comparison (Fig. 1). Controls vs. CAV0 group: 6/16 LV segments and 7/10 RV segments showed significantly reduced longitudinal myocardial velocities during systole and 5/16 RV segments during diastole. T2 was increased in all inferior segments from base to apex and in the anterior, lateral and septal segments at mid and apical level. CAV0 vs. CAV1 group: reduced longitudinal velocities in 2/16 LV segments during systole and 7/16 LV and 2/10 RV segments during diastole, without significant segmental T2 differences.
CAV 1 vs. CAV2-3 group: longitudinal velocities were reduced in the infero-septal wall during systole and in the infero-lateral LV wall and apical anterior RV wall during diastole. Segmental T2 values were significantly increased in 6/16 LV segments for CAV2-3 group.

Conclusions: Global and segmental differences between controls and HTx monitored for CAV were evidenced by our study, for LV/RV myocardial velocities and T2 values. Significant segmental differences in myocardial velocities and T2 values between controls and HTx CAV0 patients highlights structural and velocity abnormalities in HTx patients despite normal CAV status. Interestingly, RV showed to be already affected at CAV0 with both systolic and diastolic velocity abnormalities. TPM is sensitive to detect segmental velocity abnormalities already at CAV0 stage and variations between CAV0 to CAV1 stages.

4D phase-contrast MRI study of the hemodynamic changes in the aorta and its branches before and after endovascular treatment of the aortic dissection

Benoit Cosset[1,2], Loic Boussel[1,2], Philippe Douek[1,2], Fadi Farhat[2], Monica Sigovan[1]
1. Univ Lyon, INSA-Lyon, UCBL 1, CNRS, Inserm, CREATIS UMR 5220, U1206
2. Department Cardio-vascular Surgery, Hospices Civils de Lyon
3. Department of Radiology, Hospices Civils de Lyon, Lyon

Purpose:
In clinical practice, radiological evaluation of the aortic dissection (AD) is limited to morphologic imaging of the lumen by either CTA or MRA. However, functional information on blood flow can be obtained with Phase contrast MRI (4DFlow) in the true and false lumen in AD. To the best of our knowledge, only one research study demonstrated a functional evaluation of AD with 4DFlow, unfortunately this study was limited to un-operated patients.
We hypothesize that 4DFlow can be used to verify the perfusion of the aortic branches and therefore perform an early evaluation of the endovascular treatment of AD. In order to assess the added value of MRI in the management of AD, we evaluated the hemodynamics in the aorta and its branches before and after endovascular treatment of the AD.

Methods:
This is an analytical, prospective, monocentric study. We included patients with aortic dissection requiring endovascular treatment according to surgical guidelines and after multidisciplinary discussion at our institution. MRI was performed on an Ingenia 3.0T MR system (Philips, Best, The Netherlands). The protocol included dynamic gadolinium-enhanced MR angiography (4DTRACK) and 4D Flow. The primary outcome was the comparative measurement of the flow in the aortic true lumen before and after endovascular treatment of the AD. Secondary outcomes were the comparative measurement of the flow in the aortic false lumen, in the visceral branches of the aorta, in renal arteries and through intimal tears before and after endovascular treatment of the aortic dissection, the presence of helicoidal flow before and after endovascular treatment of the aortic dissection. Data was analyzed with CVI 42 Software (Circle Cardiovascular imaging Inc. Calgary, Canada).

Results:
3 patients were included to date, between June 2018 And March 2019. Measurements in the true and false lumen were performed at three different levels: Isthmic level, pulmonary artery level and diaphragmatic level.
Pre-operative phase-contrast MR exam detected helicoidal flow in the false lumen in all the cases. The initial helicoidal flow disappeared in all the cases after endovascular treatment. A new helicoidal flow appeared downstream the endoprothesis in one case (Figure).
Intra-stent measures were similar to extra-stent measures demonstrating that reliable velocity quantification was possible even in the presence of a metallic stent.
We observed an increased mean flow in the true lumen and a decreased mean flow in the false lumen after endovascular treatment of the AD. Mean flow in the truncus celiacus (TC), in the mesenteric artery (MA) and in the renal arteries (RA) remained stable.

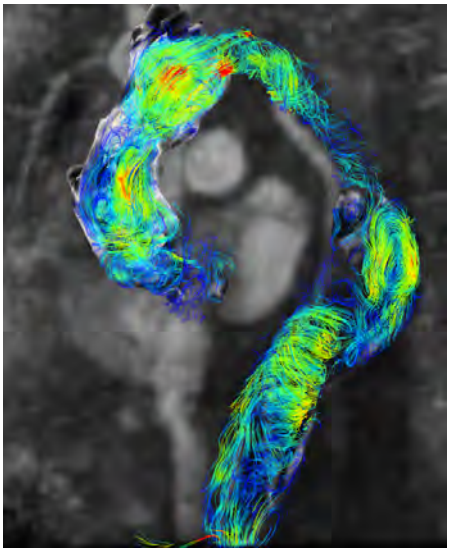

Figure: 4D phase-contrast MRI after treatment of a type A aortic dissection by frozen elephant trunk: Visualization of the aortic flow through the streamline technique: Presence of a helicoidal flow (red arrow) downstream the endoprosthesis.

Discussion:
Increased flow in the true lumen and decreased flow in the false lumen demonstrates the good implantation of the endoprothesis with a good closure of the primary tear. The similarities of the intra-stent and the extra-stent flow data validates the reliability of the intra-stent velocity measures. As none of the patients presented pre-operative malperfusion syndrome, stability of the flow in the aortic branches translates a good perfusion of the branches and therefore the good implantation of the endoprothesis. 4D phase-contrast MRI was able to perform quantitative and qualitative evaluation of the flow in dissected aorta before and after endovascular treatment. 4D phase-contrast MRI, by performing an early hemodynamic evaluation of the aorta might be helpful in the management of the aortic dissection.

A Similarity-Based Data Clustering Approach for Fast Reconstruction of Untriggered and Ungated Whole-Heart MRA

John Heerfordt[1,2], Kevin K. Whitehead[3], Jessica A.M. Bastiaansen[1], Lorenzo Di Sopra [1], Christopher W. Roy[1], Mark A. Fogel[3], Matthias Stuber[1,4], Davide Piccini[1,2]

[1]Department of Diagnostic and Interventional Radiology, Lausanne University Hospital and University of Lausanne, Lausanne, Switzerland; [2]Advanced Clinical Imaging Technology, Siemens Healthcare AG, Lausanne, Switzerland; [3]Children's Hospital of Philadelphia, Philadelphia, USA; [4]Center for Biomedical Imaging (CIBM), Lausanne, Switzerland;

Purpose: Recent advances have enabled high resolution whole-heart MRA using continuous acquisitions (1,2) that do not require ECG-triggering or navigator technology and enable cardiac and respiratory motion-resolved reconstruction (3). Such approaches also aim to simplify planning and provide predictable scan times when compared to conventional solutions. However, they usually comprise computationally demanding reconstructions incorporating extraction of physiological signals (1,3), image registration (1), and/or compressed sensing (3). Since these reconstructions oftentimes are impractical directly at the scanner, what usually is displayed is a motion-degraded image from all data, with all cardiac and respiratory motion states combined. The aim of this work was to investigate if similarity-based clustering of imaging data from a continuous, untriggered, and ungated acquisition can be used to reconstruct a motion-consistent whole-heart image with a high level of motion artifact suppression, without the need for a computationally demanding reconstruction or making any prior assumptions about the underlying physiological processes.

Input	Data Selection Algorithm	Output
One vector for each interleave with a stack of 1D SI-oriented projection images from several coil elements	1. PCA dimensionality reduction to $\mathbb{R}^{100}$ 2. k-means clustering (k = 10-15 according to silhouette criterion) 3. Select the interleaves of the largest cluster	Whole-heart MRA volume after gridding, Fourier transform and coil combination

Figure 1. Overview of the proposed method. The clusters are visualized as a low-dimensional embedding using t-SNE (8) for display purposes. The reformatted image, reconstructed from the largest cluster, depicts a pediatric patient with an anomalous RCA (arrow).

Methods: Five non-contrast datasets from healthy volunteers and five contrast-enhanced datasets from pediatric cardiac patients were included in this study. Eight scans were acquired at 1.5T and two at 3T (MAGNETOM Aera, Avanto and Prisma, Siemens Healthcare). The volunteer scans were fast-interrupted steady state (4) acquisitions, that provide intrinsic fat-suppression, performed with a recent continuous 3D radial sequence (5). The patient scans were done with a continuous gradient echo sequence, following the same 3D radial sampling pattern (6), after administration of ferumoxytol (7). Sequence parameters: Scan time: 7-8 minutes, Resolution: $(1.1\ mm)^3$, FOV: $(220\ mm)^3$, 5181-5749 interleaves with 22-24 readouts each. In the 3D radial sampling pattern, the first readout in each interleave is consistently oriented in the superior-inferior (SI) direction. The proposed algorithm exploits the inherent (dis-)similarity between these SI-readouts, to automatically sort the acquired interleaves into different clusters (Figure 1). Assuming that the largest cluster contains the most common motion state, its data are selected and used to reconstruct a static 3D image. We compared such reconstructions to motion-blurred counterparts obtained from all the acquired readouts. For analysis, the size of the selected cluster was assessed, measurements of blood-myocardium CNR and blood SNR were performed (6) and the visibility of the coronary arteries was examined, as a surrogate endpoint for motion suppression. Moreover, the computation time for the algorithm's different steps were ascertained for one of the datasets.

Table 1. Quantitative results

Metric \ Data	Non-contrast volunteers: All Data	Non-contrast volunteers: Sel. Data	Patients with contrast: All Data	Patients with contrast: Sel. Data
Blood-Myocardium CNR	4.5 ± 2.3	**4.6 ± 1.8**	17.6 ± 9.8	**19.3 ± 6.3**
Blood SNR	**18.8 ± 4.0**	14.7 ± 1.7	**30.6 ± 12.4**	29.0 ± 9.1
Visible Prox. RCA	0/5	**4/5**	4/5	**5/5**
Visible Mid RCA	0/5	**4/5**	2/5	**5/5**
Visible Distal RCA	0/5	**2/5**	0/5	**4/5**
Visible LM	0/5	**4/5**	4/5	**5/5**
Visible Prox. LAD	1/5	**5/5**	4/5	**5/5**
Visible Mid LAD	0/5	**5/5**	0/5	**2/5**
Visible Distal LAD	0/5	**4/5**	0/5	**1/5**
Visible LCX	0/5	**3/5**	1/5	**2/5**

Results: The largest cluster contained on average 15 ± 4% of the total acquired data. The CNR was slightly higher after data-selection whereas the SNR decreased (Table 1). The proposed algorithm allows for better visualization of the coronary artery segments than the motion-blurred reconstructions (Table 1, Figure 2). The dimensionality reduction and clustering part of the algorithm accounted for 10% of the total reconstruction duration of one minute on a desktop workstation.

Discussion: Sorting free-running imaging data based on the similarity of SI-readouts, without making any assumptions on underlying physiological processes, showed promise for fast reconstruction of a motion-consistent 3D volume with visible coronary arteries. The algorithm seemingly improved the visualization of the coronary arteries which advances the hypothesis that the largest cluster contains data from an anatomically similar state. The slight improvement observed in CNR is likely due to a better-defined myocardium in the static reconstructions. The loss in SNR can be explained by the higher degree of undersampling after data selection. The algorithm remains to be further optimized and its performance should be systematically compared to conventional whole-heart MRA. If this approach can be used for acquiring and reconstructing whole-heart coronary MRA in less than 10 minutes without any gating or triggering, the technique might contribute to an improved clinical workflow.

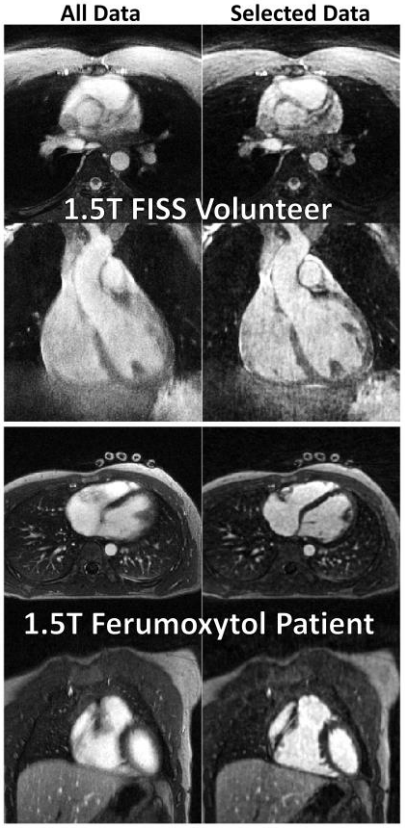

Figure 2. Volunteer without contrast (top) and pediatric patient with ferumoxytol (bottom)

References: [1] Pang J, MRM 2014, 72(5):1208–17 [2] Coppo S, MRM 2015, 74(5):1306–16 [3] Feng L, MRM 2018, 79(2):826–38 [4] Koktzoglou I, MRM 2018, 79(4):2077-86 [5] Bastiaansen J, arxiv.org/abs/1903.03498, 2019 [6] Piccini D, MRM 2011, 66(4):1049–1056 [7] Prince M, J. Xray. Sci. Technol. 2003, 11:231–40 [8] Van der Maaten L., Journal of Machine Learning Research 2008, 9:2579-2605

Assessing MS Lesions with USPIO (Ferumoxytol) enhanced Susceptibility Weighted FLAIR (USPIO$^+$-swFLAIR)

E. Mark Haacke[1], Evanthia Bernitsas[2], Karthikeyan Subramanian[1], Yongsheng Chen[2], David Utriainen[3], Pavan Kumar[1].

Department of [1]Radiology and [2]Neurology, Wayne State University School of Medicine, Detroit, MI, USA;

[3]SpinTech, Inc., Bingham Farms, MI, USA.

Purpose: Multiple Sclerosis (MS) is an immune-mediated demyelinating and neurodegenerative disease characterized by a wide range of symptoms and multiple progressive disease courses [1]. T2 FLAIR is sensitive to white matter (WM) lesions in patients with multiple sclerosis (MS) [2]. Susceptibility weighted image (SWI) has been increasingly used for studying neurological disorders, cerebral microbleeds, arterial venous malformations, hemorrhages and many venous diseases especially with the recently developed USPIO enhanced SWI [3]. The pathological role of the venous vasculature within the MS lesions is currently unknown. It is vital to define the etiology of demyelinating and inflammatory lesions to better understand the disease [4]. Assessing MS lesions with a combination of these tools is of great interest to characterize WM lesions in MS. Although there is recognition of the central vein concept in MS lesions, evaluating the entire venous system has not been done with a USPIO contrast agent [5-7]. The objective of this study is to characterize MS lesions by visualizing lesion-penetrating vessels using USPIO$^+$-swFLAIR.

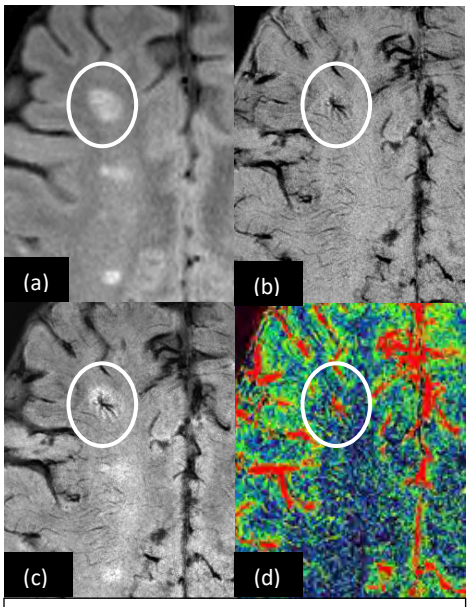

Figure 1. The T2 FLAIR image (a) shows a hyperintense lesion and the corresponding slice in tSWI (b) shows a venous angioma. USPIO$^+$-swFLAIR (c) provides tremendous visualization of these penetrating veins that appear to define the MS lesions as shown in the T2 FLAIR data (a). The penetrating vessels can also be visualized as high signal in the CD map (d).

Methods: High resolution pre-contrast 3D SPACE T2 FLAIR and pre-, post-contrast SWI were performed on patients with MS at 3T. A dose of 3mg/kg Ferumoxytol was administered as an off-label contrast agent in this study. For post processing, a set of susceptibility weighted FLAIR (swFLAIR) images were generated using pre-contrast SWI, phase, pre-contrast quantitative susceptibility mapping (QSM), post-contrast tSWI along with the T2 FLAIR image, which will be referred to as USPIO$^+$-swFLAIR hereafter. A capillarity density (CD) map was generated by taking the ratio of signal changes between pre- and post-contrast SWI images to observe and monitor changes in the microvasculature that may lead to functional changes. MS lesions were identified by their high intensity in T2 FLAIR data and pre contrast QSM data to differentiate them from normal appearing WM (NAWM). The USPIO+-swFLAIR and CD maps were then assessed for their appearance within MS lesions and NAWM.

Results: USPIO$^+$-swFLAIR provides visualization of penetrating vessels into the WM lesions showing vascular engorgement and venous angiomas exactly corresponding to the borders of the WM lesion. These venous angiomas of the medullary veins appear to define the lesion. They cannot be seen on the original T2 FLAIR, pre-contrast QSM or pre-contrast swFLAIR. MS lesions were represented as high intensity relative to surrounding NAWM in both FLAIR and QSM data. When combined, as swFLAIR, lesions appeared either as T2 FLAIR only or as both T2 FLAIR and QSM contributions to the map. Intralesional veins were more engorged than veins outside the WMH.

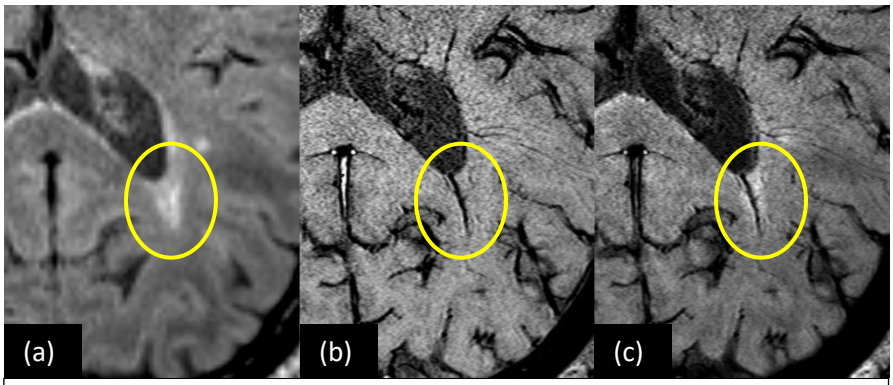

Figure 2. The FLAIR (a) image shows a hyperintense lesion and the corresponding slice in SWI (b) shows a dialated vessel. USPIO$^+$-swFLAIR (c) visualizes how the dialated vessel lies within the hyperintense FLAIR lesion.

Discussion: The different contrasts, especially the swFLAIR images, make it possible to recognize abnormal vasculature in the MS lesions. Not only were angiomas seen in these studies, but dilated veins also demarcated the lesion territory. Dilated veins may be markers for future changes within the lesion and are presumably primary to all MS lesions.

References: [1] Lassmann, et al., Brain Pathol. 2007, 17(2):210-8. [2] Filippi, et al., Brain 1996, 119(pt4)1349-55. [3] Liu, et al., JMRI 2018, 47(3):621-33. [4] Kaunzner, et al., Brain 2019, 142(1):133-45. [5] Grabner, et al., JMRI 2011, 33(3):543-9. [6] Sati, et al., Radiology 2012, 265(3):926-32. [7] Gabr, et al., MRM 2018, 80(3):1132-7.

Self-Navigated, Free-Breathing 3D Left Atrial Late Gadolinium Enhancement MRI at 1.5 Tesla: A Preliminary Study for Evaluation of Image Quality and Quantification of Atrial Fibrosis in patients with Atrial Fibrillation

Suvai Gunasekaran[a], Daniel C Lee[b], Bradley Knight[b], Ryan Avery[a], Hassan Haji-Valizadeh[a], Philip Greenland[b], Rod Passman[b], Michael Markl[a], Daniel Kim[a]

[a] Department of Radiology, Northwestern University Feinberg School of Medicine, Chicago, IL, United States
[b] Division of Cardiology, Northwestern University Feinberg School of Medicine, Chicago, IL, United States

Purpose: Given the thin nature of the left atrial (LA) wall and the need to perform respiratory gating, the clinical translation of LA late gadolinium-enhanced (LGE) MRI has proven difficult, particularly at 1.5T MRI scanners. To address this gap, we sought to develop a self-navigated, free-breathing 3D LA LGE pulse sequence using stack-of-stars k-space sampling, balanced steady-state free precession (b-SSFP), and Golden-angle RAdial Sparse Parallel (GRASP) reconstruction for quantifying atrial fibrosis in patients with atrial fibrillation (AF) at 1.5T.

Methods: 15 patients (11 males, mean age = 63 ± 6 years) with AF (12 paroxysmal, 3 persistent) were scanned on 1.5 T MRI scanners (Siemens, AERA or AVANTO) using the proposed pulse sequence with the following parameters: 288 x 288 x 96 mm^3 FOV, 1.5 x 1.5 x 2 mm^3 spatial resolution, 350 heartbeats scan duration, and oblique sagittal orientation sampling the left side of the heart. As shown in Figure 1, GRASP reconstruction was performed with self-navigation of respiratory motion and temporal total variation as the sparsifying transform, as previously described (1). During post-processing, we applied adaptive optimized nonlocal means (AONLM) filtering (2) to determine whether AONLM is capable of increasing the apparent SNR and image quality without significant blurring. For qualitative assessment, images were independently evaluated by two attending readers on a 5-point scale (1=worst, 3=acceptable, 5=best) for each of three categories (conspicuity of LA wall, noise, artifact), and the overall image quality index was defined as the sum of three scores, where 9 is defined as clinically acceptable. For quantitative assessment, LA SNR and edge sharpness were computed. Finally, the best resulting images were analyzed using commercial software (ADAS 3D, Galgo Medical) to quantify LA fibrosis (Fig. 2C), which was subsequently tested against relevant clinical characteristics (Table 1).

Results: Use of AONLM significantly ($p < 0.05$) increased SNR (from 18.22 to 30.13), whereas edge sharpness was not significantly different (from 1.38mm to 1.42mm) (see representative images in Fig. 2A-B). The median image quality index was significantly ($p<0.05$) higher with filtering (11) than without (8). Figure 2C shows fibrosis quantification of a persistent AF patient with mean atrial fibrosis of 20.41%. The mean LA fibrosis of our patients was 6.4 ± 4.9%. As shown in Table 1, unpaired t-tests demonstrated non-significant differences for all variables, except for AF type ($p=0.0040$).

Discussion: This study demonstrates that the proposed 3D LA LGE sequence using stack-of-stars k-space sampling, b-SSFP readout, GRASP reconstruction, and AONLM filtering is capable of producing clinically acceptable image quality (>9) for quantifying LA fibrosis in patients with AF at 1.5 T.

References: 1. Haji-Valizadeh H, et. al. Magn Reson Med 2019. 2. Manjon JV, et. al. J Magn Reson Imaging 2010.

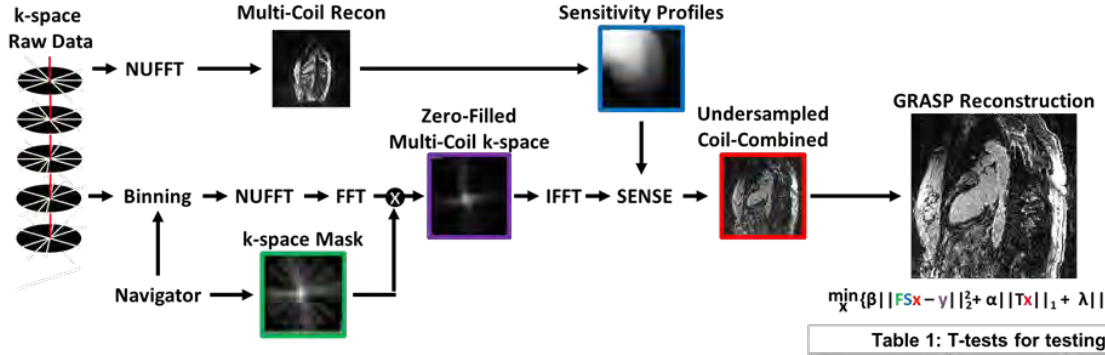

Figure 1. GRASP reconstruction pipeline

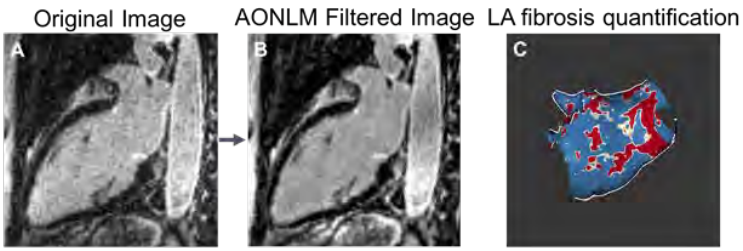

Figure 2. Representative 3D LA LGE image (A) with adaptive optimized nonlocal means filtering (B). Representative image of 3D LA fibrosis quantification (C) (blue = no fibrosis, gray = border zone, red = core fibrosis).

Table 1: T-tests for testing differences in LA fibrosis

Characteristic	Variable	N	Total LA Fibrosis (%)	P-value
Age	< 60	5	9.9 ± 10.8	0.25
	≥ 60	10	5.5 ± 3.2	
Sex	M	11	7.8 ± 7.5	0.46
	F	4	4.7 ± 3.7	
AF type	Paroxsymal	12	4.7 ± 2.8	0.004
	Persistent	3	15.9 ± 10.9	
Max. LA Vol./BSA	Normal	12	6.7 ± 7.4	0.82
	Elevated	3	7.8 ± 3.4	
Prior Ablation	No	11	5.4 ± 3.1	0.13
	Yes	4	11.3 ± 11.9	
CHA_2DS_2-VASc	0-2	9	7.5 ± 8.4	0.71
	3-4	6	6.1 ± 3.3	

Evaluating the Vessel Wall Permeability of Abdominal Aortic Aneurysm using 3D Dynamic Contrast-Enhanced MRI: a feasibility study

Bing Tian[1], Qi Liu[1], David Saloner[2], Jianping Lu[1], and Chengcheng Zhu[2]

1Department of Radiology, Changhai hospital of Shanghai, Shanghai, China,

2 UCSF, San Francisco, CA, United States

Purpose:

This study aims to 1) investigate the feasibility of 3D dynamic contrast-enhanced (DCE) MRI to evaluate the vessel wall permeability of abdominal aortic aneurysm(AAA), and 2) assess the relationship between Ktrans and AAA diameter/intraluminal thrombus (ILT).

Methods:

13 patients with AAAs (diameter 4.85 ± 0.94cm) were scanned on a 3T Siemens Skyra scanner. MRI was acquired using 1) a previous developed 3D T1-weighted black blood fast-spin-echo sequence and 2) a 3D DCE sequence using fast gradient-echo (VIBE). TR/TE: 6.30/2.90ms. 3mm slice thickness, 1.5mm in-plane resolution, 40 slices; temporal resolution 13s, a total of 40 phases. AAA diameter was measured on black blood MRI images using our previous published method. ILT thickness was measured on the transverse slice of maximal aneurysm diameter and maximal ILT diameter was used. Based on the volume distribution of ILT on the black blood MRI, two types of ILT was divided into two types for patients with ILT: Type 1: Fresh ILT was present; Type 2: Without fresh ILT. 3D DCE MRI images was analyzed on the work station of Siemens scanner using 4D Tissue software. ROIs were carefully drawn on aneurysm wall and ILT (if available) of AAA and Ktrans was obtained for both aneurysm wall and ILT. Ktrans were derived based on the previous published model [2] and the arterial input function was from the same scan. Spearman's r was used to evaluate the correlation of DCE Ktrans with AAA diameter and ILT thickness. Mann-Whitney test was used to compare DCE Ktrans between aneurysm wall and ILT. DCE Ktrans differences were also investigated as a function of ILT types.

Results:

11/13 patients were found to have ILT (Type1:8 and Type2:3) and [3/13 patients' AAA diameter was ≥5.5cm.] There was a positive correlation between Ktrans and AAA diameter (r=-0.57; P=0.01). A relatively weak, non-significant negative correlation was found between Ktrans and ILT thickness (r=-0.32; P=0.34). DCE Ktrans of aneurysm wall [0.11(0.05,0.18) min^{-1}] was significantly higher than that of ILT [0.04(0.02,0.05) min-1] (P=0.01). There was no significant difference of DCE Ktrans between different types of ILT (with fresh ILT [0.09(0.04,0.15) min-1] vs. without ILT [0.14(0.06,0.18) min-1], p=0.31).

Discussion:

To our knowledge, this is the first study applying 3D high resolution DCE for AAA. DCE has rarely been studied for AAA. Previous 2D DCE studies of AAAs had temporal resolution of 18s, and spatial resolution 1.6×1.6×6 [2,3]. In our study, we improved the temporal resolution to 13s, and spatial resolution to 1.5×1.5×3. Although AAA diameter is used for clinical management decisions, it has some limitations. From our study, we found Ktrans values of aneurysm wall was negatively correlated with AAA diameter. DCE may be another important method for AAAs risk evaluation which needed to be tested in a larger cohort of patients. ILT is a common feature in AAAs and has been studied as a potential marker of progressive AAA disease. Previous studies showed thick ILT can induce localized hypoxia and inflammation, and weaken the arterial wall. Although the presence of ILT may indicate higher risk, the role ILT thickness is still unclear. We also found no clear relationship between ILT thickness and Ktrans. Besides another important finding was Ktrans value of aneurysm wall was significant higher than that of ILT. This agree with histology studies that vasa vasorum is present in the adventia, but not present in ILT [4]. Previous study also found AAAs with fresh ILT grew two times as fast as AAAs without fresh ILT [4]. But there was no significant difference of DCE Ktrans between AAAs with different types of ILT in our study. The reason may be due to small patients number, and further larger scale study is needed.

Conclusion:

3D DCE MRI can be used to evaluate the vessel wall permeability of AAA with high temporal and spatial resolution.

References:

[1] Nguyen VL, Backes WH, Kooi ME, et al. Quantification of Abdominal Aortic Aneurysm Wall Enhancement With Dynamic Contrast-Enhanced MRI: Feasibility, Reproducibility, and Initial Experience. J Magn Reson Imaging. 2014;39(6):1449-56. doi: 10.1002/jmri.24302.

[2] Nguyen VL, Kooi ME, Backes WH, van Hoof RH, et al. Suitability of Pharmacokinetic Models for Dynamic Contrast-Enhanced MRI of Abdominal Aortic Aneurysm Vessel Wall: A Comparison. PLoS One. 2013;8(10):e75173. doi: 10.1371/journal.pone.0075173.

[3] Nguyen VL, Leiner T, Hellenthal FA et al. Abdominal aortic aneurysms with high thrombus signal intensity on magnetic resonance imaging are associated with high growth rate. Eur J Vasc Endovasc Surg, 2014;48:676-684.

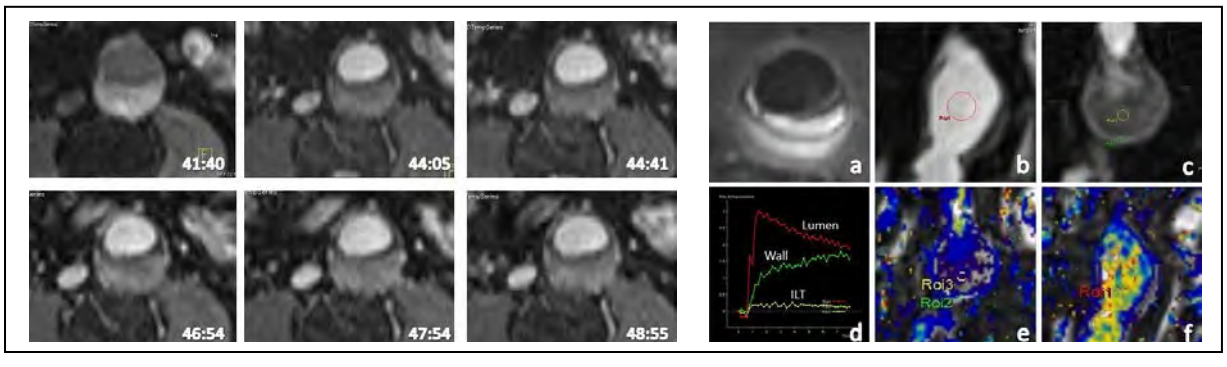

Compare the Characteristics of Different Types Spontaneous Intracranial Artery Dissection on High Resolution MRI Vessel Wall Imaging

Bing Tian, Xia Tian, Zhang Shi, Qi Liu, Jianping Lu
Department of Radiology, Changhai hospital of Shanghai, Shanghai, China

Purpose:
This study aims to compare the characteristics of different types spontaneous intracranial artery dissection on high resolution MRI(HR-MRI) vessel wall imaging.

Methods:
Fifty-six patients (12 female, age 50±14) with approved spontaneous intracranial artery dissection(DSA and clinical diagnosis) were scanned on a 3T Siemens Skyra scanner with pre- and post-contrast 3D T1-weighted SPACE (0.5mm isotropic). Patients were divided into four groups based on the morphological characteristics on pre-contrast 3D T1-weighted SPACE imaging. Type 1 corresponded to classic dissecting aneurysms, type 2 aneurysms were segmental ectasias, type 3 aneurysms were dolichoectatic dissecting aneurysms and type 4 aneurysms were saccular aneurysms unrelated to the branching zones. Consistency of clinical staging(acute, subacute, chronic stage) and imaging types was evaluated. The characteristics of spontaneous intracranial artery dissection were evaluated including intraluminal contrast enhancement(an area of intraluminal contrast enhancement on post-contrast SPACE images), and artery wall enhancement(degree of enhancement was assessed based on a visual grading system as follows: grade 0, similar to that of normal vessel walls; grade 1, greater than that of grade 0 but less than or similar to that of muscle; and grade 2, greater than that of muscle). The characteristics of spontaneous intracranial artery dissection were compared among different types.

Results:
Of the 56 aneurysms, 48 were located in the vertebrobasilar system, and the other 8 aneurysms were located in the anterior circulation. There were 22 patients for type 1, 10 for type 2, 14 for type 3, and 10 for type 4. Patients were classified into acute (n=18), subacute (n=18), and chronic (n=20) stages according to the time intervals from symptom onset. The clinical staging was in good consistency with imaging types(p=0.000, r=0.732). There was significantly different of intraluminal contrast enhancement and vessel wall enhancement among the four types groups(p=0.030, F=1.223; p=0.000, F=0.697).

Conclusion:
The 3T HR-MRI reveals the vessel wall characteristics and provides distinguishing findings between different types spontaneous intracranial artery dissection.

Discussion:
Spontaneous intracranial artery dissection always show stenosis/occlusion or dilation on traditional angiography images such as computed tomography angiography (CTA), magnetic resonance angiography (MRA), and digital subtraction angiography(DSA). The definite diagnostic criteria of spontaneous intracranial artery dissection is the presence of an intimal flap and a double lumen[1]. However, in cases without a definite dissection sign, precise diagnosis may not be easy to achieve. Patients with lumenal dilatation and intramural hematoma may be misdiagnosed as intracranial aneurysm. Compared to luminal angiographic techniques, high resolution magnetic resonance imaging is more helpful to the diagnosis and differential diagnosis the dissection from other vascular pathologies such as atherosclerosis or aneurysm[2]. The classification of different types spontaneous intracranial artery dissection provide a rationale for modes of treatment. Intraluminal contrast enhancement and artery wall enhancement, which is suggestive of intraluminal thrombus formation, is strongly correlated with ischemic symptoms in patients with spontaneous cervical artery dissection[3]. In this study, we divided patients into two groups according to the morphological characteristics on pre-contrast 3D T1-weighted SPACE imaging. Intraluminal contrast enhancement and artery wall enhancement were both strongly correlated with ischemic symptoms in patients with spontaneous intracranial artery dissection according to the previous studies. The results of our study may be helpful to understand the change of different types of spontaneous intracranial artery dissection as a whole and provide more information for treatment decision.

References:
[1] Uemura M, Terajima K, Suzuki Y, et al. Visualization of the Intimal Flap in Intracranial Arterial Dissection Using High-Resolution 3T MRI. J Neuroimaging. 2017 Jan;27(1):29-32.
[2] Jung SC, Kim HS, Choi CG, et al. Quantitative Analysis Using High-Resolution 3T MRI in Acute Intracranial Artery Dissection.J Neuroimaging. 2016 Nov;26(6):612-617.
[3] Coppenrath E, Lenz O, Sommer N, et al. Clinical Significance of Intraluminal Contrast Enhancement in Patients with Spontaneous Cervical Artery Dissection: A Black-Blood MRI Study. Rofo. 2017 Jul;189(7):624-631.

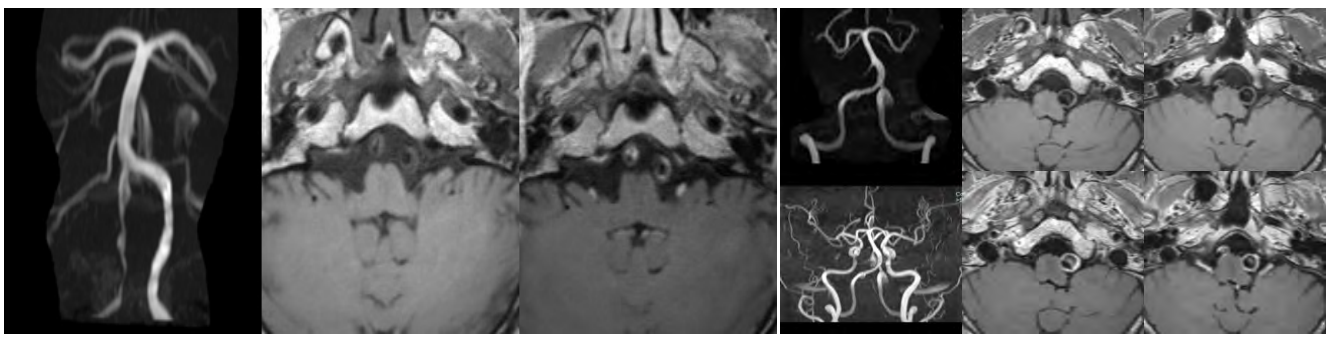

Single-bolus quantitative 3D myocardial perfusion imaging without breath holds or ECG gating via respiratory-compensated MR Multitasking

Anthony G. Christodoulou[1], Nan Wang[1,2], Jaime L. Shaw[1], Xiaoming Bi[3], Yibin Xie[1], Christopher Nguyen[1,4], Debiao Li[1,2]
[1]Biomedical Imaging Research Institute, Cedars-Sinai Medical Center, [2]Department of Bioengineering, UCLA,
[3]Siemens Healthineers, [4]Cardiovascular Research Center, Massachusetts General Hospital

Purpose Quantitative first-pass myocardial perfusion MRI shows great potential for diagnosing coronary artery disease. However, it is challenging to accurately measure fast-changing gadolinium (Gd) concentrations throughout the whole moving heart. Approaches typically use some combination of ECG triggering, breath holds, dual-bolus acquisition, and multislice 2D acquisition, which leads to difficult workflows and limits spatial coverage.

Here we propose a non-ECG, free-breathing, single-bolus, 3D method to overcome these limitations. We employ the MR Multitasking framework[1], which models multidimensional images as low-rank tensors[2] and which has previously been demonstrated for quantitative non-ECG, single-bolus 2D myocardial perfusion. We extend its capabilities to 3D free-breathing perfusion imaging by adding stack-of-stars encoding and 3D respiratory motion compensation, which has been shown to benefit low-rank myocardial perfusion imaging[3]. This new method is demonstrated and evaluated in 10 healthy volunteers against a triggered, breath-held, dual-bolus 3-slice reference.

Methods *Image model:* We obtain a 6-D image $I(\mathbf{x}, c, \tau, h)$, a multidimensional function of spatial location **x**, cardiac phase *c*, saturation recovery (SR) time τ, and heartbeat index h. This image is modeled as a low-rank tensor, and a respiratory motion operator $M\{\cdot\}$ in the forward model compensates for differing respiratory displacement in each heartbeat.
Pulse sequences: The proposed method employed an ECG-free, continuous-acquisition SR-FLASH prototype 3D pulse sequence, using stack-of-stars acquisition with in-plane golden-angle ordering and variable-density Gaussian random sampling of k_z. Subspace-training/self-gating data were interleaved by collecting the 0° spoke at $k_z = 0$ every fourth readout. The reference method was a multislice ECG-triggered, breath-held SR-FLASH dual-bolus pulse sequence.
Image reconstruction: We first obtained a "real-time" reconstruction, $\tilde{I}(\mathbf{x}, t) = I\big(\mathbf{x}, c(t), \tau(t), h(t)\big)$, which has only one time dimension (elapsed time t) using low-rank matrix imaging[2]. Systolic images from each cardiac cycle were extracted from $\tilde{I}(\mathbf{x}, t)$; translational motion was estimated by registering each systolic image to the last systolic image, minimizing mutual over an automatically delineated cardiac region. Measured data $\mathbf{d}$ were motion-compensated by applying linear phase modulation in k-space ($M^{-1}\{\mathbf{d}\}$). Low-rank tensor imaging was then performed using MR Multitasking[1].
Analysis: Multitasking systolic myocardial blood flow (MBF) was calculated by: 1) fitting a time-resolved T1 map $T_1(\mathbf{x}, h)$ at end-systole; 2) calculating a time-resolved Gd concentration map $Gd(\mathbf{x}, h) = \Delta R_1(\mathbf{x}, h)/\gamma$, where γ is the T1 relaxivity of the contrast agent; then 3) Fermi deconvolution[4] of myocardial Gd concentration by the LV Gd concentration. For the dual-bolus reference, Fermi deconvolution of myocardial T1 weighted images by the scaled LV T1-weighted images was performed.
Imaging parameters A total of *n*=10 healthy volunteers were imaged on a 3T scanner (Biograph mMR, Siemens). Multitasking pulse sequence parameters were FA=10°, TR/TE=3.2/1.4 ms, FOV=288×288×96mm^3, matrix size=144×144×12, spatial resolution=2×2×8mm^3, scan time=60 s. Image reconstruction was performed for 20 cardiac bins and 88 saturation times. A 0.05 mmol/kg dose of Gadavist at a rate of 4 mL/s was administered at rest, immediately after the start of scanning. A 3-slice dual bolus reference (dilution factor: 4) was collected 20 min prior to Multitasking imaging.

Results Example multidimensional perfusion images and bullseye MBF plots are shown in Fig. 1. Mid, apical, and basal short-axis images, long-axis reformats, and temporal profiles along *h* are shown for both systolic and diastolic cardiac phases. The reconstructed images contain little influence from respiratory motion, and clearly depict Gd dynamics. MBF values for the dual-bolus (0.6±0.2 mL/g/min) and Multitasking (0.8±0.4 mL/g/min) scans were all in the normal range[4], with Multitasking reporting higher flows (p<0.001).

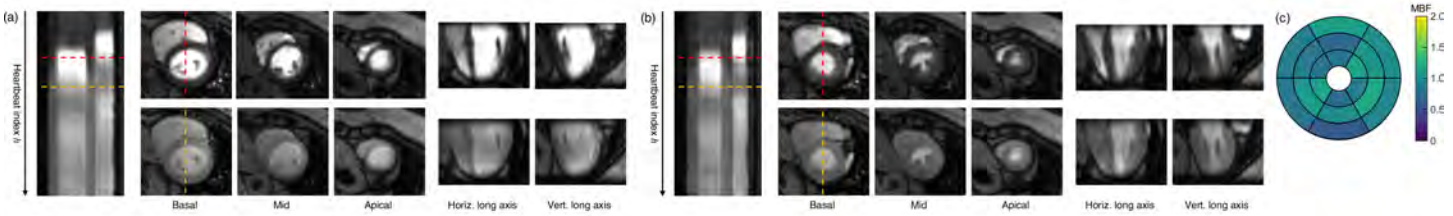

Fig. 1 Example multidimensional perfusion images at τ=150 ms. Mid, apical, and basal short-axis images, long-axis reformats, and temporal profiles along h are shown for both (a) diastolic and (b) systolic cardiac phases, at peak blood pool contrast and at peak myocardial contrast. (c) Bullseye plot of quantified MBF.

Discussion 3D non-ECG, free-breathing, single-bolus quantitative first-pass myocardial perfusion imaging is feasible with MR Multitasking, which has the potential to simplify workflow and increase success rate. Future directions include evaluating the method for stress perfusion, reserve measurements, and applicability to clinical studies.

References

[1] Christodoulou AG, Shaw JL, Nguyen C, Yang Q, Xie Y, Wang N, Li D. *Nature Biomed Eng*. 2018;2(4):215-226.
[2] Liang Z-P. *Proc IEEE-ISBI*. 2007:988–991.
[3] Zhou R, Huang W, Yang Y, Chen X, Weller DS, Kramer CM, Kozerke S, Salerno M. *JCMR*. 2018;20(1):6.
[4] Jerosch-Herold M, Wilke N, Stillman AE, Wilson RF. *Med Phys*. 1998;25(1):73-84.
[5] Lee DC, Johnson NP. *JACC: CVI*. 2009;2(6):761–770

3D MRI morphometric changes in ascending thoracic aortic aneurysm: going beyond diameters

Thomas Dietenbeck[1], Sophia Houriez--Gombaud-Saintonge[1,2], Umit Gencer[3], Alain Giron[1], Gilles Soulat[3], Elie Mousseaux[3], Philippe Cluzel[1,4,5], Alban Redheuil[1,4,5], Nadjia Kachenoura[1]

[1]Sorbonne Université, INSERM, CNRS, Laboratoire d'Imagerie Biomédicale, Paris, France, [2]ESME Sudria Research Lab, Paris, France, [3]HEGP, Paris, France, [4]Institut de Cardiologie, Groupe Hospitalier Pitié Salpêtrière APHP, Paris, France, [5]Institute of Cardiometabolism and Nutrition (ICAN), Paris, France

Aim: Currently, aortic dilation characterized through local maximal diameter measurement is used for guiding the indication of prophylactic thoracic aorta surgery. However, 20 to 40% of patients with aortic dissection following aneurysm have maximal aortic diameters below the recommended threshold for surgery [1]. Thus our objective was to study if 3D morphological indices were more sensitive to subclinical changes in aortic geometry and less hampered by slice orientation and obliquity than diameters measurement.

Method: We studied 278 individuals (171 men, age: 53±15y): 119 healthy volunteers, 53 hypertensive patients (HT) and 106 patients (AP) with aneurysmal ascending aorta (AAo) among whom 44 had a bicuspid aortic valve. All patients had 3D MRI of the aorta used for automated volumetric segmentation [2] resulting in 5 morphometric indices (length, maximal diameters, volumes, curvature and tortuosity) that were measured from sino-tubular junction to brachiocephalic artery for the AAo segment. Aortic measures were compared across groups using ANOVA and pairwise comparisons.

Results: While a significant increase in diameter was only found in aneurysmal patients (tricuspid AP (APt), bicuspid AP (APb): +43%, p<0.001; bicuspid AP (APb): +44%, p<0.001) as compared to healthy controls, the AAo elongation was significant in all groups (HT: +8%, p < 0.01; APt: +38%, p < 0.001; APb: +39%, p < 0.001) resulting in a substantial increase in AAo volume (HT: +17%, p<0.05, APt: +168%, p < 0.001; APb: +180%, p < 0.001). Aortic morphology analysis also revealed an unfolding of the aorta with AAo dilation as characterized by a decreased curvature (APt: -17%, p<0.01; APb: -13%, p<0.01) and an increased tortuosity (HT: +28%, p<0.001; APt: +28%, p<0.001; APb: +41%, p<0.001). In multivariate analysis, AAo length, diameters and volumes were significantly associated with age, sex and group (p<0.001) but not with BMI and central systolic blood pressure (cSBP). AAo curvature was associated with age, sex, BMI and group (p<0.001) and AAo tortuosity was associated with BMI (p<0.001), cSBP (p<0.05) and group (p<0.01).

Discussion: 3D aortic morphological indices revealed significant changes in the ascending aorta even in hypertensive patients where AAo dilation measured by maximal diameters was not significant. These subclinical changes might occur in an intertwined process with blood-flow alterations ultimately leading to aneurysm and dissection. These indices and their clinical value should however be confirmed on larger longitudinal populations.

	Healthy Controls	Hypertensives	Tricuspid aneurysmal patients	Bicuspid aneurysmal patients
N	119	53	62	44
Gender (M/F)	61 / 58	27 / 26	47 / 15	36 / 8
Age (y)	48 ± 14	52 ± 12	64.7 ± 12 ‡	52.1 ± 17
BMI (kg.m^{-2})	23.7 ± 2.9	26.1 ± 4.5 ‡	25.9 ± 4.4 ‡	24.7 ± 4.2
cSBP (mmHg)	112 ± 13	129 ± 12 ‡	122 ± 15 †	117 ± 16
cDBP (mmHg)	79 ± 9	88 ± 10 ‡	81 ± 10	80 ± 11
AAo L (mm)	53.9 ± 8.6	58.3 ± 8.4 †	74.3 ± 11.1 ‡	74.7 ± 14.5 ‡
AAo D (mm)	28.8 ± 3.8	29.9 ± 3.3	41.2 ± 5.5 ‡	41.4 ± 6.7 ‡
AAo V (mL)	32.7 ± 12.5	38.3 ± 12.8 *	87.6 ± 28.2 ‡	91.4 ± 38.6 ‡
AAo Curvature	0,031 ± 0,006	0,032 ± 0,006	0,025 ± 0,005 ‡	0,027 ± 0,008 †
AAo Tortuosity	0,10 ± 0,04	0,13 ± 0,04 ‡	0,13 ± 0,05 ‡	0,14 ± 0,06 ‡

Table 1: Patient characteristics and MRI aortic measures.
*p < 0.05, †p < 0.01 or ‡p < 0.001 for comparison against healthy controls, BMI: body mass index, cSBP: central systolic blood pressure, cDBP: central diastolic blood pressure, AAo: ascending aorta, L: length, D: diameter, V: volume

References

[1] L. Pape *et al.*, "Aortic diameter >or = 5.5 cm is not a good predictor of type A aortic dissection: observations from the International Registry of Acute Aortic Dissection (IRAD)," *Circulation*, vol.116 (10), pp.1120-1127, 2007.
[2] T. Dietenbeck *et al.*, "3D aortic morphology and stiffness in MRI using semi-automated cylindrical active surface provides optimized description of the vascular effects of aging and hypertension," *CBM*, 2018, vol.103, pp.101-108.

Quantifying mitral valve regurgitation from 4D flow MRI using semi-automated flow tracking

Carmen PS Blanken[1], Jos JM Westenberg[2], Jean-Paul Aben[3], Geertruida P Bijvoet[4], Steven AJ Chamuleau[5], Aart J Nederveen[1], Tim Leiner[5], R Nils Planken[1] and Pim van Ooij[1]

[1]Amsterdam UMC, location AMC, [2]Leiden UMC, [3]Pie Medical Imaging, [4]Maastricht UMC, [5]UMC Utrecht, Netherlands.

Purpose: Cardiac 4D flow MRI offers novel possibilities to quantify mitral valve regurgitation (MVR). Retrospective valve tracking enables forward blood flow quantification over the heart valves, taking into account valvular motion[1]. However, quantification of MVR at valve level can suffer from flow incoherency, causing signal loss and an underestimation of regurgitant flow. A suggested solution is to measure 1-2 cm proximal to the valve and perpendicular to the regurgitation: flow tracking[2]. The purpose of this study was to compare regurgitant flow over the mitral valve as quantified by semi-automated flow tracking and valve tracking in clinical MRI data.

Methods: 26 MVR patients (8 mild-moderate, 8 moderate-severe, 10 severe, as diagnosed by echocardiography[3]) underwent cardiac MRI including 4D flow MRI at 1.5T (30 cardiac phases, free-breathing, retrospective ECG-gating, three-directional VENC of 150-280 cm/s, spatial resolution of 2.89x2.89x3.5mm^3 for severe MVR and 1.45x1.45x6mm^3 in the other groups). Mitral valve (MV) and aortic valve (AV) flow volumes were quantified from 4D flow MRI by dedicated software (CAAS MR Solutions 5v1 - 4D Flow, Pie Medical Imaging) with through-plane valve motion correction as assessed on two-, three- and four-chamber (2CH, 3CH, 4CH) cine bSSFP. **1)** MV regurgitant flow volume (Rvol) was quantified using flow tracking and valve tracking, see Figure 1. **2)** To test inter-valve consistency, MV and AV forward flow were quantified using valve tracking at annulus level. **3)** Left-ventricular stroke volume (LVSV) was quantified by short-axis bSSFP volumetry for indirect MVR quantification ($Rvol_{INDIRECT}$ = LVSV – AV flow). Agreement between MV and AV net flow was evaluated with a Wilcoxon signed rank test, as well as agreement between 4D flow MRI-derived Rvol and $Rvol_{INDIRECT}$. Orthogonal regression and Bland-Altman analysis were performed with $p<0.05$ considered significant.

Results: Flow tracking measured higher Rvol than valve tracking ($p<0.001$), see Figure 2 - top. MV net flow turned out higher than AV net flow for valve tracking ($p<0.001$) but not when Rvol was quantified with flow tracking ($p=0.97$), see Figure 2 - bottom. Interestingly, when comparing with indirect quantification (LVSV - AV flow), Rvol measured with flow tracking was higher ($p=0.005$) whereas Rvol measured with valve tracking was not ($p=0.253$), despite a trend towards underestimation of Rvol for severe MVR using valve tracking (Figure 2 - top).

Discussion: In this study, the application of semi-automated flow tracking provided better quantification of MVR by 4D flow MRI than valve tracking, in particular in severe MVR. Good agreement between MV and AV net flows indicated good accuracy of flow tracking. In conclusion, we found that flow tracking provided more accurate quantification of MVR than valve tracking due to measurement at a location of less incoherent flow.

References: 1. Kamphuis et al, Radiology 2018, 2. Calkoen et al, JCMR 2015, 3. Vahanian et al, 2013.

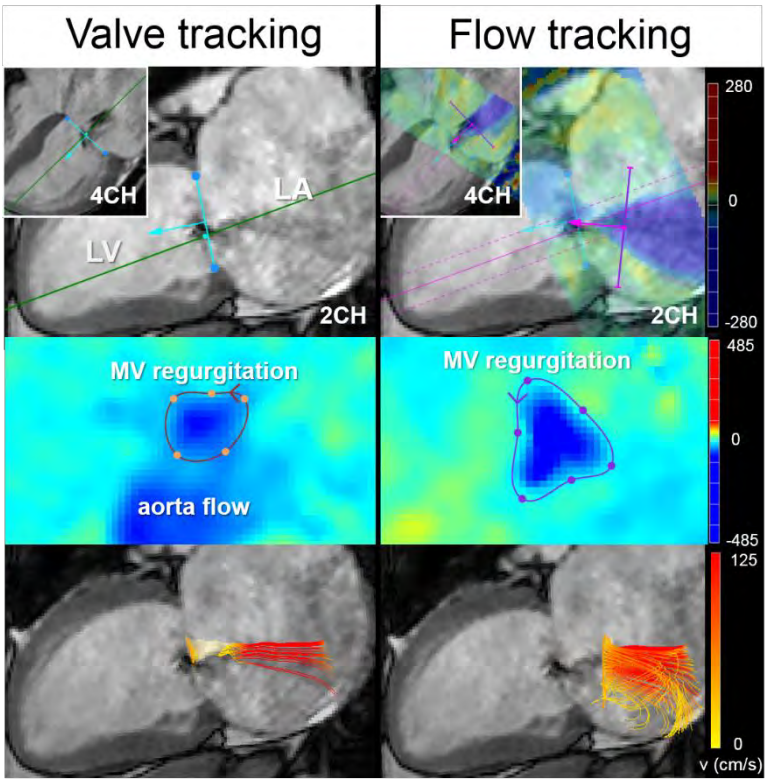

Figure 1: Valve tracking and flow tracking in severe MVR. Top) Measurement plane initialization, with an additional plane for flow tracking during regurgitation. Middle) Flow area contouring in 4D flow velocity projection. Bottom) Streamlines.

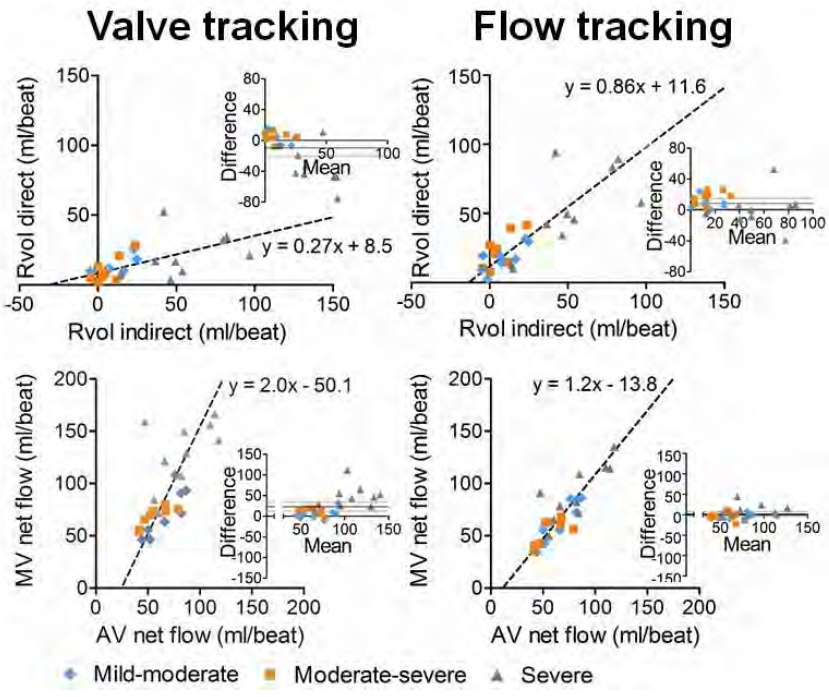

Figure 2: Orthogonal regression and Bland-Altman plots of: top) Rvol vs $Rvol_{INDIRECT}$ (= LVSV - AV flow) and bottom) MV and AV net flows (forward – backward flow volume), for valve tracking (left) and flow tracking (right). MV and AV net flows should be equal.

Aurélien Bustin[1], Gastao Cruz[1], Imran Rashid[1], René M. Botnar[1], Claudia Prieto[1]
[1]Department of Biomedical Engineering, School of Biomedical Engineering and Imaging Sciences, King's College London, UK;

PURPOSE: Whole-heart sub-millimeter isotropic resolution coronary MR angiography (CMRA) provides detailed information of the coronary arteries and cardiac anatomy. Recently, a low-rank patch-based reconstruction technique (3D PROST[1]) has been proposed to achieve sub-millimeter isotropic resolution CMRA in a predictable scan time. However, this approach only corrects for 2D translational respiratory motion of the heart and image quality can be affected by residual non-rigid motion. In this study, we sought to achieve free-breathing non-rigid motion corrected whole-heart sub-millimeter isotropic resolution Cartesian CMRA in a clinically feasible scan time by integrating 3D PROST into a highly accelerated non-rigid motion correction framework.

METHODS: Acquisition & Reconstruction – CMRA acquisitions were performed with an undersampled variable density Cartesian spiral-like acquisition[1,2]. A 2D image-based navigator preceded each spiral-like arm acquisition to enable beat-to-beat 2D translational respiratory motion correction and 100% scan efficiency[3]. To account for 3D non-rigid motion, respiratory binning was performed by sorting the CMRA data into five respiratory phases. Respiratory-resolved CMRA images were reconstructed using a soft-gated iterative SENSE technique and used to estimate 3D bin-to-bin non-rigid motion fields via image registration. A motion-compensated[4] 3D CMRA image was then reconstructed at end-expiration by integrating the obtained non-rigid motion fields into a motion-compensated 3D PROST[1] reconstruction.

Imaging – Five healthy subjects (3 males, range 25-35 years) and five patients (3 males, range 35-68 years) underwent accelerated whole-heart CMRA with isotropic resolution of 0.9mm^3 on a 1.5T MR scanner (Siemens Magnetom Aera). Data were acquired in free-breathing with the following parameters: ECG-triggered 3D bSSFP, undersampling factor of x5, FOV=320x320x86-114mm^3, FA=90°, T_2-preparation duration=40ms, TE/TR=1.6/3.7ms, bandwidth=890Hz/pixel, subject-specific mid-diastolic acquisition window. Patients received sublingual glyceryl trinitrate (800 mcg) prior to CMRA. Images were reconstructed to a resolution of 0.6mm^3 and vessel sharpness and length of the right and left coronary arteries (RCA/LAD) were measured after reformatting[5]. For the healthy subject study, the proposed non-rigid PROST reconstruction was compared against translational correction only[1] and previously proposed non-rigid motion-compensated SENSE reconstruction[4].

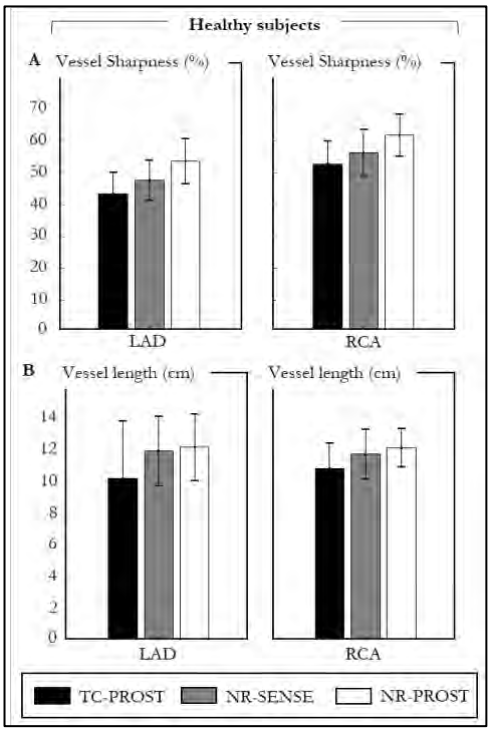

Fig 1. Coronary visible vessel length and % vessel sharpness are reported for the 5 healthy subjects for both LAD and RCA after translational motion correction only (TC-PROST), non-rigid SENSE reconstruction (NR-SENSE) and the proposed non-rigid-PROST reconstruction (NR-PROST).

RESULTS: Average scan times were 6min50±55sec (healthy subjects) and 8min25±1min (patients) with 100% respiratory scan efficiency. Accelerated non-rigid PROST allows for improved vessel sharpness and vessel length of both RCA and LAD compared to translation-only corrected PROST and non-rigid SENSE (Figure 1). CMRA images in patients show an excellent delineation of the coronary vasculature (Figure 2). High image quality and good visualization of the distal coronary segments are observed with non-rigid-PROST, with vessel length (RCA: 14±2cm, LAD: 11±2cm) and vessel sharpness (RCA: 56±6%, LAD:57±3%) comparable to that of the healthy subject study.

DISCUSSION: We demonstrate the feasibility of combining high undersampling factors with non-rigid motion corrected 3D PROST reconstruction to obtain high-quality CMRA with 0.9mm^3 spatial resolution under free-breathing, and in a clinically feasible scan time (<10min). Future work will investigate the potential of this framework in a larger cohort of patients with coronary artery disease.

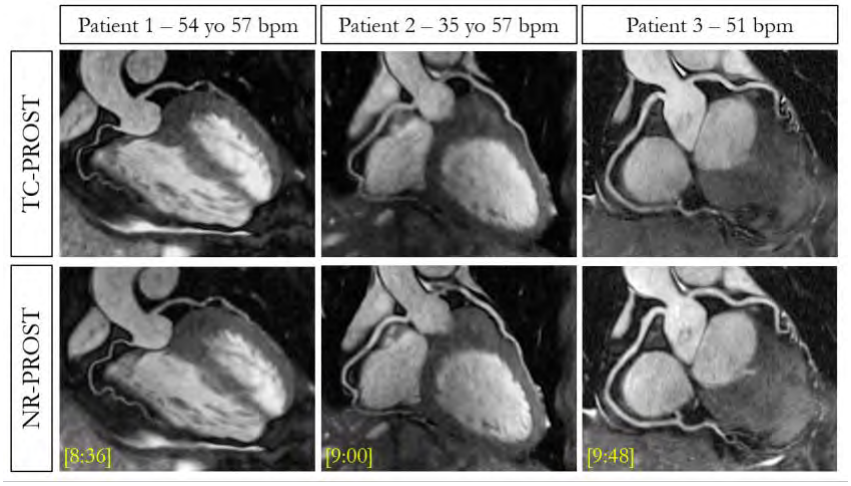

Fig 2. Reformatted CMRA along the RCA and LAD for 3 CAD patients acquired with isotropic resolution of 0.9mm^3 and reconstructed with translational (TC-PROST) and the non-rigid (NR-PROST) framework.

REFERENCES: [1] Bustin, MRM 81:102-115 (2019); [2] Prieto, JMRI 41:738-746 (2015); [3] Henningsson, MRM 67:437-445 (2012); [4] Cruz, MRM 77:1894-1908 (2017); [5] Etienne, MRM 48:658-666 (2002).

An automatic grading method for severity of white matter lesions

Xiaomeng Wu[1], Shuai Liu[2], Xihai Zhao[2], Xin Wu[1], Fei Shang[1]

1.Department of Biomedical Engineering, School of Life Science, Beijing Institute of technology, Beijing, China;

2. Center for Biomedical Imaging Research, Department of Biomedical Engineering, School of Medicine, Tsinghua University, Beijing, China;

Background and Purpose

White matter lesions (WML) are considered as cerebral small vessel disease and associated with Alzheimer`s disease, stroke and other diseases[1]. Grading of WML can provide quantitative information and assist prediction of development and prognosis of the disease, but it is laborious and mainly based on radiologist`s subjectivity. In this study, automatic grading of white matter lesions based on decision tree with reference to Fazekas rating scales[2] was constructed.

Methods

Study sample: The study protocol was approved by institutional review board and written consent form was obtained from each subject. A total of 325 subjects were recruited in this study. Each subject underwent MR imaging on a 3.0 Tesla MR scanner with FLAIR sequence in different center. The number of cross-sectional brain images ranged from 17 to 22. **Data analysis**: All data were graded by experienced radiologists based on Fazekas rating scale which rates PVH (Periventricular Hyperintensities) and DWMH (Deep White Matter Hyperintensities) respectively from grades 0 to 3. **Image processing**: Images processing was divided into three steps (Fig1): 1. Preprocessing: Each FLAIR dataset was warped into MNI (Montreal Neurological Institute) space, then WML were extracted by SPM and LST toolbox[3] and divided into PVH and DWMH based on their location; 2. Features extraction: Number and size of lesions were calculated at different anatomic region; 3. Grading: The PVH and DWMH scores were obtained by decision tree, the rules of decision tree was designed according to rating scale (Fig 2).The final score is the sum of these two scores.

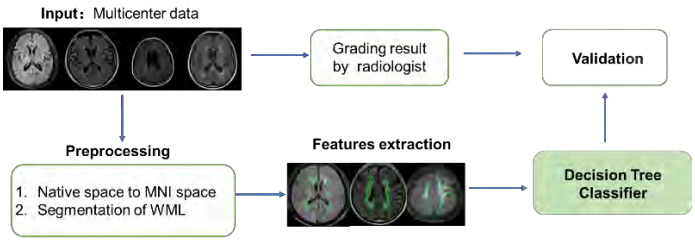

Fig 1. Overview of the proposed framework

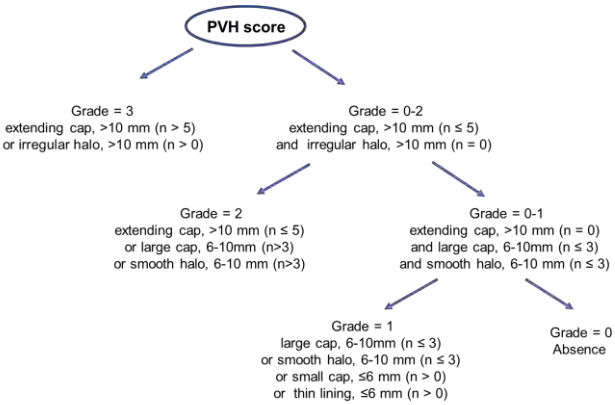

Fig 2. The decision tree for PVH score

Table 1. Comparison of automatic grades and radiologists' grades

Grades difference	PVH score	DWMH score	Final score
0	63.7%	54.4%	40.3%
1	97.2%	95.4%	85.2%

Results

In this study, 40.3% scores graded automatically were same with radiologists' scores, 85.2% were within 1 grade difference (Table 1). For PVH and DWMH score, the precision within 0,1 grade difference were 63.7%, 97.2% and 54.4%, 95.4%.

Discussion and Conclusion

Grading of WML was largely disturbed by observers` subjectivity which would lead to a poor inter repeatability and this bias mainly appeared in adjacent grades. If the difference within 1 grade was considered acceptable, our results showed that automatic grading results were consistent with professional results. The method based on the decision tree avoids the rating difference of intra-reader or inter-reader, it is a more robust method to grading WML than human rating.

References

[1]. Wardlaw J M, et al. Journal of the American Heart Association, 2015, 4(6). [2]. Fazekas F, et al. AJR Am J Roentgenol. 1987; 149:351-356. [3]. Paul Schmidt, et al. Neuroimage, 2012; 59(4):3774–3783.

4D Flow MRI Quantification of Flow Disorganization in Aging and Aortic Dilation

Sophia Houriez--Gombaud-Saintonge[1,2], Ariel Pascaner[4], Gilles Soulat[3], Umit Gencer[3], Thomas Dietenbeck[1], Damian Craiem[4], Emilie Bollache[1], Yasmina Chenoune[2], Elie Mousseaux[3], Nadjia Kachenoura[1]

1.Sorbonne Université, INSERM, CNRS, Laboratoire d'Imagerie Biomédicale (LIB), Paris, 2. ESME Sudria Research Lab, Paris 3.HEGP, Paris ,4. IMETTYB - Universidad Favaloro - CONICET, Buenos Aires

Purpose: Referral to surgery in thoracic aortic aneurysms (TAA) is based on maximal diameters (Dmax) measured from imaging, which are known to have a high diagnosis failure rate [1]. In addition to geometry, 4D flow MRI [2] provides a comprehensive flow imaging. Thus, our aim was to evaluate the ability of 4D flow MRI quantitative flow indices to characterize TAA.

Methods: We studied 20 patients (66 ± 14 years) with TAA and tricuspid valve (TAVd) with Dmax 43±5mm and 56 healthy controls (30 subjects ≤50 years named YC, mean age:36±9 years; 26 subjects >50 years named OC, mean age: 65 ± 9 years). All underwent aortic MRI with 4D flow MRI and anatomical 3D spoiled gradient echo SPGR sequence for a precise measurement of diameters. After aortic segmentation on the 4D flow MRI peak systolic phase, ascending aortic (AA) volume of backward flow (V_{BF}) was calculated in addition to maximal velocity jet angle (Angle) and eccentricity (Ecc) [3] (Figure 1). Receiver operating characteristic analysis was performed to assess ability of such flow indices to characterize AA dilation.

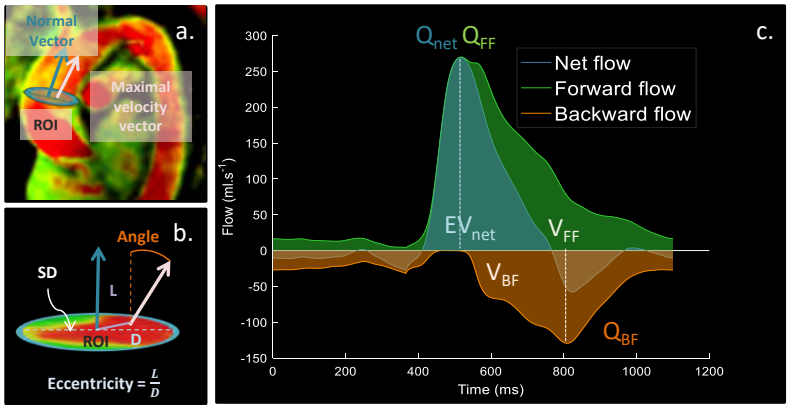

Figure 1: Aortic 4D flow MRI indices. a) 4D flow MRI systolic velocities in a TAVd patient and illustration of a ROI b) flow angle, eccentricity, and standard deviation (SD) c) time-resolved net, forward and backward flow curves (Q: peak, V:Volume)

Results: While AA Dmax varied by 1.4 folds between TAVd and OC, V_{BF} varied by 6.5 folds and Ecc and Angle varied by 1.3 to 1.7 folds between the two groups (Figure 2). Moreover, in TAVd patients, V_{BF} varied by 12.7 folds between AA as compared to descending aorta (DA). Finally V_{BF} varied consistently with age and was able to detect AA dilation with an accuracy of 0.98, while Ecc and Angle had an accuracy of 0.78 and 0.89, respectively (Figure 3).

Discussion: 4D flow MRI was used to provide an insight into quantitative flow indices and their ability to characterize aortic alterations with aging and disease. Variation of such flow indices, specifically backward flow in aneurysmal aorta is substantially higher than variations in diameters. Their added clinical value to rupture or dissection prediction needs to be demonstrated in larger longitudinal studies.

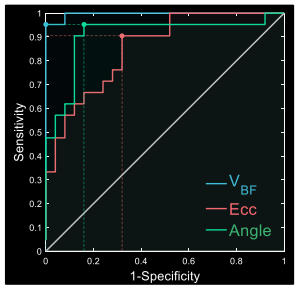

Figure 3: ROC curves of indices extracted from 4D flow MRI

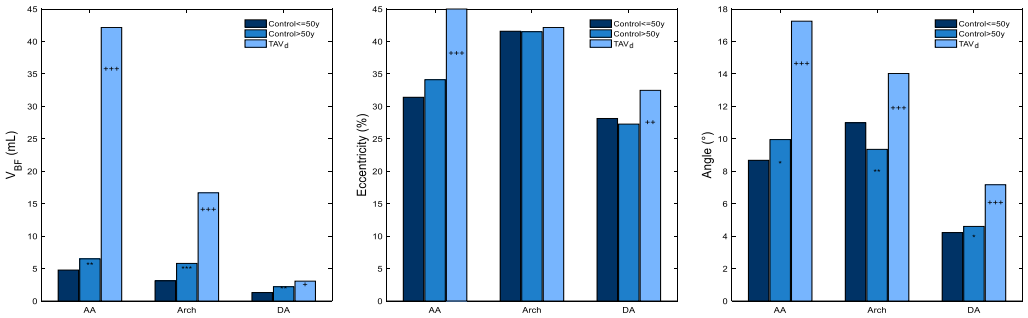

Figure 2: Flow indices along the aorta for each group. AA: ascending aorta, DA: descending aorta (≤50y *vs.* >50y: *:p<0.05, **:p<0.01, ***:p<0.001|TAVd *vs.* >50y: $^{+}$:p<0.05, $^{++}$:p<0.01, $^{+++}$:p<0.001).

References:

[1] L. A. Pape *et al.*, "Aortic diameter >or = 5.5 cm is not a good predictor of type A aortic dissection: observations from the International Registry of Acute Aortic Dissection (IRAD)," *Circulation*, vol. 116, no.10, pp.1120–1127,Sep. 2007.

[2] M. Markl, A. Frydrychowicz, S. Kozerke, M. Hope, and O. Wieben, "4D flow MRI," *J. Magn. Reson. Imaging JMRI*, vol. 36, no. 5, pp. 1015–1036, Nov. 2012.

[3] M. Sigovan, M. D. Hope, P. Dyverfeldt, and D. Saloner, "Comparison of four-dimensional flow parameters for quantification of flow eccentricity in the ascending aorta," *J. Magn. Reson. Imaging JMRI*, vol. 34, no. 5, pp. 1226–1230, Nov. 2011.

Evaluation of Contrast Dynamics in the Juvenile German Swine as Applied to CE-MRA: a Study using 4 Different Gadolinium Contrast Agents

Jeffrey H. Maki[1,2], Guenther Schneider[3], Toshimasa J. Clark[1], Miles A. Kirchin[4], Gregory J. Wilson[2,5]
1 – University of Colorado, Aurora, CO, USA 2 – University of Washington, Seattle, WA, USA
3 - University Hospital of Saarland, Homburg, Germany 4 – Bracco Imaging, Milan, Italy 5 – Bayer, Whippany, NJ, USA

Introduction:

It is becoming clear that intravascular signal intensity is highly sublinear with respect to Gd concentration ([Gd]) in CE-MRA. This occurs for several reasons: a) the SPGR signal intensity (SI) curve drops off with increasing R1, b) R1 itself is sub-linear at high blood concentrations due to exclusion of Gd from the RBC and rapid water exchange through the RBC membrane (1), and c) R2* values, while linear wrt [Gd], are quite high during 1st pass CE-MRA, meaning significant R2*-related signal loss can occur due to the use of a gradient echo sequence (2). This translates to faster Gd injections not necessarily increasing peak SI, and instead merely shortening the bolus length, which can lead to artifacts such as blurring.

The above synopsis, while well accepted, is based on the physics of the SPGR sequence and relaxivity work performed in *ex-vivo* human blood. We explore here an animal model to validate these conclusions in CE-MRA.

Methods:

Eight juvenile German swine (53-63 kg) were investigated. First, extracted arterial blood was doped with each of 4 Gd agents (1-30 mM) - gadoteridol (ProHance, Bracco), gadobenate (MultiHance, Bracco), gadobutrol (Gadavist, Bayer), gadofosveset (Ablavar, Lantheus). R1 and R2* was measured *ex-vivo* at 1.5T per refs. (1,2).

Next, two pigs each were administered three separate doses (0.1 mmol/kg, excepting gadofosveset 0.03 mmol/kg) of a different Gd agent at varying injection rates (1, 2, or 3 mL/s) during which concurrent time-resolved 3D SPGR imaging of the aorta was performed (Siemens Aera, TR/TE 4.6/1.4 ms, α=30^0, temp res 1.7 s). During image acquisition, approximate 0.5 mL aliquots of arterial blood was continuously sampled (2 s intervals) through an indwelling aortic catheter, and archived for mass spectrometry determination of [Gd].

Finally, two additional 3D CE-MRA studies were performed on each pig (random order 1 and 3 mL/s injections, TR/TE 2.9/1.05 ms, α=25^0) in order to subjectively evaluate for blurring in the CE-MRA.

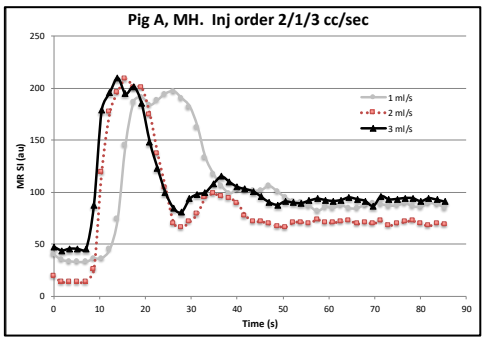

Fig 1. Example pig SI vs time data 3 sequential injections single dose (0.1 mmol/kg) gadobenate.

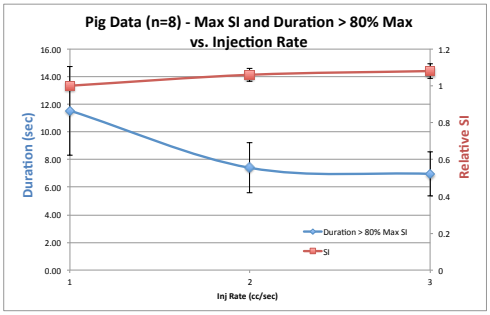

Fig 2. Average data 8 pigs (2 each agent) – relative SI (normalized to 1 mL/s injection - red) and duration plateau > 80% max SI (blue).

Results:

Sublinear blood R1 vs. [Gd] and linear relatively high and agent independent blood R2* was appreciated for all contrast agents, analogous to in humans (1,2).

Fig. 1 shows example pig SI vs. time data for a pig receiving gadobenate injections. Note very little increase in SI with increasing injection rate, but much longer bolus duration for the slower 1 mL/s injection. This held true the across the agents, as expected (Fig. 2 - red line SI, blue line duration). Subjective reader assessment of blurring was noticeably less for the 1 mL/s vs. the 3 mL/s CE-MRA studies. Mass spectrometry data is pending and will be analysed and correlated with expected Gd concentrations and SI to assess how well predictions of SI based on estimated R1 and R2* perform.

Discussion:

Data from pigs approximating human size validates human data (3) similarly demonstrating faster injection rates of contrast (> 1 mL/s) minimally increase SI, and only act to shorten the bolus duration and possibly increase blurring. Once mass spectrometry analysis of bolus data is completed, it will be possible to ascertain how well current modeling techniques estimate [Gd] and the resultant intravascular SI during the passage of contrast, thus better validating current modeling techniques.

References:

1. *Wilson GJ, Woods M, Springer CS et al. Magn Reson Med 2014;72:1746–54.*
2. *Wilson GJ, Springer CS Jr, Bastawrous S, Maki JH. Magn Reson Med 2016;77:2015–27.*
3. *Wilson GJ, Maki JH. J Magn Reson Imaging 2016;44:1664–72.*

3D Whole-heart Free-breathing qBOOST-T2 Mapping

G. Milotta[1], G. Ginami[1], A. Bustin[1], R. Neji[1,2], C. Prieto[1], R.M. Botnar[1]
[1]School of Biomedical Engineering and Imaging Sciences, King's College London; [2]MR Research Collaborations, Siemens Healthcare

Introduction: Cardiac MRI enables the assessment of whole-heart anatomy with both bright- and black-blood contrast. Quantitative myocardial T2 mapping enables non-contrast tissue characterization, with increased myocardial T2 values reported to correlate with oedema and myocardial inflammation [1]. However, conventional T2 maps and anatomical images are acquired sequentially with different geometries and at different motion states, thus increasing scan time and requiring offline image registration. Here we propose a novel accelerated quantitative 3D whole-heart sequence (qBOOST-T2) which provides co-registered high-resolution 3D bright-blood, black-blood and T2 map volumes from a single free-breathing ~11min scan.

Methods: The framework of the proposed qBOOST-T2 sequence is shown in Fig.1. Three interleaved bSSFP volumes are acquired with an undersampled Variable Density Cartesian spiral-like trajectory [2] and with 1) T2prep-Inversion Recovery (IR), 2) T2prep and 3) no preparation modules, respectively. 2D low resolution image navigators (iNAVs) [3] are acquired prior to each image acquisition in order to estimate and correct for translational respiratory motion, enabling 100% respiratory scan efficiency. Each 4x undersampled 3D volume is independently reconstructed with a 3D patch-based reconstruction (3D-PROST) [4]. The T2prep-IR bright-blood volume is used for anatomy visualization, a PSIR reconstruction between the first and the third volume is performed to obtain the black-blood volume, and the 3D T2 map is obtained by matching the acquired signal on a pixel-by-pixel basis to a simulated dictionary obtained via extended phase graph (EPG) simulations [5]. Five healthy subjects and two patients were scanned on a 1.5T scanner (Siemens Magnetom Aera). The proposed prototype qBOOST-T2 sequence was compared in 3 short axis slices with a breath-hold T2 prepared 2D-bSSFP T2 mapping sequence [1].

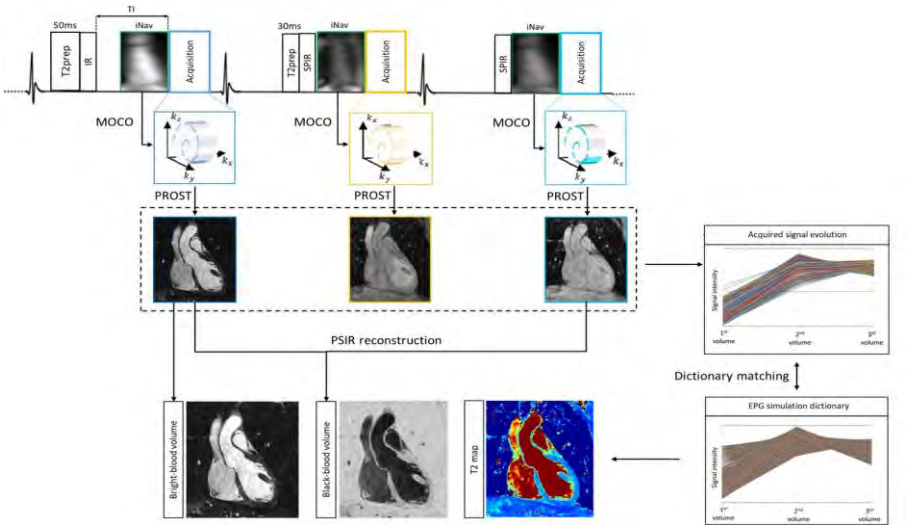

Figure 1 - Proposed sequence: Three interleaved bSSFP bright-blood volumes are acquired with: 1) T2prep-IR, 2) T2prep and 3) no preparation modules. 2D-iNAVs are acquired to estimate/correct SI and RL translational motion. Each volume is reconstructed with 3D PROST reconstruction. Black-blood images are obtained via PSIR reconstruction between the T2prep-IR prepared dataset (anatomy image) and the third volume. T2 map is generated by matching the measured signal and an EPG simulated dictionary. Acquisition parameters included FA=90deg, resolution=1x1x2mm^3, 14 start-up echoes for iNAV, T2prep$_{1st\text{-}heartbeat}$=50ms, T2prep$_{2nd\text{-}heartbeat}$=30ms, TI=110ms and total scan time=11±1.2min

Results: Healthy subjects: Uniform T2 maps were observed with the proposed approach in different reformatted views (Figure 2A). Good agreement (r = 0.849, P < 0.001) was found between average T2 values obtained with the proposed approach and the standard 2D bSSFP T2 mapping sequence (T2=51±3ms and T2=49±2ms respectively).

Patients: The proposed qBOOST-T2 mapping sequence provided a septal T2 value of 51.1±1.5ms averaged from apical to basal slices. The average septal T2 value obtained with standard 2D T2 mapping was 48.0±2.1ms. Good agreement (r = 0.827, P < 0.005) was found between the two techniques.

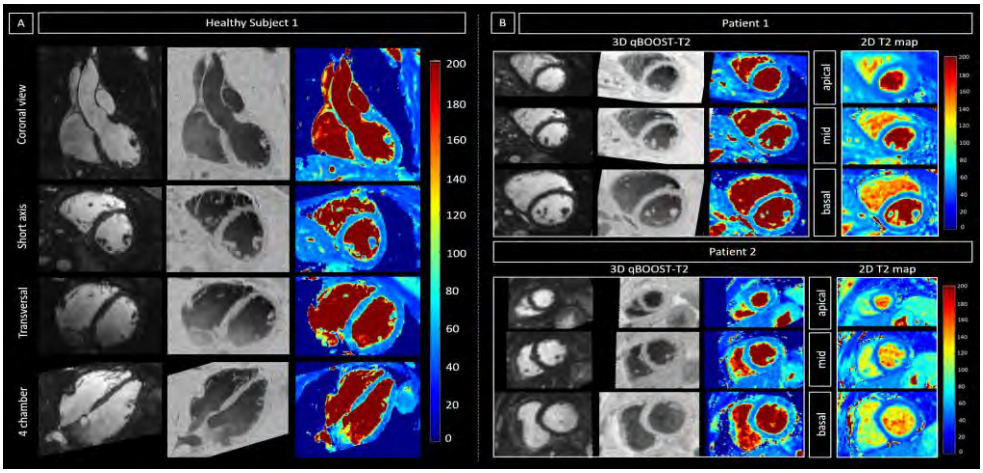

Figure 2 – A: Co-registered bright-blood, black-blood volumes and 3D T2maps for one representative healthy subject acquired with the proposed qBOOST-T2 sequence. Reformatted coronal, short axis, transversal and four chamber views are shown. B: Comparison between 2D short-axis standard T2 maps and short-axis (apical, mid and basal slice) reformatted 3D qBOOST-T2 maps for two patients. Additionally, bright-blood and black-blood short axis reformatted images are shown for the qBOOST-T2 acquisition

Conclusion: The proposed accelerated qBOOST-T2 sequence allows the simultaneous acquisition of 3D co-registered high-resolution bright- and black-blood volumes and T2 maps for comprehensive assessment of cardiovascular disease in a clinically feasible scan time of ~11min. The proposed approach showed good agreement with regard to T2 quantification accuracy and precision in comparison with the standard bSSFP T2 mapping sequence.

References: [1] Giri S. et al. JMRM, 2009. [2] C. Prieto et al JMRI, 2015. [3] A. Bustin et al., MRM, 2018. [4] M. Henningsson et al., MRM, 2012. [5] M. Weigel, JMRI, 2015.

Feasibility and wall shear stress quantification accuracy of compressed sensing aortic 4D flow MRI: a dual-center, dual-field strength (1.5, 3T) study

Emilie Bollache[1], Liliana E Ma[2], Ashitha Pathrose[2], Alex J Barker[3], Kelvin Chow[2,4], James C Carr[2], Paul WM Fedak[5], Ning Jin[4], Julio Garcia[5], Michael Markl[2]

[1]Laboratory of Biomedical Imaging, Sorbonne Université, Inserm, CNRS, Paris, France; [2]Department of Radiology, Northwestern University, Chicago, USA; [3]Department of Radiology, University of Colorado, Denver, USA; [4]Cardiovascular MR R&D, Siemens Medical Solutions, USA; [5]University of Calgary, Canada

Purpose: The use of 4D flow MRI in clinical routine is still hampered by long scan times and the need for multi-center data on large populations. A previously developed compressed sensing (CS) aortic 4D flow MRI sequence prototype was shown to provide 2-minute scan time with velocity and flow rate indices in good agreement with conventional 4D flow at a single center at 1.5T [1]. The purpose of the present work was to extend the feasibility study to a second center at 3T and to investigate the ability of this technique to provide accurate aortic wall shear stress (WSS) measurements.

Methods: Healthy volunteers (HV) and patients were prospectively recruited and scanned at Northwestern University (NU) in Chicago (25 HV [46±18 yrs, 11 men], 26 patients with various aortic and/or valvular diseases [61±14 yrs, 20 men], 1.5T MAGNETOM Aera, Siemens Healthcare, Germany) and University of Calgary (UC, 10 HV [48±13 yrs, 6 men], 10 patients with congenital heart disease (n=5), bicuspid aortic valve (BAV, n=4) or aortic dilation (n=1) [50±16 yrs, 7 men], 3T MAGNETOM Prisma, Siemens Healthcare), after Institutional Review Board approval and written informed consent. Each underwent CS (acceleration factor R=7.7) and conventional (GRAPPA R=2) 4D flow MRI of the thoracic aorta with matched imaging parameters (TR=4.3-5.1 ms, TE=2-2.4 ms, flip angle=7-15°, spatial resolution=2.7-4.2x2-2.8x2.4-3.5 mm^3, temporal resolution=35-41 ms, Venc=1.5-4 m/s), retrospective ECG gating and respiratory triggering, resulting in a total of n=142 datasets. CS acquisition volume further included whole heart coverage at UC. Each conventional and CS 4D flow dataset was analyzed by a researcher blinded to the image acquisition techniques, including correction for eddy currents and velocity aliasing, automated aortic volume segmentation using an in-house deep learning-based method [2] with manual correction when necessary. Quantification included peak systolic velocity in the ascending aorta (AA), arch, and proximal descending aorta (DA) using a previously described maximal intensity projection approach [3], and 3D peak systolic maximal WSS along the inner and outer curvature of the AA, arch and DA [4].

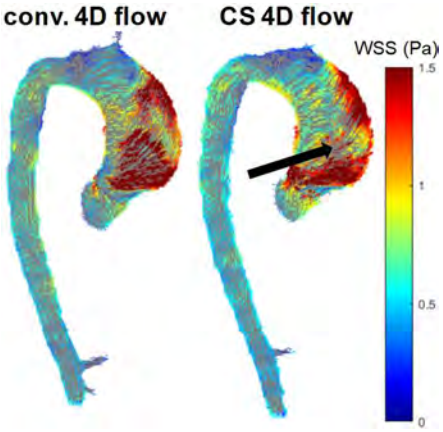

Results: Scan times were 7:09±2:50 and 1:53±0:26 minutes at NU, 7:47±3:24 and 3:35±1:23 min at UC for the conventional and CS 4D flow scans (p<0.0001), respectively. The Figure provides a representative example of peak systolic 3D WSS distribution throughout the aorta as assessed using both techniques in a BAV patient recruited at UC, showing that CS 4D flow was able to overall reproduce aortic blood flow patterns despite WSS underestimation (arrow). The Table summarizes regional measurements in patients and HV for both institutions as well as the comparison between CS and conventional 4D flow. Differences in peak velocity and WSS reached up to 15% and 18% at NU, 8% and 16% at UC, respectively.

	NU						UC					
	HV (n=25)			Patients (n=26)			HV (n=10)			Patients (n=10)		
	conv.	CS	% diff	conv.	CS	% diff	conv.	CS	% diff	conv.	CS	% diff
Peak systolic velocity (m/s)												
AA	1.53±0.20	**1.35±0.15***	-11±9.7%	2.36±0.97	**2.32±0.92***	-5.2±12%	1.48±0.27	1.37±0.21	-6.4±9.4%	1.80±0.78	**1.68±0.74***	-7.2±7.8%
arch	1.14±0.23	**1.03±0.18***	-9.0±8.1%	1.17±0.42	**1.04±0.32***	-8.5±13%	1.00±0.21	**0.93±0.22***	-7.5±6.9%	0.98±0.33	0.95±0.27	-0.3±19%
DA	1.23±0.29	**1.04±0.25***	-15±7.7%	1.16±0.52	**1.03±0.34***	-8.7±12%	1.10±0.17	**1.06±0.17***	-3.9±4.5%	1.28±0.35	1.18±0.28	-6.7±8.9%
Peak systolic maximal WSS (Pa)												
inner AA	1.40±0.22	**1.17±0.21***	-16±10%	1.60±0.59	**1.38±0.52***	-12±15%	1.40±0.28	1.31±0.24	-5.1±13%	1.41±0.40	**1.19±0.25***	-13±13%
outer AA	1.26±0.21	**1.19±0.24***	-4.5±13%	1.63±0.69	**1.52±0.61***	-5.4±12%	1.39±0.32	1.21±0.17	-9.6±20%	1.40±0.52	1.25±0.31	-5.8±16%
inner arch	1.18±0.23	**1.08±0.19***	-7.9±8.2%	1.11±0.36	**0.98±0.33***	-11±11%	1.15±0.22	**1.05±0.22***	-8.4±11%	1.19±0.30	**1.07±0.29***	-11±7.7%
outer arch	1.07±0.21	**0.93±0.17***	-13±5.7%	1.26±0.55	**1.01±0.42***	-18±9.7%	1.07±0.28	**0.93±0.22***	-13±11%	1.19±0.35	**0.99±0.25***	-16±6.8%
inner DA	1.24±0.27	**1.08±0.23***	-12±11%	1.02±0.29	**0.93±0.26***	-7.6±8.6%	1.14±0.20	**1.07±0.18***	-5.7±5.8%	1.29±0.37	**1.11±0.33***	-14±5.3%
outer DA	1.21±0.29	**1.00±0.23***	-17±11%	0.98±0.36	**0.91±0.33***	-6.4±7.2%	1.11±0.16	**0.99±0.18***	-11±8.4%	1.34±0.42	**1.21±0.33***	-8.6±12%

NU: Northwestern University; UC: University of Calgary; HV: healthy volunteers; conv., CS: conventional, compressed sensing 4D flow MRI; AA, DA: ascending, descending aorta; WSS: wall shear stress. *: p<0.0001 between CS and conv. using a Wilcoxon signed rank test. Difference relative to conv. values are provided.

Discussion: CS aortic 4D flow MRI was feasible at both 1.5 and 3T, providing significantly shortened scan times and aortic peak velocity within 15% of conventional 4D flow. These dual-center results were in agreement with previous initial findings reported in 20 HV and 11 patients at 1.5T [1]. Similar results were observed in WSS values, which were underestimated by up to 18% when using CS 4D flow especially in patients. Further work and larger studies on more homogeneous patient groups are warranted to demonstrate the clinical relevance of this promising new technique.

References: [1] Ma LE et al. *Magn Reson Med* 2019;81(6):3675-90. [2] Berhane H et al. *ISMRM* 2019;4734. [3] Rose MJ et al. *J Magn Reson Imaging* 2016;44:1673-82. [4] Potters WV et al. *J Magn Reson Imaging* 2015;41(2):505-16.

3D Whole-heart Isotropic Resolution Motion Compensated Joint T1/T2 Mapping

G. Milotta[1], G. Ginami[1], A. Bustin[1], R. Neji[1,2], C. Prieto[1], R.M. Botnar[1]
[1]School of Biomedical Engineering and Imaging Sciences, King's College London; [2]MR Research Collaborations, Siemens Healthcare

Introduction: Tissue characterization, including identification and quantification of fibrosis and oedema, plays an important role in many myocardial diseases. Conventionally, 2D T1 and T2 maps are acquired sequentially under several breath-holds[1-2]. These approaches however achieve limited spatial resolution and coverage. In this work, we sought to develop a free-breathing motion compensated isotropic resolution 3D whole-heart sequence for joint T1/T2 mapping and anatomical water and fat imaging.

Methods: The proposed framework is shown in Fig.1. Three ECG-triggered interleaved magnetization prepared 3D volumes are acquired with two-point Dixon, spoiled gradient echo (GRE) readout and Variable Density Cartesian trajectory with spiral-like profile order and undersampling factor of 4x[3-4]. The three datasets are acquired with 1) Inversion Recovery (IR) preparation, 2) no preparation and 3) T2 preparation pulse (T2prep). Low resolution 2D image navigators (iNAVs)[5] are acquired prior to imaging to estimate and correct for translational respiratory motion, enabling 100% scan efficiency. Translational motion correction is performed for each echo, and the undersampled volumes are jointly reconstructed with a 3D patch-based low-rank reconstruction (HD-PROST)[4]. A water-fat separation algorithm[6] is used to generate fat and water images for each dataset, and the 3D water images are normalized on a voxel-by-voxel basis to obtain the signal evolution across the three acquired volumes. Quantitative T1 and T2 maps are generated by matching the measured signal to a simulated dictionary obtained with extended phase graph (EPG) simulations[7]. The proposed framework was tested on a standardized T1/T2 phantom and on 4 healthy subjects at 1.5T (Siemens Aera) and compared with conventional 2D MOLLI T1[1] and T2prep based bSSFP T2 mapping[2].

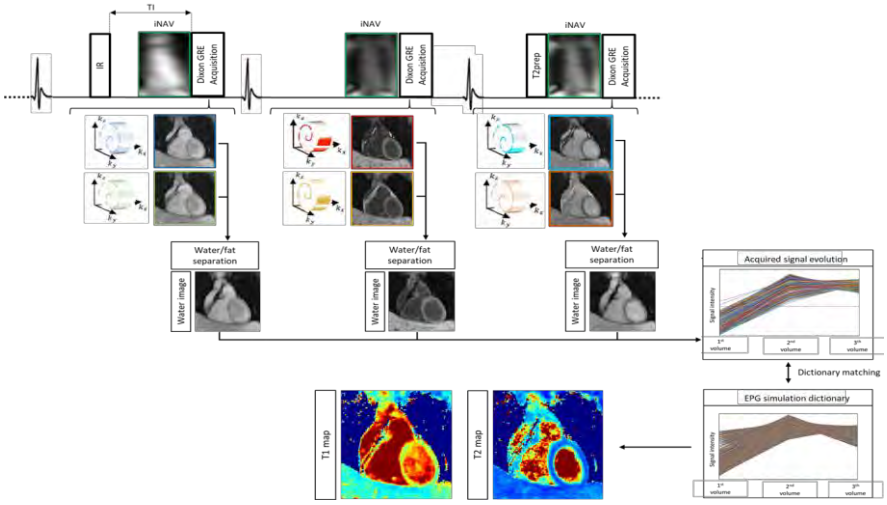

Fig. 1 - Proposed sequence: Three interleaved GRE volumes are acquired with Dixon encoding and 1) IR, 2) no preparation and 3) T2prep preparation. 2D-iNAVs are acquired to estimate/correct superior inferior and left-right translational motion. The volumes are reconstructed with HD-PROST[4]. A fat/water separation algorithm is used to obtain the water images and T1 and T2 maps are generated by matching the measured signal with an EPG-simulated dictionary. Acquisition parameters included FA=8deg, TR/TE1/TE2=6.71/2.38/4.76ms, isotropic resolution=1.8mm[3], 14 start-up echoes for iNAV, TI=120ms, T2prep=50ms, and total scan time=9.6±0.8min

Results: Good agreement (Fig.2A) was found between the proposed approach and reference phantom values for both T1 and T2 quantification (R2 = 0.968 and R2 = 0.998 respectively).

The proposed joint T1/T2 mapping resulted in septal T1 and T2 values of 1192±66ms and 49.1±3.3ms averaged from apical to basal slices in healthy subjects (Fig.2B). The average septal T1 and T2 values obtained with standard 2D MOLLI T1 mapping and bSSFP T2 mapping were 1006±38ms and 47.0±3.2ms, respectively.

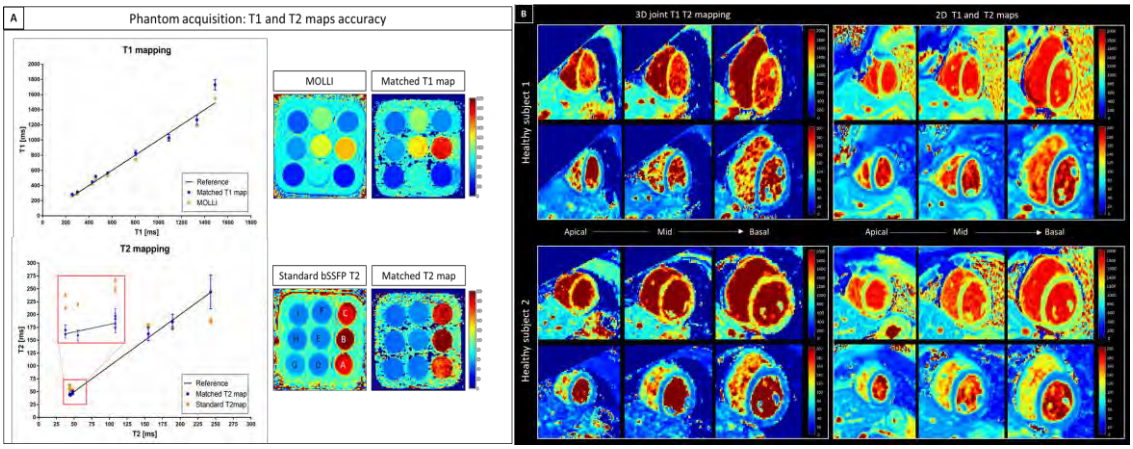

Fig. 2 – A: Comparison between T1 and T2 values obtained with the proposed 3D joint T1/T2 sequence and vendor reference. Values obtained with 2D T1 MOLLI and T2prep based T2 mapping are also included. Good agreement was observed between the proposed sequence, standard T1 and T2 mapping technique and phantom reference values. B: Comparison between 2D short-axis standard MOLLI T1 and bSSFP T2 maps and short-axis (apical, mid and basal slice) reformatted joint T1 and T2 maps for two healthy subjects.

Conclusion: The proposed motion compensated isotropic resolution joint T1/T2 mapping allows the simultaneous acquisition of 3D co-registered T1 and T2 maps and anatomical water and fat images in a clinically feasible scan time of ~10min. The proposed approach showed good agreement with reference T1 and T2 values in a standardized T1/T2 phantom and good agreement with 2D bSSFP T2 mapping in healthy subjects, whereas a T1 overestimation was observed with respect to 2D MOLLI T1 maps as expected, with a slightly lower precision.

References: 1) D. R. Messroghli et al., MRM, 2004. 2) Giri S. et al. JMR, 2009. 3) C. Prieto et al., JMR, 2015. 4) A. Bustin et al., MRM, 2019. 5) M. Henningsson et al., MRM, 2012. 6) Berglund J. et al., MRM, 2011 7 M. Weigel, JMR, 2015.

4D Hemodynamic Signatures: A novel concept for the evaluation of abnormal flow dynamics in aortic valve disease

Mohammed S.M. Elbaz[1], Michael B. Scott[1], Alex J Barker[4], Ryan Avery[1], Patrick McCarthy[2], Chris Malaisrie[2], Robert O. Bonow[3], James Carr[1], Michael Markl[1,5]

[1]Department of Radiology, [2]Cardiac Surgery, Cardiology[3] Northwestern University Feinberg School of Medicine, Chicago, IL, USA; [4]University of Colorado, CO, USA; [5]Department of Biomedical Engineering, Northwestern University, Evanston, IL, USA

Purpose: 4D flow MRI studies have shown that aortic valve disease, such as bicuspid aortic valve (BAV), can significantly alter aortic 3D hemodynamics and introduce complex flow changes (flow jets, vortex/helix flow). However, existing flow metrics quantify only partial components of the overall complex flow changes or use aggregated quantities (e.g., peak, average) that underutilize the comprehensive information (3D+time) provided by 4D flow MRI. Here, we propose a novel concept that captures unique ***hemodynamics signatures*** of normal and altered aortic 3D flow dynamics. This concept is based on the stochastic derivation of a signature of pair-wise velocity vector disparities throughout the aortic volume and cardiac cycle. The aims of this study were to 1) evaluate the feasibility of this novel concept to identify distinct hemodynamic signatures in BAV patients compared to controls and 2) to assess its potential for automated detection and grading of aortic valve stenosis and regurgitation.

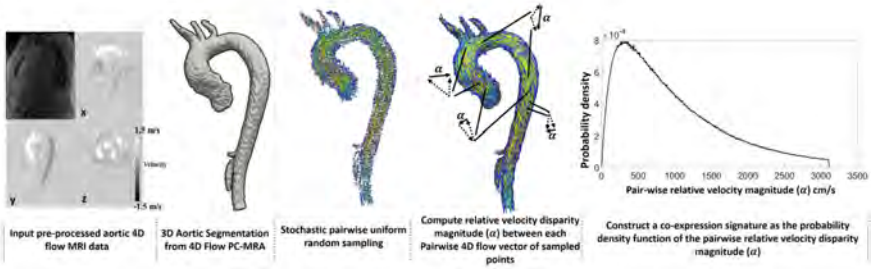

Fig. 1: Summary of the construction stage of the hemodynamic co-expression signature shown, for simplicity, in a 3D example – the methodology used here is extended to 4D.

Methods: ***Study Cohort and MR Imaging:*** A total of 338 subjects (209 BAV patients all with Left-Right fusion pattern, 153 male, age:49±15yr; 129 healthy controls, 65 male, age: 47±16yr, p=0.30) were retrospectively enrolled from an IRB-approved study. All patients underwent standard-of-care cardiothoracic MRI including 4D Flow (free breathing with respiratory navigator gating, spatial resolution = 2-3mm^3, temporal resolution = 33–43ms, venc = 150–450 cm/s).

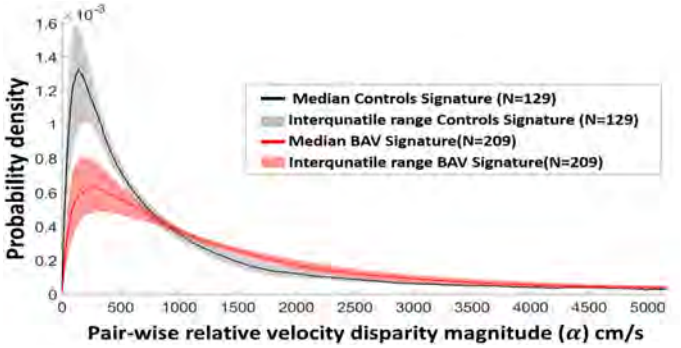

Fig.2: Results of derived hemodynamic signature of BAV patients vs. controls

Hemodynamic signature: The analysis is composed of two stages: **(I) Signature construction (Fig.1)**: 1) Segment the aorta volume from preprocessed 4D Flow MRI data. 2) Exclude supra-aortic Branches 3) Create an ***M***×3 matrix (**V**) concatenating all velocity vectors within the aorta over the cardiac cycle (***M***= # aorta voxels * cardiac time frames). 4) Perform stochastic discrete uniform random sampling of N_s voxel pairs over the rows of matrix **V**. N_s = 10×***M*** was used (average: 3 million sample pairs per subject). 5) For each sample pair, compute the relative velocity disparity magnitude (α) of the corresponding velocity vectors as the L2 norm of the vector difference. 6) The subject's hemodynamic signature (**S**) is constructed as the probability density function (pdf) of the α values with *B*=1000 bins.

Signature Dissimilarity: The Earth Mover's Distance (EMD) of pdfs was used to define a dissimilarity metric to compare the hemodynamics signatures of different subjects[1]. Baseline signature dissimilarity values were established for controls by comparing each control's signature to all other controls using EMD. A cumulative dissimilarity index (***D***) was then computed for each control as the sum of its dissimilarity to all other controls. Finally, a cumulative dissimilarity index for each BAV patient (***D***) was calculated as the sum of its dissimilarities against all controls.

Results (Fig 2, 3): As shown in Fig. 2, controls presented consistent hemodynamic signatures while BAV patients showed distinctly altered hemodynamic pdfs, characterized by elevated velocity disparity (i.e., lower probability density for small α values and the wider pdf). Importantly, Fig.3 shows significant differences in cumulative dissimilarity indices (**D**) between BAV patients with different aortic valve stenosis and aortic valve regurgitation severity and compared to controls.

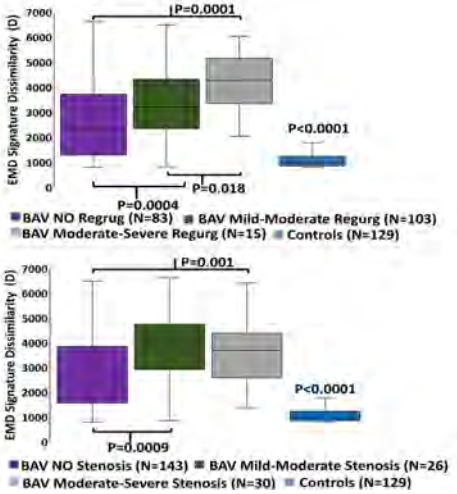

Fig.3: Comparison of the cumulative EMD dissimilarity index (D) of BAV patients with different degrees of stenosis and regurgitation & vs. controls

Discussion: The findings of this study demonstrate the feasibility of a novel 4D hemodynamic signature concept to identify distinctly altered volumetric hemodynamics in the aorta of BAV patients and discriminate different degrees of aortic valve disease (stenosis, regurgitation). This automated quantitative signature exploits the entire 4D flow MRI velocity field information by encoding the distribution of the time-resolved flow co-disparities over the entire aorta to capture intrinsic patient-specific 4D hemodynamic properties. Future studies will extend the technique to other cardiovascular diseases. ***Ref.***: *[1] Rubner Y etal. Int J Comput Vis. 2000;40:99-121.* ***Ack.***: *Grant support by AHA19POST34380379, R01HL115828, R01HL133504*

Ferumoxytol MR Angiography vs Doppler US for vascular mapping before haemodialysis arteriovenous access creation

Sokratis Stoumpos[1,2], Alfred Tan[3], Ram Kasthuri[3], Aleksandra Radjenovic[2], David B Kingsmore[1], Patrick B Mark[1,2], Giles Roditi[3]

1. Renal and Transplant Unit, Queen Elizabeth University Hospital, Glasgow, UK
2. Institute of Cardiovascular and Medical Sciences, BHF Glasgow Cardiovascular Research Centre, University of Glasgow, Glasgow, UK
3. Department of Radiology, Queen Elizabeth University Hospital, Glasgow, UK

Purpose: Doppler ultrasound (US) is routinely performed for vascular mapping prior to placement of a haemodialysis arteriovenous (AV) access but has the disadvantage of no direct visualisation of the central vasculature. Ferumoxytol is a non-nephrotoxic superparamagnetic iron oxide preparation which provides an alternative to gadolinium for magnetic resonance angiography (MRA). The aim of this study was to compare ferumoxytol-enhanced MRA (FeMRA) with Doppler US in assessment of the central and upper extremity vasculature in chronic kidney disease (CKD) patients due for vascular access creation.

Methods: This was a prospective comparative single-centre study approved by the local Research Ethics Committee. All patients enrolled had FeMRA and Doppler US performed on the same day. Two independent readers analysed the FeMRA to assess reproducibility of the technique and a third reader analysed the US. Comparisons of arterial and vein lumen diameter, vessel stenosis or occlusion, and central venous or arterial stenosis were performed. Interclass correlation coefficients (ICC), mean differences (with 95% CI) and Bland-Altman plots were used to examine inter-reader variability. Based on accepted standards for the creation of an AV access an algorithm was created to predict AV access outcome relying on mapping findings. Two binomial logistic regression models were created with AV access outcome as the dependent variable and age, sex, the presence of diabetes and US prediction algorithm (model 1) or FeMRA prediction algorithm (model 2) as the predictor variables.

Results: Seventy-eight upper limb mappings were obtained from 69 patients (mean age 58 +-13 years; 53.4% men; 34.5% diabetics) between December 2016 and August 2018. For 58 AV accesses (49 autogenous fistulas and 9 synthetic grafts) created, an outcome could be ascertained. FeMRA showed excellent inter-reader repeatability (ICC 0.91-0.99) for all parameters assessed. FeMRA identified 18 central vasculature stenoses (7 in cephalic arch, 6 in subclavian vein, 3 in brachiocephalic vein, and 2 in subclavian artery – Figures). Vessel course, tortuosity, accessory veins, anatomical variants and the presence of occlusion or stenosis in arm vessels was better assessed with FeMRA. On multivariable regression analyses FeMRA mapping was the only independent predictor of AV access outcome [odds ratio (OR): 15.7 (95% CI 3.6-68.5); p<0.001].

Discussion: MR angiography with ferumoxytol prior to AV access creation better predicted access outcome compared to Doppler US. Its value is not limited in identification of central vessels pathology but it also showed peripheral arterial and venous disease under-recognised with US.

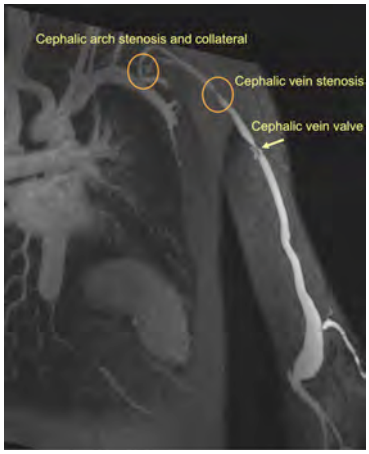

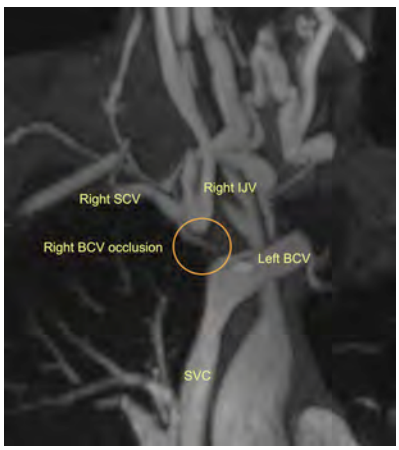

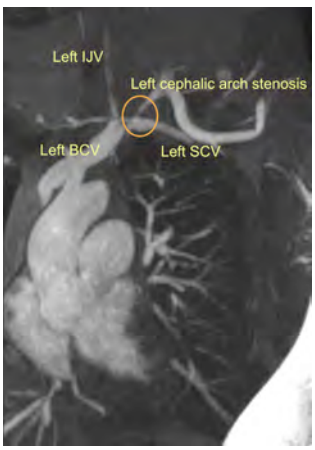

Highly accelerated compressed sensing 4D flow for evaluation of aortic hemodynamics

Ashitha Pathrose[1], Liliana Ma[1,2], Haben Berhane[3], Michael Baran Scott[1,2], Kelvin Chow[1,4], Christoph Forman[5], Ning Jin[6], Ali Serhal[1], Ryan Avery[1], James Carr[1,2], Michael Markl[1,2]

[1]Department of Radiology, Feinberg School of Medicine, Northwestern University, Chicago, US, [2]Department of Biomedical Engineering, Northwestern University, Chicago, US, [3]Lurie Children's Hospital, Chicago, US, [4]Cardiovascular MR R&D, Siemens Medical Solutions USA, Inc., Chicago, US, [5]Siemens Healthcare, Erlangen, Germany, [6]Cardiovascular MR R&D, Siemens Medical Solutions USA, Inc., Cleveland, US

Purpose: Recently, a highly accelerated, compressed sensing (CS) 4D flow framework prototype that enables aortic 4D flow under 2 minutes with inline reconstruction on the scanner under 5 minutes was developed and tested in 20 volunteers and 11 patients[1]. While this study compared CS with conventional 4D flow, in vivo studies did not systemically assess the impact of different CS acceleration factors on flow analysis. Thus, the purpose of this study was to evaluate the performance of CS 4D flow at three different acceleration factors and compare it to conventional 4D flow in patients with aortic disease.

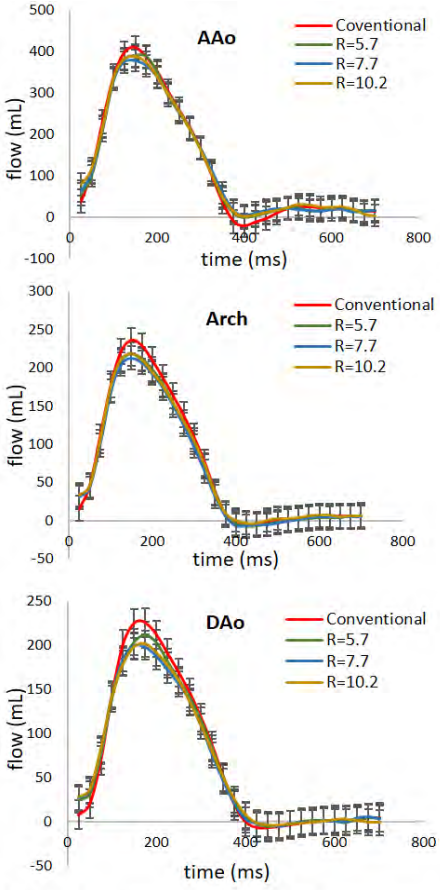

Figure 2: Time averaged flow-time curves of conventional and CS 4D flow

Methods: The study cohort included 14 patients with aortic disease (61±16 years; 10 men; n=8 with aortic root ectasia [6 TAV, 2 BAV], n=4 with type-B aortic dissection, n=2 with thoracic aortic aneurysm) on a 1.5T MRI system (MAGNETOM Aera, Siemens Healthcare, Germany). All patients underwent four 4D flow MRI scans of the thoracic aorta: Conventional 4D flow MRI with R=2 (GRAPPA) and 3 prototype CS-accelerated 4D flow scans with effective acceleration rates R=5.7, 7.7, and 10.2. All scans were acquired with navigator gating and retrospective ECG triggering and equivalent volumetric coverage, spatiotemporal resolution, and venc (TR = 4.8-5 ms, TE = 2.1-2.4 ms, spatial res. = 3.6-4.2x2.4-2.8x2.4-3.5 mm^3, temp. res = 38.5-40.5 ms, venc = 1.5-3.5 m/s). All 4D flow acquisitions were performed after administration of contrast agent (Gadavist, Bayer Healthcare, Berlin, Germany). After background phase correction, noise filtering, and anti-aliasing, a 3D segmentation of the thoracic aorta was created based on a calculated 3D phase contrast MR angiogram. Velocity maximum intensity projections (MIPs, Fig.1) were used to visualize blood flow and quantify peak systolic velocities in 3 selected regions of interest; the ascending aorta (AAo), aortic arch (arch), and descending aorta (DAo). Three 2D planes were placed orthogonally at the AAo, arch, and DAo for time-resolved evaluation of flow (Fig.1).

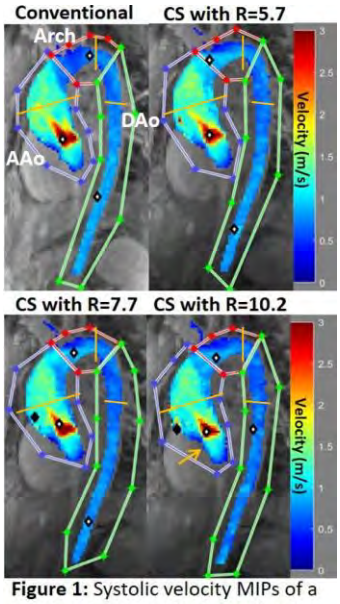

Figure 1: Systolic velocity MIPs of a representative patient showing 3 different regions and planes

Results: Total scan time for CS studies with R=5.7, 7.7, 10.2 and conventional 4D flow were 3.5±1.3, 2.9±1.1, 2.0±0.6, and 9.9±3.0 minutes, respectively. The MIPs were visually similar to the conventional 4D flow for R=5.7 and 7.7, but R=10.2 showed underestimation at the AAo in every patient (Fig.1). Peak flows at Arch and DAo were significantly lower for the CS studies when compared to the conventional 4D flows (Table 1). While CS studies significantly underestimated the peak flows and velocities, the percent changes were within 7%, 11% and 10% for R=5.7, 7.7, and 10.2 respectively. The average percent changes for the hemodynamic parameters were -3.3%, -6.7%, and -4.8% for R=5.7, 7.7, and 10.2 respectively. Time-averaged flow curves showed a similar pattern, with underestimation in CS 4D flows (Fig. 2).

		Conventional	R=5.7	p value	R=7.7	p value	R=10.2	p value
Peak Velocity (m/s)	AAo	1.9±0.8	1.8±0.8	0.10	1.7±0.8	0.01	1.7±0.7	0.04
	Arch	1.0±0.4	0.9±0.4	0.15	0.9±0.3	0.15	0.9±0.3	0.01
	DAo	1.2±0.7	1.1±0.5	0.79	1.0±0.4	0.04	1.1±0.4	0.63
Peak Flow (mL/s)	AAo	420±174	413±138	0.78	401±150	0.35	411±145	0.73
	Arch	241±82	225±75	0.02	218±74	0.02	224±80	0.02
	DAo	233±74	218±66	0.04	205±60	0.00	207±62	0.00
Net Flow (mL/cycle)	AAo	91±33	90±28	0.87	90±32	0.84	91±26	0.97
	Arch	51±18	47±16	0.06	46±15	0.06	49±18	0.13
	DAo	48±18	46±13	0.30	44±13	0.12	45±15	0.16

Table 1: Average hemodynamic parameters for conventional and CS 4D flow

Discussion: This study demonstrates the clinical feasibility of a highly accelerated CS 4D flow protocol in patients with aortic disease. CS 4D flow at R=10.2 reduced the scan time by 80%, with under 10% underestimation of flow values and is recommended for further investigations. This study was limited by a small sample size with a heterogeneous disease profile. Future investigations will include CS 4D flow studies on larger and homogenous cohorts using different regularization weights for improved quantitative agreement between the two methods. **References:** [1] Ma et al. Magn Reson Med. 2019

Optimisation of Technical Factors for Contrast Enhanced MRA for Thoracic Outlet Syndrome

Lirong Yin, Dr Sivanathan Chandramohan
Department of Diagnostic Radiology, Singapore General Hospital, Singapore
e-mail: yin.li.rong@sgh.com.sg

Purpose

Performing MRA for thoracic outlet syndrome is normally very challenging which is also made difficult by imaging in 2 different arm positions. We aim to present the institution's current practice, and to propose a standardised protocol, with optimised technical factors to ensure the reproducibility of contrast enhanced 3D MR angiography for thoracic outlet syndrome (TOS) .This will improve workflow efficiency and improve patient's experience.

Methods

All our cases are performed on 3T machine (Magnetom Skyra, Erlangen, Germany).

Thoracic outlet contrast enhanced 3D MR Angiography Protocols

Pulse Sequence	Slice Thickness(mm)	TR/TE(ms)	Voxel Size(mm)	Flip Angle	No of Excitations	Time To Acquisition (s)	iPAT factor	Bandwidth(Hz/pixel)
FLASH 3D	0.9	3.13/1.13	0.9x0.9x0.9	20	1	16	4	590

Results

In this poster will show how to optimize the following factors, flow rate and time of injection. signal-to-noise ratio (SNR) , temporal resolution and spatial resolution. Time constraints given by arrival of contrast and breath-hold capabilities of patients, also means that a delicate balance between speed and resolution has to be obtained.

Conclusion

An improved scan protocol and parameters would enable, improved delineation and greater understanding of the complex and dynamic thoracic outlet anatomy. Additionally, patients who presented with such symptoms, may find it difficult to stay still while performing the procedure. It is therefore crucial that the technical factors are optimised to ensure completion of study, efficiency of scan time and most importantly, patient's experience.

References

1 .Ersoy H, Steigner ML, Coyner KB, et al. Vascular thoracic outlet syndrome: protocol design and diagnostic value of contrast-enhanced 3D MR angiography and equilibrium phase imaging on 1.5- and 3-T MRI scanners. AJR Am J Roentgenol. 2012;198:1180–1187. doi: 10.2214/AJR.11.6417.
2 . Raptis, C., Sridhar, S., Thompson, R., Fowler, K., Bhalla, S. Imaging of the patient with thoracic outlet syndrome. *RadioGraphics*. 2016;36:984–1000
3. Molina JE, D'Cunha J. The vascular component in neurogenic-arterial thoracic outlet syndrome. *Int J Angiol*. 2008 Summer;17(2):83-7. PubMed PMID: 22477393; PubMed Central PMCID: PMC2728415.

Non-Contrast-Enhanced Abdominal MRA at 3T using Velocity-Selective Pulse Trains

Dan Zhu[1,2], Wenbo Li[2,3], Dapeng Liu[2,3], Guanshu Liu[2,3], Farzad Sedaghat[2], Yigang Pei[2,3,4], Taehoon Shin[5,6], and Qin Qin[2,3]
[1]Biomedical Engineering, Johns Hopkins School of Medicine, [2]Radiology, Johns Hopkins University School of Medicine, [3]Kirby Center, Kennedy Krieger Institute, [4]Radiology, Xiangya Hospital, Central South University, [5]Division of Mechanical and Biomedical Engineering, Ewha Womans University, [6]Department of Medicine, Case Western Reserve University

Purpose: We aim to achieve 3D non-contrast-enhanced abdominal arteriography with a large FOV utilizing velocity-selective (VS) pulse trains [1-4] at 3T.

Methods: The pulse sequence diagram is displayed in Fig. 1a. A VSS pulse train was placed right before acquisition modules to suppress static tissue. An adiabatic spatially selective inversion (SSI) pulse or a velocity-selective inversion (VSI) pulse train was applied with inversion delays to null static tissue background and venous signal. Fig. 1b) and 1c) show the VS profiles of VSI and VSS module respectively and their parameters are listed in Table 1. Velocity-encoding gradients were applied along 45° between left to right and foot to head direction. When inversion pulses were not applied, the VSS module alone does not separate arterial from venous blood. Respirational triggering was utilized in this sequence.

Experiments were performed on a 3T Philips scanner using a 32-channel chest array for reception. Comparisons of VSS-only angiography, SSI+VSS and VSI+VSS arteriography were conducted on 9 healthy subjects (45±15 yrs. 4 females). The acquisition parameters for the 3D bSSFP module of a coronal slab are: TR/TE= 4.7/2.2ms, Resolution=1.4(FH)×1.4(LR)×2.0(AP)mm, FOV=300(FH)×400(LR)×120(AP)mm, BW=1330.3Hz, TFE factor=70, Compressed Sensing (CS) factor=8. Delay time after SSI and VSI modules were 1200 and 700ms respectively. Total acquisition times were 3-4 minutes depending on breathing periods. SSI slabs were placed on an image slab and extended 10cm toward foot direction.

Relative contrast ratios were analyzed as (artery signal – tissue signal) / artery signal. Four circular ROIs of arteries were manually drawn on abdominal aorta or iliac arteries at hepatic, renal, aortic bifurcation and iliac bifurcation levels. Background tissue ROIs were drawn on liver (for hepatic level), kidney (for renal level, right and left averaged), and the area below aorta bifurcation (for aortic bifurcation and iliac bifurcation levels).

Results: MIPs of VSS, SSI+VSS and VSI+VSS images of 2 subjects are demonstrated in Fig. 2 as examples. Arterial, venous and portal system could be identified in VSS prepared angiography. Arteriography with SSI/VSI+VSS sequences suppresses venous and portal system and enhances the arterial system. SSI+VSS provides better arterial details (e.g. small branches of renal arteries) while VSI+VSS preserves distal arteries (e.g. iliac arteries).

Averaged relative contrast ratios of major abdominal arterial segments are compared in Fig. 3. VSS shows about 0.60-0.65 artery to tissue contrast at all levels except a lower contrast of 0.38 at the hepatic level. SSI+VSS and VSI+VSS displayed comparable contrast of 0.58-0.75 at hepatic, renal and aortic bifurcation levels. At the iliac bifurcation, SSI+VSS yielded much lower contrast than VSI+VSS, 0.15 vs 0.43, reflecting the benefit of the VSI preparation for the distal branches.

Discussion: The feasibility of 3D abdominal VS-MRA sequences utilizing advanced VSS pulse trains for background tissue suppression and SSI or VSI modules for artery-vein separation was evaluated at 3T for large spatial coverage. The SSI prepared method is inflow based and thus could be hampered by slow flow velocity. The VSI based approach was less sensitive to slow arterial inflow and demonstrated better performance on distal part of abdominal arterial branches.

References: [1]Shin T, et.al. MRM 2013;69:p1268; [2] Shin T, et.al. MRM 2013;70:p1229; [3] Qin Q, et.al. MRM 2016;75:p1232; [4] Li W, et.al. MRM 2018;79:p2014;

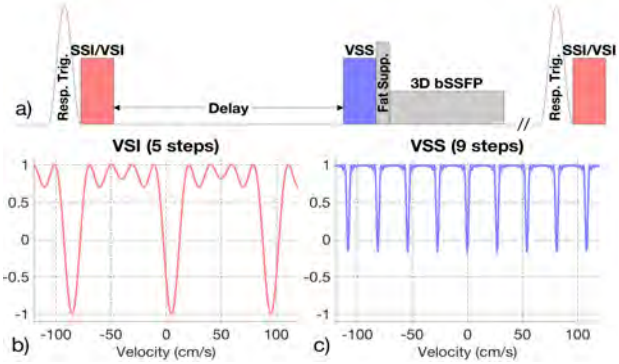

Figure 1: a) Arteriography sequence with SSI/VSI and VSS modules, and velocity-selective profiles of b) VSI and c) VSS modules.

	T_{vs} (ms)	N_{step}	T_{step} (ms)	T_{ramp} (ms)	T_G (ms)	G_{max} (mT/m)	Refocusing Pulses	V_c (cm/s)	FOS (cm/s)
VSS	99	9	11	0.2	0.5	29	Block	-3/3	27
VSI	55	5	11	0.2	0.5	8.75	Block	-13/23	90

Table 1: velocity-selective pulse parameters

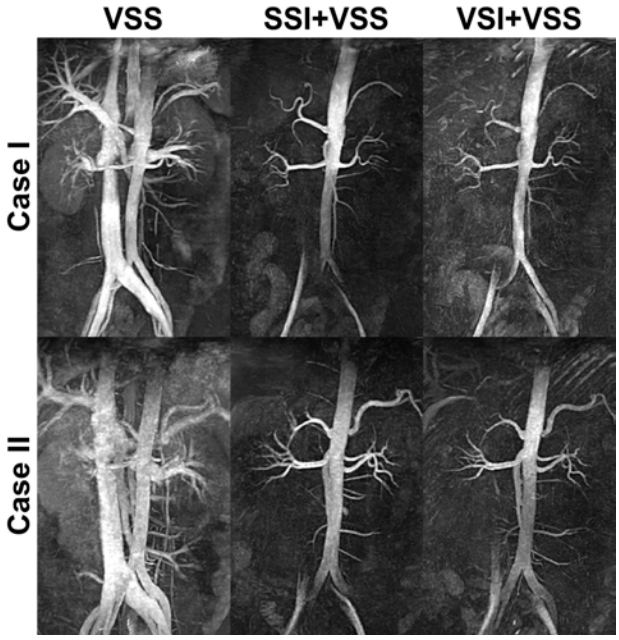

Figure 2: MIP Images of 2 subjects: I) 58 year-old female and II) 33 year-old male.

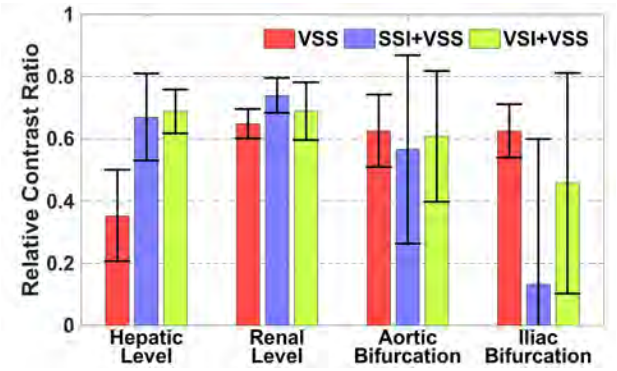

Figure 3: Relative contrast ratios of major arteries using VSS, SSI+VSS and VSI+VSS scans.

The assessment value of plaque enhancement load of multiple cerebrovascular beds in new cerebral infarction based on 3D MR vessel wall imaging

Bin Cui, Zhiqun Wang, Weimin Zheng.

Department of Radiology, Peking university aerospace clinical college of medicine, Beijing, China

Purpose: Intracranial and extracranial atherosclerosis is the main cause of ischemic stroke with a high recurrence rate. Due to the influence of blood flow reserve, collateral circulation and other factors, the stenosis degree of vessels in a single bed can ‘t directly predicts the occurrence of ischemic events. To investigate the relationship between contrast enhancement of atherosclerotic plaques in multiple cerebrovascular beds and acute cerebral infarction using 3D MR vessel wall imaging.

Methods: All the patients with ischemic stroke underwent 3D MR vessel wall imaging for multi-vascular beds of intracranial and extracranial carotid arteries (MAGNETOM Skyra, Siemens, Erlangen, Germany, 20-channel head coil). The examination was performed using precontrast and postcontrast 3D T1-weighted imaging-SPACE (3D T1WISPACE) sequence. The following sequence parameters were selected: TR/TE=900/15ms, field of view (FOV)=170×170mm^2, slice thickness =0.53mm, and voxel size=0.5×0.5×0.5mm^3. According to the DWI signal, the patients were divided into two groups of new and old cerebral infarction. The numbers of plaques (NP) on multiple cerebrovascular beds (intracranial, extracranial, total of intracranial and extracranial segmental) were computed and compared between the two groups. The plaque enhancement score (PES) was calculated according to no enhancement (0 points), mild enhancement (1 point) and obvious enhancement (2 points). Plaque enhancement rate ((PER, %) was calculated according to the ratio of plaque enhancement score/number of plaques. The correlation between plaque characteristics and the presence of new infarcts was measured by using logistics regression analysis and the sensitive indexes to differentiate the two groups were identified by receiver operating characteristic curve (ROC) analysis.

Results: A total of 157 patients (111 males, mean age 54.36±12.95 years) were enrolled, including 75 patients with new infarcts and 82 patients with old infarcts. A total of 1,106 plaques were found, including 665 intracranial plaques and 441 extracranial plaques. The NP, PES and PER of multi-vascular beds were significantly different between the two groups. Logistic regression analysis revealed that the value of total PES (OR, 1.23; 95% CI, 1.09-1.38) and intracranial PER (OR, 2.53; 95%CI, 1.10-5.85) were significantly correlated with the new infarction ($p<0.01$). In discriminating the two groups, the combined total PES and intracranial PER had higher area-under-the-curve (AUC=0.78) than that of single index, which reached sensitivity of 60% and specificity of 85% at cutoff value of 0.45.

Discussion and Conclusion: Previous analyses of vascular lesions in ischemic stroke were focused on the characteristics of single vessels, including the degree of stenosis, plaque composition, distribution and enhancement, which could not reflect the overall plaque load of multi-vascular beds lesions and further assess the severity of new infarcts of patients. In this study, the number, enhancement score and enhancement rate of plaques in the multi-vascular bed of patients with and without new cerebral infarction were retrospectively analyzed. It was found that the number, enhancement score and enhancement rate of plaques in the multi-vascular bed of patients with new cerebral infarction were significantly higher than those in the group without new cerebral infarction. The intracranial plaque enhancement rate and the overall plaque enhancement score were significantly correlated with the judgement of new ischemic lesions, suggesting that the intracranial and extracranial artery plaque load, especially the enhancement load, may be an effective indicator to judge the severity of atherosclerotic cerebral infarction.

References:1. Li D, Dai W, Cai Y, et.al. Atherosclerosis in stroke-related vascular beds and stroke risk: A 3-D MR vessel wall imaging study. Annals of Clinical and Translational Neurology, 5(12), 1599–1610.

2. Xu Y, Yuan C, Zhou Z, et al. Co-existing intracranial and extracranial carotid artery atherosclerotic plaques and recurrent stroke risk: a three-dimensional multicontrast cardiovascular magnetic resonance study. J Cardiovasc Magn Reson. 2016 Dec 2;18(1):90.

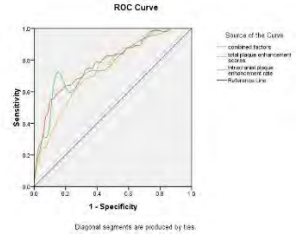

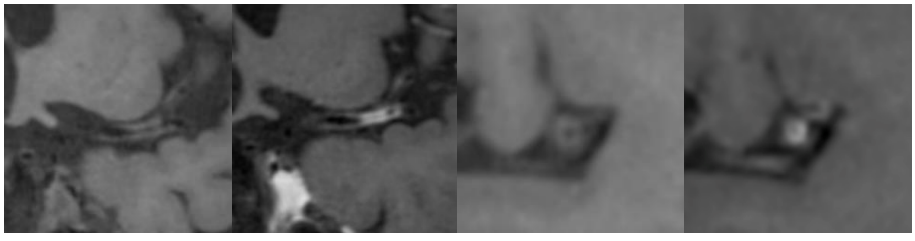

precontrast and postcontrast 3D T1WISPACE of left MCA(COR and TRA)

Validation of Hemodynamic Analysis using High Spatial Resolution 3-dimentional Phase-Contrast Magnetic Resonance Imaging with 7-tesla MR Scanner

Shunsuke Tajima[1,2], Haruo Isoda[3,1], Masaki Fukunaga[4], Yoshiaki Komori[5], Roshani Perera[1], Takashi Mizuno[2], Norihiro Sadato[4], Shinji Naganawa[6]

[1]Department of Radiological and Medical Laboratory Sciences, Nagoya University Graduate School of Medicine, Nagoya, Japan, [2]Department of Medical Technology, Nagoya University Hospital, Nagoya, Japan, [3]Brain & Mind Research Center, Nagoya University, Nagoya, Japan, [4]Department of System Brain Science, National Institute for Physiological Sciences, Okazaki, Japan, [5]Department of Research and Collaboration, Siemens Healthcare K.K., Tokyo, Japan, [6]Department of Radiology, Nagoya University Graduate School of Medicine, Nagoya, Japan

Purpose: Hemodynamics play an important role in intracranial aneurysm initiation, growth and rupture. Magnetic resonance fluid dynamics (MRFD) and computational fluid dynamics (CFD) are used to evaluate hemodynamics of intracranial arteries [1]. Previous study demonstrated that 3-dimentional (3D) cine phase-contrast (PC) magnetic resonance (MR) [2] needs to be performed with high spatial resolution in order to perform for small vessels such as intracranial arteries [3]. We expect that we will be able to obtain 3D PC MR with high signal to noise ratio (SNR) and high spatial resolution using 7-tesla (T) MR scanner, and to perform precise MRFD for intracranial artery. The purpose of this study was to evaluate high spatial resolution MRFD using 7T MR scanner in comparison to 3T MR scanner.

Methods: This study was approved by our institutional review board. An internal carotid-posterior communicating artery aneurysm silicone model and 10 healthy volunteers who underwent 3D PC MR (voxel size: 3T, 0.5 mm; 7T, 0.35mm and 0.5mm) and 3D time of flight MR angiography using 3T MR scanner and 7T MR scanner were included in the study. After performing MRFD and CFD analyses hemodynamics obtained from MRFD in each MR system were compared with hemodynamics obtained from CFD as a reference. 3D velocity vector map, correlation coefficients of velocity magnitude, angular similarity index (ASI) [4] of velocity vector and magnitude similarity index (MSI) [4] of velocity vector were selected as evaluation items.

Results and discussion: In the comparison using the aneurysm model, a noisy appearance of velocity vectors near vascular wall was seen in MRFD of 3T MR scanner, but these were not seen in MRFD of 7T MR scanner. The 3D velocity vector map of MRFD of 7T MR scanner appeared to be similar to those of CFD in view of the velocity vector could be accurately measured with high SNR at the low flow velocity region along the vascular wall. In the comparison using the aneurysm model and healthy volunteers, each evaluation item obtained by 7T was higher than those by 3T. In the comparison of healthy volunteers, statistically significant differences were shown in ASI and MSI ($p<0.05$). It was estimated that the velocity vectors could be measured with high accuracy using high spatial resolution and high SNR 7T MR scanner.

Conclusion: 7T MR scanner is superior to 3T MR scanner in achieving high spatial resolution MRFD.

Acknowledgement: This research has been carried out as a collaborative research project between National Institute for Physiological Sciences and Nagoya University.

Reference:

1) Isoda H, et al. Neuroradiology, 52, 913-920, 2010.
2) Markl M, et al. J Magn Reson Imaging.17, 499-506, 2003.
3) Fukuyama A, et al. Magn Reson Med Sci. 2017; 16: 311-316
4) Berg P, et al. J Biomech Eng. 2014;136(4).

Transfer Learning Produces Better Reconstruction of Highly-Accelerated, Single-shot LGE Images than Conventional Deep Learning with Limited Training Data

Daming Shen[1, 2], Hassan Haji-Valizadeh[1, 2], Sushobhan Ghosh[3], Daniel Kim[2]

[1] Biomedical Engineering, Northwestern University, Evanston, Illinois, United States
[2] Department of Radiology, Northwestern University, Chicago, Illinois, United States
[3] Department of Computer Science, Northwestern University, Evanston, Illinois, United States

Purpose: To determine whether transfer learning (TL) approach is capable of leveraging access to a large database of similar image types and produce better reconstruction of highly-accelerated single-shot late gadolinium enhanced (LGE) images than conventional deep learning.

Methods: We tested our hypothesis on limited LGE data sets with 1.6 mm x 1.6 mm spatial resolution obtained from 12 patients (mean age = 51.1 ± 20.3 years; 6 females) who were scanned on 1.5T scanners (Aera and Avanto, Siemens). Image reconstruction was performed on a GPU workstation equipped with Pytorch. As shown in Figure 1, we trained a deep learning (DL) network (residual U-Net (1) for complex data, layer depth = 3, 64 features on the first layer) using prospectively obtained 2-shot (42 radial spokes per shot), breath-held LGE data sets (101 images, with compressed sensing [CS] (1) reconstruction, total variation as the sparsifying transform) from 12 patients as reference and retrospectively undersampled 1-shot, zero-filled data (42 rays per image) as input. For TL, we pre-trained the U-Net with existing 5,811 (42 rays per frame) zero-filled and the corresponding CS reconstructed (total variation as the sparsifying transform) real-time cine (3) images (which have similar image content) from 19 patients (mean age = 66.1 ± 12.0 years; 8 females) as input/output pairs. For testing, we prospectively obtained 1-shot LGE (42 rays per image) data sets from 10 other patients (mean age = 56.5 ± 16.2 years; 6 females) and compared TL to CS and DL reconstructed images.

Results: As shown in Figure 1, TL produced sharper images and fewer residual artifacts than DL. For edge sharpness, DL (2.3 ±0.4 mm) was significantly ($p<0.05$) worse than TL (1.8 ±0.4mm) and CS (1.9 ± 0.4mm). For CNR, CS (15.9 ± 7.6) was significantly ($p<0.05$) worse than TL (33.5 ± 18.8) and DL (27.0 ± 15.7). The reconstruction time for DL and TL (0.7 ± 0.0s) was significantly ($p <0.05$) lower than CS (49.6 ± 1.1s).

Discussion: This study demonstrates a TL approach to rapidly reconstruct 1-shot LGE with better image quality than a conventional DL approach and higher reconstruction speed than CS, thereby making it a good fit for clinical translation.

References: [1] Ronneberger O, et. al. Springer 2015; [2] Lustig M, et. al. Magn Reson Med 2007; [3] Haji-Valizadeh H, et. al. Magn Reson Med 2018.

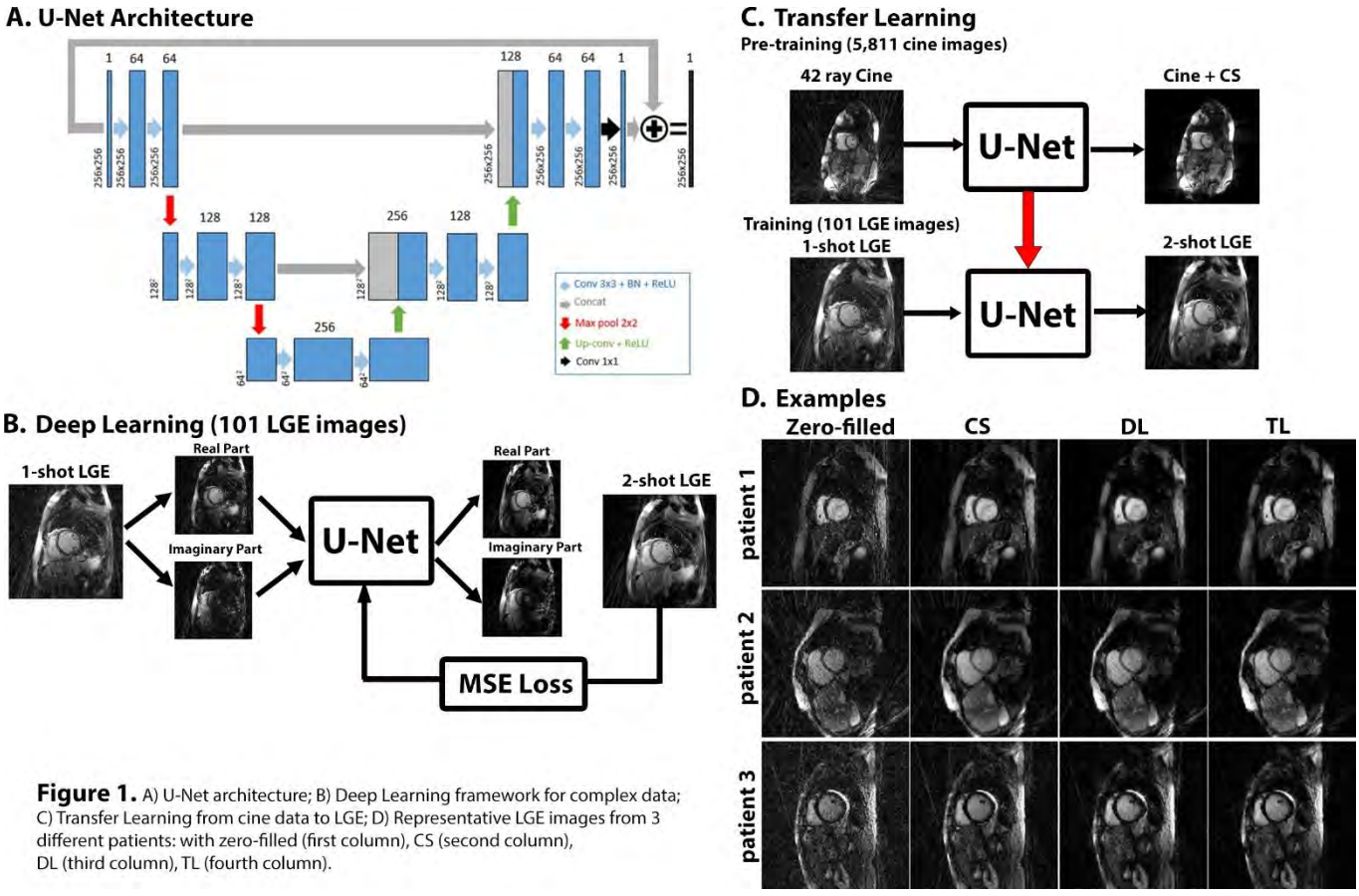

Figure 1. A) U-Net architecture; B) Deep Learning framework for complex data; C) Transfer Learning from cine data to LGE; D) Representative LGE images from 3 different patients: with zero-filled (first column), CS (second column), DL (third column), TL (fourth column).

Wall Shear Stress Quantification in the Context of 4D Flow MRI Simulation on Carotids

Sébastien Levilly[1], Jérôme Idier[1], Félicien Bonnefoy[2], David Le Touzé[2], Perrine Paul-Gilloteaux[3], Saïd Moussaoui[1], Jean-Michel Serfaty[4]

[1]Laboratoire des Sciences du Numérique de Nantes (LS2N), 1 rue de la Noë, BP 92101, 44321 Nantes Cedex 3, France
[2]Laboratoire de recherche en Hydrodynamique, Énergétique, et Environnement Atmosphérique (LHEEA), 1 rue de la Noë, BP 92101, 44321 Nantes Cedex 3, France
[3]CNRS, SFR Santé François Bonamy UMS 3556, IRS-UN, 8 quai Moncousu, BP 70721, 44007 Nantes Cedex 1, France
[4]UF Imagerie Cardiaque et Vasculaire Diagnostique, CHU de Nantes, France

Purpose

4D PC-MRI allows spatio-temporal imaging of the blood-flow velocity in a region of interest during a cardiac cycle [1]. However, the resolution and the signal-to-noise ratio (SNR) are limited by acquisition constraints. In these conditions, the quantification of biomarkers such as the wall shear stress (WSS) is a challenging problem. Then, it can be tackled by considering some a priori information such as the morphology [2] and the smoothness [3]. The WSS is a local phenomenon which can be studied locally [3] while other strategies aim to regularize the whole domain [2] before computing the WSS. The proposed method addresses the problem locally by modeling the vessel wall and the velocity field near a point of interest which can be used to compute the WSS.

Methods

We propose a solution in four steps starting with the modeling of the vessel wall by a parametric surface centered on the point of interest. We then propose a parametric velocity model for which the velocity cancels at any point of the surface. This velocity model is set with a trivariate second-order polynomial. The velocity model for a point of interest can be used to compute the WSS on this point and all the segmentation points in the neighborhood. Consequently, the multiple estimations of the WSS on a given point can be used to get the WSS along with a confidence index.

Results & Discussion

This work has been tested on synthetic MRI data using, as velocity ground truth, four carotids CFD simulations kindly provided by the CREATIS Laboratory. Our method is compared to the solution proposed by Potters et al. (2014) [3] which is currently used in many clinical studies [4] and can be considered as a state of art reference. Our results present significant advantages in term of quantification and correlation for SNR ranges corresponding to 3T and 7T MRI with a resolution of 1 mm ISO or 0.7 mm ISO. Different strategies are studied to enhance the algorithm robustness such as considering more a priori information.

References

[1] M. Markl, A. Frydrychowicz, S. Kozerke, M. Hope and O. Wieben, « 4D flow MRI », *J. Magn. Reson. Imaging*, vol. 36, n°5, pp. 1015-1036, 2012.

[2] J. Sotelo, J. Urbina, I. Valverde, C. Tejos, P. Irarrázaval, D. E. Hurtado and S. Uribe, « Quantification of wall shear stress using a finite-element method in multidimensional phase-contrast MR data of the thoracic aorta », *J. of Biomechanics*, vol. 48, n°10, pp. 1817-1827, 2015.

[3] W. Potters, P. van Ooij, H. Marquering, E. vanBavel and A. J. Nederveen, « Volumetric arterial wall shear stress calculation based on cine phase contrast MRI. »», *J. Magn. Reson. Imaging*, vol. 41, n°2, pp. 505-516, 2014.

[4] P. van Ooij, M. Markl, J. D. Collins, J. C. Carr, C. Rigsby, R. O. Bonow, S. C. Malaisrie, P. M. McCarthy, P. W. M. Fedak, A. J. Barker, « Aortic valve stenosis alters expression of regional aortic wall shear stress: new insights from a 4-dimensional flow magnetic resonance imaging study of 571 subjects », *J. Am. Heart Assoc.*, vol. 6, n°9, 2017.

An *in vitro* and *in silico* validation study for PC MRI and derived bio-markers

Marco Castagna[1,2], Sébastien Levilly[3], Perrine Paul-Gilloteaux[1], Félicien Bonnefoy[2], Jérôme Idier[3], Jean-Michel Serfaty[1,4], David Le Touzé[2]
[1]Institut du thorax, INSERM UMR 1087, CNRS UMR 6291, Nantes, France
[2]LHEEA research department, École Centrale Nantes, Nantes, France
[3]LS2N, École Centrale Nantes, Nantes, France
[4]Imagerie cardiaque et vasculaire diagnostique, CHU Nantes, Nantes, France

Purposes. Recently, the attention of physicians has focused on the employment of blood velocity derived biomarkers, such as *Wall Shear Stress* (WSS), to quantify cardiovascular risks for clinical decision making. These biomarkers can be estimated from *Phase-Contrast MRI* (PC MRI) measurements, but clinical applications are limited by their spatial resolution [1]. The purpose of this work is to validate 2D and 3D PC MRI acquisitions with the employment of a *Mock Circulation Loop* (MCL). Velocity data in the MCL were measured with *Laser Doppler Velocimetry* (LDV) and compared with numerical results obtained through a *Computational Fluid Dynamics* (CFD) study. Successively, LDV data were employed to validate 2D and 3D PC MRI velocity measurements, flow rate calculation, and WSS estimation.

Methods. The MCL is composed (Fig.1) by a pulsatile gear pump (a) (CardioFlow5000, Shelley Medical Imaging Technologies), connection pipes (b), a *Vascular Phantom* (VP) (c), which was designed as a squared PMMA channel (25x25x345 mm) to easily allow LDV measurements, a reservoir (d), and a *Blood Mimicking Fluid* (BMF), which was composed by a 0.6:0.4 (in weight) water-glycerol mixture (ρ = 1098 Kg/m^3, μ = 0.00345 Pa·s). During MRI investigations, a plastic box rounding the VP contained an agarose gel to simulate human tissues. Data were compared on a cross section located 265 mm downstream the VP inlet, and for three steady flow rates Q = 15, 50, 100 ml/s. LDV was performed with a Nd:YAG laser system (e) (fp50, ILA Gmbh), point spacing was 0.4 mm, and samples were acquired for 30 s. The mean of sample distribution was taken to be the point velocity. LDV velocity profiles were filtered with a *Locally Weighted Scatterplot Smoothing* and interpolated to fit MRI data sizes, with Matlab. Since VP Geometry was symmetrical, a Cartesian mesh of 431250 elements was generated (Star CCM+, Siemens) for one fourth of the whole VP volume to reduce computational time. Numerical data were obtained with a finite volume method (Star CCM+, Siemens), and interpolated to fit LDV data size. MRI campaign was carried out on a 1.5 T machine (Aera, Siemens). Voxel size (interpolated) and FOV were 1.22x1.22x6 mm and 150x300 mm for 2D, 2.22x2.22x2 mm and 288x319 mm for 3D. Acquisitions were performed with retrospective gating, velocity data were averaged over the 30 acquired phases. VENC was selected to keep Echo Time TE ≤ 4.8 ms [2] and to be as close as possible to VENC = 2V_{mean}, resulting in VENC = 16, 18, 30 cm/s for Q = 15, 50, 100 ml/s, respectively. Flow quantification for WSS and Flow rate was performed as Stalder et al. [3], with Matlab. Finally, data comparison was carried out with Pearson correlation coefficient ρ_{XY} and *Root Mean Squared Error* RMSE. For flow rate, a percentage error with the theoretical value Q is given.

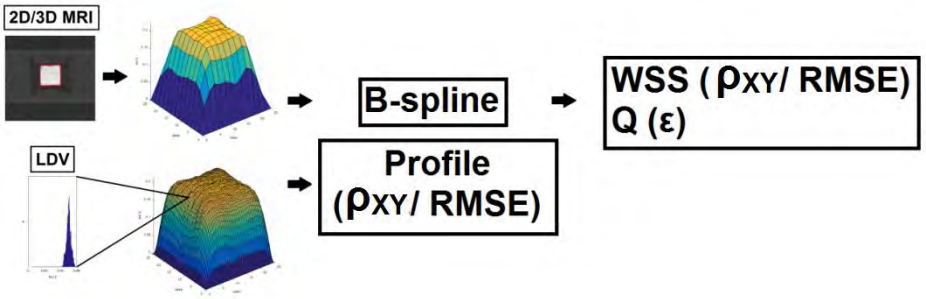

Results & discussion. LDV was highly correlated with CFD, ρ_{XY} = 0.984, RMSE = 0.005 (mean over Q), with 2D MRI (ρ_{XY} = 0.960, RMSE = 0.003), and with 3D MRI (ρ_{XY} = 0.958, RMSE = 0.002). Concerning WSS, LDV was more correlated with 2D (ρ_{XY} = 0.684, RMSE = 0.002) than with 3D (ρ_{XY} = 0.407, RMSE = 0.001). For flow rate, percentage errors [%] were ε_{15} = 12.96, ε_{50} = 1.86, ε_{100} = 3.06 and ε_{15} = 6.14, ε_{50} = 2.68, ε_{100} = 0.60 for 2D and 3D MRI respectively. Generally, data showed a good agreement, even if for WSS LDV-3D MRI correlation was weaker, probably for its poorer resolution. Future developments of the present study include a more thorough statistical analysis of data here presented and a pulsatile flow campaign with the same MCL configuration.

References

1. Dyverfeldt et al. *4D flow cardiovascular magnetic resonance consensus statement*. JCMR 17:72-91 (2015)
2. O'Brien et al. *MRI Phase Contrast velocity and flow errors in turbulent stenotic jets.* J Magn Reson Imaging 28:210-218 (2008)
3. Stalder et al. *Quantitative 2D and 3D Phase Contrast MRI: Optimized analysis of blood flow and vessel wall parameters.* Magn Reson Med 60:1218-1231 (2008)

Methemoglobinemia and T1 Contrast

Seong-Eun Kim[1], Ronald Day[2], Matthew Alexnader[1],
Dennis L Parker[1], and J Scott McNally[1]

[1]UCAIR, Department of Radiology and Imaging Sciences, [2]Department of Pediatrics, University of Utah,

Purpose: Gadolinium is an excellent contrast agent for MRI. However, there are increasing concerns about its safety[1]. One potential alternative agent is endogenous intracellular methemoglobin (MetHb)2, a paramagnetic molecule that is normally present in small amounts in our blood cells[3]. Intracellular levels of MetHb can be increased by exposing blood to nitric oxide or sodium nitrite[4]. The previous in vitro studies suggest that an intracellular MetHb level less than 10% sufficiently increases the T1-weighted signal of blood to be an effective contrast agent[2,5]. The purpose of this work is to evaluate the change of T_1 of blood according to a transient increase in intracellular MetHb in an in vivo animal model.

Method: 2D single shot(ss) EPI sequence was modified to acquire images of the slice of interest at different inversion recovery times after one nonselective inversion recovery pulse application[6]. T_1 was measured by fitting the signal recovery curve. All of MRI studies were performed on a 3T MRI system. We performed two animal MRI studies, a canine genetic model, and a rabbit MetHb induction model. 3D TOF and 3D MPRAGE images were acquired from a CYB5R deficient dog with a MetHb level of 19% and 4%, before and after treatment with methylene blue, respectively. For the MetHb induction study, a nitric oxide gas was inhaled by a rabbit until 12% level of MetHb was reached. The levels of oxyhemoglobin, carboxyhemoglobin and MetHb in blood were monitored by pulse oximetry. Our 2D ss EPI with IR sequence was performed on a rabbit before and after MetHb induction. T_1 maps were created and displayed using homemade software.

RESULTS: Fig 1 shows results from a canine hereditary methemoglobinemia. 3D TOF(a,b) and MPRAGE(c,d) images show change in venous signal before and after rescue with methylene blue. TOF signal intensity of paraspinal veins with MetHb levels of 19% and 4% were 1.64±0.14 (a) and 1.09±0.11(b), respectively. MPRAGE signal intensity of extra jugular veins were 1.54±0.07(c) and 0.87±0.06 (d), respectively. Fig 2 shows T_1 map before and after MetHb induction. The yellow arrows on T_1 maps show that the elevation of MetHb level after nitric oxide inhalation can be quantified by the difference in T_1 values measured from baseline and MetHb induction. Mean T_1 values of extra jugular veins with baseline and MetHb level of 12% were measured as 1576±280 ms(a) and 870±160 ms(b), respectively.

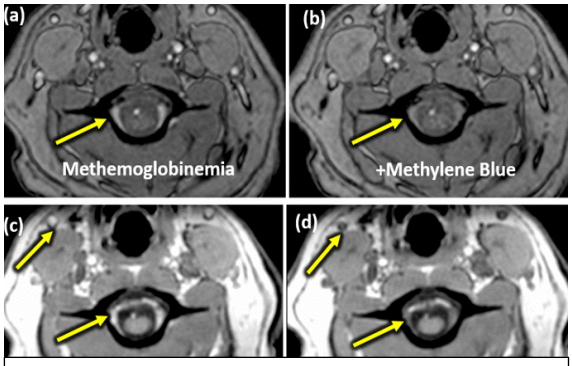

Fig 1 Canine Genetic Model with rescue

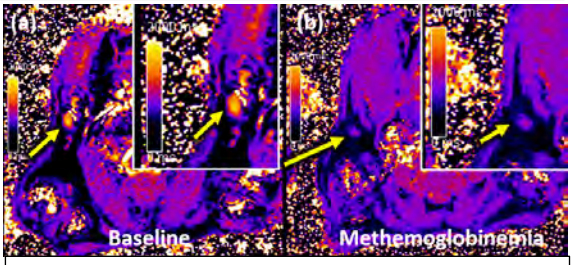

Fig 2 Rabbit MetHb Induction Model

DISCUSSION: In our canine model, there was a noticeable difference in intravascular signal intensity on T1-weighted sequences (Fig 1). There was also evidence of tissue enhancement with higher MetHb levels. Our rabbit model demonstrated that the elevation of MetHb level resulted T_1 shortening (Fig 2). T_1 relaxation time can be used to assess the localization and amount of MetHb level directly and with high sensitivity. The FDA has approved nitric oxide gas for the treatment of newborns with pulmonary hypertension and sodium nitrite for cyanide poisoning. However, MetHb decreases the oxygen carrying capacity of blood. As a result, high levels of intracellular metHb are not safe for individuals who cannot tolerate a transient decrease in oxygen[7]. Therefore, we need to investigate the safety and efficacy of a transiently induced increase in intracellular MetHb. We also need to further characterize time course of T_1 change and to determine location of T_1 signal changes on venous vs. arterial or intravascular vs. extravascular.

REFERENCES:

1. Grobner T. Nephrol Dial Transplant. 2006;21(4):1104-8.
2. Umbreit J. Am J Hematol. 2007;82(2):134-44
3. Day RW, J Cardiovasc Magn Reson. 2005;7(4):667-9.
4. Wright RO, et al. Ann Emerg Med. 1999;34(5):646-56
5. Jaffey JA, et al. J Vet Intern Med. 2017;31(6):1860-5.
6. Guo JY, et al. Med Phys, 2005:32(4), 1083-93.
7. Thunberg CA, et al. Ann Card Anaesth. 2015 Jul-Sep; 18(3): 394–402

AI based semi-automated quantification of left atrial flow dynamics in atrial fibrillation

Justin Baraboo[1,2], Liliana Ma[1,2], Haben Berhane[3], Michael Scott[1,2], Patrick McCarthy[4], Daniel C. Lee[5], Rishi Arora[5], Philip Greenland[5], Rod Passman[5], Daniel Kim[1,2], Michael Markl[1,2]
[1]Northwestern Biomedical Engineering, [2]Northwestern Radiology, [3]Lurie Children's Hospital of Chicago, [4]Northwestern Cardiothoracic Surgery, [5]Northwestern Medicine, Cardiology

Purpose: Atrial fibrillation (AF) is the most common cardiac arrhythmia and can result in thrombus formation in the left atrium, a leading cause of ischemic stroke. Clinical risk scores, such as CHADS-VASc[1], are the current standard for stroke risk stratification in AF; however, these systems are based in empirical clinical parameters and suffer from limited predicative power. Previous work has shown that left atrial (LA) and left atrial appendage (LAA) 3D blood flow dynamics, such as peak velocity or flow stasis, may be correlated with risk for atrial thrombus formation and thus stroke risk.[2] While 4D flow enables evaluation of time-resolved 3D hemodynamics, it is limited by insufficient blood-tissue contrast needed for accurate identification of the LA and LAA for subsequent volumetric analysis of atrial flow. We previously investigated registration of high contrast Gd-enhanced (CE) MR angiography (CE-MRA) to 4D flow data for optimized combination of flow (stasis, 4D flow) and more accurate anatomical information (CE-MRA).[3] Thus, the goal of this study was to use an AI to automatically segment the LA in 4D flow and CE-MRA for registration and evaluation of atrial hemodynamics.

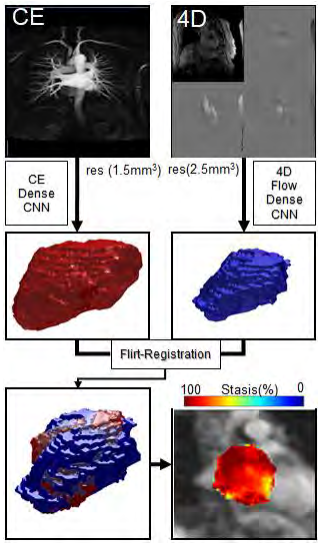

Figure 1: CE and 4D flow scans are segmented by AI and registered using FLIRT. Registered CE-MRA segmentation is used to calculate stasis.

Methods: 24 AF patients [age 66±8 years, 15 Male] underwent 4D flow MRI [PEAK-GRAPPA R=5, 2.4-2.7mm^3, 77 ms] with coverage of the left side of the heart as part of a clinical pulmonary vein mapping protocol prior to catheter ablation. This protocol included a CE-MRA [1.3-1.8mm^3]. A 3D phase contrast MRA was calculated from 4D flow data and used to manually segment the left atrium (Mimics, Materialise, Belgium). CE-MRAs were also segmented. CE scans missing part of the LA were excluded and not manually or AI segmented. Using the manual segmentations as ground truth, two distinct convolutional neural networks (3D hybrid U-Net[4]/DenseNet[5] design) were trained, one for 4D flow scans and the other for CE scans. Leave-one-out cross validation was used to maintain as much training data as possible. Dice index (DSC) was used to quantify segmentation accuracy. After segmentation, the CE-MRA LA was registered to the 4D flow LA using FLIRT[6]. Flow analysis was then performed, calculating flow stasis by finding a percentage of voxels below 0.1 m/s and determining peak velocities, that is, the averaged top 5% of velocities[2] (**Fig 1**). Flow characteristics and LA volumes were compared between manual CE and 4D flow registrations and AI segmented CE and 4D flow registrations. CHADS-VASc scores were calculated for each patient.

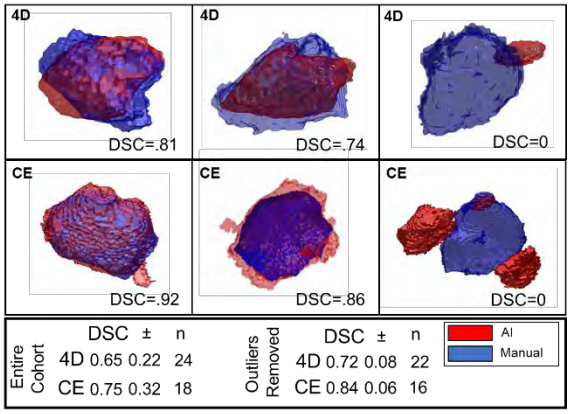

Figure 2: Manual (blue) and AI (red) segmentations of the LA for best, average, and worst scans. DSC scores are reported below for entire cohort and removal of two segmentations that failed to find the LA.

Results: AI segmentation results are shown for the entire cohort and excluding two failed segmentations (**Fig 2**). Stasis (Manual: 65±16, AI: 61±22%), peak velocities (.27±.05,.29±.06 cm/s), and LA volumes (148±58,120±60mL) were not found to be statistically different between manual and AI for CE to 4D registration by paired T-tests (lowest p>.14, n=18). Stasis values for manual and AI segmented, stratified by low risk (CHADS-VASc <2) and high risk (CHADS-VASc ≥2) are shown and are not statistically different between methods (p>.29, p>.60 respectively) (**Fig 3**).

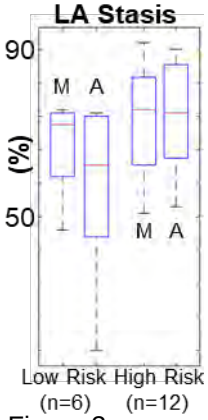

Figure 3. (**M**)anual and (**A**)I LA stasis box plots for low risk and high risk CHADS-VASc scores.

Discussion: AF analysis is challenging due to irregular heartbeats and respiratory motion. This has previously necessitated two manual segmentations. AI segmentations were successful in finding the LA in all but two scans, despite limited training data. CE segmentation had a higher DSC scores due to higher quality data. Registration of the CE to the 4D flow allowed the final region to preserve LA volume better. Overall, AI performed similarly to manual analysis for broad flow quantifications and LA volume, although the 4D flow, alone, often underestimated the LA volume. Future work will expand this data set and training mechanisms to better preserve LA volume. Furthermore, networks will be developed to segment the LAA and quantify its flow.

References 1. T. Van Staa *J Thromb Hemost* doi: 10.1111/j.1538-7836.2010.04085.x. 2.M. Markl *Investigative Radiology* 2016 doi: 10.1097/RLI.0000000000000219. 3.L. Ma *SCMR Conf* 2019. 4.C. Ozgun *MICCAI* 2016 doi: 10.1007/978-3-319-46723-8_49, 5.G. Huang *IEEE CVPR.* 2016. arXiv 1608.06993. 6.M. Jenkinson *NeuroImage* 2002 doi: 10.1006/nimg.2002.1132.

In vitro 4D Flow MRI high and low velocity encoding strategies corroborate in vivo 4D flow hemodynamics in the false lumen of type B aortic dissection patients

Sylvana García-Rodríguez, PhD; Bradley D. Allen, MD; Philip Corrado, Christopher J. François, MD
Department of Radiology, University of Wisconsin-Madison

Purpose: The complex interplay of anatomy and hemodynamics of type B aortic dissection (TBAD) has been increasingly studied with 4D Flow MRI. Advanced hemodynamic characterization of the false lumen (FL) with 4D Flow has the potential to help risk stratify these patients, but varying pulse sequence parameters such as velocity encoding (VENC) may impact the accuracy and reproducibility of 4D flow measurements. In this pilot study, we sought to understand 1) differences in in vivo and in vitro FL hemodynamics using patient-specific 3D printed models, and 2) assess how VENC may influence this analysis.

Figure 1: TBAD MRA. Arrow: entry tear; *: FL.

Methods: Following an IRB-approved and HIPAA-compliant protocol, retrospective data from two patients (Subject 1, 55 year-old female; Subject 2, 40 year-old male) with TBAD were identified. *In vivo MRI*: PC VIPR 4D Flow MRI scanning (MR750, GE Healthcare, Waukesha, WI) was performed with parameters: 320 x 320 x 320 mm FOV (1.25 mm isotropic spatial resolution) and FA = 10. Subject 1: 1.5T scanner, TR/TE = 6.94/2.23, VENC = 120 cm/s. Subject 2: 3T system, TR/TE = 6.23/2.06, VENC = 250 cm/s. *Patient-Specific Models*: In vitro anatomical models were segmented (Mimics, Materialise; Leuven, Belgium) from MRA (Subject 1) and CTA (Subject 2) data to generate models for 3D printing. The geometries were hollowed and tubing connections were added at inlets (ascending aorta, AAo) and outlets (descending aorta (DAo) and main arteries). The two geometries were 3D printed to scale using selective laser sintering. *In vitro MRI:* Each physical model was connected to a pulsatile pump (BDC PD-1100, BDC Laboratories, Wheat Ridge, CO) that circulated water at a maximum input flow of 4 L/min, following a physiological flow waveform (35% systole, 60 bpm). In vitro 4D Flow MRI was performed on a 1.5T scanner (MR750, GE Healthcare, Waukesha, WI) with parameters: 320 x 320 x 320 mm FOV (1.25 mm isotropic spatial resolution), TR/TE = 6.72/2.82 ms, FA = 8, and scan time 10 minutes. For each model, two settings for velocity encoding (VENC) were used: 70 and 150 cm/s. *Velocity distribution*: Complex difference images of each 3D printed model and in vivo scan were used for segmenting the FL (Mimics). Mask coordinates were imported into a custom-developed Matlab tool and histograms of the FL velocity magnitude distribution were computed for each time step within the cardiac cycle. Peak systole was estimated from mid-AAo flow measurement (EnSight; CEI Inc, Apex, NC).

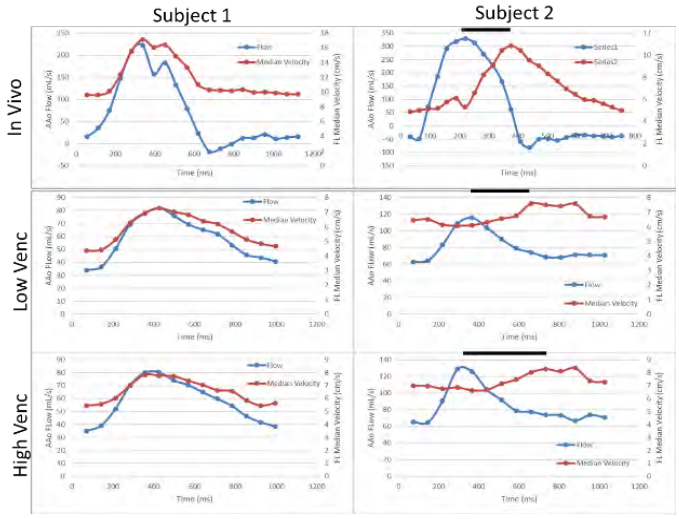

Figure 2: AAo Flow (blue, mL) and FL median velocity (red, cm/s) through the cardiac cycle (x-axis [ms]). Black line: peak-to-peak

Results: Subject 1 had a proximal DAo entry tear with FL outflow through both iliac arteries. Subject 2 had large mid-DAo entry tear with no FL outflow (Fig. 1). Both subjects ultimately required TBAD surgical repair (Subject 1: 2.2 years after initial imaging; Subject 2: within 1 week of initial imaging). Subject 1 had an average growth rate of 5 mm/yr and reached a maximal diameter of 60 mm in the DAo. Subject 2 had a maximal DAo diameter of 58 mm at the time of presentation. Peak median velocities in the FL and peak flow in the aorta were both reduced in the in vitro models relative to in vivo data, likely related, at least in part, to differences in flow rate between in vivo and in vitro conditions (Table). Interestingly, the peak-to-peak time difference between peak systole (from AAo peak flow) and peak median FL velocity was negligible in Subject 1, but ranged from 157 ms (in vivo) to 514 ms (in vitro high venc) in Subject 2. (Table, Fig. 2). Overall, these within-patient trends were consistent between in vivo and both flow states of the in vitro models, despite different absolute numbers.

		AAo Peak Flow (mL/s)	Peak Median Velocity (cm/s)	Peak-to-Peak Difference (ms)
Subject 1	In Vivo	328	17.1	0
	Low Venc	115	7.3	0
	High Venc	126	7.8	71
Subject 2	In Vivo	222	10.8	157
	Low Venc	82	7.6	294
	High Venc	81	8.4	514

Discussion: We have shown that in two patients with significantly different TBAD phenotypes, FL flow and velocity trends measured by 4D Flow MRI are similar in both in vivo and high and low VENC in vitro models. Moreover, we have observed that Subject 2, who required surgery at the time of presentation, had a peak-to-peak time lag between peak systole and FL peak velocities, while subject 1 had no peak-to-peak lag and did not require immediate surgery. These patterns were also observed in the models, despite the difference in in vivo and in vitro aorta material properties. It is not clear if this peak-to-peak delay is function of anatomy of the entry tear or size, location, and lack of FL outflow. Our limited sample size does not allow for firm conclusions; however, the data is compelling and suggests more work is needed to better understand relevant hemodynamic parameters, the impact of VENC settings, and the contribution of 3D printed models to optimize in vivo 4D Flow MRI acquisition and risk stratification in TBAD patients.

Regularization parameter optimization for intracranial 4D flow imaging with compressed sensing

Maria Aristova[1], Ning Jin[2], Liliana Ma[1], Alireza Vali[1], Michael Scott[1], Susanne Schnell[1]

1. Northwestern Feinberg School of Medicine, Dept. of Radiology
2. Siemens Healthineers

Purpose: While 4D flow MRI is a promising method for the assessment of intracranial blood flow across a variety of pathophysiologies[1, 2, 3] it is still hindered by long scan times. In other applications, compressed sensing (CS) using continuous wavelet transform with spatial and temporal regularization has enabled aortic 4D flow in 2 minutes, while preserving quantitative information[4]. However, this method has not been optimized for intracranial applications, which often require a large field of view and higher spatial resolution. The purpose of this work was thus to optimize regularization parameters for intracranial applications using a dedicated MR-compatible neurovascular flow phantom.

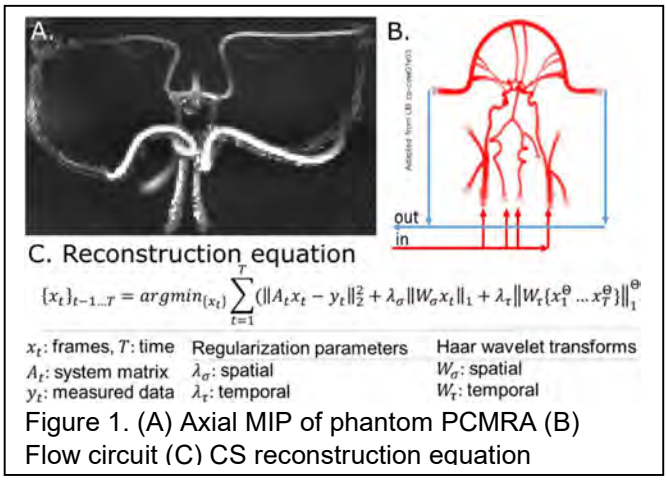

Figure 1. (A) Axial MIP of phantom PCMRA (B) Flow circuit (C) CS reconstruction equation

Methods: The pulsatile flow phantom circuit (Figure 1A-B) consisted of a silicone model of the Circle of Willis with multiple aneurysms (COW01V03: United Biologics, CA, USA) suspended in contrast-enhanced water, and integrated into a flow circuit with a pulsatile blood pump (model 1421, Harvard Apparatus: Holliston, MA, USA). Gadobutrol (Gadavist: Bayer AG, Germany) was added to 2% by volume in flowing fluid, 1% in static fluid. The flow circuit was operated at 1172ms pulse, stroke volume 25mL to mimic intracranial flow. Reference and CS 4D flow MRI was acquired with TE/TR 2.8/5.6 and 2.9/5.6 ms respectively, flip angle 20°, venc 120cm/s, 25 retrospectively gated timeframes, and 1.0mm isotropic resolution at 1.5T (MAGNETOM Aera: Siemens Healthcare, Germany).

CS spatial regularization (Figure 1C) weighting λ_σ was varied from 0.001 to 0.002 (optimal value in aorta: 0.0015), the scaling factor for temporal regularization $\lambda_\tau/\lambda_\sigma$ was varied from 3 to 5 (optimal value in aorta: 5) and acceleration factor R was 7.7 (optimal value for aorta). Non-CS reference scans were acquired with standard GRAPPA R = 2. Net flow and median velocity were quantified (on average 30 planes per vessel) using in-house analysis tools[5,6] (Matlab: Mathworks, MA, USA). Background phase was corrected with a flow-off scan[7]. Bland-Altman analysis was used to assess agreement between CS and conventional measurements of net flow, and median velocity, for internal carotid, middle cerebral, and basilar arteries. Values for a single timepoint at 269.8ms were used to account for phantom pulsatility. Image quality of the pseudo-complex phase-contrast angiogram segmentation (PCMRA) was assessed by Dice score[8] for at a uniform intensity threshold vs. R=2 reference.

Results: Flow and median velocity underestimation decrease with lower $\lambda_\tau/\lambda_\sigma$ (one-way ANOVA p= 8.6×10^{-4} and 4.1×10^{-6} respectively). Flow underestimation was significant ($p\leq0.0005$ for Bland-Altman bias) for all regularization parameter values tested, and was 21.7-28.5% (normalized to individual vessel flow) or 0.40-0.64mL/cycle (over all vessels, average flow 3.96 mL/cycle) for $\lambda_\tau/\lambda_\sigma$ = 5 (Figure 2A-B). Segmentation agreement was 76.7±1.2% across all cases (Figure 2C).

Discussion: Compressed sensing with L1 Haar wavelet regularization has the potential to substantially decrease scan time while maintaining reasonable data quality for intracranial applications. Optimal parameters differ from the aorta. Future directions include further reducing spatial regularization to achieve flow estimation 10%, and in vivo testing in healthy controls and neurovascular disease patients.

References : 1. Turski P et al. Neurovascular Imaging 2016 2:8 (2016). **2.** Rivera-Rivera LA et al. J. Cereb. Blood Flow Metab. 2016; 36:1718-1730. **3.** Schnell S et al. Curr Opin Neurol. 2016;29(4):419-28. **4.** Ma LE et al. Magn Reson Med. 2019;81(6):3675-3690. **5.** Bock J et al, ISMRM 2007. **6.** Vali A et al. Magn Reson Med. 2019. **7.** Lorenz R et al. Magn Reson Med. 2014 Jul;72(1):33-40. **8.** Zou et al. Acad Radiol. 2004 Feb; 11(2): 178–189.

Acknowledgements: American Heart Association 18POST33990451, 16DG30420005; National Institutes of Health R01HL115828, R21NS106696, R21HL130969, F30HL140910; Circle of Willis model loan from United Biologics; Northwestern Research Shop staff.

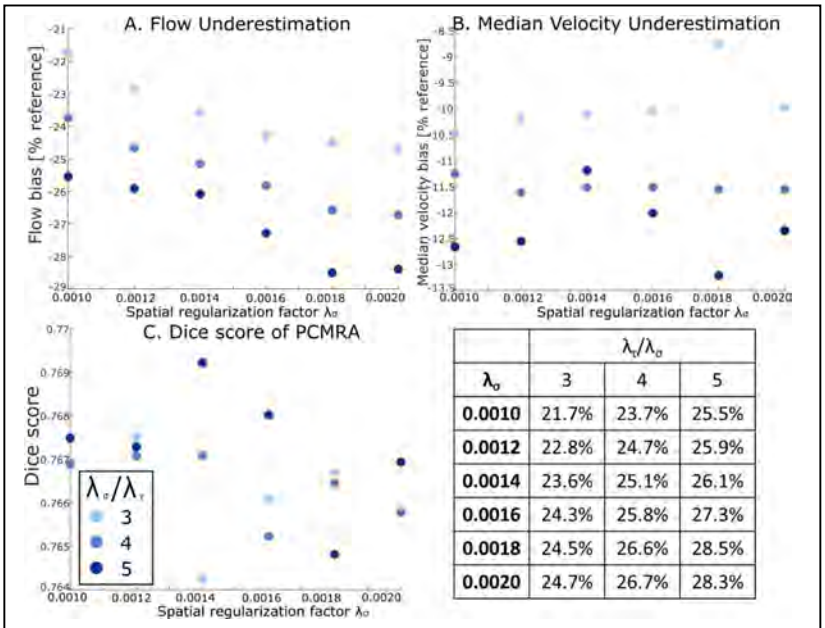

λ_σ	$\lambda_\tau/\lambda_\sigma$ 3	4	5
0.0010	21.7%	23.7%	25.5%
0.0012	22.8%	24.7%	25.9%
0.0014	23.6%	25.1%	26.1%
0.0016	24.3%	25.8%	27.3%
0.0018	24.5%	26.6%	28.5%
0.0020	24.7%	26.7%	28.3%

Figure 2(A) Flow underestimation, (B) Median velocity underestimation, (C) Dice score for PCMRA vs. reference (score 1 indicates good agreement) (D) Flow underestimation for each regularization parameter pair as percentage of flow values

FFR AND PRESSURE DROP ASSESMENT ACROSS SEVERE ILIAC ARTERY STENOSIS: 4D FLOW MRI-BASED COMPUTATIONAL FLUID DYNAMICS VS IN-VIVO MEASUREMENTS

S. Skopalik[1], P. Hall Barrientos[3], J. Matthews[4], A. Radjenovic[2], P. Mark[2], G. Roditi[2], M. C. Paul[1*]
[1] School of Engineering, University of Glasgow, Glasgow, UK,
[2] Institute of Cardiovascular & Medical Sciences, University of Glasgow, Glasgow, UK
[3] Queen Elizabeth University Hospital, Glasgow, UK
[4] Canon Medical Research Europe Ltd, Edinburgh, UK
*Email: Manosh.Paul@glasgow.ac.uk

Introduction: Fractional flow reserve (FFR) is considered to be the current "gold standard" for assessing the severity of atherosclerotic coronary artery stenotic disease [1]. However, it has not as yet been tested for assessment of stenotic disease in other common areas such as the iliac, femoral and renal arteries. FFR is and invasive and costly method associated with certain risks: it requires drug administration, specialist equipment, an operating room and a medical team [2]. Nevertheless, FFR is a good and simple index of predicting the haemodynamic severity of a stenosis, which makes it desirable to test this principle for non-invasive evaluation of other vessels, such as the iliac arteries.

Purpose Computational fluid dynamics (CFD) combined with high quality medical imaging data can be a viable non-invasive alternative to catheter derived pressure measurements for FFR calculation. CFD analysis can be performed for a wide range of vessels, extending its applications to vessel where conventional catheterisation may not be viable. Furthermore, CFD results can provide a much wider spectrum of data beyond pressure which can be used to assess the flow field in diseased arteries. To test this, in-silico measurement of FFR for a patient with iliac artery stenosis has been the focus of this study.

Method: Time-resolved 3D PC-MRI (4D Flow) measurements were conducted on a patient with a focal 78% area reduction (and >50% diameter reduction) left iliac artery stenosis as part of a comprehensive non-invasive assessment. The morphological 3D geometry of the abdominal aorta and both iliac arteries were also reconstructed from the non-invasive imaging data. Pulsatile CFD simulations were performed using inlet mass flow rate extracted form MRI data and pulsatile pressure boundary conditions based on catheter pressure measurements taken during iliac artery stenting procedure.

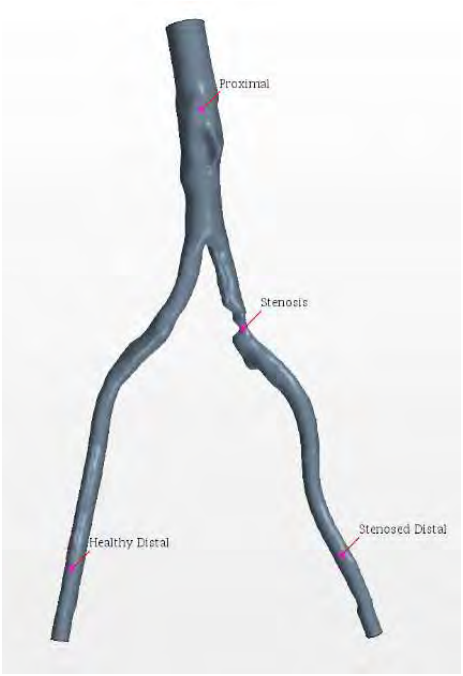

Figure 1: Geometry overview with pressure measurement points indication

Results and Discussion: Pressure was recorded over time at four locations on the model as shown in Figure 1. The pressure gradient was compared to the values measured by Archie et. al [3] for a study group with stenosis severity between 76% and 90% area reduction. Systolic pressure gradient and mean pressure gradient from CFD are 42.9 mmHg and 19.5 mmHg respectively, which appear to be in good agreement with reference measurements of 50 ± 23 mmHg and 18 ± 10 mmHg for systolic and mean flow respectively. In addition, vFFR was calculated from the CFD data and compared to the findings of Kobayashi et al [4]. Mean vFFR was 0.84 which is in good agreement with hyperaemic FFR of 0.84 ± 0.10 reported in the reference paper. Based on these results the study concludes that vFFR has good potential to characterise iliac artery stenotic disease.

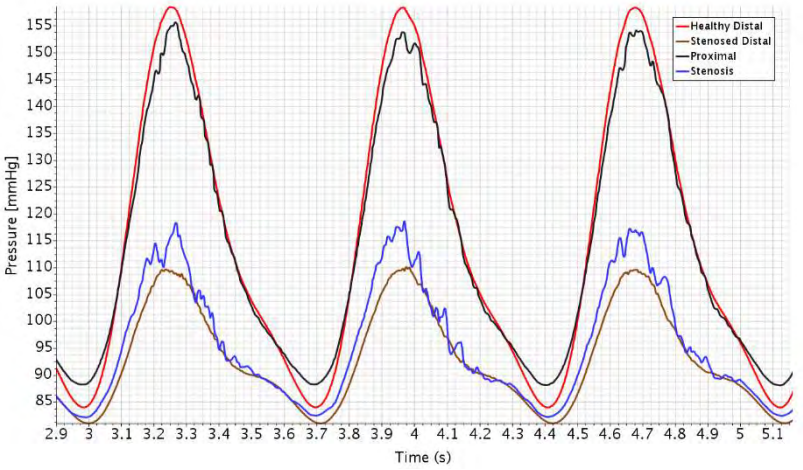

Figure 2: Pressure waveforms recorded at four different locations over three pulse cycles.

Acknowledgements

This work is kindly funded by Medical Research Scotland (grant PhD-888-2015) and Canon Medical Research Europe Ltd.

References:

1. Morris, P.D., et al., *"Virtual" (Computed) Fractional Flow Reserve: Current Challenges and Limitations.* JACC: Cardiovascular Interventions, 2015. **8**(8): p. 1009-1017.
2. Min, J.K., et al., *Noninvasive Fractional Flow Reserve Derived From Coronary CT Angiography: Clinical Data and Scientific Principles.* JACC: Cardiovascular Imaging, 2015. **8**(10): p. 1209-1222.
3. Archie, J.P., *Analysis and Comparison of Pressure Gradients and Ratios for Predicting Iliac Stenosis.* Annals of Vascular Surgery, 1994. **8**(3): p. 271-280.
4. Kobayashi, N., et al., *Measuring Procedure and Maximal Hyperemia in the Assessment of Fractional Flow Reserve for Superficial Femoral Artery Disease.* Journal of Atherosclerosis and Thrombosis, 2016. **23**(1): p. 56-66.

Improved Magnetic Resonance Angiographic Contrast Using Deep Transfer Learning Reconstruction

Ioannis Koktzoglou[1,2] and Robert R. Edelman[1,3]

[1]Radiology, NorthShore University HealthSystem, Evanston, Illinois, United States
[2]Radiology, Pritzker School of Medicine, University of Chicago, Chicago, Illinois, United States
[3]Radiology, Feinberg School of Medicine, Northwestern University, Chicago, Illinois, United States

Purpose: In the field of machine learning, transfer learning refers to transfer of knowledge gained in solving one problem and applying it to solve a different but related problem. We hypothesized that transfer learning using a deep convolutional neural network (CNN) trained on magnetic resonance angiographic (MRA) data obtained in one vascular bed could be applied to improve the image quality of another vascular bed. In this work we tested this hypothesis by applying a deep CNN trained on nonenhanced MRA data obtained in the neck to nonenhanced MRA data obtained in the lower extremities.

Methods: This study was approved by our institutional review board and all human subjects provided written informed consent. Nonenhanced MRA of the neck (n=6) was acquired using a prototype ungated 3-shot radial fast low-angle shot (FLASH) quiescent interval slice-selective (QISS) sequence [1], and nonenhanced MRA of the lower extremities (n=24) was acquired with a cardiac-gated Cartesian balanced steady-state free precession (bSSFP) QISS sequence [2]. Raw radial k-space data from the neck QISS exams (acquired using a golden angle trajectory) was reconstructed offline, generating two image sets: "single-shot" images which were reconstructed from only the first imaging shot (i.e. 68 of 204 radial views); and "3-shot" images reconstructed from all three acquired imaging shots (i.e. 204 views). Using these two data sets, a U-net deep CNN [3] leveraging small overlapping image patches was trained to generate 3-shot data from single-shot data. The deep neural network, trained from neck MRA data, was subsequently transferred and applied to cardiac-gated single-shot Cartesian QISS image data obtained in the lower extremities. The standard and deep transfer learning-enhanced QISS images of the lower extremities were compared on the basis of arterial-to-background contrast computed on source and maximum intensity projection images. Arterial-to-background contrast was quantified as S_a/S_b-1, where S_a and S_b denote the mean signals of arterial and background tissue, respectively.

Results: Source images from the original and deep transfer learning-enhanced lower extremity QISS MRA data sets are shown in Figure 1a. Compared to the standard, original source images, lower extremity QISS images obtained with the proposed deep transfer learning reconstructive strategy reduced the appearance of static background tissue and apparent noise, as well as improved arterial-to-background contrast and arterial signal homogeneity without loss of arterial detail. Arterial-to-background contrast values on source images were approximately 22% larger within the images reconstructed with deep transfer learning. Deep transfer learning-based reconstruction was also found to improve arterial-to-background contrast on full-thickness coronal maximum intensity projection images (Figure 1b), with mean contrast improvements of 28%, 35%, and 16% obtained in the pelvis, thigh, and calf, respectively.

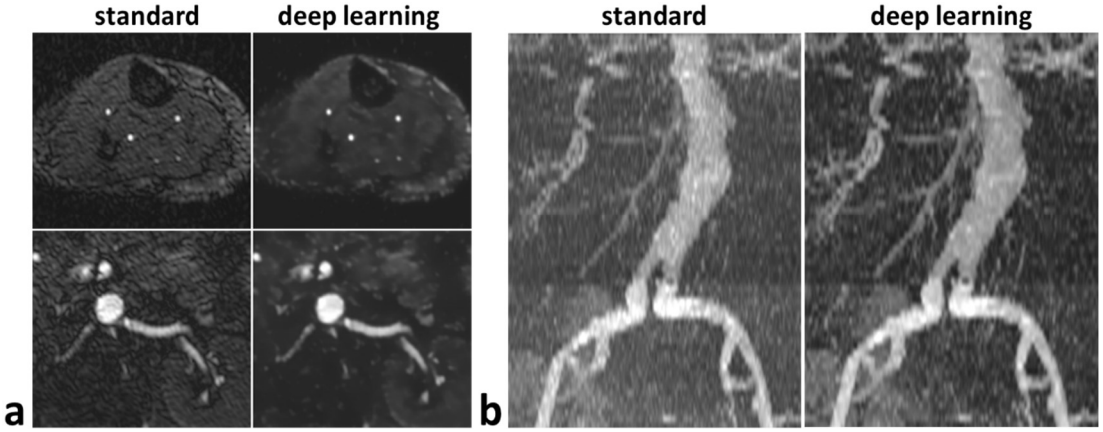

Figure 1: Comparison of (a) axial source and (b) coronal maximum intensity projection images obtained with standard and deep transfer learning reconstructions. Note the improved arterial signal homogeneity and arterial-to-background contrast obtained with deep transfer learning reconstruction.

Discussion: Despite the use of MRA data obtained in different vascular beds (neck versus lower extremity) and with different imaging sequences (ungated radial FLASH versus cardiac-gated Cartesian bSSFP), deep transfer learning-based reconstruction was found to be a useful strategy for improving arterial-to-background contrast on source and maximum intensity projection images. With further validation and refinement, we anticipate that this deep transfer learning reconstructive strategy will be useful for improving the image contrast and quality of MRA, especially in clinical scenarios or anatomic locations where routine acquisition of high signal-to-noise ratio images is technically difficult or impractical.

References: [1] Koktzoglou et al. Magn Reson Med. 2018 Feb;79(2):683-691. [2] Edelman RR et al. Magn Reson Med. 2010 Apr;63(4):951-8. [3] Ronnenberger et al. 2015. arXiv:1505.04597

Funding: National Institutes of Health (NIH) grants R01 EB027475, R01 HL130093, and R21 HL126015.

Association between Intraplaque Hemorrhage and Ipsilateral Cerebral Blood Flow in Patients with Carotid Moderate to Severe Stenosis: A Multi-contrast MR Vessel Wall Imaging Study

Ran Huo[1], Huimin Xu[1], Ying Liu[1], Jin Li[2], Zheng Wang[1], Tao Wang[3], Huishu Yuan[1], Xihai Zhao[4]

1. Department of Radiology, Peking University Third Hospital, Beijing, China; 2. Department of Radiology, The Affiliated BenQ Hospital of Nanjing Medical University; 3. Department of Neurosurgery, Peking University Third Hospital, Beijing, China; 4. Center for Biomedical Imaging Research, Tsinghua University, Beijing, China.

Background and Purpose: Cerebral blood flow (CBF) has been well established to be a strong indicator for ischemic stroke. Although carotid artery atherosclerosis can lead to decrease of CBF, the collateral circulation will preserve the CBF to some extent when carotid artery stenosis occurred. It has been shown that patients with chronic carotid artery stenosis usually had better collateral circulation whereas acute luminal narrowing or occlusion develops poor collaterals [1]. We hypothesized that the occurrence of carotid intraplaque hemorrhage (IPH) may rapidly result in luminal stenosis and much lower CBF subsequently than those without IPH. **This study sought to investigate the correlation between carotid IPH and CBF in the ipsilateral middle cerebral artery (MCA) territory by using multi-contrast MR vessel wall imaging and compute tomography perfusion (CTP).**

Methods: **Study sample**: Patients with carotid moderate to severe stenosis (50-99% stenosis) and large plaque which is defined as lesions with maximum wall thickness (Max WT) > 4 mm were recruited in this study. The exclusion criteria were as follows: 1) hemorrhagic stroke; 2) cerebral neoplasms; and 3) contraindication to MR examination. **MR imaging**: All patients underwent MR imaging for carotid arteries on a 3.0T MR scanner with 8-channel carotid coil to acquire the following multi-contrast MR vessel wall imaging sequences: 3D time-of-flight: TR/TE 17.6/ 6.7 ms, flip angle 8°, and slice thickness 2 mm; 2D T1-weighted: TR/TE 850/ 13.44 ms and slice thickness 2 mm; 2D T2-weighted: TR/TE 2000/ 96.6 ms and slice thickness 2 mm; and Simultaneous Non-contrast Angiography intraplaque hemorrhage (SNAP) imaging: TR/TE 9.6/ 4.0 ms, flip angle 12°, and slice thickness 1 mm. The FOV was 140 × 140 mm^2, in-plane spatial resolution was 0.55 × 0.55 mm^2 and the longitudinal coverage was 32 mm for all imaging sequences. A routine CT perfusion was also performed for all patients. **Image review**: The plaque components including lipid-rich necrotic core (LRNC), IPH and calcification (CA) were identified and the Max WT and luminal stenosis were measured for the index artery with most severe stenosis bilaterally. The CBF in the ipsilateral middle cerebral artery territory was measured. **Statistics**: The CBF was compared between patients with and without plaque components using Mann-Whitney U test. Univariate and multivariate linear regressions were used to determine the correlation between plaque features and CBF.

Results: In total, 87 subjects (mean age, 65.10 ± 8.04 years; 75 males) were included, of which 71 (81.6%), 86 (98.9%), and 71 (81.6%) had carotid CA, LRNC, and IPH, respectively. Patients with carotid IPH had significantly lower CBF than those without (39.52 ± 7.21 ml/100g/min vs. 45.46 ± 8.05 ml/100g/min, $P = 0.022$, Fig. 1). No significant differences were found in CBF between patients with and without CA ($P = 0.58$). Carotid IPH was significantly correlated with CBF before (β = -5.94; 95% CI, -9.99 to -1.89; $P = 0.005$) and after (β = -6.85; 95% CI, -11.43 to -2.27, $P = 0.004$) adjusted for carotid stenosis, Max WT, and clinical risk factors (Fig. 2). No significant correlations were found between other plaque components and CBF (all $P > 0.05$).

Discussion and conclusions: Carotid artery IPH is independently associated with decrease of ipsilateral CBF, suggesting that patients with carotid hemorrhagic plaque may develop much reduced cerebral perfusion.

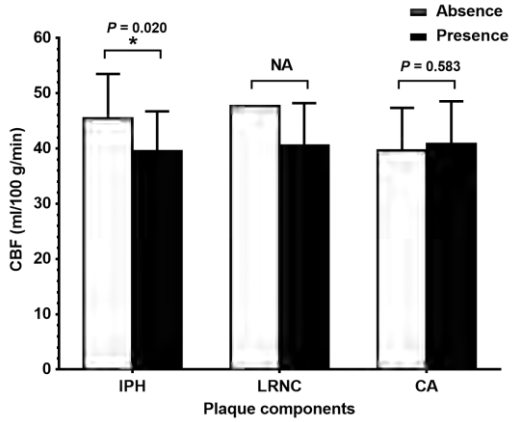

Fig. 1 Comparison of CBF according to plaque components.

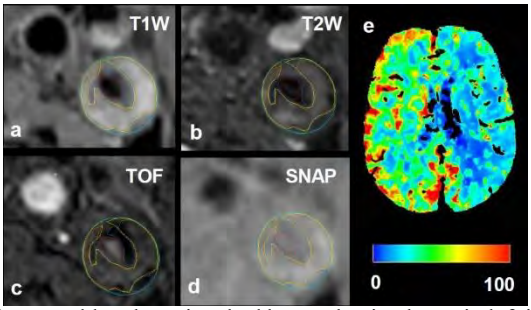

Fig. 2 A 61 years old male patient had hemorrhagic plaque in left internal carotid artery and ipsilateral decreased CBF. The IPH, LRNC and CA were segmented with orange, yellow, and blue contours.

References: [1] T. Kucinski, *et al*. Neuroradiology. 2003; 45: 11–18.

Ungated 3D Stack-of-Stars QISS Fast Low-Angle Shot MR Angiography for High Resolution Evaluation of the Carotid Bifurcation: Initial Protocol Optimization at 3 Tesla

Ioannis Koktzoglou[1,2], Nondas Leloudas[1], Jianing Pang[3], Archie L. Ong[2,4], Robert R. Edelman[1,5]

[1]Radiology, NorthShore University HealthSystem, Evanston, Illinois, United States
[2]University of Chicago Pritzker School of Medicine, Chicago, Illinois, United States
[3]Siemens Medical Solutions USA Inc., Chicago, Illinois, United States
[4]Neurology, NorthShore University HealthSystem, Evanston, Illinois, United States
[5]Radiology, Feinberg School of Medicine, Northwestern University, Chicago, Illinois, United States

Purpose: Nonenhanced high spatial resolution evaluation of the carotid bifurcation is typically performed using 3D time-of-flight (TOF) magnetic resonance angiography (MRA). However, 3D TOF carries drawbacks including sensitivity to motion and suboptimal suppression of background signal. The purpose of this work is to report and optimize a 3D stack-of-stars ungated quiescent interval slice-selective (QISS) fast low-angle shot (FLASH) sequence for high resolution imaging of the carotid bifurcation, with an emphasis on initial protocol optimization at 3 Tesla.

Methods: QISS MRA is predominantly a 2D technique that has proven accurate for diagnosing lower extremity arterial disease without the use of contrast agents [1]. Recent studies have also applied variants of 2D QISS for nonenhanced evaluation of the head and neck arteries [2,3]. However, practical limits on the slice profile and slice thickness achievable with 2D QISS may impede precise portrayal of the carotid bifurcation. In this work, a prototype 3D implementation of QISS leveraging a stack-of-stars k-space trajectory and a FLASH readout was implemented and applied for high spatial resolution evaluation of the carotid bifurcation. Imaging experiments were performed on a clinical 3T scanner (MAGNETOM Skyra^{Fit}, Siemens Healthcare, Erlangen, Germany) Typical imaging parameters were as follows: 20×20 cm field of view, 352 matrix, 0.57×0.57 mm in-plane spatial resolution (two-fold interpolated to 0.28×0.28 mm), 15 ms inter-echo spacing, 3.9 ms echo time, 15° flip angle, ≈600 Hz/pixel receiver bandwidth, 8 slabs, 12 1.6-mm-thick slices (two-fold interpolated to 24 0.8 mm slices) per slab, 2 imaging shots per slice-encoding step, acquisition of 60 radial views per imaging shot. In optimizing image quality of the 3D stack-of-stars QISS protocol, we investigated the impacts of: (a) tilted optimized nonsaturating excitation (TONE) radiofrequency pulses; (b) sequence repetition time (TR) and inflow time to readout center (TI); (c) the radial view acquisition order (sequentially traversing all slice-encoding (i.e. k_z) steps before incrementing the radial view or vice versa); and (d) the method for background signal suppression (saturation-recovery versus inversion-recovery).

Results: We found that ungated 3D stack-of-stars QISS provides high spatial resolution MRA of the carotid bifurcation with a uniform level of background signal suppression (**Figure 1**). Strategies that optimized image quality in initial studies included the use of TONE radiofrequency pulses, saturation-recovery (instead of inversion-recovery) for background signal suppression, sequential acquisition of all slice-encoding steps prior to incrementing the radial view, and sequence TR and TI times of ≈1.5 s and ≈1.0 s, respectively. Initial comparisons with 3D TOF MRA revealed that ungated 3D stack-of-stars QISS MRA has the potential for more uniform background signal suppression, while being less sensitive to pulsation and motion artifacts, and avoiding phase wrap which is often seen with 3D TOF MRA.

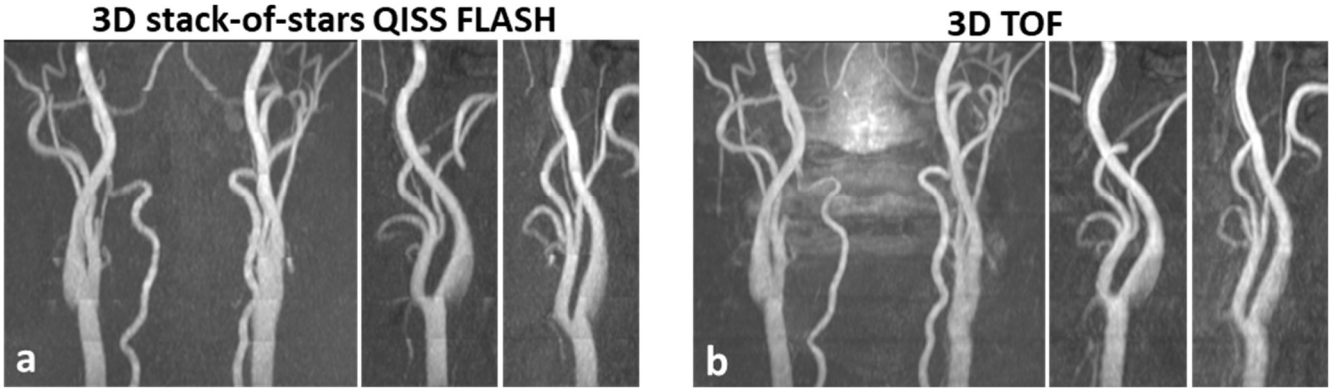

Figure 1: Full-thickness frontal and 20-mm-thick oblique lateral maximum intensity projection images obtained with **(a)** ungated 3D stack-of-stars QISS MRA implemented with TONE radiofrequency pulses, saturation-recovery-based background suppression, and TR and TI times of 1.5 s and 1.0 s, in comparison with **(b)** 3D TOF MRA.

Discussion: Ungated 3D QISS MRA using a stack-of-stars FLASH readout is a promising technique for high spatial resolution evaluation of the carotid bifurcation that provides uniform background signal suppression and the potential for reduced motion sensitivity with respect to 3D TOF. Further optimization and evaluation of the protocol is underway.

References: [1] Edelman et al. Magn Reson Med 2010;63:951–958. [2] Koktzoglou et al. Magn Reson Med 2016;75:2072–2077. [3] Koktzoglou and Edelman. Magn Reson Med 2018;79:683–691.

Funding: National Institutes of Health (NIH) grant R01 EB027475.

Findings in Potential Living Donors of Kidneys
Retrospective Analysis of ceMRA/MRV

Manuela A. Aschauer, Anja K. Greiner, Judith Kahn, Sabine Zitta
Medical University of Graz, Austria

Purpose: The goal of this study is to quantify and describe the anomalies of potential living kidney donors who have had an ceMRA/MRV evaluation.
Patients/ Methods: Between 2009-2018: 104 cases (76 f/28 m); mean age 59y (min. 20y, max. 75y); Transplantation occured in 64,4%; Radiological findings were reevaluated regarding number and origin of arteries, number of veins, length measurement, other anomalies and compared with surgical reports
MR-scanners: SIEMENS® 3T Verio (n=103) or 1,5T Symphony (n=1) with body martrix and spine coil Contrast agents: Dotarem® (n=31; 0,2ml/kg), Gadovist® (n=73; pat. >=75kg 10ml; pat. <75kg 7,5ml); bolustiming 1ml, automated injection 2ml/s; ceMRA/MRV; flash3D with 3D reconstruction and spin; consists of four dynamic phases (native, arterial, venous, equilibrium) lasting around 18 sec. depending on anatomy; 1 breathhold each phases (Fig.1); THK 1mm - 1,4mm depending on the anatomy, TR/TE/3.12/1.13, flipangle: 16 degree, Matrix: 512x312; T2 and T1 images before and after contrast; MR-urography (Fig. 2)
Results: Three arteries were not described primarily in the radiological report due to human error. All were found retrospectively during our evaluation. One artery was not described due to technical limitations or unknown cause (not found retrospectively). Two early branching renal arteries presumingly resulted in two artery recipient anastomoses. One definite accessory artery in MRA was not found during surgery and consecutively not transplanted without major complication. Two renal veins were seen twice in ceMRV and also during transplantation (Fig. 4). The most common venous anomalies included multiple renal veins, insufficient gonadal veins, retroaortic veins and venous connections to bigger retroperitoneal veins (Fig. 3, 4, 5).
Lumbar arteries/ veins, visceral arteries/veins including inferior mesenteric artery as well as peripheral visceral artery branches could be identified in all cases, demonstrating a homogenous quality in showing vessels as small as 1.5mm.
Discussion: Because 3 of 4 renal arteries were found in our second look evaluation, we would recommend a reevaluation of all images by an experienced radiologist together with the surgeon before transplantation, like it is common practice for all tumor patients. 3D-reconstruction is helpful but source images of all dynamic phases, subvolume, MIP and MPR are necessary for final diagnosis. In MRA the need of cyclic contrast agent volume is around one tenth of that in CT. Preliminary results suggest that MR/ceMRA is a sufficient method for preoperative evaluation of living donors since it does not use radiation and has virtually no side effects.

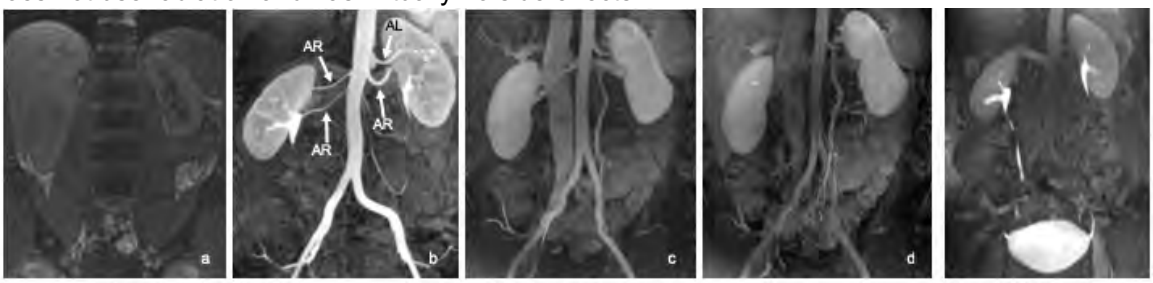

Fig.1: a) native- b) arterial- c) venous- d) equilibrium phase (different donors)
b) Right kidney showing 2 Aa. renales (AR); A. lienalis (AL)

Fig. 2: MR-Urography

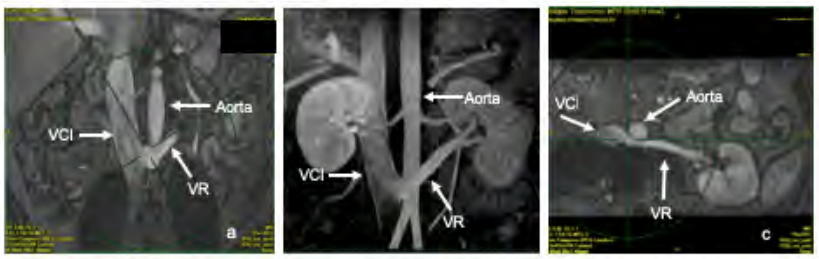

Fig. 3: a) b) c) Retroaortic V. renalis sin. (VR) with deep confluence into V. cava inferior (VCI)

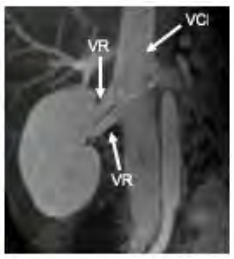

Fig. 4: Right Kidney with 2 Vv. renales (VR)

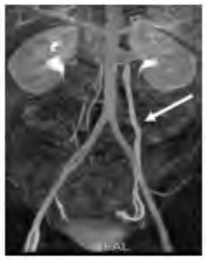

Fig. 5: Insufficiency of the V. ovarica

References available: manuela.aschauer@medunigraz.at

Application of ASL Technique for Carotid Artery Stenosis: Initial Experience

Keiji Igase[1),2)], Nari Kimura[2)], Ichiro Matsubara[2)], Yoshiaki Kumon[2)],
Takanori Ohnishi[2)], Kazuhiko Sadamoto[2)]

1) Department of Advanced Neurosurgery, Ehime University Graduate School of Medicine
2) Department of Neurosurgery, Washokai Sadamoto Hospital, Matsuyama, Japan

(Introduction) Qualifying cerebral blood flow (CBF) using MRI has been difficult in decade, because of its complexity harboring both temporal and special factors. Recently arterial spin labeling (ASL) technique has shown up and has been upgraded by using MRI with high magnetic field, and this method can be useful for imaging of cerebral blood flow. This time we examined ASL in terms of cerebrovascular dyanamics of carotid artery stenosis patients.

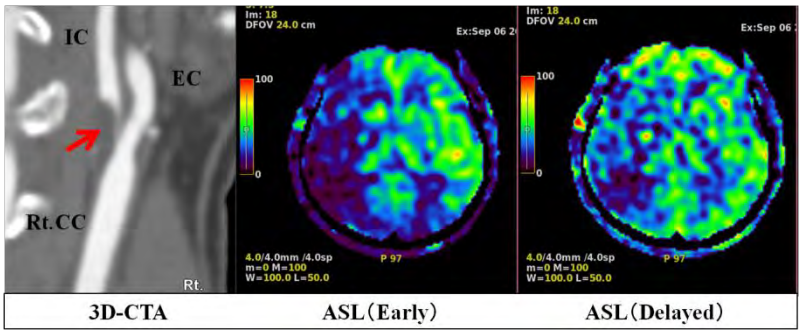

(Methods) Consecutive 12 patients (mean age: 72.3±6.3 years old; Male 9 and Female 3) with an unilateral carotid artery stenosis of more than 50 % diagnosed by 3T MRI during 1 year (from April 2018 to March 2019) were enrolled in this study. All patients underwent both 3T MRI (Discovery 750w: GE healthcare) and SPECT (Infinia 3: GE healthcare) studies, in former examination carotid MR angiography and ASL imaging were acquired, meanwhile in latter CBF analysis was performed using ^{123}I-IMP. In carotid MR angiography the grade of carotid artery stenosis was calculated in reference to NASCET, and in ASL study dual images acquired at both 1500 (early) and 2500 (delayed) milliseconds were applied, on each image the ratio of signal intensity (lesion/healthy hemisphere) was calculated on the slice including lateral ventricle body. In SPECT study both rest and acetazolamide administered CBF (ml/100g/min) were measured, and the ratio of CBF (lesion/healthy hemisphere) was also calculated.

(Results) Both the ratio of signal intensity on early and delayed ASL images were closely correlated with the ratio of acetazolamide administered CBF (R^2=0.81 and 0.85, respectively) but rest CBF (R^2=0.11 and 0.09, respectively). Moreover, the numerical value of early to delayed signal intensity ratio from ASL image had also strong association with the carotid stenosis (R^2=0.84).

(Discussion) Though in general ASL revealing perfusion image[1)], given that our results, ASL images may express cerebrovascular reserve not but rest cerebral dynamics. Besides, considering our last results in the case with higher carotid stenosis the blood flow containing labeled proton would more slowly reach the tissue, implying that ASL data should be time-dependent and reliable.

(Conclusion) New technique of ASL using MRI would be feasible to evaluate the cerebrovascular dynamics without contrast-enhancement.

(Reference) 1) J-C Ferre et al. Arterial spin labeling (ASL) perfusion: Techniques and clinical use. Diagnostic and Interventional Imaging (2013) 94, 1211-1223

Initial Results of Reynolds Stress Tensor Quantification using Flow-MRF

Sebastian Flassbeck[1], Simon Schmidt[1], Mark E. Ladd[1], and Sebastian Schmitter[1,2]
[1]Medical Physics in Radiology, German Cancer Research Center (DKFZ), Heidelberg, Germany,
[2]Physikalisch-Technische Bundesanstalt (PTB), Braunschweig and Berlin, Germany

Purpose: Flow-MRF is a recently presented technique[1] allowing simultaneous quantification of velocities and relaxometric parameters of static tissue, based on the MR Fingerprinting framework[2]. This technique allows the velocities to be quantified in shorter scan times than convectional phase contrast based methods. Further, higher velocity encoding moments (m_1) can be used, while maintaining a large dynamic range of uniquely quantifiable velocities. These features make Flow-MRF interesting for the quantification of the Reynolds stress tensor (RST). The RST is often quantified in stenotic flow conditions where high peak velocities occur and the large m_1-values of Flow-MRF make the sequence more sensitive to the turbulence induced signal dephasing. In this work, the feasibility of Flow-MRF to quantify the RST is investigated.

Methods: The quantification of the RST with Flow-MRF is based on the method proposed by Haraldsson et al[3]. In Flow-MRF the velocity compensated signal (S_0) is estimated alongside the tensor, unlike the previously presented methods. Further, the tensor is estimated based on approximately 50 undersampled time frames per cardiac phase in the reconstruction. A sequence diagram of the radial Flow-MRF sequence is shown in Fig.1, alongside a section of the velocity encoding pattern. Here, the range of applied m_1 values varied between +/- 30 $mT/m \cdot ms^2$, which corresponds to a 20cm/s encoding velocity (venc) in a double sided encoding. The focus in this work was entirely on the velocity quantification, thus unlike previously shown implementations of Flow-MRF[1], no inversion preparation was used and the flip angle (FA) was fixed for all TRs, which prevents T_1 and T_2 quantification. Preliminary investigations revealed that variable FAs result in complex dependencies of S_0 on the FA-pattern, the inflow behavior and the relaxation times of the fluid. The makes a quantitative description of the signal magnitude difficult, which is necessary for the RST quantification. In the case of a fixed FA, signal magnitude is a function only of S_0 and the RST, while the signal phase uniquely encodes the mean velocity of a voxel.

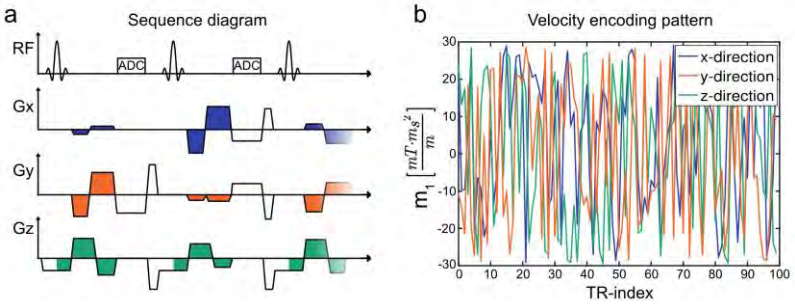

Figure 1: Sequence diagram of proposed sequence (a). Used velocity encoding pattern is shown in (b).

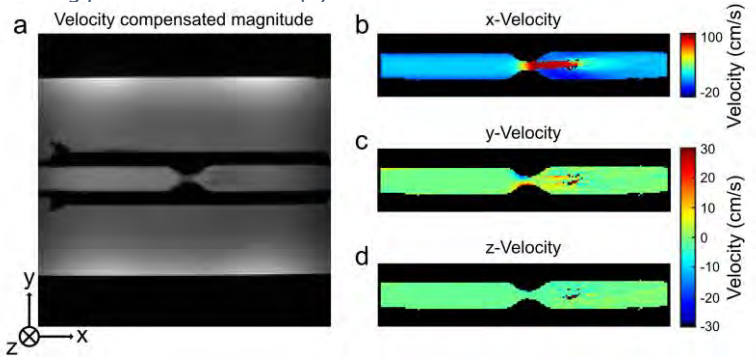

Figure 2: Magnitude image of phantom experiment (a). Flow-MRF velocity maps of a single cardiac phase are shown in (b-d).

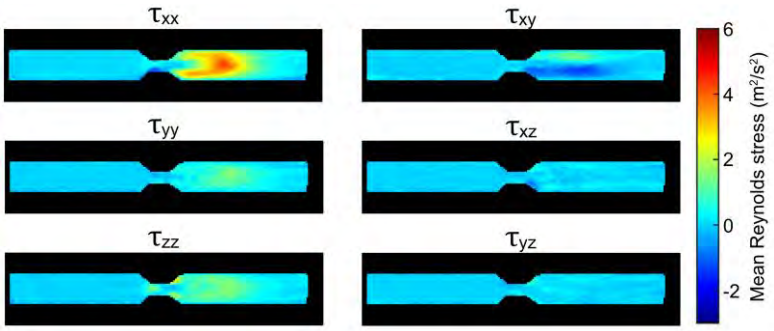

Figure 3: Time-averaged entries of RST quantified by Flow-MRF.

The quantification of RST was performed in a coronal slice through a stenosis phantom displayed in Fig.2a. The velocity jet creates turbulent flow regimes at its edges. The Flow-MRF sequence was acquired with 30 radial projections per frame in 3min 59s with a spatial resolution of 0.8×0.8×5mm3 and a temporal resolution of 39.2ms. To increase the signal for the RST maps, the reconstructed in-plane voxel-size was doubled (1.6×1.6×5mm^3) during reconstruction.

Results: Figure 2 shows the Flow-MRF velocity maps of a single cardiac phase. The mean velocity upstream of the stenosis is 11.9 cm/s and increases to 103.9 cm/ within the stenosis, matching the expected 9-fold velocity increase due to the 88.9 % stenosis. The velocity quantification fails in a few pixels at the end of the velocity jet due to strong signal dephasing. This is supported by the τ_{xx} component in Fig.4a showing the highest degree of signal dephasing in such locations. The shape of the magnitude of the RST components quantified by Flow-MRF agree with a reference measurement based on the method by Haraldsson et al[3].

Discussion: In this work, we demonstrate the feasibility of quantifying simultaneously RST and velocities using a Flow-MRF based approach. The slice selective readout in Flow-MRF might lead to an underestimation of τ_{xz} and τ_{yz} components. This motivates further investigations into volume selective readouts and isotropic resolutions. The robustness of Flow-MRF against phase aliasing lifts the constraints of the maximum m_1, which is expected to allow higher precision in the quantification of the RST but also leads to increased sensitivity to finite skewness or kurtosis of the velocity distributions[4].

References: [1] Flassbeck S. et al. MRM 2019. [2] Ma D. et al Nature, 2013. [3] Haraldsson H. et al. MRM, 2018. [4] Dyverfeldt P. MRM 2011.

Arterial stiffness in bicuspid or tricuspid aortic valve aortopathy assessed by 4D flow MRI

Ariel F. Pascaner[1], Sophia Houriez--Gombaud-Saintonge[2,3], Gilles Soulat[4], Umit Gencer[4], Thomas Dietenbeck[2], Yasmina Chenoune[3], Nadjia Kachenoura[2], Elie Mousseaux[4], Damian Craiem[1], Emilie Bollache[2]

[1]IMETTYB – CONICET – Universidad Favaloro, Buenos Aires. [2]Sorbonne Université, INSERM, CNRS, Laboratoire d'Imagerie Biomédicale, Paris. [3]ESME Sudria Research Lab, Paris. [4]Hôpital Européen Georges-Pompidou, Paris.

Purpose: Both aortic stiffening and dilatation are associated with higher cardiovascular risk. However, arterial stiffness variations in the presence of tricuspid (TAV) or bicuspid (BAV) aortic valve aortopathy are still unclear [1]. The aim of this work was to provide a comprehensive assessment of aortic stiffness, through both aortic distensibility (AD) and pulse wave velocity (PWV), in patients with either TAV or BAV and/or aortic dilation using MRI.

Methods: We included 18 patients with normal TAV and dilated ascending aorta (DTAV, 65±14 years, 11 males), 19 patients with a non-stenotic BAV without severe regurgitation (55±15 years, 17 males) and control groups, which were matched on age, gender and blood pressure to each of the DTAV (Ctl-DTAV) and BAV (Ctl-BAV) groups. All subjects underwent thoracic aortic axial 2D through-plane phase-contrast (PC) and 4D flow MRI examination (resolution: 1.24x1.24 mm^2, 11 ms and 1.5x1.5x2.2-2.4 mm^3, 16.9-25.3 ms, respectively; Venc: 200-400 cm/s). Local ascending (AA) and descending (DA) aortic distensibility (AA-AD and DA-AD, respectively) was measured using PC data using fully automatic, previously validated software [2]. After correcting for eddy currents, systolic aortic volume was semi-automatically segmented from 4D flow data to subsequently calculate blood flow rate in reconstructed planes perpendicular to the aorta centerline, every 5 mm. We calculated the transit time (TT) between the most distal and each subsequent flow waveform using a Wavelet transform [3]. Finally, regional AA-PWV and DA-PWV were computed as the linear regression slope of the corresponding distance vs. TT points. In addition, PWV was computed in the aortic arch using 2D PC data and a single oblique plane to manually measure the arch length (Arch-PWV).

Results: As expected, both DTAV and BAV groups showed significantly increased maximum diameter when compared to their respective control group: 47±5 vs. 31±3 mm and 44±4 vs. 31±4 mm, respectively (both $p<0.001$). Figure 1 provides local and regional aortic stiffness indices according to each group, showing that there were no significant differences in any of the computed parameters between both patient groups with respect to controls.

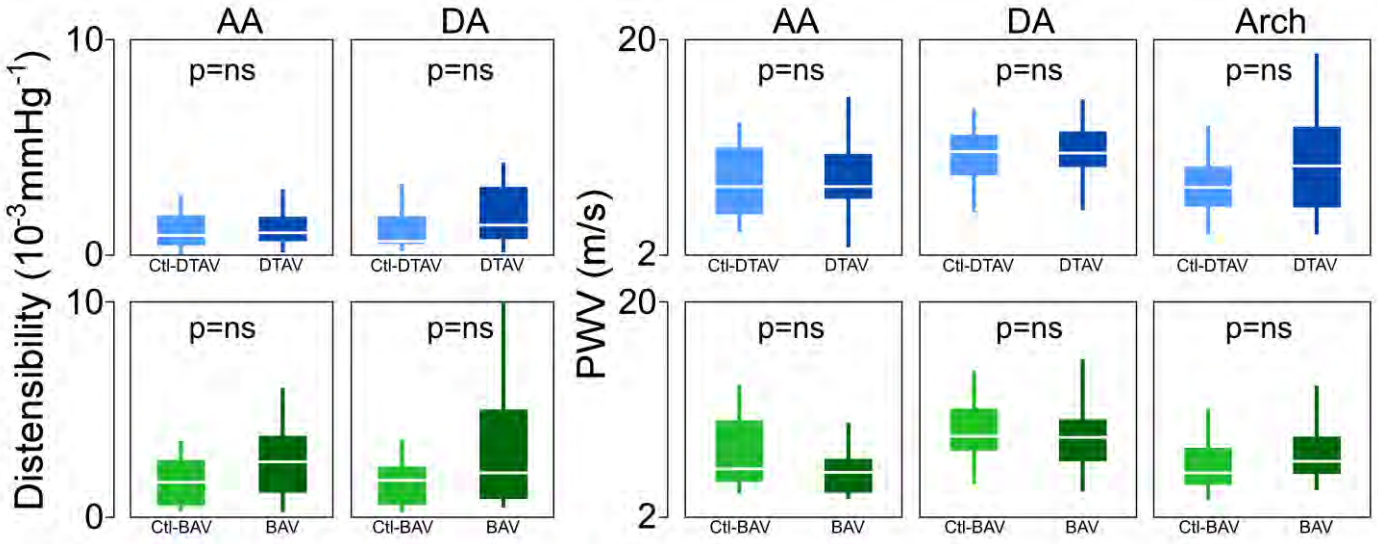

Figure 1. Top row: Ctl-DTAV (light blue) vs. DTAV (dark blue), lower row: Ctl-BAV (light green) vs. BAV (dark green). From left to right: AA-AD, DA-AD, AA-PWV, DA-PWV and 2D-PWV. Significance levels of Wilcoxon tests are shown.

Discussion: Patients with aortopathy showed no differences in arterial stiffness with respect to healthy controls, either assessed by distensibility or by pulse wave velocity in any region of the aorta. PWV, whether computed using 2D or 4D data, was unchanged, in agreement with a previous study in abdominal aorta aneurysms [4]. Moens-Korteweg equation predicts a negative compensatory effect on PWV caused by dilatation. Our findings might indicate a complex relationship between a chronical increase in aortic diameter and tissue stiffness. Accordingly, stiffening and dilatation process should be further investigated in larger longitudinal studies.

References:

[1] A. Guala *et al.* "Influence of Aortic Dilation on the Regional Aortic Stiffness of Bicuspid Aortic Valve Assessed by 4-Dimensional Flow Cardiac Magnetic Resonance: Comparison With Marfan Syndrome and Degenerative Aortic Aneurysm," *JACC Cardiovasc Imaging*, 2018.

[2] A. Herment *et al.* "Automated segmentation of the aorta from phase contrast MR images: validation against expert tracing in healthy volunteers and in patients with a dilated aorta," *J Magn Reson Imaging*, vol. 31, pp. 881-8, 2010.

[3] S. Houriez--Gombaud-Saintonge *et al.* "The assessment of aortic pulse wave velocity using 4D flow magnetic resonance imaging: Methods comparison," *CinC*, 2017.

[4] A. Abbas *et al.* "Thoracic but not abdominal phase contrast magnetic resonance-derived aortic pulse wave velocity is elevated in patients with abdominal aortic aneurysm," *J Hypertens*, vol. 33, pp. 1032-8, 2015.

Is It Necessary for Patients with Internal Carotid Artery Occlusion to Undergo 3D Head-neck MR Vessel Wall Imaging before Endovascular Revascularization?

Huilin Zhao[1], Jin Zhang[1], Yan Zhou[1], Xiaosheng Liu[1], Xihai Zhao[2], Chun Yuan[2,3], Jianrong Xu[1]

1. Radiology, Renji Hospital, Shanghai Jiao Tong University, Shanghai, China; 2. Center for Biomedical Imaging Research, Department of Biomedical Engineering, Tsinghua University School of Medicine, Beijing, China; 3. Radiology, University of Washington, Seattle, WA, USA

Purpose: Diagnosis of internal carotid artery occlusion (ICAO) by angiography no longer satisfies neurosurgeons' needs for vascular recanalization [1]. The 3D MR vessel wall imaging (MR-VWI) techniques have been developed to accurately visualize and quantify both the carotid lumen and the vessel wall components [2]. In this study, we aimed to evaluate the characteristics of pre-procedural 3D head-neck MR-VWI in patients with ICAO and its relationship to technical success rates.

Methods: Patients who were diagnosed as ICAO by conventional contrast-enhanced MR angiography (CE-MRA) were included in this study. The 3D head-neck MR-VWI protocol was conducted to acquire SPACE sequence [3] using a 3.0T whole-body clinical scanner (MAGNETOM Skyra, Siemens Healthcare, Germany) with a 20-channel head-neck coil. The patients subsequently underwent DSA and endovascular recanalization within 1 week after 3D head-neck MR-VWI. Patients were divided into two groups according to technical success or not in endovascular recanalization. Two experienced radiologists reviewed the MR-VWI with consensus. The morphologic characteristics regarding the occlusion stump, occlusion distribution, intraplaque hemorrhage (IPH) over the occluded segment and the visibility of residual lumen in the distal carotid segment were evaluated.

Results: A total of 30 patients (22 men, mean age 62.3 years old, range from 46 to 71 years) were included in this study. Twenty patients underwent successful endovascular recanalization. The Table summarized the characteristics of ICAO on 3D MR-VWI. There were no significant differences in the stump conditions and distal lumen collapse between the success group and the failure group. Compared with the failure group, the success group exhibited significantly lower prevalence of occlusion site over consecutive C1 segment (20.0% vs. 90.0%, P<0.001) and higher prevalence of IPH over start part of occlusion (65.0% vs. 10.0%, P=0.004, Figure 1, 2).

Table. MR-VWI identified characteristics of ICAO

MR-VWI characteristics	Success group (n=20)	Failure group (n=10)	P Value
Stump conditions			
tapered	12(60.0%)	4(40.0%)	0.301
blunt	4(20.0%)	5(50.0%)	0.091
no stump	4(20.0%)	1(10.0%)	0.488
Occluded distribution over C1 segment	4(20.0%)	9(90.0%)	<0.001
Distal lumen collapse in C1 segment	8(40.0%)	3(30.0%)	0.838
IPH over start part of occlusion	13(65.0%)	1(10.0%)	0.004

the chi-square test.

Discussion: Our results showed that patients with a lower extent of occlusion and more IPH presence in the proximal carotid segment had a higher success rate of recanalization. Our findings indicate that 3D head-neck MR-VWI may play a role in the patient selection of carotid ICAO for endovascular recanalization.

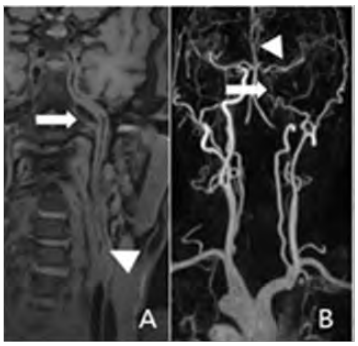

Fig.1 An example case of successful recanalization. 3D MR-VWI showed more information of occlusion site limited to C1 (triangle, A: curved from SPACE) with the distal lumen collapse (arrow, A) than CE-MRA (arrow, B)

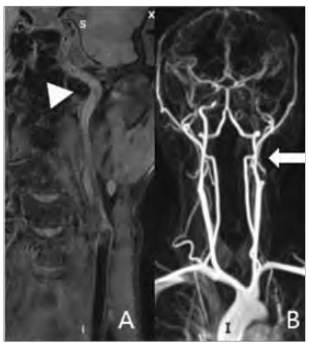

Fig.2 An example case of failure recanalization. 3D MR vessel wall imaging showed long occlusion from C1 to C6(triangle, A: curved from SPACE). B: CE-MRA

References

[1] Han Y, et al. *J Cardiovasc Magn Reson*. 2018;20(1):60.

[2] Zhang N, et al. *J Cardiovasc Magn Reson*. 2018;20(1):39.

[3] Xie Y, et al. *Magn Reson Med*. 2015;75(6):2286-94.

Chemical exchange saturation transfer (CEST) cardiovascular magnetic resonance for assessment of amyloid light-chain amyloidosis patients

Xiao Li[1], Si-si Huang[1], Jian Wang[1], Yi-han Cao[1], Zhengwei Zhou[2], Linda Azab[2], Zixin Deng[2], Debiao Li[2], Jing An[3], Yi-ning Wang[1], Zhengyu Jin[1]

1.Department of Radiology, Peking Union Medical College Hospital, Chinese Academy of Medical Sciences & Peking Union Medical College, Beijing, China.

2.Siemens Shenzhen Magnetic Resonance Ltd., Siemens MRI Center, Shenzhen, China.

3.Biomedical Imaging Research Institute, Cedars-Sinai Medical Center, Los Angeles, USA.

Purpose To investigate the feasibility of chemical exchange saturation transfer (CEST) cardiovascular magnetic resonance (CMR) to assess myocardial involvement in amyloid light-chain amyloidosis (AL) patients, and its correlation with classic CMR parameters.

Methods This prospective study recruited 20 AL patients (age, 56.9 ± 9.1 years; M/F, 14/6) who underwent gadolinium-enhanced CMR, and 20 healthy subjects (age, 52.7 ± 8.1 years; M/F, 11/9) who underwent non-contrast enhanced CMR. CEST images were acquired by an improved single-shot FLASH [1], and global myocardial signal was measured.

Results Compared to the healthy subjects, the CEST signal of AL patients was decreased significantly (1.24 ± 0.05 vs 0.83 ± 0.02, P <0.001). The hypointense region in the CEST map closely matched the bright area in the late gadolinium enhancement (LGE) image. In patients with negative LGE, CEST signal was already decreased (1.24 ± 0.05 vs 0.11 ± 0.09, P = 0.027).

Discussion The lower CEST signal in bright region of the LGE image is consistent with reduced metabolic activity. CEST CMR is a promising non-contrast technique to early diagnose myocardial involvement in AL patients.

References

1.Zhou Z, Nguyen C, Chen Y, et al. Optimized CEST cardiovascular magnetic resonance for assessment of metabolic activity in the heart. Journal of Cardiovascular Magnetic Resonance, 2017, 19(1):95.

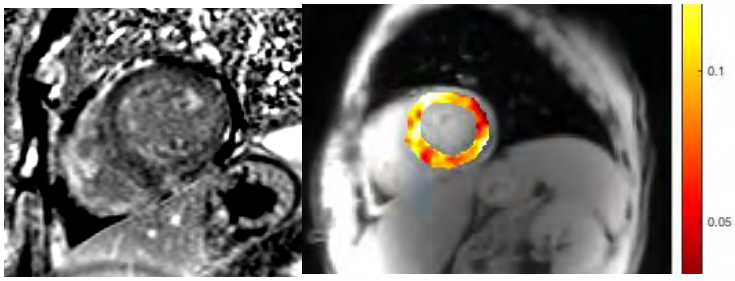

Fig 1. F/53y, Mayo Stage III, diffuse LGE and CEST signal hypointensity (0.09).

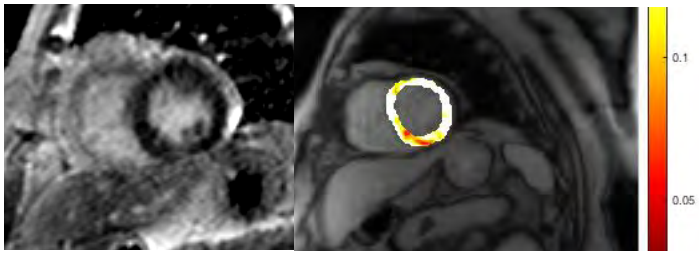

Fig 2. F/55y, Mayo Stage I, focal LGE and CEST signal hypointensity (0.13).

Ferumoxytol-Enhanced MRA for Evaluation of the Pulmonary Vascular Network

Arash Bedayat[1], Kim-Lien Nguyen[1,2], Ashley E. Prosper[1], John M. Moriarty[1], J. Paul Finn[1]

[1]Diagnostic Cardiovascular Imaging Laboratory, Department of Radiology, David Geffen School of Medicine at UCLA;
[2]Division of Cardiology, David Geffen School of Medicine at UCLA and VA Greater Los Angeles Healthcare System

Purpose: We aimed to compare the diagnostic performance of steady state ferumoxytol-enhanced magnetic resonance angiography (FE-MRA) with gadolinium-enhanced magnetic resonance angiography (Gd-MRA) to assess pulmonary vasculature in patients who underwent chest MRA.

Methods: In this IRB-approved and HIPAA-compliant study, thirty-six consecutive adult patients (age 51, IQR 17 – 77 years; 16 male) underwent FE-MRA, following slow infusion of ferumoxytol 4mg/kg. Thirty-six consecutive age and gender matched adult patients (age 51, IQR 17 – 77 years; 17 male) underwent Gd-MRA following infusion of gadobenate (Multihance, Bracco). Breath-held, high resolution steady state FE-MRA and Gd-MRA were acquired through the chest, abdomen and pelvis. Using a 5-point Likert image quality scale, a single reviewer blinded to clinical data scored the pulmonary arteries, superior and inferior pulmonary veins, inferior vena cava, and superior vena cava on single phase, steady state FE-MRA, and the first and second pass (arterial and venous delay) Gd-MRA. A score of 5 represented excellent intravascular opacification and well-defined vessel wall, Non-parametric tests were used for group comparison.

Results: All patients underwent technically successful FE-MRA and Gd-MRA without any adverse events. There was no significant difference between the two groups regarding age and gender ($p>0.05$). Compared to arterial phase Gd-MRA, the overall opacification of pulmonary arteries, IVC and SVC on FE-MRA was substantially better ($p=0.002$, Table 1). Opacification of inferior and superior pulmonary veins on FE-MRA and arterial phase Gd-MRA was comparable. Compared to venous phase Gd-MRA, the overall opacification of pulmonary arteries, superior and inferior pulmonary veins, IVC and SVC on FE-MRA was substantially better ($p=<0.001$, Table 1).

Discussion: Steady state FE-MRA is simple and powerful tool for visualization of the pulmonary vascular network. As an alternative to Gd-MRA, FE-MRA enables exquisite enhancement of the pulmonary vascular tree in patients who may not be candidates for Gd-MRA. Potential applications include diagnosis of pulmonary embolism and pulmonary hypertension. Integrative multimodal MRI with 4D-fflow imaging may offer additional insight into cardiopulmonary physiology and mechanisms of cardiopulmonary disease states.

References

1. Finn JP, et al. Ferumoxytol vs. Gadolinium agents for contrast-enhanced MRI: Thoughts on evolving indications, risks, and benefits. *J Magn Reson Imaging*. 2017 Sep;46(3):919-923.
2. Nguyen KL et al. MRI with ferumoxytol: A single center experience of safety across the age spectrum. *J Magn Reson Imaging*. 2017 Mar;45(3):804-812.

Table 1: Scoring for intravascular enhancement of the pulmonary vascular network on steady state FE-MRA relative to multiphase Gd-MRA

	PA	Inferior PV	Superior PV	IVC	SVC
FH-SS	4	4	4	4	4
Gd-arterial	3.5	4	4	1	1
Gd-venous	2	2	2	2	2

IPV, inferior pulmonary vein; IVC, inferior vena cava; PA, pulmonary artery; SS, steady state; SPV, superior pulmonary vein; SVC, superior vena cava

Towards Automated Cranial 4D Flow Cranial Analysis

Carson A. Hoffman[1], Grant S. Roberts[1], Sara Berman[2], Laura Eisenmenger[2], Oliver Wieben[1,2]
[1]Department of Medical Physics, University of Wisconsin, Madison, WI, [2]Department of Radiology, University of Wisconsin Madison, WI

Purpose

4D Flow MRI is a non-invasive imaging technique that enables the characterization of vascular anatomy and hemodynamics over a large imaging volume of interest. Detailed, multi-segmental analysis of the brain has been hindered by the complex cranial vasculature and long post processing times. Here we introduce an extension to a previously established 4D flow post processing tool[1] that automatically segments and quantifies hemodynamic parameters in all vessel segments without the need for user interaction. This simplified post processing pipeline allows for robust and repeatable analysis and provides users the ability to easily visualize and quantify complex cranial 4D flow datasets.

Methods

Ten cranial scans were acquired on healthy controls after patient consent and IRB approval. Imaging was performed on a clinical 3T scanner (MR750, GE Healthcare) using 4D flow MRI with an under-sampled radial acquisition, PC VIPR[2]. Imaging parameters included: image volume: 22x22x22 cm, isotropic spatial resolution = 0.68 mm; VENC = 80 cm/s; scan time: ~7 min, retrospective cardiac gating. The data was reconstructed into 20 cardiac phases with temporal radial view sharing[3] and image volumes of 320x320x320 voxels. Time-resolved flow analysis was completed in 13 locations: internal carotid arteries (ICA), basilar artery, middle cerebral arteries (MCA), posterior cerebral arteries (PCA), straight sinus, superior sagittal sinus, and transverse sinuses (TS).

An interactive 4Dflow processing tool (Figure 1) was implemented in Matlab2018b (Mathworks, Natick, MA) based on a previously established centerline flow processing scheme[1]. The interactive 4D tool provides improved angiograms, better centerline generation, quick vessel selection, automated background phase correction, easy visualization of quantitative parameters and less computer memory requirements. A quantitative flow comparison was completed between the original and the extended in-house tools by two individuals on PC workstations with 16GB and 32GB RAM. Analyzed outcomes included: ease of vessel selection (score), repeatability between users, time for flow analysis, and precision of local flow.

Results

The number of missed vessels reduced from 16.2% to 3.8% when analyzed in the extended 4D tool. The MCA, PCA, and TS accounted for 25 of the 26 missed vessels. Bland-Altman analysis of flow quantification between users had a reduction in mean difference and 95% confidence intervals (CI) from -0.1 [-1.88,1.68] ml/s with the old tool to 0.042 [-0.37, 0.45] ml/s with the new tool. The angiogram generation and centerline labeling times decreased from 48.6 sec to 13.2. The vessel selection and pulsatile flow verification times decreased from 15.2 min to 5.0 min (1.17 min and 0.38 min per plane), respectively. The average percent error in local flow quantification was 2.8±2.6% for the old tool and 2.9±2.2% for the new tool. A z score test on percent error between the 2 methods showed a mean and 95% CI of -0.071 [-0.5, 0.4] %.

Discussion

Both analysis tools showed a high repeatability between users with a slight improvement for the new 4D Flow tool. The extended 4D Flow analysis tool provided angiograms and centerlines with improved vessel visibility and selection capabilities for short and small vessel sections. Additional users and cases, which will be analyzed in the future, will help further investigate repeatability between tools. We have successfully added additional post processing functionality and visualization while reducing the time needed for completing a multi-vessel cranial analysis. The consistency of local flow measurements for both implementations showed an average error <3% maintaining the robust flow quantification at selected vessel locations. Future tool improvements are currently underway to allow the analysis of product 4D flow datasets from various clinical vendors (GE, Siemens, Philips). Such analysis tools with high repeatability and robustness will be needed for high volume and for long-term cranial flow studies.

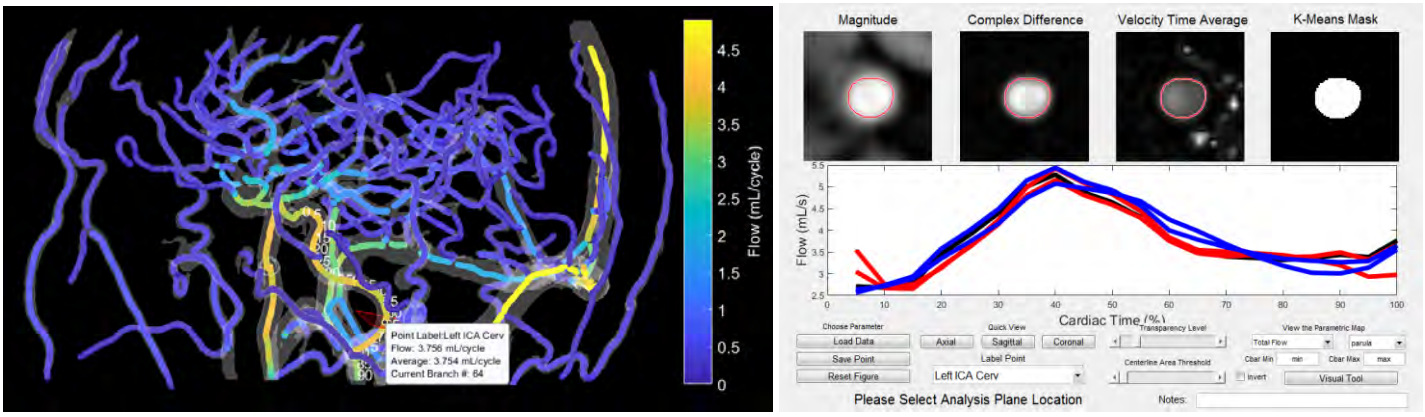

Figure 1 4D flow post processing tool with 3D interactive graphical user interface. Quantitative parameters (area, flow, pulsatility index, etc.) color encode the centerlines of all automatically segmented vessel. As the user moves the cursor in 3D the cross-sectional images and flow cycle are updated in real time.

References: [1] Schrauben, E. et al JMRI 2015;42:1458–64. [2] Johnson, K. M. et al MRM. 2008; 60(6), 1329-1336. [3] Liu, J. et al IEEE TMI 2006; 25(2):148-57.

4D Flow MRI and Doppler Wire Arterial Flow Analysis Pre-/Post-Liver Embolization in Swine

Carson Hoffman[1], Ece Meram[2], Sarvesh Periyasamy[3], Paul Laeseke[2], and Oliver Wieben[1,2]
[1]Medical Physics, University of Wisconsin Madison, Madison, WI [2]Radiology, University of Wisconsin Madison, Madison, WI [3] Biomedical Engineering, University of Wisconsin Madison, Madison, WI

Purpose

Transarterial embolization (TAE) describes the delivery of embolic particles via catheters in order to block the vascular supply of a region of tissue or tumor. It is an effective treatment for unresectable hepatocellular carcinoma (HCC) given the predominantly arterial blood supply of tumor cells as opposed to primarily portal venous supply of normal liver tissue, which induces selective ischemia and necrosis in tumors while largely sparing background liver tissue. The degree to which arterial branches are embolized is currently determined by qualitative radiographic techniques, leading to subjective clinical endpoints. The addition of quantitative information, pre- and post- intervention, would help in the assessment of baseline flow states and treatment-related changes, both of which are critical in determining optimal treatment pathways and endpoints. We hypothesize that 4D Flow MRI can improve the care of HCC patients by providing comprehensive quantitative hemodynamic information before and after TAE. In this feasibility study, we report on quantitative hepatic artery hemodynamics pre- and post-embolization in an in vivo swine model with 4D Flow MRI and doppler wire validation.

Methods

5 swine (~55 kg) were anesthetized with 1.5% isoflurane supplemented with O2. To help establish baseline hepatic flow states, first, 4D Flow MRI data of the abdomen were acquired with a radially undersampled sequence, PC VIPR[1], on a clinical 3T system (Discovery MR750, GE Healthcare): imaging volume: 32x32x32 cm, acquired spatial resolution=1 mm isotropic, VENC=50 and 100 cm/s, scan time: ~15 min; retrospective cardiac and respiratory gating. Three of the five subjects, were then transferred to an angiography suite where doppler wire (Volcano FloWire, Phillips) velocities were acquired just distal to the catheter tip in the common hepatic artery (CHA) and embolized vessel pre- and post- TAE. The proximal left or right hepatic artery was either partially or completely embolized with embolic particles (Embospheres, 100-300 µm) under fluoroscopic guidance. Finally, 4D Flow MRI was repeated with identical parameters ~20 min after the embolization. Flow Processing: PC MRI angiograms and velocity vector maps were generated via offline time averaged reconstruction. The hepatic arterial networks were segmented from the PC angiogram using Mimics (Materialize). Ensight (CEI) was used for the visualization of vessel anatomy and placement of analysis planes: CHA, left hepatic (LH), left medial (LM), left lateral (LL), right hepatic (RH), right medial (RM), right lateral (RL), and gastroduodenal (GDA) arteries. The analysis planes were exported to a customized software package[2] for dynamic manual vessel segmentation and hemodynamic analysis. Doppler wire velocities were analyzed with in house code developed in MATLAB R2018b (Mathworks, Natick, MA). Velocity values from pre- and post- embolization were compared between modalities to assess changes related to TAE.

Results

Before embolization, the summation of the average flow in either the 1st order (LH+RH+GDA) or 2nd order branches (LL+LM+RL+RM+GDA) , when normalized to the 0th order branch (CHA), were similar (1.11±0.35 and 1.11±0.34, respectively; Figure 1). The standard deviation of normalized flow values ranged from 30.5% in low order branches to 92.1% in high order branches. Based on fluoroscopic images, partial (~50%) stasis in 2nd swine, and near full stasis in 1st and 3rd swine were achieved. The velocity in the CHA decreased post-embolization for both 4D Flow MRI and doppler wire with greater reductions when embolizations were performed to full stasis. Residual flow in the embolized vessel in the 2nd swine (RH) allowed for post-velocity measurement (reductions of 46.7% for MRI and 46.1% for doppler wire) (Figure 2).

Discussion

4D Flow MRI was able to quantify flow in the 1st order and 2nd order hepatic arteries with conservation of flow (11% error). The levels of standard deviation could be related to the variations in vasculature between swine. The embolization endpoints affected the ability to resolve velocity changes in the embolized vessels as well as the variations in the CHA. 4D Flow MRI and doppler wires were successfully used to characterize embolization-related velocity changes in the hepatic arteries. The quantitative parameters provided by these techniques could supplement the current subjective assessment of embolization success which relies on the visual inspection of radiographic images.

References: 1) Johnson, K. M. et al MRM 2008; 60(6), 1329-1336. 2) Stalder AF, et al MRM 2008;60(5):1218-1231.

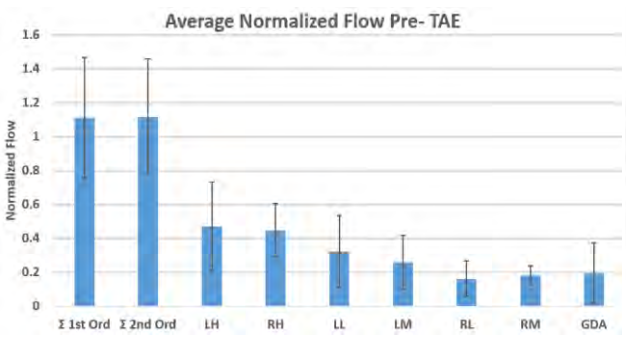

Figure 1 4D Flow MRI hepatic arteries normalized to the CHA. Conservation of flow showed good agreement for 1st order and 2nd order branches.

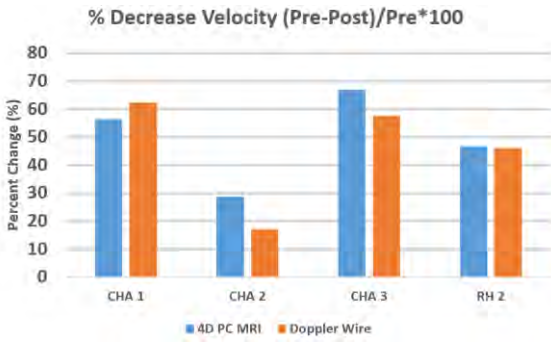

Figure 2 Percent velocity reductions in the CHA and embolized vessels. The variation between MRI and Doppler Wire is <10%.

Correlation based perfusion mapping using low-dose time-resolved contrast enhanced MRA: Preloaded contrast media does not affect its image quality

Bum-soo Kim, Yoon-Ho Nam, Yangsean Choi, Jinhee Jang, So-Lyung Jung, Na-Young Shin, Kook-Jin Ahn

Department of Radiology, Seoul St.Mary's Hospital, The Catholic University of Korea, Seoul Korea

Purpose: Correlation based time-delay (CTD) map generated from time-resolved contrast enhanced MRA (TR CEMRA) is robust technique to estimate correlation-based time-delay for relatively low signal-to-noise of low-dose TR CEMRA. The purpose of this study was to explore the effect of preloaded contrast media upon the CTD map in the evaluation of patient with carotid stenosis.

Materials and Methods: Twenty-four patients who have stenoocclusive lesion underwent DSA, and two sets of supraaortic low dose TR CEMRA with injection of half dose (0.05 mmol/kg gadolinium-based contrast agent), respectively. The second acquisition was done at 3 minutes after completion of 1st sequence. CTD maps of the brain were automatically generated from supraaortic low-dose TR CEMRA data. Mean time-delay was automatically calculated from 9 predefined areas of each cerebral hemisphere. Mean time-delay, arterial input and venous output were all compared for those from 1st and 2nd TR CEMRA by paired sample t-test.

Results: There was no statistical difference in mean time delay in total 18 predefined areas between CTD maps from 1st and 2nd TRCEMRA, and those parameters all showed high paired sample correlation ($p<0.01$, r value 0.769~0.927). In patients with SPECT available, Time delayed lesion on CTD map well matched with perfusion lesion on the SPECT (Fig. 1).

Conclusion: Preloaded contrast media does not influence time-delay on CTD map of patients with carotid stenoocclusive disease.

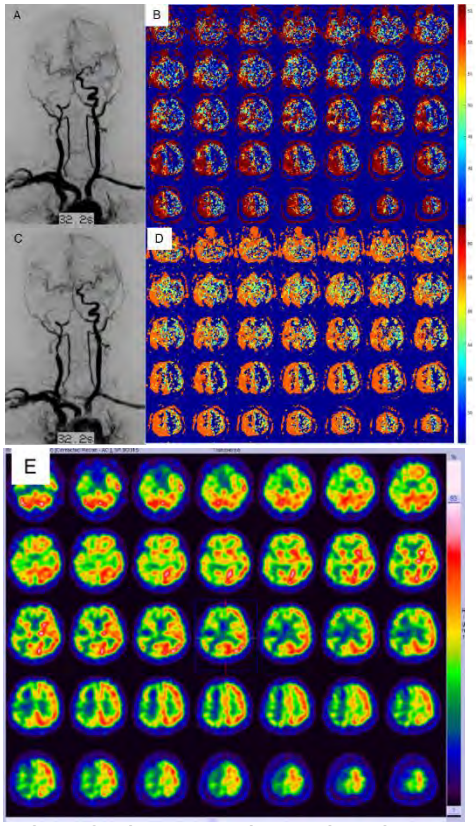

Fig.1.The 1st TR CEMRA (A) and CTD map (B) well correlates with 2nd TR CEMRA (C) and CTD map (D), in demonstration of occlusion of right internal carotid artery, and relevant time-delay in right MCA and ACA territories. Those lesions are well matched with perfusion defect on SPECT (E).

References:

1. Nam Y, Jang J, Park SY et al., Correlation-based perfusion mapping using time-resolved MR angiography: A feasibility study for patients with suspicions of steno-occlusive craniocervical arteries. Eur Radiol 2018;(11):4890-4899

MRV Depiction of Anatomical Variations of the Femoral and Popliteal Veins

Peter Douglas & Giles Roditi

NHS Greater Glasgow & Clyde, Glasgow, Scotland

Introduction - Anatomical variations of the popliteal and femoral veins are relatively common and can have important clinical implications [1,2]. However, they are rarely described in the modern imaging literature and in our experience not well known by radiologists. This is likely because conventional venography is now hardly ever performed and did not describe the deep anatomical course well while these veins are also not well depicted or recognised by ultrasound (sthe commonest imaging modality) nor evaluated by CT. However, the deep veins are just as well depicted as the superficial leg veins on MRI which shows their anatomical course exquisitely.

Methods - The images of 200 consecutive patients undergoing our standard previously described extended phase high spatial resolution contrast-enhanced MRA studies of the femoropopliteal segments were retrospectively evaluated for variations in anatomy of the femoropopliteal venous segments. These were categorised as per the classification of Uhl, Gillot and Chahim [1].

Results – Standard modal anatomy of the femoropopliteal venous segment was the commonest situation but variant bitruncular (duplicated femoral and/or popliteal segments of varying lengths) anatomy is common and less commonly unitruncular configurations (axiofemoral and deep femoral) were found in similar proportions to the anatomical studies - examples of each including mixed variations are presented.

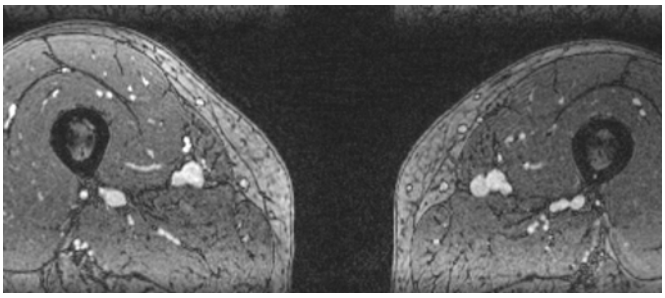

Example of patient with bilateral femoral vein duplications plus axiofemoral vein variant in the right leg.

Discussion - Variants of femoropopliteal venous anatomy are common, venous evaluation is easily added to standard arterial MRA studies and the finding of duplicated femoropopliteal segments can allow their use in reconstruction surgery when superficial veins are unsuitable.

1 - Anatomical variations of the femoral vein. Uhl J-F, Gillot C and Chahim M. Jouranl of Vascular Surgery Volume 52, Number 3

2 - Variations in Lower Limb Venous Anatomy: Implications for US Diagnosis of Deep Vein thrombosis. Quinlan D J, Alikhan R, Gishen P & Sidhu PS. Radiology 2003; 228:443–448 s

Fusion of computational fluid dynamic flow data into 4D flow MRI using machine learning

David Rutkowski[1], Dahan Kim[2], Shiva Rudraraju[1], Alejandro Roldan[1], Kevin M. Johnson[3,4]
Depts. of Mechanical Engr.[1], Physics[2], Medical Physics[3], and Radiology[4], University of Wisconsin-Madison

Purpose: Hemodynamic metrics can be of great value in cardiovascular disease diagnosis and treatment planning (1). Such metrics can be derived from three-dimensional, time-resolved, velocity information that is measured with four dimensional (4D) flow magnetic resonance imaging (MRI) (2). Yet, the flow field information provided by 4D flow MRI can be flawed due to image noise and the relatively low spatial resolution in small vascular geometries. Alternatively, computational fluid dynamics (CFD) can provide much higher spatial and temporal flow resolution. Furthermore, its basis in the governing equations of fluid flow leads to physics-bounded solutions. However, the validity of CFD is limited by its reliance on patient-specific geometries and input boundary conditions. The purpose of this work is to develop a machine learning paradigm (Figure 1) which fuses information from 4D flow MRI and CFD using supervised learning, to provide high resolution, physics-based, patient-specific flow fields.

Methods: First, a CFD based training was created using subject derived and mock vessel geometries. Five cerebral vascular geometries were derived from high-spatial-resolution digital subtraction angiography (DSA) data. These five vascular geometries were then manually modified by changing inlet and outlet vessel angles and aneurysm shape and size in 3-matic (Matrialise, Leuven, Belgium) to create 25 physiologically-plausible vascular geometry iterations. Additionally, five mock vessels were designed in Solidworks (Dassault Systèmes) to represent a wider variety of flow path configurations. The 30 vascular geometries were then imported into CONVERGE CFD Software (Convergent Science, Madison, WI), where blood flow simulations were performed at 6 different physiological-based pulsatile inlet flow waveforms, for a total of 180 simulations (figure 1a,b). The high resolution CFD flow fields were then used to train a convolutional neural network (CNN) to estimate velocity fields from corrupt velocity field, generated from simulating a 4D flow data acquisition (per minibatch) accounting for random levels of complex domain gaussian noise, background signal, and spatial resolution reduction. Aggressive data augmentation was used including spatial rotations and flips, and velocity scaling. A blockwise, 3D residual based CNN was used with a 32 cubic input patch in the high resolution CFD domain, using a mean square error loss metric. Finally, preliminary results were generated applying the CNN to whole brain 4D flow (3) in subjects with known neurovascular disease.

Results: 180 CFD simulations were run until convergence, with an average optimized run-time of approximately 1.5 hours per case. Flow results were converted to image format and semi-automatically cropped at vessel boundaries to remove areas of potential flow divergence in the images. The resulting CFD data was run through the neural network with a computation time of approximately 12 hours. When the trained network was applied to a corrupted velocity field with added error, background noise was decreased by 64%, and velocity error was reduced from 20% in the corrupted velocity field to 8% in the post-training velocity field.

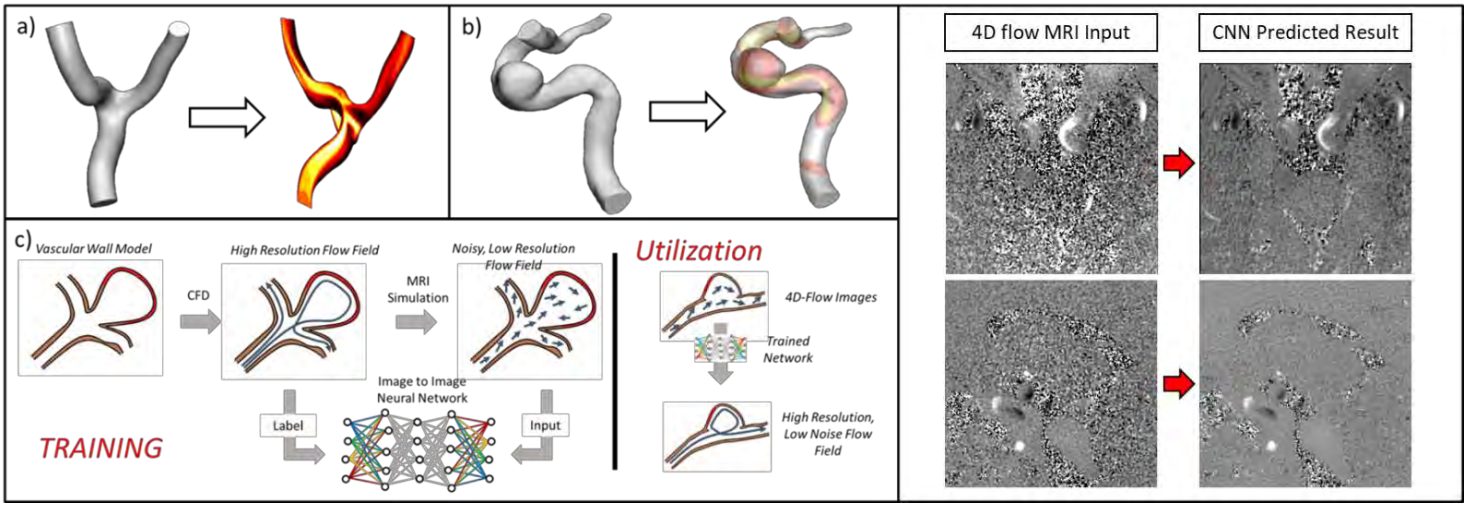

Figure 1: Machine learning strategies are used to improve 4D flow MRI flow data with computed flow fields from CFD. a) Mock vessel geometry and simulated flow results b) patient-specific aneurysm geometry and simulated flow field c) neural network training and utilization method overview d) Test case results using the trained network.

Discussion: Augmentation of 4D flow MRI data with CFD-informed training networks may provide a method to produce highly accurate physiological flow fields. In this preliminary work, the potential utility of such a method was demonstrated with high resolution patient-specific CFD data and a simulated MRI flow test case. Next steps include validating the neural network in patient flow data and fixing other common flow imaging errors and limitations, such as aliasing and phase wrapping, intra-voxel dephasing, image artifacts, and resolution limits. In future work, such data may be utilized to improve 4D flow MR images with the trained network, therefore improving the quality of clinically-relevant flow results that can be obtained with 4D flow MRI.

References:

1. Sengupta PP, et al. JACC Cardiovasc Imaging 2012;5(3):305-316.
2. Markl M, et al. J Magn Reson Imaging 2012;36(5):1015-1036.
3. Johnson KM, et al. Magn Reson Med 2008;60(6):1329-1336.

Multi-scale brain pulsatility assessment using accelerated spiral MRI: Initial Feasibility

Leonardo A. Rivera-Rivera[1], Dahan Kim[2], and Kevin M. Johnson[1, 2]
[1]Medical Physics, [2]Radiology, University of Wisconsin-Madison, Madison, WI, United States

Purpose: Pathologies such as dementia can manifest with altered biomechanics in different compartments at different scales (e.g. vessels, capillaries, tissue) [1]. Noninvasive quantitative assessment of vascular flow and tissue motion is feasible with MRI; however, scan times can be long due to requirements for volumetric time-resolved imaging and the need for multiple acquisitions to encode a wide dynamic range. Spiral trajectories [2] offer the opportunity to reduce scan times and additionally reduce echo time for robust motion encoding schemes with manageable scan times. In this study, we test the feasibility of a multi-scale brain imaging platform for velocity and displacement encoding with spiral sampling using 3D PC and 2D DENSE MRI.

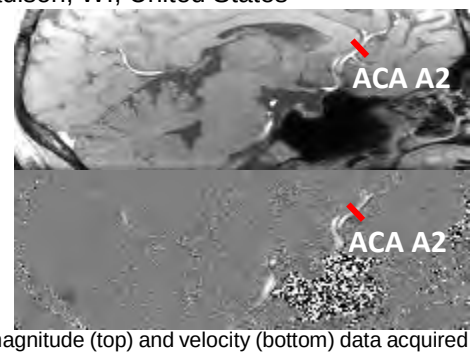

Fig 1: 4D flow magnitude (top) and velocity (bottom) data acquired with spiral readout and Venc of 80 cm/s allows assessment of flow in small arteries including A1, A2 and A3 segments of the anterior cerebral artery.

Methods: *Subjects*: Eight healthy volunteers (mean age = 29 ± 6y, 1F) participated in this study. *MRI: Two* volumetric, time-resolved PC MRI data with 3-directional velocity encoding were acquired on a 3.0T clinical MRI system (Signa Premier, GE Healthcare) using a 48-channel head coil (GE Healthcare) with a 3D distributed spirals undersampled sequence [3,4], with the following imaging parameters: V_{enc} = 80 cm/s, a separate acquisition with V_{enc} = 7.5 cm/s, imaging volume = 24x24x8 cm^3, 0.75x0.75x1 mm^3 resolution and TR/TE=7.8/2.2 ms (for high V_{enc}), 0.94x0.94x1 mm^3 resolution and TR/TE=18/3.9 ms (for low V_{enc}) and scan time ~ 5.5 min/per scan. Image reconstruction was performed retrospectively using a local-low rank constraint with block shifting of 8x8x8 blocks and a manually tuned regularization parameter [5]. Using peripheral gating data, velocity images were reconstructed into 10 cardiac phases. In addition, prospectively gated 2D single shot spiral DENSE images were acquired in the same MRI system using a ramped flip angle approach [6]. Imaging parameters include D_{enc} = 0.175 mm, 5 slices, FOV = 24x24x1 cm^3, 3.75x3.75 mm^2 in-plane resolution, 10 cardiac time frames, TR/TE ~ 100/2.1 ms and scan time ~ 40sec per slice. Phase data from 4D flow and 2D DENSE images were unwrap using a Laplacian approach prior generation of velocity and displacement images [7]. Cut planes and ROIs were place in MATLAB to quantify flow in the internal carotid and basilar arteries (ICA, BA) and CSF in cerebral aqueduct. Tissue displacement was measured from ROIs placed in the slice at the level of the cerebral aqueduct.

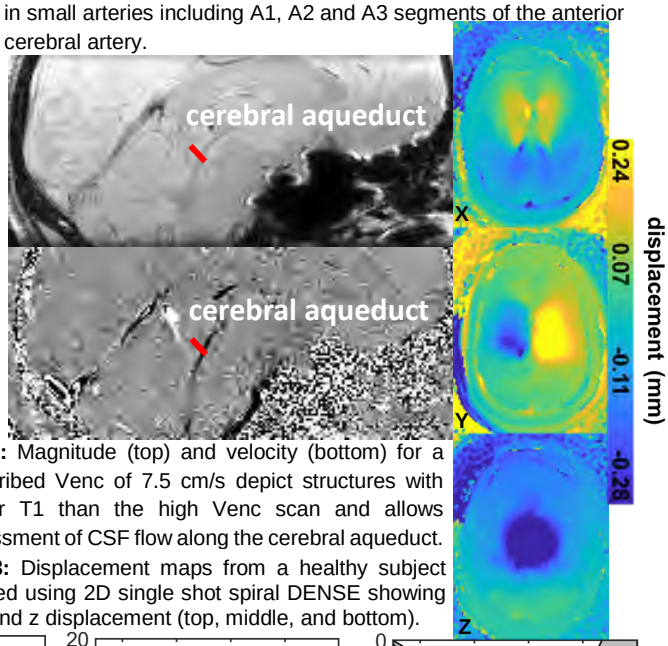

Fig 2: Magnitude (top) and velocity (bottom) for a prescribed Venc of 7.5 cm/s depict structures with longer T1 than the high Venc scan and allows assessment of CSF flow along the cerebral aqueduct.

Fig 3: Displacement maps from a healthy subject derived using 2D single shot spiral DENSE showing x, y and z displacement (top, middle, and bottom).

Results: Figure 1 shows magnitude images derived from the high V_{enc} acquisition on a healthy volunteer. The spiral based acquisition shows high spatial resolution and depiction of small arteries including at the A3 level. Figure 2 shows results from a low V_{enc} acquisition, where high resolution magnitude and velocity data allows assessment of CSF in the cerebral aqueduct. Tissue displacement maps are shown in figure 3. Quantitative measures are displayed in figure 4, where blood flow in the ICA & BA (a), CSF flow (b), and tissue displacement (c) are characterize along the cardiac cycle.

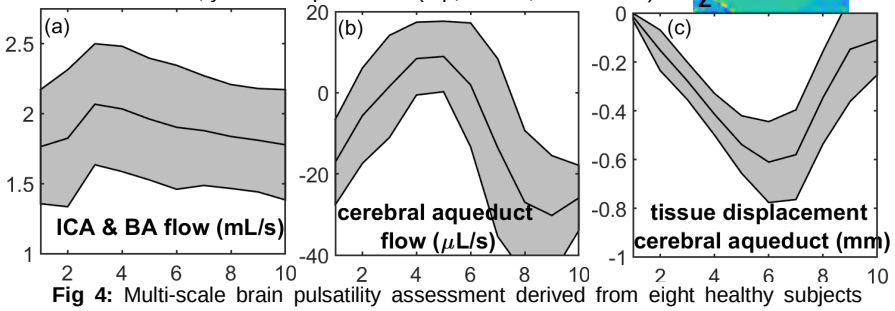

Fig 4: Multi-scale brain pulsatility assessment derived from eight healthy subjects (n=8): (a) flow in the ICA & BA derived using a 4D flow with spiral readout acquisition with high Venc (80 cm/s), (b) flow in the cerebral aqueduct using a low Venc (7.5 cm/s) acquisition and (c) displacement from tissue proximal to the cerebral aqueduct derived using 2D single shot spiral DENSE with Denc = 0.175 mm.

Discussion: Spiral based 4D flow MRI shows improved depiction of small arteries that are difficult to resolve using standard radial 4D flow MRI. This allows pulsatile flow assessment in large and small arteries. A low V_{enc} acquisition can then be used to probe CSF flow pulsatility in different regions of the brain. CSF pulsatile flow can be related to the cardiac cycle and cerebral arteries. Finally, tissue response to the cardiac cycle, arterial and CSF pulsations can be characterize with displacement maps using DENSE. A delayed response to the arterial peak is observed in CSF flow, followed by tissue displacement response, which suggests cerebrovascular compliance. In this study we have demonstrate the feasibility of a platform for multi-scale brain pulsatility assessment allowed by rapid MRI with spiral readouts in <15min. This platform holds potential to probe disease such as dementia, high intracranial pressure [8] and others.

References: [1] Sweeney MD, et al. Alzheimer's & Dementia. 2019; 15(1):158-167. [2] Kasper L, et al. Neuroimage. 2018; 168:88-100. [3] Johnson KM, et al. MRM. 2008; 60(6): 1329–1336. [4] Turley DC, et al. MRM. 2013 70:413–419. [5] Jimenez JE, et al. MRM. 2018; 80(4):1452-1466. [6] Adams AL, et al. NMR Biomed. 2019; 32(2). [7] Loecher M, et al. JMRI. 2016; 43(4):833-42. [8] Saindane AM, et al. AJNR. 2018; 39(2):311-316.

Accelerated 4D-flow MRI using Machine Learning (ML) Enabled Three Point Flow Encoding

Dahan Kim[1], Laura Eisenmenger[3], and Kevin M. Johnson[2,3]
Departments of Physics[1], Medical Physics[2], and Radiology[3], University of Wisconsin – Madison, USA.

PURPOSE: 4D-flow MRI is a valuable tool for characterizing cardiovascular disease (1,2); however, its utilization is often hindered by the long scan time resulting in part from the necessary multiple velocity encodings. In general, a minimum of four encodings are required to solve voxel-wise for three velocity components and a reference background phase (3) from susceptibility, chemical shift, coil phase, and gradient errors. The background phase is spatially complex in spoiled gradient echo (sGRE) based 4D-flow; however, in the case of bSSFP flow encoding in the neck, phase reference free imaging has been achieved in the neck using polynomial background phase fitting (4). This has not been extended to sGRE imaging or other complex organs. Yet, recent progress in the related problem of phase estimation in deep learning based quantitative susceptibility mapping (QSM) (5) suggests machine learning may be capable of learning spatially complex phase fields. Given this, we hypothesize is that a properly trained convolutional neural network (CNN) has potential to determine the background phase inherently from spatial fitting without requiring an explicit encoding. In this work, we examine the feasibility of using CNN to accurately determine three velocity components from only three flow encodings, potentially reducing the scan time of 4D-flow MRI by 25%.

METHODS: Data was included from subjects undergoing whole brain 4D-flow (6) with 4-point referenced encoding and 0.7mm isotropic resolution. 3-directional velocity components were first determined using all 4 encodings (called 'actual velocities') using standard reconstruction including background phase offset corrections. 113 subjects were used for training and 28 subjects were used for testing and evaluation. For machine learning, we used a fully 3D CNN with U-net architecture (7) that takes randomly selected 64x64x64 sub-volumes instead of the entire image volume. The complex-valued images of the 3 flow encodings were used as an input for the CNN, which learned to estimate 3 velocity components (called 'estimated velocities') minimizing mean square error loss. Following training, 3 velocity components were estimated by CNN using only the 3 flow encodings and were compared against the actual velocities determined from 4 encodings. The estimated velocities produced by CNN were once again corrected for any residual background phase to determine if the CNN successfully learned background phase eddy current corrections.

RESULTS: There was no meaningful difference between the estimated velocities with and without additional background phase correction, indicating that the CNN successfully estimated the background phase from 3 flow encodings (see Table 1). There was high correlation between estimated and actual velocities (R^2=0.9718 and 0.9716, with and without additional background phase correction, respectively), indicating that CNN estimated velocities from 3 encodings with high precision. For all 3 velocity components, the slope was 5% less than 1 (0.9514 and 0.9501, with and without additional background phase correction), indicating that, while the CNN estimates the velocities with high precision, it systematically underestimated the velocities by 5%.

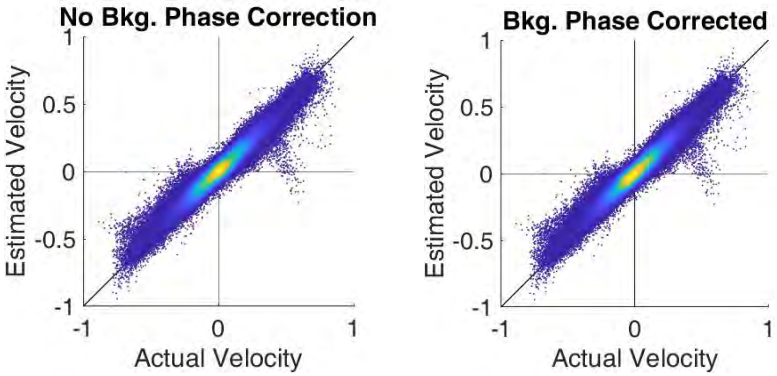

Figure 1. Correlation between velocity estimated by CNN using 3 flow encodings and actual velocity determined from 4 encodings.

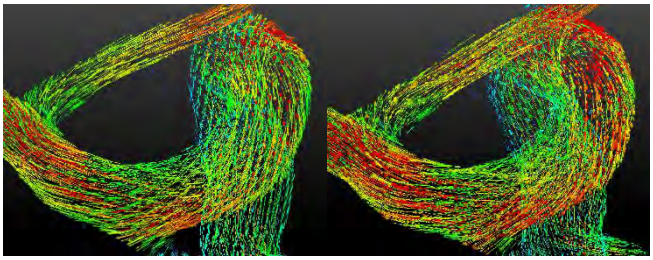

Figure 2. 3D-rendering of ICA and MCA blood flow using the proposed ML-enabled 3-encoding method (right) and 4-encodings (left)

	No Bkg. Phase Correction	Bkg Phase Corrected
Correlation (R^2)	0.9716	0.9718
Slope	0.9501	0.9514
y-intercept	0.0012	0.0017

Table 1. Statistical measures of correlation between ML-estimated velocities from 3 encodings and actual velocities from 4 encodings, with and without additional background phase correction.

DISCUSSION: This work demonstrates that a CNN can successfully estimate background phase and 3 velocity components in 4D-flow MRI using only 3 flow encodings, thus potentially reducing the scan time by 25%. However, the source of 5% under-estimation of velocity values still requires further investigated.

REFERENCES:

1. Markl et al. JMRI 2007; 25(4):824-831
2. Ebbers et al. MRM 2001; 45(5):872-879.
3. Johnson et al. MRM 2012 63(2): 349-355
4. Nielsen et al. MRM 2009; 61(5): 1096-1102.
5. Rasmussen et al. bioRxiv 278036.
6. Gu et al. AJNR 2005 26(4):743-9
7. Ronneberger et al. arXiv: 1505.04597 7.

Imaging the Circle of Willis with 3D Time of Flight MRA – A Comparison between Spiral and Cartesian Acquisition at 1.5T

Hui Wang[1, 2], Matthew Lanier[1], Melvyn Ooi[3], Dinghui Wang[4], Gregory Lee[1], Brynne Williams[1], Lacey Haas[1], Kelsey Wineland[1], and Charles Dumoulin[1]

[1]Radiology, Cincinnati Children's Hospital Medical Center, Cincinnati, OH, USA [2]Philips Healthcare, Cincinnati, OH, USA, [3]Philips Healthcare, Phoenix, AZ, USA, [4]Mayo Clinic, Rochester, MN, USA

Purpose

Non-contrast MR angiography (MRA) is an important technique for the diagnosis and follow-up of vascular diseases, especially in children, a population where gadolinium contrast material administration should be minimized given recent concerns with gadolinium retention in the body. Time of Flight (TOF) MRA using Cartesian coverage of k-space is routinely used in the evaluation of intracranial vessels (1). Spiral MRI (2-3) provides several advantages vs. routine (Cartesian) MRI, including scan efficiency (4), and robustness to flow (5), aliasing, and geometric distortions. However, spiral MRI has not gained widespread clinical adoption due to its greater demands on system fidelity, and reconstruction complexity. In this study we compared 3D Time of Flight (TOF) sequences using Cartesian and spiral coverage of k-space to investigate their relative value in MRA of the Circle of Willis (COW).

Methods

All imaging was performed on a Philips Ingenia™1.5T scanner using a standard 15 channel phased array head coil. Five healthy volunteers were scanned in this feasibility study. For each subject, three scans were acquired. The first scan was a standard Cartesian 3D FFE sequence. The second scan was a spiral 3D FFE sequence with single echo (Spiral-Fast), and the third scan was a spiral 3D FFE sequence with dual-echo Dixon method (6). The 3D Spiral sequence was a stack of spirals with fully sampled spiral-out readout (7). The reconstruction was performed on the scanner console (~1sec/slice). Field of view (FOV) (200 x 200 x 80 mm^3) and voxel size were matched between Cartesian scan (0.5 x 0.8 x 1.4 mm^3) and Spiral scans (0.63 x 0.63 x 1.4 mm^3). The Cartesian parameters used were: TR/TE = 25/6.9 msec, 20º flip angle, a sampling window (tau) of 11.5 msec and a partial echo acquisition of 62.5% in the readout direction, scan time = 3:02 min. The Spiral-Fast parameters were: TR/TE = 34/2.3 msec, 23º flip angle, scan time = 1:23 min. The Spiral-Dixon parameters were: TR/TE1/TE2 = 39/1.9/4.2 msec, 24º flip angle, scan time = 2:53 min. Both spiral scans used tau = 19.8 msec and 21 spiral interleaves per kz-encoding. All three scans had 4 chunks with 20 mm slab thickness. The 3D slab was excited with a Tilted Optimized None-saturating Excitation (TONE) pulse (8), which results in a linear varying flip angle over the slab.

Results

In all subjects, all scans were acquired successfully. Fig 1 shows the maximum intensity projection (MIP) of one volunteer with Cartesian, Spiral-Fast, and Spiral-Dixon. Spiral-Fast sequence performs 2.2 times faster than Cartesian acquisition for 3D TOF MRA in COW imaging, with comparable image quality. Spiral-Dixon has comparable scan time to Cartesian, but shows clearer vessel delineation with superior fat suppression.

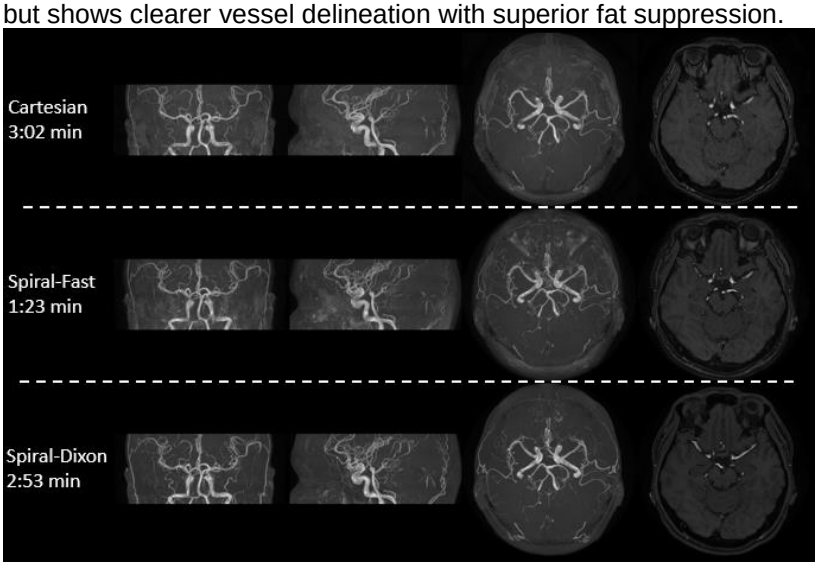

Fig.1 MIP images in the coronal (1st column), sagittal (2nd column), and axial (3rd column) directions for 3D Cartesian ToF (top row), fast Spiral ToF (middle row), and Spiral-Dixon ToF (bottom row). The 4th column are source images from the middle slice.

Discussion

We have demonstrated that spiral 3D TOF MRA is feasible in scanners with standard hardware configurations and online reconstruction. Spiral MRA can achieve shorter scan time, due to the high efficiency in sampling k-space. Combining with Dixon technique, Spiral can achieve superior results with better fat suppression. Therefore, it is suitable for pediatric population who are usually less tolerant in longer scans. The next step is to validate this technique in pediatric patients.

References

[1] Nishimura DG. MRM 1990; 14:194-201. [2] Ahn CB et al. IEEE Trans Med Imaging 1986;5(1)2-7. [3] Meyer CH et al. MRM 1992;28(2):202-213. [4] Pipe JG et al., ISMRM 2010; p3114. [5] Nishimura DG et al., MRM 1995;33(4):549-556. [6] Zwart NR et al., ISMRM 2016; p1834. [7] Pipe JG et al., MRM 2014;71(1):278-285. [8]. Atkinson D. et al, Radiology 1994;190(3), 890-894.

Plaque Burden of Carotid Atherosclerotic Stenosis Influences Collateral Circulation

Huimin Xu[1], Ran Huo[1], Ying Liu[1], Jin Li[2], Zheng Wang[1], Huishu Yuan[1], Xihai Zhao[3]

1. Department of Radiology, Peking University Third Hospital, Beijing, China; 2. The Affiliated BenQ Hospital of Nanjing Medical University, Nanjing, China; 3. Center for Biomedical Imaging Research, Tsinghua University, Beijing, China.

Background and Purpose: Collateral circulations compensate blood flow for patients with decreased cerebral perfusion. The status of collaterals is significantly associated with clinical outcomes. Secondary collaterals, such as leptomeningeal anastomoses, may be anatomically present, but the enhancement of their capacity likely requires time to develop [1]. It is believed that the development of collaterals is heavily dependent on the diminished blood pressure in upstream vessels [2], such as carotid artery luminal narrowing. Since there is positive remodeling effect for elastic arteries, the progression of plaque burden may not be parallel with degree of luminal stenosis [3]. However, the relationship between carotid plaque burden and status of secondary collaterals for patients with similar degree of chronic carotid artery stenosis is still unknown. **This study aimed to determine the association of carotid plaque burden measured by MR vessel wall imaging with status of secondary collaterals in patients with chronic carotid stenosis.**

Methods: **Study sample**: Patients with carotid moderate to severe stenosis (50-99% stenosis) were recruited and underwent CT and MR imaging. The exclusion criteria were as follows: 1) hemorrhagic stroke; 2) cerebral neoplasms; 3) heart failure; 4) renal dysfunction (GFR<60ml/min); 5) iodine contrast agent allergy; 4) contraindications to MR examination. **Multiphase CTA**: The whole brain CT perfusion was performed on a 256-row wide-body detector CT scanner with 16 cm z-axis coverage, 0.5 mm slice thickness. It was initiated 8s after contrast agent injection by 10 scans and a 2 s interval, followed by 7 scans and a 4 s interval. The total scan duration was 56s. **MR imaging**: All patients underwent carotid MR vessel wall imaging on a 3.0T MR scanner with 8-channel carotid coil to acquire the following sequences: 3D time-of-flight, TR/TE 17.6/6.7 ms, flip angle 8°, and slice thickness 2 mm; 2D T1-weighted: TR/TE 850/13.44 ms, slice thickness 2 mm; 2D T2-weighted: TR/TE 2000/96.6 ms, slice thickness 2 mm; and Simultaneous Non-contrast Angiography intraplaque hemorrhage (SNAP) imaging: TR/TE 9.6/4.0 ms, flip angle 12°, and slice thickness 1 mm. The FOV, spatial resolution and longitudinal coverage was respectively 140×140 mm^2, 0.55×0.55 mm^2, and 32 mm for all imaging sequences. **Image review**: The collateral circulation score was calculated on multiphase CTA images using a 6-point scale [4]. The collaterals were divided into good collaterals (score=4-5) and poor collaterals (score=0-3) status. The plaque components including lipid-rich necrotic core (LRNC), intraplaque hemorrhage (IPH) and calcification (CA) were identified and the Max WT and luminal stenosis were measured for the index artery with most severe stenosis bilaterally. **Statistics**: Carotid plaque features were compared between patients with good and poor collaterals using Mann-Whitney U test or Chi-square. Univariate and multivariate logistic regressions were used to determine the correlation between plaque features and poor secondary collaterals.

Results: Of 93 included subjects (mean age, 65.2±8.2 years; 78 males), 74 (79.6%), 90 (96.7%), and 71 (76.3%) had carotid CA, LRNC, and IPH, respectively. Patients with poor collaterals had significantly larger Max WT than those with good collaterals (6.6±1.9 mm vs. 5.4±1.4 mm; *P*=0.010, **Fig. 1**). No significant differences were found in prevalence of plaque components between patients with poor and good collaterals (all *P*>0.05). Max WT was significantly correlated with poor collaterals before (odds ratio, 1.68; 95% CI, 1.14 to 2.42; *P*=0.009) and after (odds ratio, 1.82; 95% CI, 1.19 to 2.79, *P*=0.006) adjusted for clinical risk factors and carotid stenosis. No significant correlations were found between other plaque features and poor collateral status (all *P*>0.05).

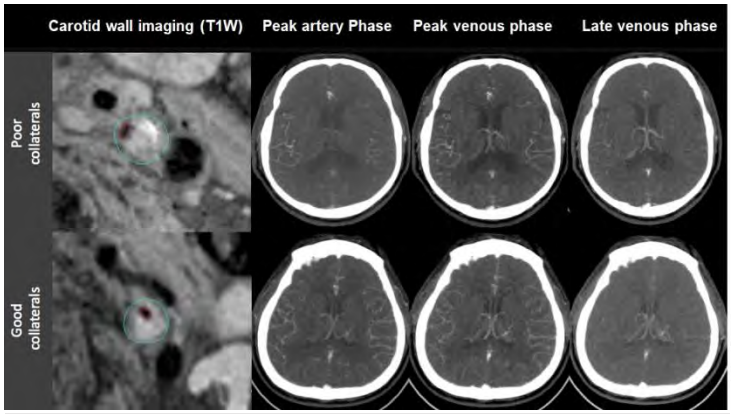

Fig.1 Two male patients had left carotid severe stenosis and poor (upper row: a 71 yrs patient with Max WT=7.5mm) and good (lower row: A 67 yrs patient with Max WT=3.8mm) collaterals.

Conclusions: Carotid artery Max MT is independently associated with secondary collateral status, suggesting that patients with larger carotid plaque burden may develop poorer leptomeningeal collaterals.

References: [1]. Stroke. 2003;34:2279-84. [2]. Neurology. 1957;7:447-58 [3]. 2011;42:347-53. [4]. Radiology. 2015;275:510-20.

Title: Automating Background Phase Correction in Cranial 4D Flow MRI

Grant S. Roberts[1], Kevin Johnson[1,2], Carson A. Hoffman[1], Laura Eisenmenger[2], Oliver Wieben[1,2]
[1]Department of Medical Physics, University of Wisconsin-Madison, WI, [2]Department of Radiology, University of Wisconsin-Madison, WI

Purpose: Phase contrast (PC) MRI is based on the principle of motion encoding using bipolar magnetic field gradients. In standard PC MRI, velocity along the gradient direction is directly proportional to a phase accrual in image space. However, many other factors contribute to phase changes unrelated to velocity, thus necessitating additional steps to generate quantitative velocity maps including: (1) the acquisition of 2 images to calculate a phase difference image rather than an absolute phase image with confounding factors; corrections for phase distortions from (2) non-linear gradients and (3) concomitant gradients[1]. Yet, there are still remaining phase errors from sources that are difficult to model deterministically, predominantly from (4) eddy currents. These can be removed by a subsequent scan with a stationary phantom and identical acquisition parameters[2] or, more frequently, through modeling of slowly-varying background phase corrections (BPC) based on static tissue. However, it requires user interaction for the identification of static tissue[3] and remains a source of error[4]. Also, it can be particularly time-consuming in 4D flow acquisitions because of its large volumetric coverage. The purpose of this study is to evaluate the performance of a fully automated 3D BPC algorithm embedded into the reconstruction with and without additional interactive BPC processing.

Methods: Ten healthy 4D flow brain scans were acquired to evaluate the degree of BP errors after: **1**) no BPC **2**) manual BPC **3**) automatic BPC **4**) both automatic and manual BPC, which is used in our current pipeline. Imaging was performed on a clinical 3T scanner (MR750, GE Healthcare) using a radially-undersampled 5-point PC-VIPR[5] acquisition with the following parameters: volume = 22x22x22 cm^3, isotropic spatial res. = 0.69 mm; VENC = 80 cm/s; scan time = 7 min., and retrospective cardiac gating (20 cardiac frames). Manual BPC was performed in a custom MATLAB GUI (Figure 1), where the user separates background tissue by adjusting thresholds for low magnitude (noise threshold) or high velocity (complex difference [CD] threshold). Similarly, the automated and integrated BPC algorithm identifies these 2 threshold values to perform the same procedure. Both methods use a 3rd degree volumetric polynomial fit to estimate phase variations in the background tissue for each velocity direction (x,y,z) (Figure 2). The effectiveness of the 4 BPC methods was evaluated using the mean absolute error (MAE) averaged over each velocity dimension: $\overline{MAE} = \frac{1}{3}\left(\sum_{d=1}^{3}\sum_{n=1}^{N}\frac{|\bar{v}_{d,n}-fit_{d,n}|}{N}\right)$ where $|\bar{v}_{d,n} - fit_{d,n}|$ is the absolute difference between the time-averaged velocity and polynomial fit in dimension *dim* at voxel *n* in the 3D image. Additionally, the noise and CD thresholds obtained by the manual BPC were compared to the thresholds in the automatic reconstruction BPC.

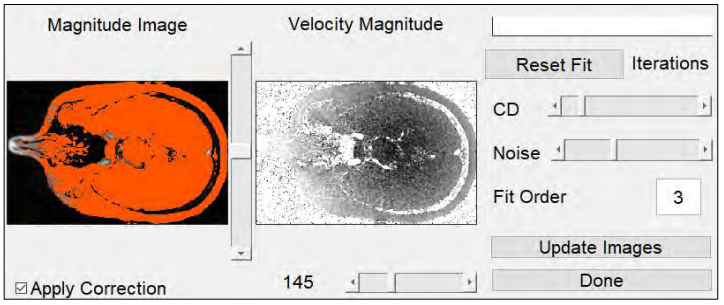

Figure 1: Manual BPC processing in our customized MATLAB GUI. The orange mask (left) overlaid on the magnitude image represents voxels identified as static background based on CD and noise thresholds (right).

Results: All 4 BPC methods were successfully evaluated on all 10 subjects. Average $\overline{MAE}$ across subjects was: **1**) 2.35±0.97 cm/s (no BPC) **2**) 0.89±0.29 cm/s (manual); **3**) 0.80±0.24 cm/s (automatic); **4**) 0.80±0.24 cm/s (automatic+manual). The automatic BPC outperformed the manual BPC and no BPC methods. Using both automatic and manual BPC resulted in negligible changes in phase correction. After manual BPC, the average CD threshold was 11.2±4.0% (of the lowest velocity values) and the noise threshold was 25.5±4.0% (of the highest magnitude values). The reconstruction used a fixed CD threshold of 8% and noise threshold of 30%.

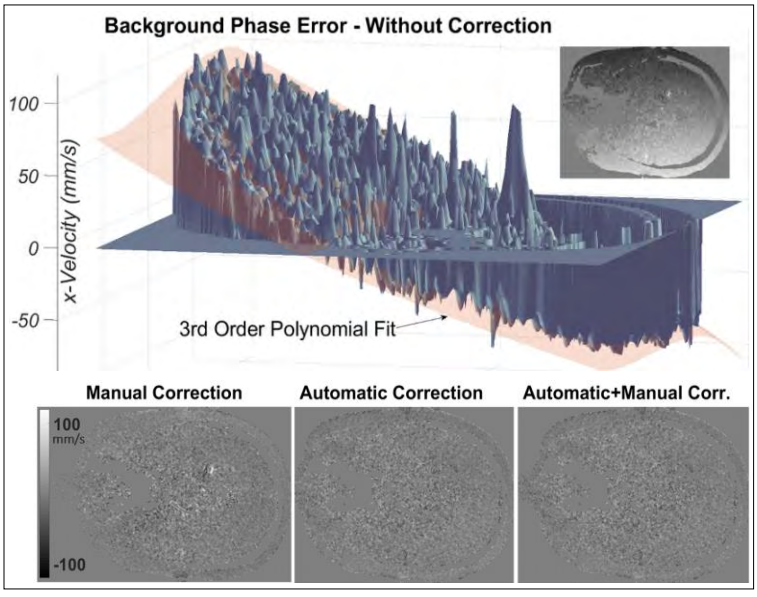

Figure 2: Surface plot of velocity (x-direction) before BPC depicting phase errors in static tissue for a single slice. The polynomial fit is shown in light red. 2D images of before and after BPC for each method is shown.

Discussion: It is concluded that automatic reconstruction BPC is sufficient (in fact, more accurate [p=0.005] than user-based threshold choices) in correcting BP errors in 4D flow brain scans. The fixed thresholds used in the reconstruction were more conservative in estimating static tissue compared to the manually-generated threshold values. Automatic BPC will result in greater reproducibility and will allow for a completely automated reconstruction post-processing pipeline. Without user interaction, the post-processing time of our 4D flow cranial analysis is estimated to reduce by ~90% (300s to 25s). These results might not apply to other body regions that can more prone to motion artefacts, e.g. from breathing.

References: [1] Nayak, K. et al JCMR 2015;17:71. [2] Chernobelsky, A. et al, JCMR 2007, 9:681-5. [3] Walker, P.G. JMRI 1993,3:251-30. [4] Gatehouse JCMR 2010 12:5. [5] Johnson, K. M. et al MRM. 2008; 60(6), 1329-1336.

Towards Single Breath-Hold Whole-Heart Coronary MRA Via Cross-Domain Deep Learning

Yibin Xie[1], Yuhua Chen[1,2], Qi Yang[3], Chengxi Yan[3], Anthony Christodoulou[1], and Debiao Li[1,2]

[1]Biomedical Imaging Research Institute, Cedars-Sinai Medical Center; [2]Department of Bioengineering, University of California Los Angeles; [3]Department of Radiology, Xuanwu Hospital.

Purpose

The early promise of coronary MRA as a noninvasive, radiation-free imaging tool for evaluating coronary artery disease (CAD) has not fully materialized to date. Despite years of technical improvements, long scan time and unreliable image quality due to motion remain the major roadblocks to its wider clinical translation[1]. In this paper we present an alternative approach to seek vast acceleration (10x) in coronary MRA acquisition by deep learning high-resolution head MRA. We aim to shorten a whole-heart coronary MRA scan to a single breath-hold, in order to improve robustness and clinical practicality.

Methods

Coronary and Head MRA: with institutional approval and informed consent, we enrolled 126 patients with known or suspected CAD who had been scheduled to undergo invasive coronary imaging. Contrast-enhanced coronary MRA were acquired within one week prior to coronary catheterization on a 3T MRI system (MAGNETOM Trio; Siemens Healthineers). A well-established ECG/navigator-gated protocol with slow contrast infusion was used[2]. Main imaging parameters included: 0.20 mmol/kg of Gd-DOTA (Dotarem; Guerbet Group) injected at the rate of 0.30 mL/s; FoV = 218x350x72mm^3; resolution = 1.3mm isotropic (interpolated to 1.0mm); iPAT = 2x (GRAPPA); and scan time = 5'32"±1'49". High-resolution TOF head MRA data from 569 healthy subjects were sourced from the NITRC neuroimaging data repository[3] with the following parameters: FoV = 240mm isotropic; and resolution = 0.8mm isotropic.

Super-resolution reconstruction: the proposed super resolution (SuperRes) framework is based on our recently developed 3D Multi-level Densely Connected Super-Resolution Networks[4]. Low-resolution (LowRes) MRA was generated by down-sampling in k-space with the following steps: 1) converting the original MRA image into 3D k-space data by applying FFT; 2) down-sampling by truncating the outer 3/4 of the k-space in each of the 2 phase encoding directions (head-foot and anterior-posterior); 3) converting the k-space data to LowRes image by applying inverse FFT and interpolating to the original image size. This process closely mimicked the actual acquisition of LowRes images. All images were divided into patches with size of 64x64x64. A total of 102 coronary MRA and 569 head MRA were included in the experiment after excluding incomplete and motion corrupted data. A total of 49/455, 12/57, and 41/57 coronary/head MRA were used for training, validation, and testing, respectively.

Results

Figure 1 shows a representative case of typical quality comparing the visualization of coronary arteries between different image sets using invasive angiography as the reference. In this example, original MRA image (**1A**) shows a high-grade stenosis (yellow arrow). LowRes image (**1B**) after down-sampling is non-diagnostic, showing obscured vessel delineation and false impression of stenoses distally (red arrows). SuperRes image (**1C**) shows restored anatomical details of the vessel segment and preserved indication of stenosis as compared with the reference x-ray angiography (**1D**).

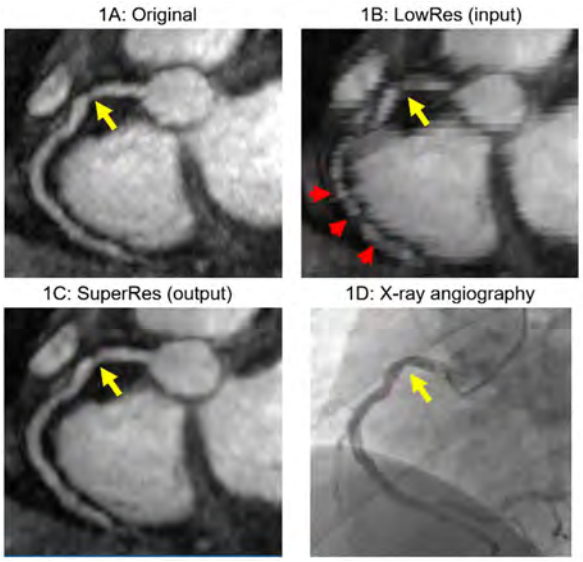

Figure 2 summarizes the quantitative evaluation of image quality and vessel sharpness in the testing group (N=41). Compared with LowRes images, SuperRes images showed significantly reduced Root Mean Square Error (0.24±0.02 vs. 0.14±0.01, P<0.001, **2A**), significantly increased Peak Signal-to-Noise Ratio (29.4±1.5 vs. 33.9±1.6, P<0.001, **2B**), and improved Structural Similarity Index (0.76±0.03 vs 0.87±0.03, P<0.001, **2C**). Vessel sharpness measurements[5] showed no significant difference between SuperRes images and original MRA images (0.57±0.29 vs 0.63±0.35, P=0.56, **2D**).

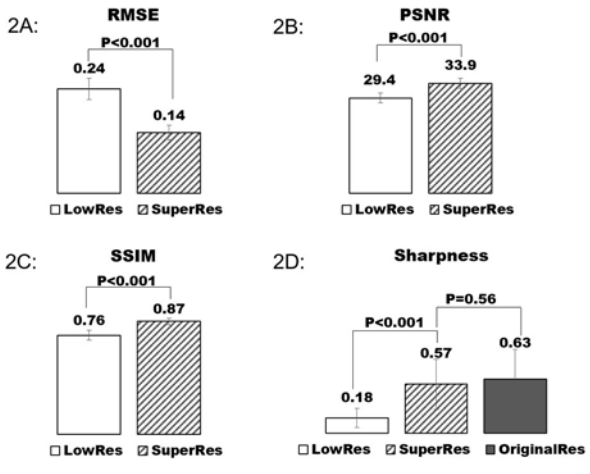

Discussion

A deep learning super-resolution framework is developed to recover lost spatial details in 10x under-sampled coronary MRA data by cross-domain training in high-resolution head MRA. Significant improvements in image quality were observed with the proposed method compared with low-resolution input images, and vessel sharpness appeared to be preserved compared with the original images. Initial validation of the technique with invasive angiography indicated equivalent performance in detecting lumen stenosis. This study demonstrated a potential approach of whole-heart coronary MRA with one breath-hold. Systemic blinded evaluation of its diagnostic accuracy is currently in progress.

References

[1]. Dweck MR, et al. *JACC CVI*, 2016; [2]. Yang Q, et al. *JACC*, 2009; [3]. Kennedy DN, et al. *Neuroimage*, 2016; [4]. Chen Y, et al. *Proc IEEE-ISBI*, 2018; [5]. McCarthy RM, et al. *Radiology*, 2003.

Is it possible to improve near-wall 4D flow MRI measurements with deep learning?

Hemanth Devarapalli[1], Sean Rothenberger[2], Kimberly Stevens[2], Julia Taylor Rayz[1] and Vitaliy L Rayz[2]
[1]Computer Information Technology, Purdue University; [2]Biomedical Engineering, Purdue University

Purpose: 4D flow MRI is capable of time-resolved 3D measurements of blood flow, however the accuracy of measured velocities is affected by low spatiotemporal resolution, and limited velocity dynamic range. Acquiring 4D flow measurements in cerebral aneurysms is particularly challenging due to small vessel sizes and complex flow fields.[1] 4D flow acquisitions resolve dominant flow features, such as high velocity jets and large-scale flow recirculation, while small flow structures and near-wall layers characterized by both low velocities and high velocity gradients, remain under-resolved and contaminated by noise. The larger scales of the flow are determined by subject-specific vascular geometry and global flow conditions, thus varying across the patients and lesions. Our hypothesis is that the smaller scales are entirely determined by the local flow dynamics and, therefore, could be reconstructed if the dominant flow structures are known. For example, by knowing the velocity a few voxels away from the wall, one can determine the velocity in the voxels adjacent to the wall. Likewise, given the faster velocities in the outer region of a vortex, one can reconstruct the slower velocities in at the vortex's center. In this study, we investigate the feasibility of using deep learning (DL) approach to reconstruct flow boundary layers formed near the wall. In order to test the hypothesis, a neural network is trained on analytical solutions of several classic flow fields and then used to reconstruct flow fields contaminated by non-uniform noise, which particularly affects near-wall voxels. Improving the accuracy of near-wall velocity data obtained with 4D flow MRI will allow reliable calculation of clinically-relevant hemodynamic factors, e.g. wall shear stress and oscillatory shear index.

Methods: Our proposed network architecture is based on Densely Connected Super Resolution Network[2]. To test the concept, the network was applied to steady flow fields contaminated by noise, including flow in cylindrical and elliptical channels and rotating flow between concentric cylinders. These simple flow fields can be viewed as the building blocks (sub-volumes) of complex physiological flows observed in aneurysmal vessels. The noise level in the voxels adjacent to the walls was higher than that added to the core of the flow. Multiple sub-volumes were taken from each data set and used to train the network and augment synthetic velocity data. Since 4D flow voxels contain three velocity components, applying pooling to get a single value at each voxel will result in information loss. Instead, we have three parallel densely connected layers for each vector dimension. The outputs of these parallel layers are assembled back to form a single volume. This assembled volume is used to calculate the error, which is back-propagated. As all three parallel layers are trained simultaneously, the network is able to learn the vector's inter-dimension dependencies. We use Mean Squared Error for the loss and flatten the vectors into their constituent dimensions to calculate the structural similarity (SSIM) to measure the quality of the output.

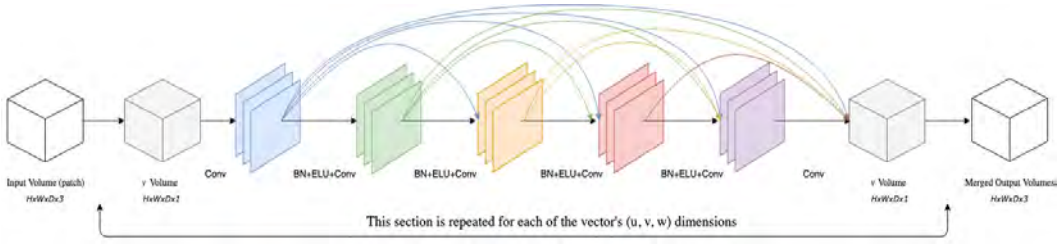

Figure 1: Proposed Network Architecture - 3D Densely Connected Network with separate paths for each

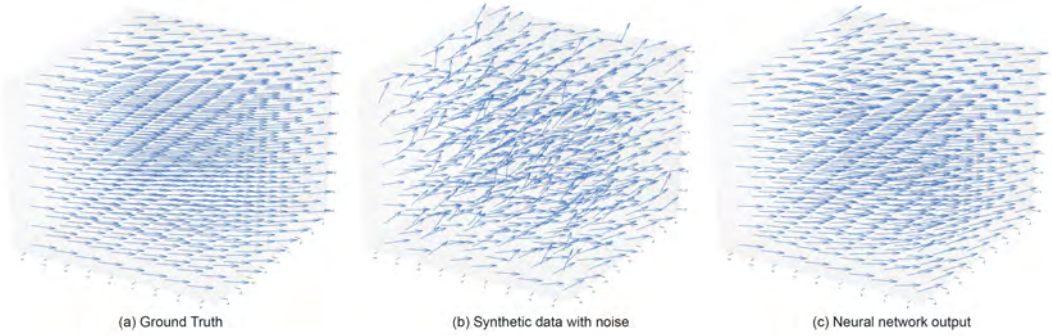

Figure 2: Velocities fields obtained with (a) analytical solution; (b) Synthetic data with added noise; and (c) Velocity reconstructed with deep learning

Results: The dataset of 6 flow fields, resulting in 1076 sub-volumes, is split into training, validation, and testing datasets with a 7:1:1 ratio. On training for 10 epochs, with 10000 iterations each, our proposed architecture achieves a SSIM of 0.8454 on the test set.

Discussion: Preliminary results indicate the feasibility of DL approach for improving the accuracy of 4D flow MRI measurements by reconstructing velocities in the near-wall layers. The neural networks trained on analytical flow fields were able to eliminate noise and correct velocity values in the voxels adjacent to the wall. The proposed algorithm will be applied to both in vitro and in vivo 4D flow data in order to further test the DL approach to 4D flow enhancement.

References: [1] Schnell S, Ansari SA, et al. Three-dimensional hemodynamics in intracranial aneurysms: influence of size and morphology, J Magn Reson Imaging, 2014. [2] Chen Y, Shi F, et al. Efficient and accurate MRI super-resolution using a generative adversarial network and 3D multi-Level densely connected network, ISBI 2018

Quantifying dynamic characteristics of BAV and associated hemodynamics using same-day echocardiography and MRI

Jeesoo Lee[1], Nadia El Hangouche[2], Ashitha Pathrose[1], James D Thomas[2], Michael Markl[1,3] and Alex Barker[4]
Departments of [1]Radiology, [2]Cardiology, and [3]Biomedical Engineering, Northwestern University, Chicago, IL USA
[4]Department of Radiology, University of Colorado Denver, Denver, CO, USA

Purpose: Bicuspid aortic valve (BAV) is one of the most common congenital heart diseases and is marked by unpredictable progression into a wide spectrum of disease ranging from minor valve sclerosis with no hemodynamic alterations to severe valvulopathy (stenosis and regurgitation) and aortopathy requiring extensive surgical interventions. Predictors of complications are unknown, and a need exists for improved imaging of biomarkers of disease. Conventional cardiac MRI combined with 4D flow MRI has been able to provide comprehensive investigation between the valve morphology and altered hemodynamics.[1] However, due to the limited temporal resolution and heart movement during acquisition, dynamic characteristics of an aortic valve (AV) and proximal flow field are difficult to quantify by MRI. On the other hand, echocardiography (echo) can capture valve motion and flow change in real-time with a high temporal resolution (~10 ms or less). Therefore, the purpose of this study is to better understand BAV by characterizing dynamic valve motion and surrounding flow with echo combined with valve morphology and hemodynamics by MRI acquired on the same day.

Methods: The cohort consists of 7 BAV patients without stenosis (age 37.4±11.7, 3 female, 6 LR, 1 RN fusion) and 36 healthy volunteers (age 51.7±18.7, 20 female). Valve opening and closing time were measured using an M-mode image generated from an echo B-mode scan (fig.1). The acceleration and deceleration time of transvalvular flow and LVOT flow were measured by using velocity waveforms obtained from continuous wave and pulsed wave Doppler echo, respectively. All timing measurements were corrected according to Bazett formula to consider heart rate variabilities between subjects. Valve morphology was characterized using 2D cine MR images acquired at the valve in a short-axis plane, and quantified by relative orifice area, orifice eccentricity and orifice aspect ratio. 4D flow MRI data was used to compute peak systolic 3D aortic wall shear stress (WSS) over the surface of the aorta.[2] Maximum wall shear stress was calculated for four different regions in the ascending aorta (proximal and distal with inner and outer region, fig.2a).

Results: A summary of the measurements and comparison between the BAV patients and healthy volunteers are shown in the table below. No significant difference was observed in valve opening, closing, transvalvular flow acceleration and deceleration times. However, the acceleration time of LVOT flow was significantly prolonged by 31% for the BAV patients ($p<0.001$). Morphology characterization revealed BAV patients had higher orifice eccentricity, aspect ratio and lower relative orifice area than controls. Maximum WSS at the ascending aorta was significantly increased for the BAV patients by 23% and 20% in the proximal inner and outer regions, respectively, and 52% and 75% for the distal inner and outer region, respectively. Increase in WSS in the proximal ascending aorta was associated with increasing orifice eccentricity (inner: $r=0.38$ $p=0.015$, outer: $r=0.33$, $p=0.035$), and decreasing valve closing time (inner: $r=-0.48$ $p=0.017$, outer: $r=-0.54$, $p=0.007$, fig.2b). LVOT flow acceleration time was weakly correlated with orifice aspect ratio ($r=0.30$, $p=0.058$).

Discussion: Same-day echo and MRI data enabled investigation of both static and dynamic characteristics of valve and surrounding flow as well as compare measurements across modalities. Opening and closing time of BAV were similar to normal trileaflet valves, despite the fusion of two leaflets that may have altered its structural property. The similar valve motion timings may also explain similar acceleration and deceleration timings of transvalvular flow. Regardless of the valve type, closing time is increased with decreasing peak systolic WSS in the proximal ascending aorta. Since low WSS indicates that a flow induces less friction to a wall, the correlation may suggest less interaction between the valve and flow indicated by low WSS would result in more relaxed valve closing. A typical elliptical orifice shape of BAV was well presented in aspect ratio with the increase in location bias quantified by eccentricity. Also, it was found that the higher the aspect ratio, the longer the LVOT took flow to reach its peak; this may indicate BAV needs higher pressure in a left ventricle to allow the blood to enter the aorta. This study was limited by the small number of BAV patients, which will be addressed in the future.

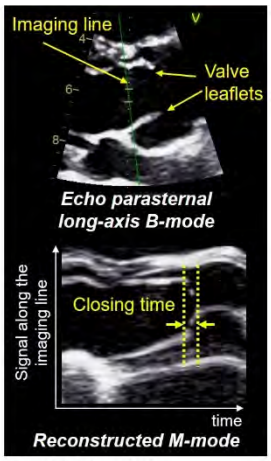

Fig.1 Valve timing measurement

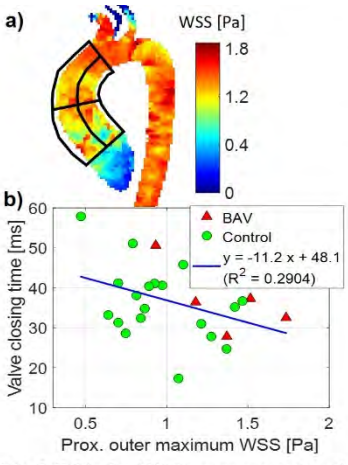

Fig.2 ROIs for WSS assessment and comparison with valve closing time

Table 1. Summary of measurements

	BAV	n	Control	n	p
Valve motion timing [ms]					
Opening	30.2 ± 6.4	5	29.8 ± 7.8	28	0.93
Closing	36.9 ± 7.6	5	36.3 ± 9.1	19	0.89
Transvalvular flow timing [ms]					
Acceleration	72.5 ± 5.4	7	77.4 ± 15.4	36	0.41
Deceleration	241.5 ± 19.2	7	237.0 ± 15.4	36	0.67
LVOT flow timing [ms]					
Acceleration	123.4 ± 19.5	7	93.5 ± 18.9	36	<0.001
Deceleration	218.8 ± 22.4	7	233.8 ± 21.6	36	0.11
Valve morphology					
Relative orifice area [%]	42.8 ± 5.1	7	48.1 ± 6.9	34	0.067
Orifice eccentricity [%]	14.2 ± 6.1	7	8.1 ± 4.4	34	0.028
Orifice aspect ratio	1.44 ± 0.1	7	1.10 ± 0.07	34	<0.001
Max. 2% WSS [Pa]					
Prox. Inner Aao	1.53 ± 0.29	7	1.24 ± 0.23	36	0.008
Prox. Outer Aao	1.50 ± 0.27	7	1.24 ± 0.25	36	0.02
Dist. Inner Aao	1.40 ± 0.28	7	0.92 ± 0.24	36	<0.001
Dist. Outer Aao	1.42 ± 0.50	7	0.81 ± 0.23	36	0.003

References:

[1] Mirabella, L., et al., Annals of biomedical engineering (2015)

[2] Potters, W. V., et al. JMRI (2015).

Multi-Modality Flow Analysis in Cerebral Aneurysms: Mass Conservation in 4D Flow and CFD Data

S.M. Rothenberger[1], J.C. Muskat[1], S. Schnell[2], C.J. Goergen[1] and V.L. Rayz[1]

[1]Weldon School of Biomedical Engineering, Purdue University; [2]Radiology, Northwestern University School of Medicine

Purpose: Hemodynamic forces are known to affect cerebral aneurysm progression. Most studies investigating intra-aneurysmal blood flow dynamics used computational fluid dynamics (CFD) to obtain velocity fields in patient-specific geometries. While providing detailed velocity distribution and flow-derived metrics, CFD models rely on multiple assumptions. On the other side, *in vivo* velocity measurements in cerebral aneurysms can be acquired with time-resolved three-directional phase-contrast MRI (4D flow MRI).[1] 4D flow MRI can be affected by limited spatiotemporal resolution and velocity dynamic range, thus reducing the accuracy of cerebral flow measurements. Intra-aneurysmal flow quantification can be improved by combining MR imaging and computational results. For merging velocities on a voxel-by-voxel basis, it is necessary to determine the error of each modality. In this study, we investigated the effects of the limited spatial resolution and dynamic range on the mass conservation of the flow in cerebral aneurysms.

Methods: Blood flow velocities in five cerebral aneurysms were measured with dual-venc 4D flow MRI at Northwestern University. The dual-venc 4D flow MRI sequence with a shared reference scan[2] was developed for capturing complex flow of slow and fast velocities without velocity aliasing. Time-of-flight MRA data were also acquired for these patients. Patient-specific models of the aneurysmal arteries were generated using TOF MRA and flow fields were computed using the solver Fluent (ANSYS Inc, USA). The inlet and outlet flow waveforms were based on the flow rates in the proximal and distal arteries measured with 4D flow. For each case, the computed flow fields were co-registered with the 4D flow data and interpolated on the grid of MRI-voxels for quantitative comparison. In addition, *in vitro* 4D flow MRI measurements were acquired in a scaled model of an ICA aneurysm. The 1:1 and 2:1 scaled models were fabricated using 3D printing and connected to a flow loop. Velocity measurements in both models were acquired with both dual- and single-venc 4D flow MRI, resulting in a total of four datasets. The flow conditions in both models matched those measured *in vivo*. For all cases, the local flow divergence was calculated to determine mass conservation errors. In order to compare the divergence across the models with different flow rates, the divergence was normalized by the upper venc value and image voxel size.

Results: For all aneurysms, there was a qualitative agreement between the flow fields acquired with single- and dual-venc 4D flow MRI and those computed with CFD. A voxel-by-voxel comparison of the velocity magnitude and direction indicated that the dual-venc reduced the discrepancy between CFD and MRI results. For all patients, the dual-venc 4D flow reduced the divergence relative to the single-venc 4D flow. The interpolated, voxel-averaged CFD data was also characterized by non-zero divergence. For all patients, the effect of the resolution for 4D flow and CFD is shown in Fig. 1. For the in vitro results, the dual-venc 4D flow acquisition reduced the spread of normalized divergence by 8.3%, and 22.8% for the 1:1 and 2:1 aneurysm models respectively. Scaling the model reduced the spread of the normalized local divergence by 54.8% and 62.0% for the single- and dual-venc 4D flow acquisitions, respectively (Fig. 2). In all cases, the divergence was increased near the wall, which can be explained by lower velocities, under-resolved steep velocity gradients and partial volume effect.

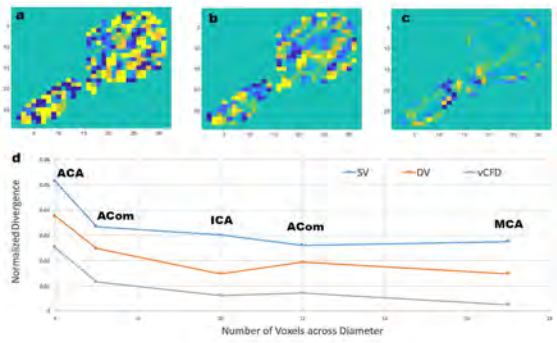

Figure 1. Flow divergence: cross-section of an MCA aneurysm for a) single-venc 4D flow; b) dual-venc 4D flow; c) voxel-averaged CFD. d) Divergence for 4D flow MRIdepends on the aneurysm size.

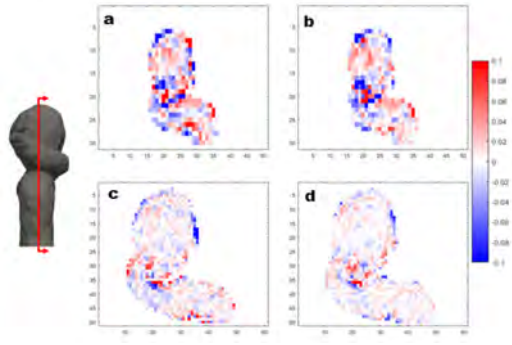

Figure 2. Divergence computed for single and dual-venc 4D flow MRI in ICA aneurysm models a) 1:1 single-venc b) 1:1 dual-venc c) 2:1 single-venc and d) 2:1 dual-venc.

Discussion: The study demonstrated the effects of the 4D flow dynamic range and spatial resolution on divergence of the measured velocity fields. While CFD does not provide the "ground truth", the computations are not affected by dynamic range and resolution and therefore can provide complementary information for the imaging results. In addition to improved imaging of low velocites in cerebral aneurysms, dual-venc 4D flow MRI improves mass conservation of the acquired flow. Understanding the contribution of the dynamic range and spatial resolution to the measurement error of 4D flow MRI is crucial for combining imaging and computational velocity data.

References: [1] Schnell et al. J Magn Reson Imaging, 2014. [2] Schnell et al. J Magn Reson Imaging, 2017

Twisting jet through stenotic bicuspid aortic valve, a 4D flow MRA insight

Nadia El Hangouche[1], Jeesoo Lee[2], James D Thomas[1], Michael Markl[3]
Departments of [1]Cardiology, [2]Biomedical Engineering, and [3] Radiology Northwestern University, Chicago, IL USA

Background: Bicuspid aortic valve (BAV) is a common congenital disease characterized by fusion of two aortic cups transforming the aortic valve orifice from round to ovale. The natural history of BAV is marked by progressive sclerosis and calcification of the aortic leaflets leading to stenosis and/or regurgitation, ultimately requiring surgical intervention. Furthermore, patients with BAV frequently have aortopathy leading to progressive dilation of the aortic root. It is recently described that the pattern of cusp fusion alters the wall shear stress distribution due eccentricity of the jet propagation downstream of the aortic valve. We sought to better characterize the jet emanating from the elliptical orifice of a stenotic BAV.

Methods: Patients were imaged using Simens Aera 1.5T MRI scanner with 4D flow sequences. The velocity magnitude distribution was extracted using Ensight 10.0 software.

Results: The cohort consists of 7 BAV patients without stenosis (6 left to right, 1 right to non coronary cusp fusion), 3 BAV patients with severe stenosis and 36 healthy volunteers. Panel A shows an axial representation of the velocity magnitude distribution at the aortic valve plan level, in a normal healthy volunteer (A1), a patient with BAV and no aortic stenosis (A2) and a patient with BAV and severe aortic stenosis (A3). Sagittal reconstructions were made according to the two axis illustrated in panel A3, along the short and long axis of the bicuspid aortic valve orifice as illustrated in panel B1 and B2 respectively. A multislice short axis along the propagation of the aortic flow is represented in panel C (C1 to C8), C1 starting at the level of the valve then every 9 mm downstream.

Discussion: The jet consistently spread out in the reconstruction along the short axis of the elliptical BAV orifice, which is distinct from the long axis where reconstrucion showed convergence of the boundaries of the jet after about couple of centimeters of propagation downstream before diverging (panel B2). Multislice transverse reconstruction along axis of the jet (panel C) clearly show that the jet shape aligns with the orifice long axis at the origin, becoming circular between 2 to 3 cm downstream, and reverses its orientation by 90°. Such axis-switching is predicted by differential interaction of the jet with traveling vortices.

Conclusion: The downstream progression of jet through a stenotic BAV is marked by the switching of its geometrical axes which can have important consequences on wall shear stress distribution.

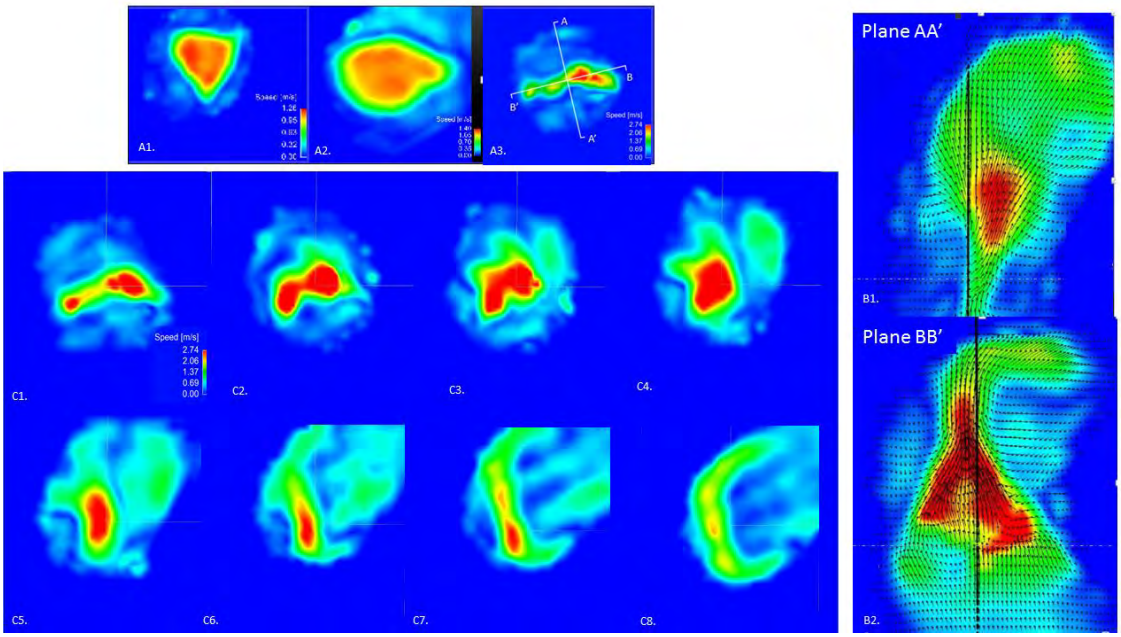

Deep Learning for Domain-invariant MR Carotid Artery Wall Segmentation

Anna Danko,[1,2] Roberto Souza,[2,3] Richard Frayne[2,3]

[1]Medical Sciences Graduate Program, Cumming School of Medicine, University of Calgary, Calgary, AB, Canada, [2]Seaman Family MR Research Centre, Foothills Medical Centre, Calgary, AB, Canada, [3]Radiology and Clinical Neuroscience, Hotchkiss Brain Institute, University of Calgary, Calgary, AB, Canada

Purpose: Magnetic resonance (MR) is frequently recommended for carotid artery imaging because of its capacity for multiple imaging contrasts, allowing it to resolve several plaque components and thus, better evaluate stroke risk.[1] Quantitative carotid artery assessment typically begins with manual segmentation, a slow process requiring qualified professionals. Deep learning has been proposed as a solution to manual segmentation, but despite achievements in computer vision, deep learning application in biomedical contexts has been limited.[2] Deep learning models trained on medical images often suffer from a lack of generalizability, *i.e.*, performance suffers when tested on new data-sets due to domain shift.[2] We propose that a model trained on a pre-existing data-set can better generalize to a new data-set by encouraging the model to learn contrast-invariant features through adversarial training. By selecting for features which are present in multiple contrasts, the model is forced to differentiate between important features (which are present across all contrasts) and conflating information, such as contrast-specific noise.

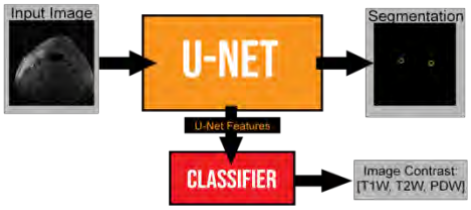

Figure 1 The proposed network schematic

Methods: The network contains two opposing components: segmentation and classification (Figure 1). The segmentation portion consists of a U-Net [3] that takes carotid images and predicts the segmentation as a mask. Features generated at the end of the U-Net encoding path, prior to max-pooling, are sent to the classifier. The classifier, which is a basic convolutional neural network, predicts the image contrast of the original image based on the features extracted by the U-Net. The loss function is inspired by the generalized adversarial network (GAN) loss function [4] and improves when the U-Net extracts features that the classifier cannot match to a specific contrast. Training data was collected from 26 atherosclerosis patients imaged locally as part of the AIM-HIGH MR sub-study,[5] and included PD-, T1- and T2-weighted images, all acquired without using contrast agent. Cross validation was done using ten of these subjects. The test data included five T1-weighted images acquired with a DANTE-Cube sequence,[6] from an ongoing local study (CARDIS). Contours for the AIM-HIGH data were provided by a central core facility (Vascular Imaging Laboratory, Seattle, WA [5]). The training data was divided into patches and underwent data augmentation during training. The model trained on all contrasts concurrently. The resulting segmentation with a threshold = 0.5, was compared to the output of an unmodified U-Net. Receiver-operator characteristic (ROC) curves, area under the curve (AUC) and Dice scores were calculated. The adversarial and unmodified U-Nets are referred to as ADV and Non-ADV, respectively.

Results: The ADV and Non-ADV models produced comparable segmentations (Figure 2). Both models were sensitive to image variations in the CARDIS test set, resulting in median Dice scores < 0.50. In comparison, when tested on AIM-HIGH data, both models achieved a median Dice score of 0.70. For 4 of 5 CARDIS subjects, the AUC for the ADV segmentations were higher than the non-ADV model (Table 1). Example ROC curves are shown in Figure 3.

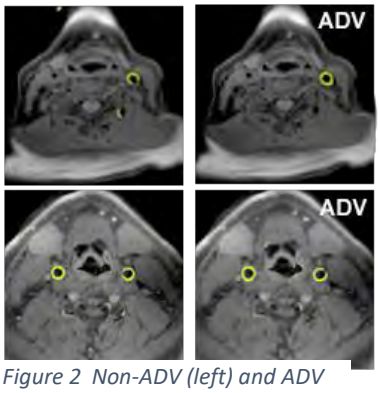

Figure 2 Non-ADV (left) and ADV (right) segmentations.

CARDIS Subject	Area under the Curve	
	Non-ADV	ADV
1	0.55 ± 0.06	0.65 ± 0.05
2	0.64 ± 0.04	0.70 ± 0.07
3	0.42 ± 0.07	0.60 ± 0.05
4	0.56 ± 0.05	0.77 ± 0.05
5	0.85 ± 0.04	0.85 ± 0.08

Table 1 This table lists the average (mean ± standard deviation) AUC from all ROC curves over the five CARDIS subjects.

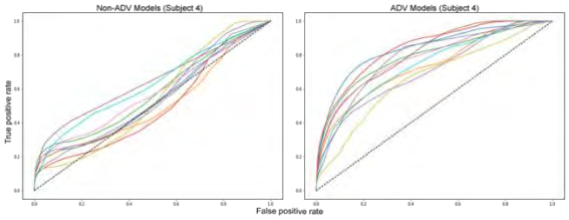

Figure 3. The Non-ADV (left) and ADV (right) ROC curves for Subject 4. The different colours represent correspond to different cross-validation folds.

Discussion: Both ADV and non-ADV models scored low on the unseen data-set (CARDIS), which was expected due to domain shift between the AIM-HIGH and CARDIS data-sets. The Dice scores, presumably, could be improved by incorporating additional pre-processing techniques on difficult slices, as well as, by increasing the number of training epochs used. Both ADV and non-ADV models produced comparable segmentations on the CARDIS data. The ROC curves, however, suggest that the ADV model is more capable of distinguishing the carotid artery vessel than the non-ADV model. This difference was more pronounced at lower thresholds. These results encourage further investigation into the use of adversarial training for overcoming domain shift.

References: 1. Saba L, *et al.*, *AJNR 2018*: **39**: E9-E31. 2. Kamnitsas K *et al*. *Information Process Med Imaging* 2017: 597-609 3. Ronneberger O *et al*. *CoRR* 2015 absL/1505.04597 4. Goodfellow IJ. *Adv Neural Inf Process Syst* 2014: 2672-2680 5. Zhao XQ, *et al.*, *Am J Cardiol* 2014: **114**: 1412-1419 6. Xie Y *et al*. *Magn Reson Med*. 2016; **75**: 2286-94.

Image processing of Phase contrast Magnetic Resonance Imaging to investigate cerebral blood flows.

Olivier Balédent, Pan Liu, Serge Metanbou, Malek Makki.
Chimère 7516, University of Picardie Jules Verne, Amiens University Hospital Amiens, France.

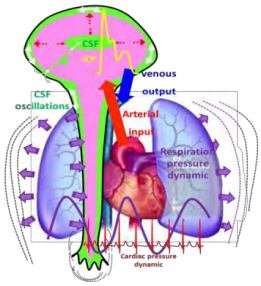

Purpose:Phase Contrast sequence (PCMRI)[1] is the unique technique to quantify in around 1-minute blood and CSF in the cranium to provide a mean flow curve of the cardiac cycle. Limitations of normal-PC exist. It is difficult, long and inaccurate to measure blood flows if patients present cardiac arrhythmia or if the cardiac signal quality is not good or if patient move. It is also not possible to take in account the breathing impact that can affect the blood flow. It is well known that respiratory movement's impacts intracranial pressure, cerebrospinal fluid flows and cerebral blood flows[2]. Nevertheless such flows investigations were not possible and stay uninvestigated! New Phase contrast MRI sequence based on Echo Planar imaging (EPI-PCMRI)[3] can now produce continuously a velocity map, more or less every 100 ms function of the machine and of the quality wanted. EPI-PCMRI provides hundreds images and need dedicated software to extract the venous and arterial flows and fully analyze those curves and their interactions. The aim of this work was to apply EPI-PCMRI to investigate cerebral blood flow by using a new image processing dedicated software.

Methods: The study was performed on a 3T scanner, with gradient strength of 40 mT/m and slew-rate of 200 T/m/s. A 32 channels head coil was used. Ten adult volunteers were included to investigate blood flow in their internal carotids and basilar arteries and in their straight and sagittal sinuses. Software was developed to segment automatically the blood vessels and extract each cardiac cycle and organize them function of the respiratory period.

	EPI PCMRI
TR	6.39
TE	3.44
temporal resolution (ms)	113
FOV	140*140
Angle:	30°
images/cardiac cycle	8-12
NB images	300
Nb of acquired cycles	30-40
duration	34 sec
Slice thickeness	4 mm
Spatial resolution	2*2 mm²
VENC cm/sec	60
Sense factor	2,5
EPI turbo factor	3

Results: Arterial cerebral blood flows was 970±290 ml/min and venous cerebral blood flows was 620±150 ml/min. Arterial and venous blood flows during inspiration were 10% higher than during expiration. Mean intracranial vascular blood volume change during cardiac cycle was 0.6±0.2 ml not significantly different between expiration and inspiration.

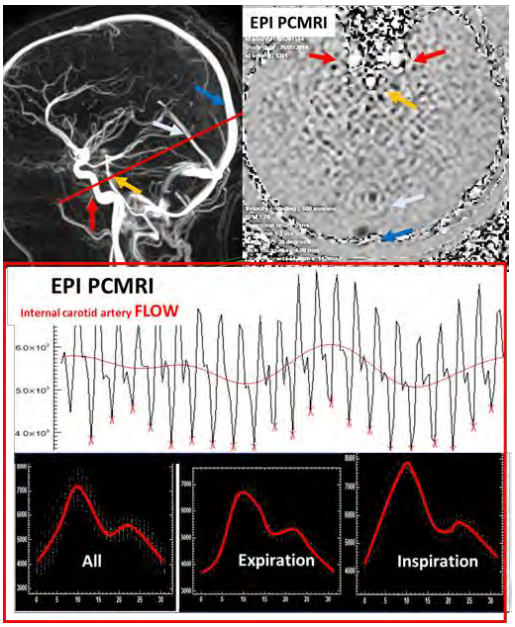

Discussion: EPI-PC images were good enough to quantify blood flows without important artefacts due to EPI acquisition. These preliminary results have shown how respiratory impact in the same way both arterial and venous cerebral blood flows. Cerebral blood volume change calculated was not impacted by breathing. But because this volume is very small this result should be interpreted with caution and need more important investigations to be confirmed. This new real time EPI-PC sequence is useful to investigate cerebral blood flow in few seconds without any cardiac or respiratory gating but needs a convivial and accurate post processing tool to be easily used in clinical practice. Such new flow investigations open new ways to better understand cerebral vascular pathologies.

References: **(1)** Feinberg D.A., Mark A.S. Radiology 1987.
(2) Skytioti M et al. Eur J Appl Physiol. 2017.
(3) Chen L et al. NeuroImage 2015.

Elucidating Vascular Etiologies of Erectile Dysfunction Using Dynamic MR Angiography

Alexandra Roudenko MD[1] Rand N. Wilcox Vanden Berg, MD[2] Christopher Song, MD[1] Darius A. Paduch, MD, Ph.D.[2]
Daniel Margolis, MD[1] Martin R. Prince, MD, Ph.D.[1]
[1] Radiology [2] Urology Weill Cornell Medicine

Purpose: Erectile dysfunction (ED) presents significant quality of life issues and is experienced by men of all ages. Organic etiologies may account for ED symptoms in up to 14.8% of men under 40 with other studies suggesting up to 87% of men may have an organic component to their ED[1,2]. Vasculogenic ED may be due to impaired arterial inflow and/or abnormal veno-occlusive mechanisms. Magnetic Resonance Angiography (MRA) has the potential to elucidate anatomic variants suggested by penile Doppler ultrasound (PDUS) or history without subjecting patients to invasive procedures or ionizing radiation. Our goal was to utilize dynamic MRA in men with suspected aberrant vascular anomalies contributing to their ED symptoms.

Methods: Adult men with signs of early shunting of blood on PDUS were invited to undergo time-resolved MRA following intracavernosal injection of erectogenic agent. 29 MRA examinations were performed on 26 patients to evaluate arterial inflow (Figure 1) and venous outflow. 3D spoiled gradient echo time-resolved imaging with stochastic trajectories (TWIST) was acquired in the coronal plane with fat suppression with parallel imaging with 3-fold acceleration and a 4.6sec temporal update rate. Anatomic co-localization and tissue characterization was performed with axial and sagittal T2 weighted images, Axial T2 weighted images with fat saturation, and axial and coronal VIBE-DIXON pre and post contrast images.

Figure 1: Normal arterial anatomy on MR angiography

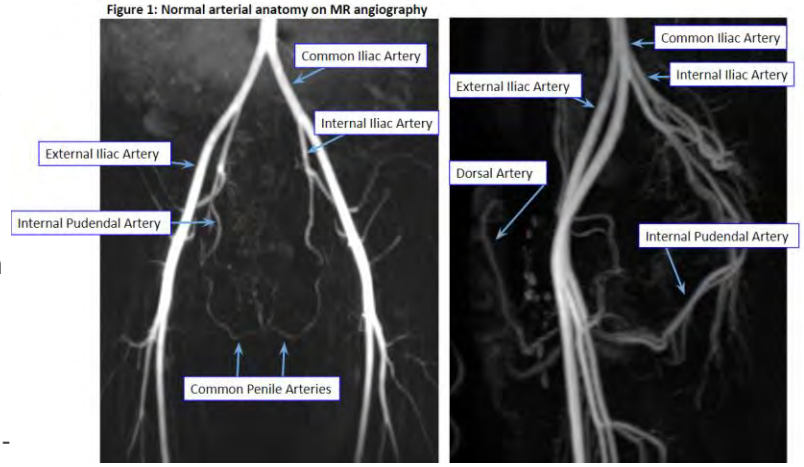

Results: Of the 29 MRA examinations, 2 patients had incomplete tumescence limiting evaluation. Of the remaining examinations, 22 patients demonstrated abnormal early venous drainage (Figure 2), 3 had a vascular plexus visualized without early venous drainage, and one patient had combined arterial inflow and venous outflow disease. Additionally, 3 patients had delayed and diminutive cavernosal enhancement compatible with arteriogenic disease. Timing data was also analyzed with opacification of iliac arteries on average 33.3 sec after contrast injection and common penile arteries on average 5.7 sec later. Dorsal and cavernosal arteries often seem at the same time although slightly earlier average time to dorsal artery visualization likely due to several patients with arteriogenic ED. Abnormal early venous drainage was on average 14 sec after iliac artery opacification and systemic veins visualized on average 22.9 sec after iliac arteries.

Figure 2: 37 yo M with ED. A. Arterial phase with asymmetrically prominent left dorsal artery. B.Early venous enhancement of vascular malformation at the left ventral glans of the penis. Systemic veins are not yet visualized.

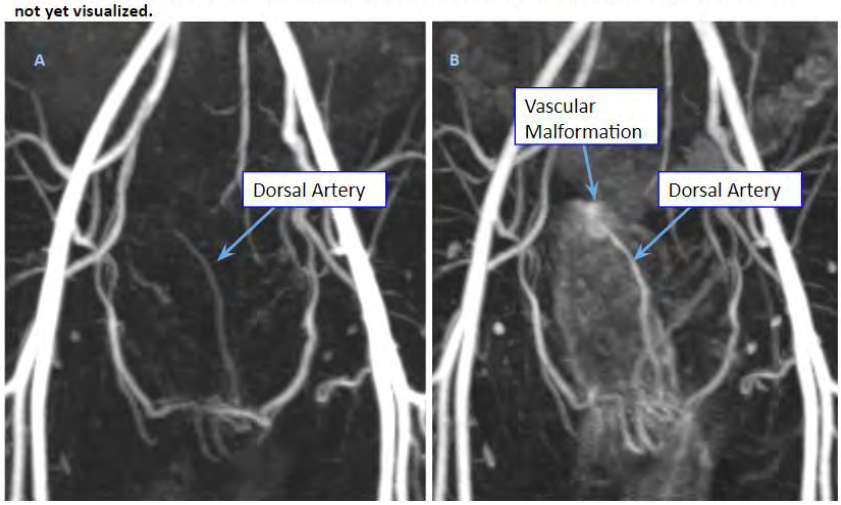

Discussion: Time resolved MRA allows for excellent temporal and spatial resolution and is a versatile non-invasive technique. We have customized a protocol specific for evaluation of vascular etiologies of ED which allows for imaging of intrapenile vasculature as well as evaluation of abnormal inflow and outflow as an etiology of ED.

References

1. Caskurlu T, Tasci AI, Resim S, et al: The etiology of erectile dysfunction and contributing factors in different age groups in Turkey. Int. J. Urol. Off. J. Jpn. Urol. Assoc. 2004; **11**: 525–9.
2. Donatucci CF and Lue TF: Erectile dysfunction in men under 40: etiology and treatment choice. Int. J. Impot. Res. 1993; **5**: 97–103.

Quantitative Assessment of Cerebral Aneurysms on Vessel Wall Imaging MRI

MD Alexander[1,2], AD DeHavenon[3], JS McNally[1], A Elkhetali[3], DL Parker[1], SE Kim[1], P Taussky[2], R Grandhi[2]
Department of Radiology and Imaging Sciences[1], Neurosurgery[2], and Neurology[3], University of Utah, Salt Lake City, UT, USA

Purpose: Vessel wall MRI (vwMRI) techniques have provided new tools for evaluation of cerebrovascular disease by allowing visualization of vessel walls themselves. Such techniques can be used in the evaluation of intracranial aneurysms. Enhancement in particular can be helpful in evaluation, with prior studies demonstrating an association between aneurysm enhancement and growth. Prior reports have also shown that aneurysm size correlates with post-contrast wall enhancement on vwMRI. These prior studies have been limited by qualitative approaches to enhancement that are inherently subjective and susceptible to bias. Additionally, further characterization of vwMRI findings following endovascular treatment of aneurysms is needed. To further evaluate this association, this study employed quantitative approaches to determine the enhancement characteristics of aneurysm walls on vwMRI, including treated and untreated aneurysms.

Methods: According to an IRB-approved protocol, prospectively maintained records were queried to identify patients undergoing vwMRI for analysis of unruptured cerebral aneurysms at a major academic medical center. Patient demographic and clinical data were tabulated. All images were acquired on a Siemens Prisma 3T MRI scanner. A board-certified neuroradiologist identified the maximum signal in the aneurysm wall on T1-weighted SPACE with DANTE images both before and after the administration of gadolinium contrast. For each variable measured, the mean of three data points was computed after obtaining the maximum single-voxel intensity values at each site of interest. Aneurysm sizes were also measured on the concomitantly acquired MRA images, as well as digital subtraction angiography (DSA), when available. Linear regression was used to correlate the outcome and predictor variables adjusted for potential confounders, including ethnicity, smoking, hypertension, aneurysm location, and treatment modality. The final model included potential confounders using a backwards stepwise selection for variables with $p<0.1$. Finally, bidirectional student's t-test was performed to compare these values between the treated and untreated groups, and linear regression was performed to assess for association between ΔWS and time since treatment.

Results: Thirty six vwMRI studies were performed during the evaluation of 23 patients with 27 unruptured cerebral aneurysms (7 fusiform, 20 saccular). Among these, ten patients also had delayed DSA, with time between initial imaging and follow up DSA being 294 (±270) days. Mean ΔWS was 1.55 (±0. 46), and mean maximum aneurysm measurement on MRA was 7.36 mm (±6.09). Seventeen aneurysms were treated, with locations and treatments summarized in Tables 1 and 2, respectively. In univariate analysis, ΔWS was associated with change in maximum aneurysm diameter (β coefficient = 3.53, 95% CI = 1.70-5.36, $p = 0.002$). In the final multivariate regression

model, ΔWS remained associated with change in maximum aneurysm diameter (β coefficient = 3.65, 95% CI = 1.05-6.25, p = 0.015). ΔWS was significantly higher in treated versus untreated aneurysms (1.91±0.68 vs. 1.50±0.41, p=0.039). For treated aneurysms, ΔWS was not associated with number of days between aneurysm treatment and vwMRI acquisition (n=23, p = 0.912). When controlling for thrombosis status among the treatment group, no change was noted.

Table 1: Aneurysm Location

ICA/Pcomm	10
AComm	2
Vertebrobasilar	3
PICA	1
PCA	1
Total	17

Table 2: Embolization Technique

Coiling	1
Balloon-Assisted Coiling	5
Stent-Assisted Coiling	1
Flow Diversion	6
Flow Diversion + Coiling	3
Vessel Sacrifice	1
Total	17

Discussion: vwMRI techniques are effective in the evaluation of cerebral aneurysms. Using quantitative techniques that improve upon prior methodologies of vwMRI analysis, this confirmed previous findings of an association between enhancement in the aneurysm wall on vwMRI and aneurysm size. Additionally, it confirmed the previously reported association between enhancement in aneurysm walls and growth on subsequent imaging. This augments prior research with more quantitative metrics less prone to bias. This study also characterizes persistent enhancement of previously treated lesions, in some cases with enhancement visualized years after embolization and in some lesions with confirmed post-treatment occlusion. Such persistent enhancement following aneurysm embolization should be considered a normal finding and does not appear to reflect presence of residual aneurysm or risk of recurrence. These findings demonstrated the utility of vwMRI in the evaluation of cerebral aneurysms.

Prevalence of IVC stenosis in Autosomal Dominant Polycystic Kidney Disease

Xiaorui Yin[1], MD, Sadjad Riyahi[1], MD, Jon D. Blumenfeld[2,4], MD, Hanna Rennert[3], MD, Irina Barash[2], MD, MS, Martin R. Prince, MD, Ph.D.[1]
[1] Radiology [2] Medicine, [3] Pathology, Weill Cornell Medicine, [4]The Rogosin Institute

Purpose: We noticed severe inferior vena cava (IVC) narrowing by extrinsic compression from renal cysts in a patient presenting with acute deep venous thrombosis. Another of our ADPKD patients presented with circulatory collapse during pregnancy and intrahepatic IVC compression caused by liver cysts that had grown during pregnancy. Here we examine MRI from 216 patients in an ADPKD research repository to identify the prevalence of IVC compression by renal or hepatic cysts compared to age gender matched patients without ADPKD.

Methods: ADPKD patients (n=216) and age/gender matched controls (n=216) scanned at 1.5T with axial/coronal SSFSE T2-weighted images and axial SSFP were evaluated for IVC stenosis from extrinsic cystic compression. To assess hemodynamic significance of stenosis, IVC area at stenosis (or mid-IVC in subjects without stenosis), proximally at iliac vein confluence, and distally at mid liver were measured. The IVC pressure below the stenosis was estimated by the left to right diameter divided by anterior to posterior diameter ratio with a value of 1 corresponding to a circular (high pressure) IVC.

IVC Parameters	ADPKD(n=216)	Controls(n=216)	P value
Mild IVC stenosis (50% to 75%)	55 (25%)	1 (0.4%)	<0.001
Severe stenosis (>75%)	35 (16%)	1 (0.4%)	<0.001
IVC LR/AP ratio	1.49±0.60	1.70±0.57	<0.0001
IVC lumen area (mm^2)			
hepatic	263 (98; 754)	278(75;664)	0.08
Mid or site of max narrowing	109 (12; 545) 132±90	136 (34;362) 150±68	0.01
At iliac vein confluence	262 (80; 569) 276 ±93	216 (56; 502) 222±86	<0.0001

Table 1. prevalence of IVC stenosis.

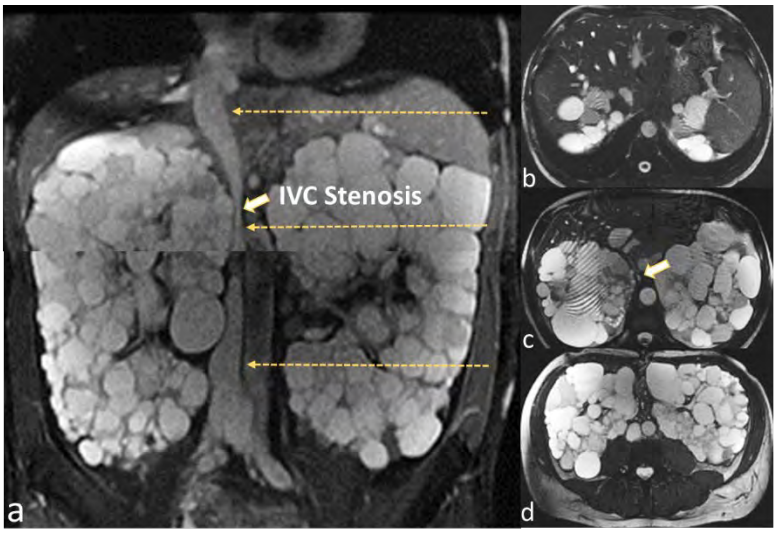

Figure. ADPKD patient with renal cysts compressing IVC (a) arrow. Axial images (b,c,d) show lumen narrowing (arrow) at IVC stenosis (c) and round shape to IVC proximal to stenosis (d) just above iliac vein confluence.

Results: IVC stenosis 50% to 75% was found in 55 (25%) ADPKD subjects and severe stenosis >75% in 35 (16%) compared to 1 (0.4%) control (p=<0.001). These stenoses were associated with dilation and a more rounded IVC shape with a lower LR/AP diameter ratio upstream from the stenosis, Tables 1 and 2, indicating elevated IVC pressure.

Parameters	No stenosis N=124	Mild stenosis N=55	Severe stenosis N=35
IVC LR/AP ratio	1.69±0.67	1.27±0.39	1.16±0.27
IVC lumen area (mm^2)			
hepatic	326±142 298(99; 754)	243±95 241(118; 554)	205±81 200(98; 437)
Mid or site of max narrowing	152±102 130(12; 545)	116±69 103(20; 273)	57±36 49(13; 154)
At iliac vein confluence	273±98 262(80; 569)	284±85 269(137; 486)	274±89 253(129; 479)

Table 2. IVC measurements.

Discussion: Our findings by MRI in ADPKD patients identified hemodynamically significant extrinsic compression of IVC by kidney and liver cysts with one associated with DVT and another associated with circulatory collapse. Spontaneous IVC thrombosis and hypotension has been previously reported in ADPKD patients with similar MRI findings as case reports (1-3). These case control data show that 16% of ADPKD patients have severe IVC compression with evidence of hemodynamic effects. Given the risk of DVT, IVC thrombosis and hemodynamic compromise under these circumstances, and the potential for other complications (e.g., peripheral edema, decreased exercise tolerance), routine assessment for IVC compression on cross-sectional imaging in ADPKD may be warranted.

References

1. Hepatogastroenterology. 2003; 50: 2188-91
2. Intern Med. 2004;43: 209-12.
3. Intern Med. 2010;49:1891-4.

A Single Reference variable Flip Angle Method for accurate dynamic T_1 quantification

Seong-Eun Kim[1] Bryant Svedin[1], Adam de Havenon[2], Matthew Alexander[1], J Scott McNally[1] and Dennis L Parker[1]

[1]UCAIR, Department of Radiology and Imaging Sciences, [2]Department of Neurology, University of Utah,

PURPOSE: T_1 weighted signal increase has been used to estimate uptake of paramagnetic contrasts such as Gadolinium (Gd)[1] on carotid atherosclerosis. T_1 is directly related to the uptake of contrast agent on the plaque over time[2]. Variable flip angle (VFA) techniques have been previously investigated to calculate T_1 where two FA alternate[3]. This can lead to possible errors if the transition from each FA steady state is not handled correctly, and must be performed with 3D acquisitions for small plaque size. This work implements a single reference (SR) VFA method using a 3D pseudo golden angle stack of stars (PGA-SOS) sequence[4] that provides a new 3D dynamic T_1 measurement for accurate contrast uptake within vulnerable carotid plaques.

METHODS: This method acquires a single reference image at the lower flip angle and all dynamic images at the higher angle. T_1 is calculated using a single reference VFA method, which accounts for the reference image T_1 remaining constant. Monte Carlo simulations determined the optimal dynamic flip angle for T_1 measurement. With IRB consent, we acquired dynamic T^1 acquisitions from four patients with carotid disease. Imaging parameters of 3D a PGA-SOS were: 0.7 mm isotropic dimension, 24 slices, TE/TR = 2.46/5.62 ms, 1518 projections. Images were reconstructed using a symmetric sliding k-space weighted image contrast (KWIC) window with 377 total and 13 innermost projections[4] giving an effective temporal resolution of 2.29 s.

RESULTS:Fig 1 shows dynamic T1 maps of a patient with carotid atherosclerotic plaque at t = 10ms(a) and t = 350ms(b). The T1 value of the plaque was deceased from 570±84 ms (red contour in (a)) to 275±48ms (b). The dynamic percent T_1 changes in the plaque (area1, Fig 1a) and normal wall (area 2) indicate the more active contrast uptake within the plaque comparing to the wall. The dynamic percent changes on four different carotid atherosclerotic plaques acquired from four patient studies were plotted on the Fig 2**.**

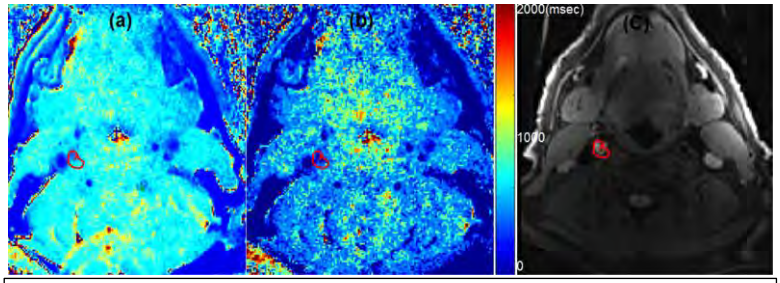

Fig 1 T1 map of a patient with carotid atherosclerotic plaque at (a) 10ms and (b) 350ms

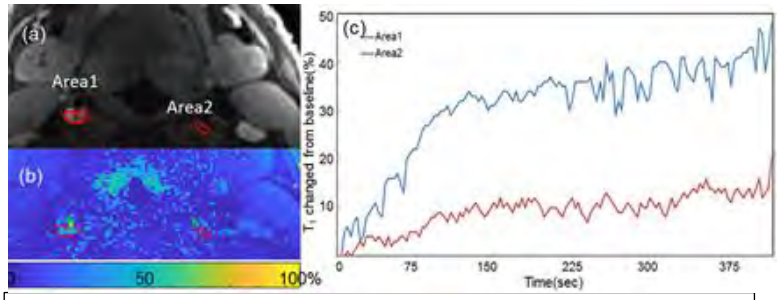

Fig 2 Peak time percent T_1 change map (b) and the dynamic percent T_1 changes (c) in area 1(plaque) and area 2(normal wall) ROIs (a).

DISCUSSION: The SR-VFA T1 method provides the possibility for dynamic T_1 measurement with high temporal and spatial resolution when combined with a PGA-SOS sequence reconstructed with a sliding KWIC window. The dynamic percent T_1 changes can provide the direct contrast uptake quantification, which may be more predictive of plaque vulnerability and a better metric to monitor treatment effects compared to visual inspection. The precision of the T_1 measurement can be optimized with proper choice of FA. Using a VFA method will amplify noise through its nonlinear nature of calculating T_1. For standard VFA, the ideal choice of FA will produce ~71% of Ernst angle signal with the two FA on different sides of the Ernst angle. A more accurate estimate of the percent of the Ernst angle signal could be simulated with much finer FA increments, or possibly an exact estimate could be derived[5].

REFERENCES:

1. Swartz RH, et al.Neurology 2009;72;6272.
2. Nicolle GM, et al. Chem Eur J. 2002:8-9.4.
3. Cheng HL et al. Magn Reson in Med. 2006: 55:566 –574.
4. Svedin BT, et al. Magn Reson Med. 2018 Mar;79(3):1407-1419.
5. Schabel MC et al. Phys Med Biol 2009;54(1):N1-8.

Determining the Number of Neck Shape-Specific Coils Required to Image the General Population

JR Hadley[1], R Merrill[1], M Beck[1], SE Kim[1], BD Bolster[2], S McNally[1], DL Parker[1]
[1]Department of Radiology and Imaging Sciences, University of Utah
[2]Siemens Medical Solutions

Introduction

We have developed prototype neck shape specific anterior neck coils that result in high SNR in the anterior neck (1). Because these coils integrate well with the OEM head coil, posterior neck and spine coils, the neck exam can be performed without removing the OEM coils from the table, allowing efficient imaging of the complete neurovascular system. We report on our experience that indicates the number of shapes needed for our carotid patient population.

Methods

Dividing neck shapes into short, medium and long necks and narrow, medium and wide necks, would indicate that up to 9 different formers could be needed to image all possible neck shapes. Because smaller necks can be imaged in a larger coil, development of a smaller coil is only justified if it provides a significant improvement in SNR.

In preliminary plans for the neck-shape-specific coils, formers were molded to fit necks of different people that were of a similar build to patients with carotid disease. Based on these formers, three different 3D printed shapes have been developed and used on a large number of research subjects and patients. Each coil has 7 loops (channels) that increase in length and width with the coil shape and thus provides the sensitivity desired for the given neck shape. Over the last 4 years, our institution has performed 179 carotid scans (160 males and 19 females). These studies were all performed on Siemens 3T MRI scanners including PrismaFit, Skyra, Verio and Trio scanners. Coil selection for these studies has been based on the fact that smaller patients can fit in the larger coils.

Results

We have determined that the majority of patients can be imaged with 3 different sized neck coils as shown in Fig 1. The resulting diameter/height for the small, medium and large coils are 10/7.2 cm, 12.7/7.8 cm, and 18/8.8 cm, respectively. Of the 179 subjects, nearly all were imaged in the medium neck-shape coil. A very small number required the large size coil. All subjects fit into at least one of the 3 coils. The small size has been recently developed and shows a substantial increase in SNR for those subjects with narrow necks.

Discussion

Although a full range of sizes and shapes were not available, our experience indicates that the great majority of subjects can be imaged well with the medium size coil. If subjects fit into none of the 3 shapes, the fall back option is to use the OEM anterior neck coils. This scenario has not happened at our institution. Future work will be to further characterize the SNR improvements that can be obtained by using the smallest fitting coil in this patient population.

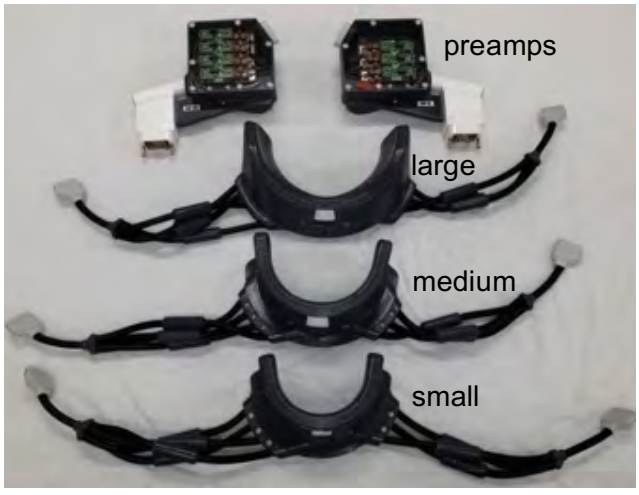

Figure 1: Three different sizes of Shape-Specific Neck coils.

References: 1. Beck et al. Interchangeable neck shape-specific coils for a clinically realizable anterior neck phased array system, Magn Reson Med. 2017 Dec;78(6):2460-2468.

We report the general results of the initial 3 shapes. , we report on our experience applying a set of these coils to our carotid artery patient population, to determine the number of different shaped coils needed to image the variations of neck anatomy of the general public

Initial Cardiac MR experience with a novel 84-element coil

Martijn Froeling, Mark Gosselink, Dennis Klomp, Tim Leiner
Department of Radiology, Center for Imaging Sciences, Utrecht University Medical Center, Utrecht, The Netherlands

Background

Cardiac MR (CMR) is a powerful modality for comprehensive assessment of myocardial structure and function. However, long acquisition times and multiple breath holds make the modality relatively expensive and difficult to sustain for patients with shortness of breath. Here we describe initial results with a prototype 72-element coil array, which will be part of a future 224 channel array.

Materials and Methods

Prior work by our group has demonstrated the theoretical and practical feasibility of highly accelerated CMR using an array consisting of a large number of small surface coils[1,2]. For the present study a dedicated high-density 72-channel cardiac array (MRCoils, Zaltbommel, Netherlands) was used in combination with the 12 channel Philips posterior coil. Measurements were performed on a Philips 3T Ingenia system with dStream architecture (Philips, Best, Netherlands). First, to evaluate the acceleration performance, a standard 2D B-SSFP CINE protocol was used (TE = 1.5ms, TR = 3.0ms, FOV 270x270mm, voxel size = 2x2x12mm, FA = 45 degrees, frames = 40). Both short axis and 4 chamber acquisitions were obtained with 2-7 SENSE acceleration. Next, a 3D bTFE sequence was used to accelerate in two directions up to SENSE 12 (RL-AP, 3x4); TE = 1.0ms, TR = 2.0ms, FOV 288x288x399mm, voxel size = 3x3x3mm, FA = 70 degrees). Finally, an optimized M2D B-TFE protocol for real-time cardiac MRI was performed (TE = 1.5ms, TR = 3.0ms, FOV 300x300mm, voxel size = 2x2x8mm, FA = 45 degrees, CS = 9) For all scans we used the default Philips reference scans and reconstruction.

Results

Noise correlation, covariance matrix, coil sensitivity and simulated g-factor map of the 72-channel coil setup are shown in figure 1. In figure 2, 2D cine images of the LVSA view (34 fr 10s BH, 8 cardiac phases) with SENSE 3 are shown. In the right panel, 6 single cardiac phase 2D cine (34fr 10s BH, 8 cardiac phases) with C-SENSE9 are shown.

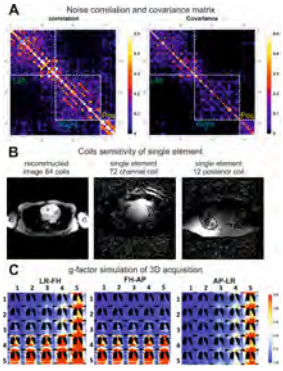

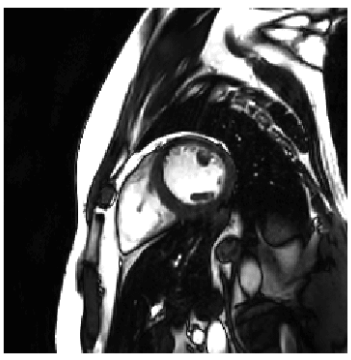

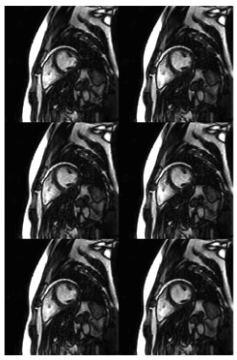

Conclusions

In initial testing our novel 72-element cardiac MR coil enabled highly accelerated cardiac CINE imaging in 2D and 3D. We demonstrated up to 7x SENSE and 9x C-SENSE acceleration in 2D, with substantial loss in SNR, but without noticeable SENSE artifacts which is not feasible with using the standard manufacturer provided hardware. In future work we plan to add second 72 channel cardiac coil to further accelerate acquisitions.

References

1. Gruber B. et al. A 256-channel Cardiac Coil for accelerated Cardiac Imaging at 3 Tesla - Evaluation of a 32- channel Prototype. Proc Int Soc Magn Reson Med 2018: 4290.
2. Gosselink M. et al. Highly accelerated cardiac imaging using a high-density 72 channel local receiver array at 3 Tesla. Proc Int Soc Magn Reson Med 2019: 1908.

PAVES Challenge: Automatic Segmentation of femoral artery and vein using 2.5D Multi-task Learning

Rui Huang[1,2], Matthew Ng[1,2], Jun Gao[3,4], Zhengyu Lin[5,6], Jun Ma[7], Fumin Guo[2], Graham Wright[1,2]
[1]Department of Medical Biophysics, University of Toronto, Toronto, Canada, [2]Sunnybrook Health Science Centre, University of Toronto, Toronto, Canada, [3]Department of Computer Science, University of Toronto, Toronto, Canada, [4]Vector Institute, Toronto, Canada, [5]Faculty of Medicine, Shanghai Jiaotong University, Shanghai, China, [6]Faculty of Science and Engineering, Sorbonne University (ex Pierre et Marie Curie University), France, [7]Department of Mathematics, Nanjing University of Science and Technology, China

Introduction

Occlusive peripheral arterial disease (PAD) is a common circulatory problem whereby narrowed arteries reduce blood flow to the limbs [1]. Detailed assessment of the below-the-knee arteries is critical in planning interventions to salvage a critically ischemic leg. Magnetic Resonance Imaging using steady-state free precession (SSFP) acquisitions provides high spatial resolution visualization of the vessel wall and areas of wall thickening/stenosis which may be used as the target for intervention. However, the image acquisitions take several minutes, during which the gadolinium contrast medium is distributed throughout both arteries and veins, resulting in "venous overlay" that makes it difficult to interpret small arteries.

This work aims to develop a fully automatic segmentation algorithm based on a deep learning method using multi-task learning to separate arteries and veins in high resolution MR images. We think that the generated arterial and venous segmentation could greatly aid in procedural planning for limb salvage.

Methods

Dataset, preprocessing, and reference segmentation:

Due to the large workload associated with manual vessel segmentation, we initially picked only the first 4 patients out of the 32 DICOM datasets provided by the PAVES challenge host. These are all of 0.5mm isovolumetric acquisition with both arterial and venous opacification. Each data set consists of 832 axial sections covering both legs, with varying in-plane matrix sizes of 192 × 832, 224 × 832, 192 × 832, and 176 × 832. We consider each leg as a separate training target and cropped each in-plane section into 2 images (matrix size = 192 × 416) each containing a single leg.

For artery segmentation, we manually labelled the artery on every 5 to 10 transverse sections and the reference segmentation of the remaining slices were obtained through linear interpolation using ITK-SNAP (http://www.itk-snap.org). For the whole vessel segmentation, we utilized a 3D level-set approach (provided by ITK-SNAP) initialized by manual seeds and refined when deemed necessary. These segmentations were refined by an expert reader and used as a reference standard for algorithm performance evaluation.

Automated segmentation algorithm:

We employed a U-net deep convolutional neural network (DCNN) [2] for automated artery and whole vessel segmentation. The model utilizes 3x3 kernels and Rectified Linear Unit (ReLU) consisting of 32 layers in total. The U-net model was implemented in 2.5D and utilized a stack of 5 adjacent axial sections as inputs to provide segmentation of the centre slice by exploiting the longitudinal information about vessels [3]. We performed data augmentation including horizontal and vertical shifting between 0 and 25 pixels, random horizontal flipping, random rotation up to 30 degrees as well as random scaling by 0.6 to 1.0 times. The output contains two binary predictions each of which produces a binary cross-entropy loss (BCE). We combined the two losses as the total loss by adding them up with equal weights. The trained U-net models were used to generate artery and whole vessel masks, from which we derived the vein segmentation by subtracting the artery from the whole vessel masks.

Results

For one patient case, it took about 1.5 hours for segmenting the arteries and 0.5 hours for the whole vessel system with artery and vein combined as a whole.

All the experiments were performed using an Intel CPU, and the NVIDIA P100 GPU. Training with 4 patients' data required 9 hours on two graphic cards testing required about 40 seconds per patient with one GPU. Figure 1 displays representative test results for veins and arteries.

We implemented our network using Pytorch 1.0.0 and trained our models until convergence using the ADAM optimizer with a learning rate of 10^{-3}. The model was trained for 120 epochs and the average BCE converged to 0.002. Segmentation accuracy was evaluated using Dice Coefficient (DC) for two legs in each 3D volume of the

patient cases. Due to time limitations, we randomly chose one patient as the test set and adopted the same method as before to label the test data to obtain a rough estimation of the model performance. The DC for the whole vessel prediction is 0.878 and for the artery is 0.751. The relatively lower DC for the artery than the whole vessel may be due to the smaller region the artery covers in each axial slice.
Although by the challenge deadline we have not finished labelling all the training sets given, visual inspection of the 3D segmentation results for all the 10 test cases seemed to be relatively interpretable to the expert reader from the challenge host.

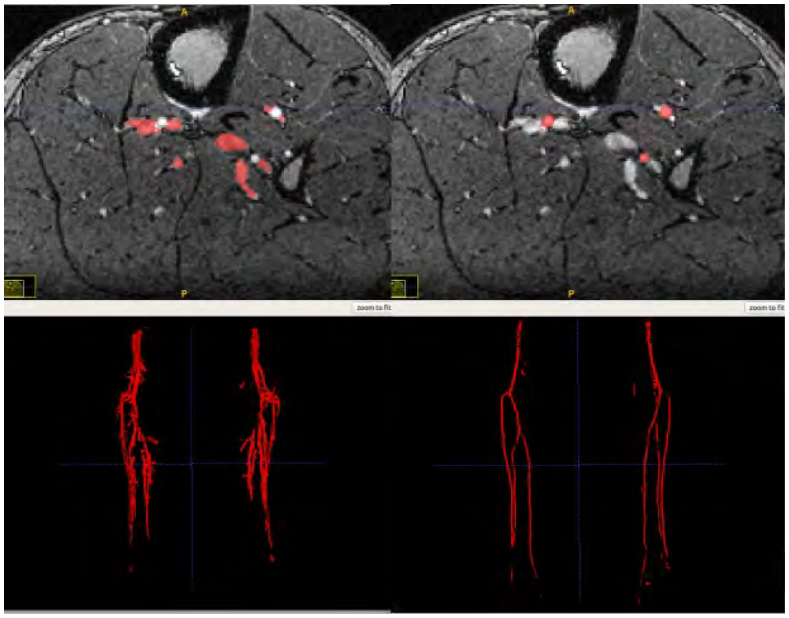

Figure 1 An example of test results in the dataset given by challenge website. The left side shows veins and the right side shows arteries. The top row shows the appearance of the segmentation results in one sample axial section; The bottom is a coronal projection of segmented vessels.

Discussion

A multi-task learning deep convolutional neural network yielded reasonable blood vessel segmentation in MR images. A 2.5D U-net could be an efficient way to segment small elongated structures, given the results in this small training set of four patients. We demonstrated visible advantages using multi-task learning compared with training two CNN models separately. Multi-task learning could not only segment both the artery and the whole vessel system through end-to-end training but also potentially eliminate the pixel classification bias and increase the segmentation accuracy, which warrants further investigation [4]. Empirically more training data would potentially increase the segmentation accuracy and this will be investigate and implemented in the future. These results suggest that the introduced workflow might be useful for the relevant research and clinical applications.

References

[1] Conte, M. S. Critical appraisal of surgical revascularization for critical limb ischemia. J. Vasc. Surg. 57, 8S–13S 2013.
[2] Olaf Ronneberger, Philipp Fischer, and Thomas Brox, “U-Net: Convolutional networks for biomedical image segmentation,” in Medical Image Computing and Computer-Assisted Intervention (MICCAI). 2015, vol. 9351 of LNCS, pp. 234–241, Springer
[3] Han, X., Automatic Liver Lesion Segmentation Using A Deep Convolutional Neural Network Method. https://doi.org/10.1002/mp.12155, 2017
[4] Caruana, R., "Multi-task learning". Machine Learning. 28: 41–75. doi:10.1023/A:1007379606734, 1997

CONDITIONALLY WEIGHTED ENSEMBLE OF DEEP MODELS FOR VESSEL EXTRACTION FROM CONTRAST ENHANCED MAGNETIC RESONANCE IMAGES

Parvın HUSEYNOVA[1], N. Sinem GEZER[2], M. Alper SELVER[3]

1 Dokuz Eylul University Electrical and Electronics Engineering, Buca, Izmir, Turkey
2 Dokuz Eylul University Department of Radiology, Balcova, Izmir, Turkey
3 Dokuz Eylul University Electrical and Electronics Engineering, Buca, Izmir, Turkey

Purpose: To obtain highly accurate segmentation and classification (i.e. artery, vein) performance for the PAVES (Peripheral Artery: Vein Enhanced Segmentation) challenge, which aims retaining the high level of anatomical detail in gadolinium enhanced high resolution MRI datasets.

Methods: A new approach for providing a unique portrait of vessel extraction from MRI is proposed. Considering its content and development steps, there are three main stages of the proposed system (Figure 1):

In the first stage, the outputs of various vesselness filters are generated with different parameters (i.e. eigenvalue levels) and their outputs are combined in such a way that maximum number of targets (vessels) is collected without a penalty for false positives (FP). In other words, the aim of the first stage is preventing FNs.

Then, at the second stage, two sets of deep models are used. The first set consists of models that are initially trained with a rigorously labeled vessel dataset, which includes hepatic/portal vascular trees of the liver acquired by contrast enhanced computed tomography (40 datasets around 7000 DICOM images). These models are adapted to PAVES by re-training their last layers via transfer learning. The second set includes models trained end-to-end with PAVES training data.

Since the database do not have ground truth (i.e. expert labeled references), which can be directly used for supervised learning, approximate ground truths are generated as follows. The TWIST sequence images, which steady state sequence images, is the target for the segmentation challenge

These are the most detailed, with a spatial resolution of about 0.5 mm.

This icon turns on fusion - this will create a coloured overlay of one image on top of the other. You should now have the high signal areas of one image mapped overlaid onto the other. In this case the I used the arterial phase (TWIST sequence) on top of the “steady state” sequence. This means that the arteries are overlaid, but the veins are not.

Several models are used for varying orientation angles (axial, coronal, sagittal etc.) to obtain the best performance at each orientation.

At the third stage, a transferred network ensemble is constructed by employing a machine learning strategy to determine the weight of each deep detector in order to eliminate FPs.

Since the proposed system includes many models, their diversity and complementarity are constantly analyzed to cover the complete solution space. Promising results are being obtained as the models are fine-tuned and new models are added.

Results: We have made two important observations:

1. Several pre-trained benchmark models including feature-classifier strategies and deep networks are tested on PAVES. The outcome of these analysis show that the performances of well-established pre-trained models do not have enough accuracy on PAVES. Therefore, conditions of practical interest are highlighted under which the existing models fail. Moreover, it is also observed that utilized model performances significantly depend on the initial training set leading to poor generalization ability.
2. Due to the frustrating performances of existing systems on PAVES, alternative strategies are proposed. Since PAVES is not as comprehensive as other benchmark data sets collected for segmentation/classification in terms of labeled ground truth data, end-to-end training of deep models could not provide significant performance. Alternatively, a transfer learning (TL) based strategy is developed to adapt existing well-established models to PAVES. The results show that the adaptation provided by re-training of the last layers with PAVES results with fine-tuned models, which provide better accuracy compared to the other models trained from scratch.

Discussion: Use of the emerging deep learning based automatic segmentation algorithms can substantially increase the accuracy of the segmentation and classification of vessels. Parallel execution of multiple models allows fusion of automatic methods showing superior performance without any additional time cost. More complicated ensemble models are required to take better advantage of the strong-suits of the individual models.

References,

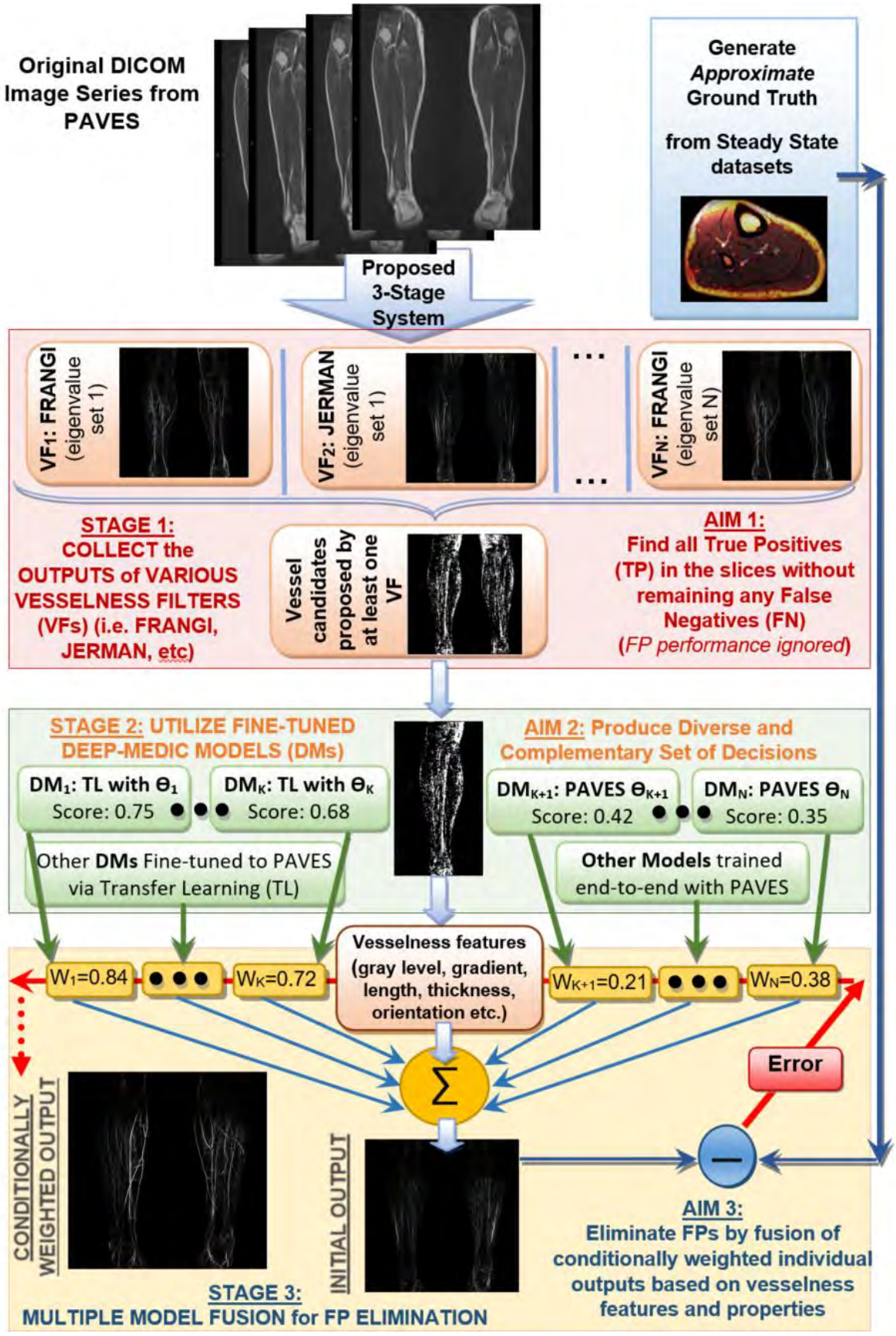
Original DICOM Image Series from PAVES
Generate Approximate Ground Truth from Steady State datasets
Proposed 3-Stage System
VF1: FRANGI (eigenvalue set 1)
VF2: JERMAN (eigenvalue set 1)
VFN: FRANGI (eigenvalue set N)
STAGE 1: COLLECT the OUTPUTS of VARIOUS VESSELNESS FILTERS (VFs) (i.e. FRANGI, JERMAN, etc)
Vessel candidates proposed by at least one VF
AIM 1: Find all True Positives (TP) in the slices without remaining any False Negatives (FN) (FP performance ignored)
STAGE 2: UTILIZE FINE-TUNED DEEP-MEDIC MODELS (DMs)
DM1: TL with Θ1 Score: 0.75
DMK: TL with ΘK Score: 0.68
Other DMs Fine-tuned to PAVES via Transfer Learning (TL)
AIM 2: Produce Diverse and Complementary Set of Decisions
DMK+1: PAVES ΘK+1 Score: 0.42
DMN: PAVES ΘN Score: 0.35
Other Models trained end-to-end with PAVES
Vesselness features (gray level, gradient, length, thickness, orientation etc.)
W1=0.84
WK=0.72
WK+1=0.21
WN=0.38
Σ
Error
CONDITIONALLY WEIGHTED OUTPUT
INITIAL OUTPUT
AIM 3: Eliminate FPs by fusion of conditionally weighted individual outputs based on vesselness features and properties
STAGE 3: MULTIPLE MODEL FUSION for FP ELIMINATION

.